

**MULTI-WAVELENGTH STUDIES ON GALACTIC
HII REGIONS**

THESIS SUBMITTED FOR THE DEGREE OF
DOCTOR OF PHILOSOPHY (SCIENCE)
IN
PHYSICS (EXPERIMENTAL)

BY

SOMNATH DUTTA

DEPARTMENT OF PHYSICS
UNIVERSITY OF CALCUTTA
JULY, 2017

To my Maa-Baba....

Acknowledgments

This thesis arose, in part, out of five years of research that I have done since I came to Satyendra Nath Bose National Centre for Basic Sciences, Salt Lake, Kolkata. This thesis would not have been possible without the help and support of the kind people around me, to only some of whom it is possible to give particular mention here.

First and foremost, I owe my deepest gratitude to my supervisor, Dr. Soumen Mondal, who has been a wonderful advisor with his great intuition on scientific problems. This thesis would not have come to the final stage without his support, useful advice and constructive feedback. I have learnt a lot from his guidance, which helped me to come up with new ideas, interesting scientific problems and most importantly to plan and carry out research by myself.

This research work would not have been completed without the active involvement of a few people around me. I would like to thank all my collaborators Dr. Jessy Jose, Dr. Ramkrishna Das, Dr. Manash Samal, Dr. Santosh Joshi. The discussion that I had with them helped me to understand the subject and to develop my own way to express my understanding of the subject.

I would like to thank Prof. Sandip Kumar Chakrabarti and Prof. Biswajit Chakraborty for several useful comments, suggestions as members of my thesis committee.

I thank all the academic and non-academic staff of SNB for providing me such a global platform, excellent research atmosphere and beautiful natural scenery. I am grateful to the Administrative staff of SNB for providing me regular monthly fellowship to carry out my research peacefully and other the necessary support during my research work.

I acknowledge the HTAC and JTAC members and technical staff of 2-m HCT, 1.3m DFOT, 1-m ST, 1.2 Mt. Abu for their assistance during observations. I thankfully acknowledge SNB library and the computer staff for their time to time help.

I would like to acknowledge my college friend Ujjal for setting up initial interest in research. I am fortunate enough to have a great friend circles, and juniors who stay very close to my heart. The memory of my daily life during my stay in S. N. Bose are eventful and enjoyable due to the presence of friends like Anindita, Biplab, Nirnoy, Chiranjit, Aslam, Kartick, Subrata, Shishir, Krishendu. Among juniors I would like to name Amit, Indranil, Debasis, Sumanta, Rakesh, Rajkumar, Alik, Rahul. I shall miss all those evenings spend in playing football at SNB football ground with Amit, Dhimadri, Samrat, Ganesh, Ransell, Subrata, Debashis, Surajit-Da, Tushar-Da, Arka-Da, which are not worth mentioning here!

I would like to thank my family for their unconditional love and support. I would like to take this opportunity to express my heart-felt gratitude to my family; Maa, Baba, elder sister, elder brother and brother-in-law for understanding me and tolerate me. It will be my audacity if I try to express their contribution in my life. Thank you very much Maa for constant support to choose my own ways of life and keeping faith on me.

And to my Wife - my love - my friend, Dipanwita, no words would be sufficient to describe the positive role played by her to help me complete this thesis. This thesis would not have been possible without her support and encouragement. Your unfailing love and support have given

me hope when needed most. Thank you very much for the strength and stamina you have created in me, you make my world ! I love you.

Finally, I would like to thank every body who played important role throughout my journey, as well as I am expressing my apology someone, I forget to mention.

Somnath Dutta
Kolkata
JULY, 2017

List of publications

Publications in refereed journal

1. The young cluster NGC 2282: a multiwavelength perspective, **Somnath Dutta**, Soumen Mondal, Jessy Jose, Ramkrishna Das, M. R. Samal, Supriyo Ghosh, 2015, Monthly Notices of Royal Astronomical Society, 454, 3597 *
2. Optical Photometric Variable Stars towards Galactic H II region NGC 2282, **Somnath Dutta**, Soumen Mondal, Santosh Joshi, Jessy Jose, Ramkrishna Das, and Supriyo Ghosh, 2017 (under review in Monthly Notices of Royal Astronomical Society)*
3. Active star formation at Galactic H II regions: the complex associated with Sh 2-149, **Somnath Dutta**, Soumen Mondal, J. Jose, Tapas Baug, M. R. Samal, 2017 (Manuscript to be submitted soon)*
4. Optical Photometric Variability in Young Stars towards Cygnus OB7 region, **Somnath Dutta**, Soumen Mondal, Santosh Joshi, 2017 (Manuscript to be submitted soon)*
5. Discovery and Phase Dependent Study of A new Mira variable MASTER Optical Transient J212444.87+321738.3 in Cygnus, Supriyo Ghosh, Soumen Mondal, Ramkrishna Das, D. P. K. Banerjee, N.M. Ashok and **Somnath Dutta** (Manuscript to be submitted)
6. Active star formation at Galactic H II region Sh 2-242, Alik Panja, Soumen Mondal, **Somnath Dutta** et al. (Manuscript under preparation)

Others

1. Stellar population and star formation histories of distant Galactic H II regions NGC 2282 and Sh2-149 complex, **Somnath Dutta**, Soumen Mondal, Jessy Jose, Ramkrishna Das, ASP Conference Series, 2016 (Under review)*
2. S. Mondal, R. K. Das, N. M. Ashok, D. P. K. Banerjee, **S. Dutta** et. al., “Near Infrared photometric and spectroscopic observations of the bright optical transient J212444.87+321738.3” , 2013, ATel #4931.

*Present thesis is based on these works.

Contents

List of Figures	viii
List of Tables	xii
1 Introduction	1
1.1 Star Formation and Giant Molecular Clouds	1
1.2 Overview of H II region	3
1.3 Triggered Star-formation in H II regions	6
1.4 Evolution of Young stars	9
1.5 H-R Diagram	12
1.6 Variable Signature of Young Stars	13
1.7 Motivation of the thesis	15
1.8 Outline of the thesis	18
2 Observations and Data Reduction	20
2.1 Telescopes and backend instruments	20
2.1.1 Photometric Data Reduction	22
2.1.2 Photometric Calibration	28
2.2 Spectroscopic reduction	29
2.2.1 Slitless spectral data	32
2.3 Archival Data sets	32
2.3.1 NIR data from WIRCam	32
2.3.2 NIR data sets from UKIDSS	33

2.3.3	NIR data from 2MASS	34
2.3.4	Mid-infrared data from <i>Spitzer</i>	35
2.3.5	Mid-infrared data from WISE	37
2.3.6	Mid and far-infrared data from IRAS	38
2.3.7	$^{12}\text{CO}(1-0)$ data from FCRAO	38
2.3.8	CO data from JCMT	39
2.3.9	Radio data	39
3	The young cluster NGC 2282 : a multi-wavelength perspective	41
3.1	Introduction	41
3.2	44
3.2.1	Observations	44
3.2.2	ARCHIVAL DATA SETS	49
3.3	Analysis and Results	51
3.3.1	Stellar density and cluster radius	51
3.3.2	Spectral Classification of Optically Bright Sources	53
3.3.3	Reddening towards the Region	56
3.3.4	Distance and Membership of the Bright Sources	57
3.3.5	Identification and Classification of YSOs	58
3.4	Discussion	65
3.4.1	Near-IR Colour-Magnitude Diagram	65
3.4.2	Optical Colour-Magnitude Diagram of YSOs	67
3.4.3	Mass Distribution	67
3.4.4	Spatial Distribution of YSOs	69
3.4.5	Disc Fraction and Age of the Cluster	69
3.5	Summary and Conclusions	70
4	Active star formation at Galactic H II regions: the complex associated with Sh 2-149	79
4.1	Introduction	79

4.2	Overview of the complex associated with Sh 2-149	81
4.3	Data Accumulations	84
4.3.1	Spectroscopic Observations	84
4.3.2	NIR Imaging	85
4.3.3	<i>Spitzer</i> -IRAC data	86
4.4	Morphology of the region	88
4.4.1	Identifying Massive stars from spectroscopic study	88
4.4.2	Optical and Infrared view	92
4.4.3	Molecular gas	94
4.4.4	Others ionizing sources	95
4.4.5	Reddening towards the complex	97
4.4.6	Young stars in the complex	100
4.4.7	Spatial Distribution of YSOs	102
4.5	Discussion	103
4.5.1	Star formation scenario	103
4.6	Conclusion	105
5	Optical Photometric Variable Stars towards Galactic H II region NGC 2282111	
5.1	Introduction	111
5.2	114
5.2.1	Observations	114
5.3	Results and discussion	117
5.3.1	Identification of variable stars	117
5.3.2	Characterization of variable stars	120
5.3.3	Period distribution	128
5.3.4	Correlation between IR excess and rotation periods and variability amplitude	129
5.3.5	Correlation between periods and masses	132
5.4	Summary and Conclusions	133

6	Photometric Variability in Young Stars towards Cygnus OB7 region	141
6.1	Introduction	141
6.2	143
6.2.1	Observations and data reduction	143
6.2.2	Archival NIR and MIR data sets	146
6.3	Identificatio of variable stars	147
6.3.1	Differential photometry	148
6.3.2	Period Estimation	150
6.3.3	Previously Known variables	151
6.3.4	New variables	152
6.4	Discussions	152
6.4.1	NIR Color-Color Diagram	152
6.4.2	Spectral index for identifying T Tauri stars	154
6.4.3	Optical Color-Magnitude Diagram	154
6.4.4	SED and physical properties of variable stars	156
6.4.5	Variability and disc correlation	156
6.5	Summary and conclusions	158
7	Summary and Future Work	164
7.1	Future Plan	169
	Bibliography	171

List of Figures

1.1	Example of H II region- RCW 82, where intense star formation activity is going on (Taken from Pomarès et al. 2009)	3
1.2	The schematic diagrams of H II regions are taken from Deharveng et al. (2010). (left) An example of spherical expanding H II region into a homogeneous medium	4
1.3	Evolutionary sequence of low-mass stars of the four classes in a similar diagram as suggested by Lada (1987) and Wilking (1989).	7
1.4	$[[3.6] - [4.6]]_0$ vs $[K - 3.6]_0$ color-color diagram for isolation of class I and Class II sources. The diagram is adopted from Gutermuth et al. 2009.	9
1.5	The four Hayashi tracks show the predicted evolutionary paths on the HR diagram	10
1.6	Example light curves and phase plots for the two periodic and irregular stars in IC 348 taken from Nordhagen et al. 2006.	15
3.1	(a) Optical color composite image of NGC 2282	43
3.2	Residuals between standard and transformed magnitudes and colours of standard stars plotted against the Landolt standard magnitudes	46
3.3	Radial density profile of the stars detected in NIR K- band towards the cluster NGC 2282.	52
3.4	Stellar surface density map of sources detected in K-band towards NGC 2282 region overlaid on the UKIDSS K-band image.	52
3.5	Flux-calibrated normalized spectra for the optically bright sources in NGC 2282.	54
3.5	continued...(H $_{\alpha}$ emission line strength	54
3.6	Extinction map over plotted on the UKIDSS K-band image.	59
3.7	Optical CMDs for all the stars within 3.15' radius of the cluster	60
3.8	Dereddened $[K - 3.6]_0$ vs $[3.6 - 4.5]_0$ CC diagram for all the sources within the cluster radius of 3.15' after removing contaminants.	60

3.9	Colour-magnitude diagrams using IRAC bands along with the candidate YSOs identified.	61
3.10	$J - H/H - K$ CC diagram of (a) NGC 2282 within 3.15' radius and (b) the reference field of same area.	63
3.11	$r - i/r - H_\alpha$ CC diagram for all the sources detected in IPHAS photometry towards NGC 2282.	64
3.12	(a) Near-IR CM diagram of the stars within 3.15' radius of NGC 2282.	66
3.13	$V/(V - I)$ CMD for the Class II sources, candidate YSOs from JHK colours and H_α emitting sources within NGC 2282 cluster.	68
3.14	J vs $(J - H)$ diagram for Class I, Class II sources, candidate YSOs detected from JHK colours and the H_α emitting sources.	68
3.15	Spatial distribution of Class I (red triangles), Class II (green circles), candidate YSOs from JHK colors (blue squares) overlaid on IRAC 3.6 μm image.	71
4.1	A low resolution FCRAO OGS $^{12}\text{CO}(1-0)$ map integrated over -49 km s^{-1} to -53 km s^{-1}	81
4.2	Optical color composite image of S149 complex	82
4.3	Color composite image of S149 complex obtained using optical emission (blue; from DSS2 survey), WISE 4.6 (green), and 12 μm (red)	84
4.4	A close-up view of S149 subregion	87
4.5	Flux-calibrated normalized spectra for the optically bright sources in S149 complex.	91
4.6	$(J-H)/(H-K)$ CC diagram of the spectroscopically classified stars in S149 Complex.	93
4.7	$J/(J-H)$ CMD for all spectroscopically classified stars in S149 complex.	93
4.8	Location of massive sources are shown in WIRCAM K -band image.	98
4.9	Extinction map overplotted on the WIRCAM K -band image.	99
4.10	IRAC CC diagram of all the uncontaminated sources identified within the region & Dereddened $[K - 3.6]_0$ vs $[3.6 - 4.5]_0$ CC diagram for all the sources	100
4.11	$K/(H - K)$ CM diagram of all stars within our target area.... & CM diagram for the control field	104
4.12	Spatial distribution of YSOs in S149 complex overplotted on the $^{13}\text{CO}(3-2)$ image	107

5.1	Optical color composite image of NGC 2282 (blue: V; green: R; red: I) obtained at 1.3m DFOT (Up is North, left is East). The cluster area is marked with white circle. Our combined monitoring observations were done at the white box region. The variable candidates are marked (see text for details).	112
5.2	RMS of the <i>I</i> -band light curves of 1627 stars towards NGC 2282.	117
5.3	Example light curves for few apparently non variable stars of different magnitude range (left three panels) and few candidate variable stars (right three panels). .	119
5.4	Example light curves of a eclipsing binary (upper panel) and probably fast stochastic variable (lower panel)	123
5.5	Example LS power spectrum of selected stars. The highest peaks are marked with red dashed lines	123
5.6	The phase <i>I</i> -band light curve of variables are shown here.	124
5.7	$(r - i)$ versus $(r - H_\alpha)$ CC diagram for all the sources detected in IPHAS photometry towards NGC 2282.	125
5.8	$(J - H)$ versus $(H - K)$ CC diagram of variable stars within 3.15' radius. . . .	125
5.9	$V/(V - I)$ CMD for variable stars towards NGC 2282.	126
5.10	A sample SED for a variable source using the SED fitting tools of Robitaille et al. (2007)	127
5.11	Distribution of periods in NGC 2282 are compared with the distributions for . .	129
5.12	Periods are plotted as a function of disk indicator NIR excess $\Delta(I - K)$	132
5.13	The light curves RMS (variability amplitude) are plotted as a function of disk indicator NIR excess $\Delta(I - K)$	133
5.14	Mass versus period is plotted for periodic variables.	134
6.1	The observed region of Cyg OB7 (Lynds 1003). The <i>I</i> -band image is taken at 1.3m DFOT	143
6.2	Residuals between standard and transformed magnitudes and colors of standard stars plotted against the Landolt	146
6.3	The observed light curve of ID6828, mean magnitude and RMS is also mentioned	147
6.4	RMS of the <i>I</i> -band differential photometric light curves of 1809 stars towards Cyg OB7 are shown in grey circles	149
6.5	Example LS power spectrum of selected stars. The highest peaks are marked with red dashed lines	150
6.6	Phase light curves of periodic variables	151

6.7	$J - H/H - K$ CC diagram of candidate variable stars in Cyg OB7.	153
6.8	$V/(V - I)$ CMD for all the sources of studied region.	155
6.9	Sample SEDs for a variable source (ID1771) using the SED fitting tools of Robitaille et al. (2007).	157
6.10	(left) Periods are plotted as a function of disc indicator $W1 - W2$ (upper panel) and NIR excess $\Delta(I - K)$ excess	157

List of Tables

2.1	Specifications of the telescopes used for our observations	22
2.2	Specifications of backend instruments, detectors and filters used for our observations	22
2.3	SExtractor Parameters	26
3.1	Log of Observations.	44
3.2	Photometric catalog of point sources towards NGC 2282. The complete table is available in the electronic form in online.	48
3.3	Details of the spectroscopically studied stars.	50
3.4	catalog of YSOs (Class I, Class II, other PMS stars and H_{α} sources).	73
4.1	Details of the IRAS sources.	83
4.2	Log of spectroscopic observations.	85
4.3	Details of the spectroscopically studied stars.	90
4.4	Physical Parameters of the massive sources.	97
4.5	Catalog of YSOs (Class I and Class II)	108
5.1	Log of Observations.	115
5.2	Catalog of the identified variable stars adopted from Paper I	136
5.3	Result of our analysis : periods, membership characteristics, IR excess, masses of the identified variable stars.	138
5.4	Parameters of the candidate variable stars (see text for details)	139
6.1	Log of Observations.	144
6.2	Catalog of the identified variable stars adopted.	160

6.3	Details of the variable stars.	162
6.4	Physical parameters of the candidate variable stars (see text for details)	163

Chapter 1

Introduction

1.1 Star Formation and Giant Molecular Clouds

Giant molecular clouds (GMCs) are main site of cold and star-forming molecular gas in the Milky Way. Understanding of their formation, evolution, chemical composition and destruction in the interstellar medium (ISM) are essential for better understanding the star formation processes in our own Galaxy and other Galaxies. Main Molecular hydrogen (H_2) tracer ^{12}CO imaging in the Milky Way enable us the panoramic view of the molecular gas distribution in the Galaxy and GMC properties (Dame et al. 1987, 2001; Solomon et al. 1987; Scoville et al. 1987; Dobbs et al. 2013). The physical properties of GMCs are studied by many authors (e.g. Blitz 1991; 1993, McKee 1999; Evans 1999, Lada 2005). These molecular clouds show the mass range of 10^3 to $10^7 M_{\odot}$ with the size ranging from 10 to 100 pc. The average temperature and densities of those clouds in GMCs are in the range $\sim 10 - 30$ K and $50 - 100 \text{ cm}^{-3}$, respectively.

Over the past several years, observations of GMC revealed that many of the fundamental processes influence the star formation. The gas forms a cold neutral phase (\sim kiloparsecs) to the creation of molecular clouds ($\sim 10-100$ pc), and further fragmented into denser structures such as clumps (~ 1 pc) and cores (~ 0.1 pc). This star-forming cores form stars (solar radius),

gravitationally bound multiple stars and planets (\sim astronomical units) therein (Williams et al. 2002; Kennicutt & Evans II 2012). The clumps or cores contain a dense gas ($> 10^4 \text{ cm}^{-3}$), which is roughly 1-10% of GMC mass (Lada et al. 1991; Lada & Lada 2003).

In a simple way, the cloud starts to collapse only when a self-gravitating spherical, isothermal and homogeneous cloud exceeds a critical mass, known as the “Jeans Mass” (Jeans 1928), and is given as ,

$$M_J = \left(\frac{\pi k T}{\mu m_H G} \right)^{3/2} \rho^{-1/2}$$

Where T is the kinetic temperature in Kelvin, ρ is mass density in gm cm^{-3} , n is the total particle density in cm^{-3} and $\rho = \mu m_H n$. μ is the mean mass/particle and could be considered as 2.29 in a fully molecular cloud with 25% helium by mass (Evans 1999). The free-fall timescale of gravitational collapse is given by Spitzer (1978),

$$\tau_{ff} = \sqrt{3\pi/32G\rho}$$

If, we consider a cold temperature ($\sim 10 \text{ K}$) and average particle density $\sim 50 \text{ cm}^{-3}$, $M_J \approx 80 M_\odot$, and the free-fall time $< 5 \text{ Myrs}$. So, GMCs contain thousands of Jeans masses with being highly unstable entities, and the free-fall collapse would lead to a formation of stars.

Over the past several decades of studies, it has shown that many of the fundamental processes influence the star formation in the individual molecular clouds. Hence, the study of such molecular clouds can directly address to the critical process of star formation. They contain a significant amount of high as well as low-mass stars in a small scale structure. It is important to study such ionized gas to understand how the formation of stars proceeds within it. The combination of the properties of H II regions, their natal molecular gas, associated young star cluster that includes massive star makes them one of the most famous celestial objects and the subject of an investigation by almost every new type of observations. Such molecular cloud is

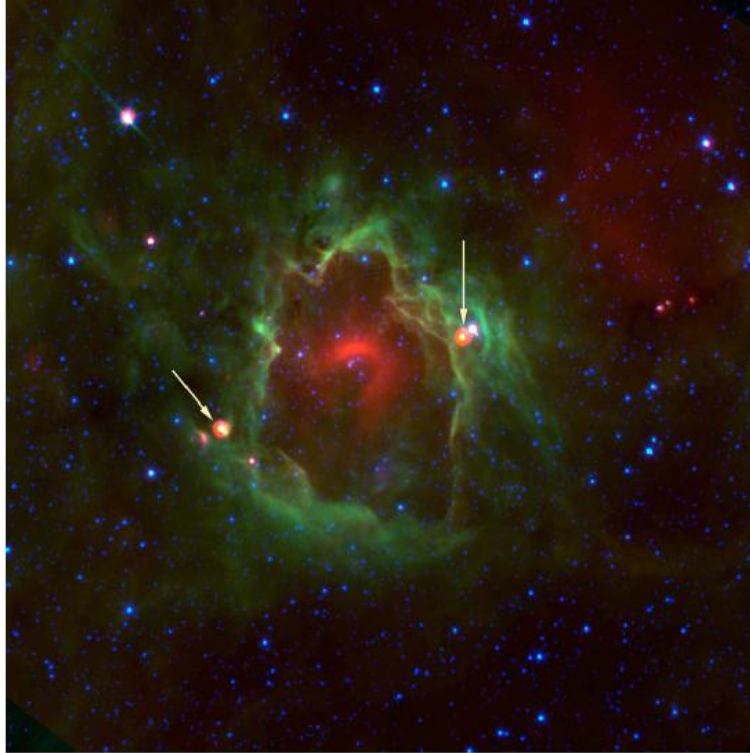


Figure 1.1: Example of H II region- RCW 82, where intense star formation activity is going on (Taken from Pomarès et al. 2009). North is up, east is left. The arrows point to the two main star formation sites.

also courageous to probe the origin of our solar system because the presence of short-lived radio nuclides in meteoritic samples has long suggested that the formation of the sun was excited by a massive star within a GMC (Goswami & Vanhala 2000; Lada & Lada 2003).

1.2 Overview of H II region

In the classical view, H II regions are manifestations of newly formed OB stars that are still embedded in their natal molecular clouds. H II regions are emission nebulae created by high-energy ultraviolet (UV) radiation from those young and massive OB stars. The OB stars have the capability to produce necessary UV radiation ($\lambda < 912 \text{ \AA}$) to ionize the surrounding hydrogen gas medium, and create a spectacular view of H II region (e.g., Fig.1.1). As they are primarily composed of hydrogen, hence the name of H II refer to ionized hydrogen (H II for

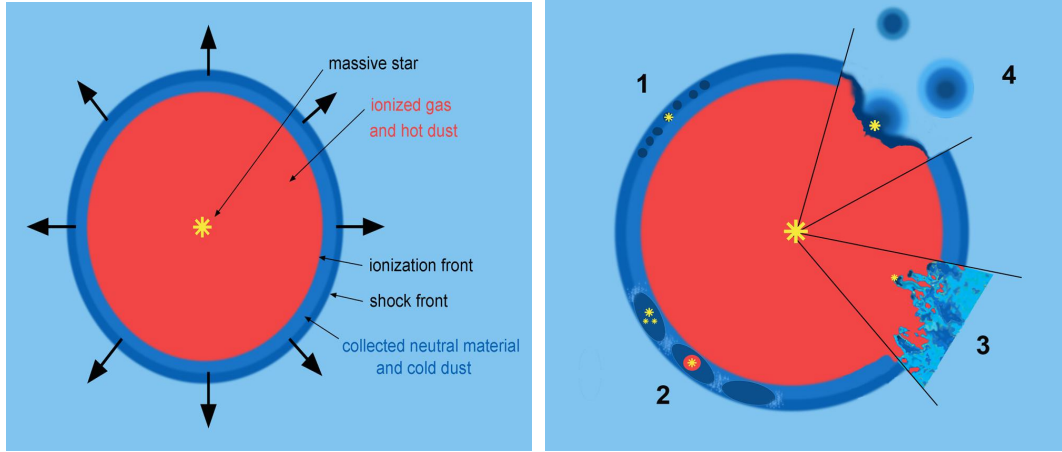


Figure 1.2: The schematic diagrams of H II regions are taken from Deharveng et al. (2010). (*left*) An example of spherical expanding H II region into a homogeneous medium. A layer of material is collected during the expansion phase. (*right*) Different processes of triggered star formation are described in the diagram, such as, small-scale gravitational instabilities (region 1); large-scale gravitational instabilities leading to the formation of high-mass fragments (region 2); ionizing radiation acting on a turbulent medium (region 3); radiation-driven compression of pre-existing dense clumps (region 4).

singly-ionized hydrogen, H I for neutral hydrogen). They have temperatures of around 10,000 Kelvin and can extend over several hundred parsecs or could be also compact within few pcs. They have a large range of densities of a few atoms per cm^3 in the diffuse nebula, to 10^6 atoms per cm^3 in the highly compact regions. H II region tracers of Galactic massive star formation, these massive stars live only ~ 10 Myr or less, compared to the negligible age of Milky Way (few billions of years), and hence these regions trace the young generation stars. Furthermore, they are the tracers of hot ionized gases in the spiral arms of our Galaxy, which help to acquire a better knowledge of the structure of our Galaxy. Understanding of these regions could reveal billion years Galactic chemical evolution.

The high mass protostellar objects resume their journey in dense, gravitationally bound, molecular cloudlets, which are undergoing quasi-static gravitational contraction. Such pre-stellar cores (PSCs) are the earliest detectable stage of a forming star. They have temperature only ~ 20 - 30 K. Their spectral energy distribution (SEDs) peak in far infrared at $\sim 200 \mu\text{m}$ (Churchwell 2002). With time PSCs become rapidly accreting, massive protostars. They produce a significant UV photon flux, which internally heats the surrounding molecular clouds and form

a detectable Hypercompact H II region (HCH II). At this stage the core become very compact (size $< 0.01pc$), dense ($n_{H_2} \geq 10^7 cm^{-3}$), and warm ($T \geq 100K$) molecular clouds (Kurtz et al. 2000). They are considered as precursors to the Ultracompact H II regions (UCH II s). Their evolution period is quite short, typically $\leq 10^5$ yr. UCH II s are the transition group which harbors still accreting protostars although many of them may already cease accretion and reached to the main-sequence phase (Beuther et al. 2006). Numerous surveys are now available allowing a better understanding of star formation in the vicinity of H II regions due to feedback of massive stars (e.g., W3/W4: Lada et al. 1978; Orion: Sugitani et al. 1989; NGC 2264: Tauber et al. 1993; IC 1396: Saraceno et al. 1996; NGC 1333: Langer et al. 1996; Rosette: Phelps & Lada 1997; Sh 2-104: Deharveng et al. 2003; RCW 120: Deharveng et al. 2009).

The pressure difference between the H II region ($\sim 10^4$ K) and the cold natal molecular cloud (~ 30 K) steers the expansion of the ionization front into the molecular cloud (Anderson et al. 2009). The ionized gas cocoons are enshrouded by ambient cold neutral molecular material, high-pressure exerted by the warm ionized gas carry on excitation mechanism. Thus, the massive stars provide positive feedback to star formation, via accumulation of neutral material at the periphery of H II regions, or via compression of pre-existing dense condensations at the IF.

The thermal radio emission from a central star can be detected from its ionization of the surrounding molecular cloud. If we assume the H II region excited by ionization front is spherically symmetric and homogeneous, the luminosity of Lyman continuum photons (in photons s^{-1}) could be estimated by (Moran 1983, Equation (5)),

$$S_* = 8 \times 10^{43} \left(\frac{S_\nu}{mJy} \right) \left(\frac{T_e}{10^4 K} \right)^{-0.45} \left(\frac{D}{kpc} \right)^2 \left(\frac{\nu}{GHz} \right)^{0.1} \quad (1.1)$$

Where S_ν is the integrated flux density in mJy, D is the distance in kpc, T_e is the electron temperature, and ν is the frequency in GHz for which luminosity to be calculated. As the central-

ized massive star ionize the surrounding neutral molecular medium, the ionization front moves more and more, and the H II region expands until an equilibrium is reached between ionization rate and recombination rate. This structure of ionized gas is termed as Strömgen sphere and the corresponding radius Strömgen radius after the Danish astrophysicist Bengt Strömgen. Assuming the ambient medium has homogeneous temperature and density, Strömgen (1939) estimated the radius as,

$$R_s = \left(\frac{3S_*}{4\pi n_0^2 \beta_2} \right)^{1/3} \quad (1.2)$$

where R_s is Strömgen radius in cm, n_0 is the initial ambient density in cm^{-3} and β_2 is the total recombination coefficient to the first excited state of hydrogen. As an expanding H II region sends a shock front into the neutral molecular medium, hence the ionizing front precedes. The radius of the region at this stage is given by (Spitzer 1978),

$$R(t) = R_s \left(1 + \frac{7c_s t}{4R_s} \right)^{4/7} \quad (1.3)$$

Where $R(t)$ is the extent of the H II region at time t and c_s , is the speed of sound. On the other hand, a photodissociation region (PDR) exists beyond the ionizing front. This region predominates with ionization potentials lower than 13.6 eV, and dissociate molecules (Hollenbach & Tielens 1997). In this respect, the PDR includes the zone where hydrogen exists in molecular form and carbon in mostly in CO form.

1.3 Triggered Star-formation in H II regions

Star formation occurs in a dense, self-gravitating gas, which requires a compression by itself or other external sources. A massive star (earlier than B 0.5) plays a vital role to ionize its nearby molecular clouds and trigger the formation of stars at the edges of H II regions. However, the

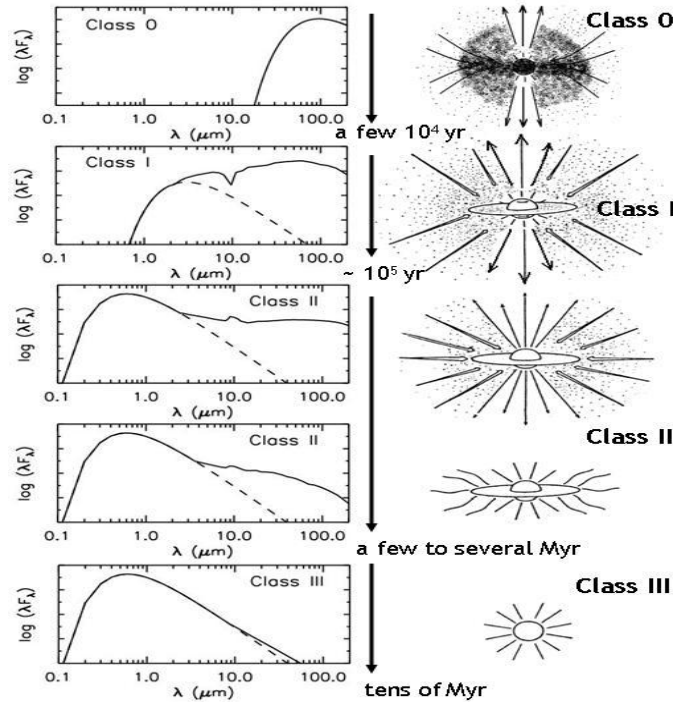


Figure 1.3: Evolutionary sequence of low-mass stars of the four classes in a similar diagram as suggested by Lada (1987) and Wilking (1989). The right panel shows stages of PMS evolution, whereas the corresponding SEDs are shown in the left panel. The figure has been adopted from <http://www.elisefurlan.com/Research.html>

stellar winds could evaporate the surrounding clouds and therefore terminate the star-forming processes in the nearby to massive stars.

Various mechanisms of triggering have been proposed in the literature (e.g., Elmegreen & Lada in 1977, Elmegreen 1998).

- The H II region may expand by interacting with pre-existing molecular clumps or globules. The high pressure exerted by the ionized gas on a clump can lead to the formation of bright rims, proplyds, and small cometary globules (Stutzki et al. 1988; Falgarone et al. 1991; Bertoldi 1989; Bertoldi & McKee 1990; and Lefloch & Lazareff 1994; Elmegreen 1998). This process is known as *radiation-driven implosion* (RDI; Fig. 1.2, region 4). The observations of few bright rims are convincingly shown to be formed from neutral globules by the expansion of H II regions in Orion (Garay et al. 1987; Churchwell et al. 1987) and M16 (Hester et al. 1996). Deep Observations in bright-rimmed clouds could

identify young embedded stars (e.g., Sugitani et al. 1991, Sugitani & Ogura 1994). Dense neutral clouds can also be squeezed by pressure from distant sources like supernovae, stellar winds or from older H II regions. Such one-sided pressure leads to the formation of comet shapes globules (Reipurth 1983, Zealey et al. 1983).

- A H II region expands more and more towards the neutral molecular cloud. A layer of neutral material is collected between the ionization front (IF) and shock front (SF). The compressed shocked layer might become gravitationally unstable with a long timescale and become dense, massive cores. This phenomenon is termed as the *collect and collapse* model (Elmegreen & Lada 1977; Whitworth et al. 1994), illustrated in Fig. 1.2. A good illustration of this model is Sh 2-212 H II region, where a thin circular ring of molecular material is collected during expansion of this H II region (Deharveng et al. 2008). It is presently fragmented at least five location in the ring. This most massive contain massive young stars exciting a UCH II region.
- Expansion of H II region around massive central stars in ambient molecular medium leads to a shell or ring-like structure. Their structures may become gravitationally unstable to form cores and eventually new stars around the periphery. The observations of Giant shells in our Galaxy and neighboring Galaxy found young stars along the edge, e.g., W3/W4 (Lada et al. 1978), Cygnus superbubble (Comerón & Torra 1994), M31 (Brinks et al. 1990).
- The interstellar turbulent effect makes the cloud clumpy. When the velocity dispersion of ambient gas is very high ($\sim 10 \text{ km s}^{-1}$), OB stars can't easily destroy the clouds, then massive clusters may form (Elmegreen & Efremov 1997). In this case, the dense cores may be randomly distributed around the H II region.
- The spontaneous collapse and star formation are seen in filaments, which is the molecular overdensity structure in the interstellar medium. They may form by magnetic processes (Elmegreen 1994) or gravitational collapse of shocked layers (Miyama et al. 1987). On

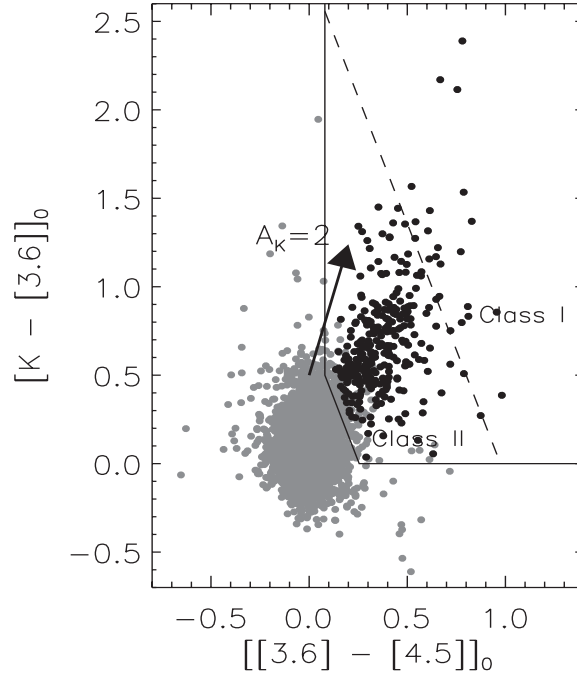


Figure 1.4: $[[3.6] - [4.5]]_0$ vs $[K - 3.6]]_0$ color-color diagram for isolation of class I and Class II sources. The diagram is adopted from Gutermuth et al. 2009.

the other hand, the interaction between a H II region and a nearby filamentary molecular cloud may lead to separation of clouds into two parts. A gravitational instability induces the formation of two cores along the filament axis (Fukuda & Hanawa 2000).

1.4 Evolution of Young stars

A molecular cloud core collapses, a protostar emerges at the center, and a circumstellar accretion disc and bipolar outflows are produced due to the high-angular-momentum material. The stars accrete mass and contract quasi-statically along the Hayashi and radiative tracks in the T Tauri phase to the zero-age main sequence (ZAMS). During all stages of their lives, stars play a significant role in the evolution of their host galaxy.

The main phases of low-mass (0.08 - $2 M_{\odot}$) young stellar objects (YSOs) are protostar, classical-T Tauri stars (CTTSs), Weak-line T Tauri stars (WTTSs). The protostellar phase of star formation is thought to be involved the free-fall collapse of dusty envelopes to stellar dimension

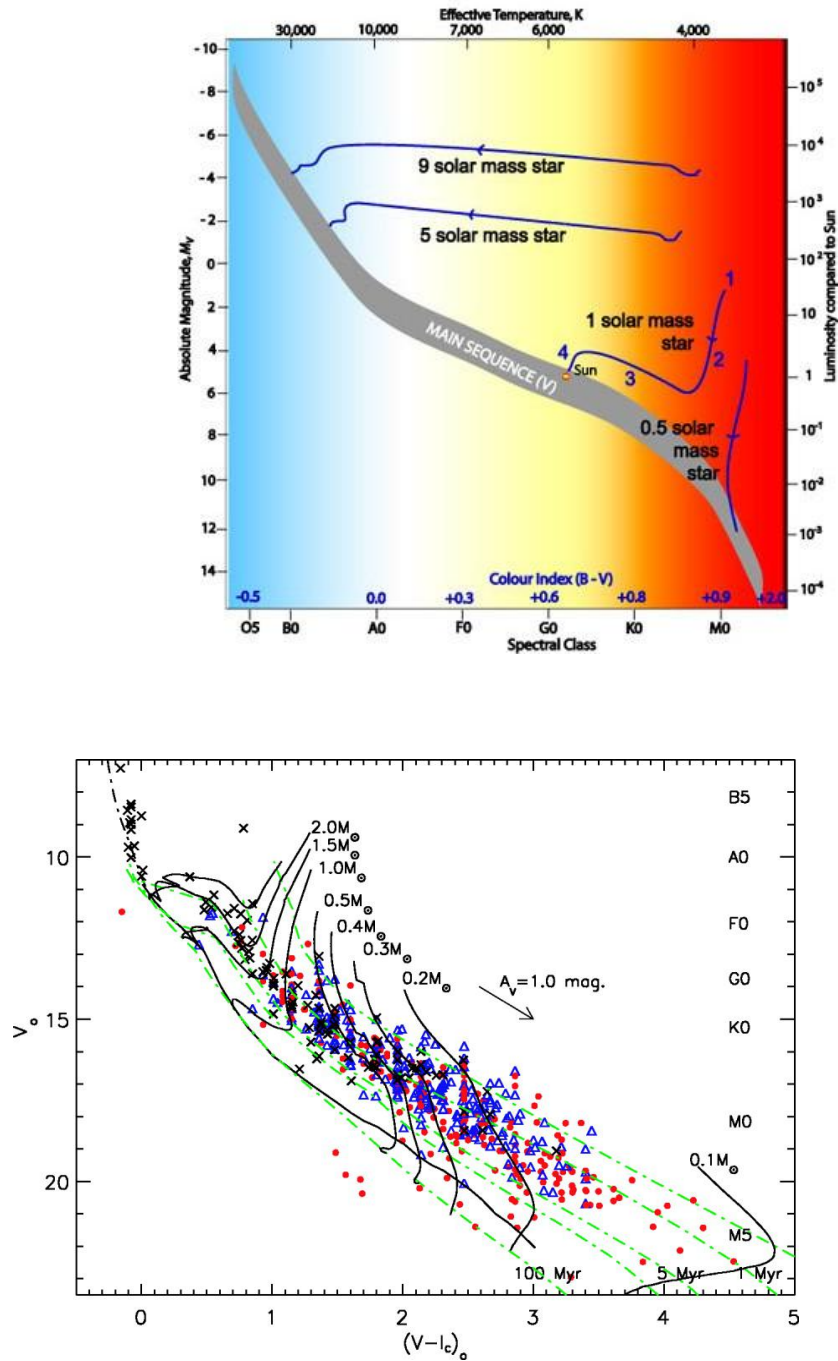


Figure 1.5: (*Top*) The four Hayashi tracks show the predicted evolutionary paths on the HR diagram for 9, 5, 1 and 0.5 solar mass stars during their protostar stages. (*Bottom*) An example of HR diagram is taken from Dahm & Simon (2005), which is basically a dereddened $V_0/(V-I)_0$ CMD for the young cluster NGC 2264. Red circles are CTTSs; blue triangles are WTTSs and black crosses are X-ray sources. The isochrones for 0.1-100 Myr and evolutionary tracks for 0.1-2.0 M_{\odot} from D’Antona & Mazzitelli (1994) are also shown. The solid diagonal line is the Pleiades main sequence, whereas the dot-dashed black line represents the upper main sequence of Balona (1984).

in their parent molecular cloud. The CTTSs objects exhibit strong H_α emission in their spectra with equivalent width $EW_{H_\alpha} \geq 10 \text{ \AA}$ (Herbig & Bell 1988). CTTSs are optically visible as they possess the only fraction of their natal envelope. Mass accretion rates in some cases $10^{-5} M_\odot yr^{-1}$ for short duration, otherwise it ranges from $10^{-9} M_\odot yr^{-1}$ to $10^{-6} M_\odot yr^{-1}$ (Basri & Bartout 1989). Many optical surveys of T-Tauri association recognized that a significant number of stars show weak H_α emission ($EW_{H_\alpha} < 10 \text{ \AA}$), but they are still associated with star-forming regions. These stars are called WTTSs. WTTSs have no/small accretion disc. It is assumed that WTTSs are of older population than CTTSs.

The evolutionary phases of YSOs are often classified by their infrared-millimeter spectral-energy-distribution (SED; Lada 1987). Four classes of YSOs have been proposed as Class 0, I, II, and III. Evolutionary sequence of low-mass stars of the four morphological classes are shown in Fig. 1.3. The properties of these sources are as follows:

- Class 0 sources are young protostars with thick ($10^3 - 10^4$) AU, cold (~ 20 K) envelope, from which it accretes mass towards central region. A collimated outflow and a disc from the central region are seen. The age of Class 0 sources are $\lesssim 0.01$ Myr.
- In Class I protostars, a significant fraction of the envelope has already been accreted onto the central source, and the disc is $\sim 400 - 1000$ AU in extent. They have ages approximately ~ 0.1 Myr. The outflow activity is still present but with a wider opening angle and a lower mass-accretion rate than at the Class 0 stage (Bontemps et al. 1996).
- Class II is the infrared designation of CTTSs, and their energy spectra peak $\sim 1-10 \mu\text{m}$ with moderate IR excess reaching beyond $100 \mu\text{m}$ (Strom K. M. et al. 1989, Cohen et al. 1989). Their emission originates from optically thick disc ($100 - 400$ AU) and photosphere. The youngest members of this class drive outflows, and active accretion. After ~ 10 Myr of a life time, they start to dissipate their accretion disc.

- Class III sources are the SED classification of WTTSs. They show as a pure blackbody SEDs, implies a very little or no IR excess peaking at optical or infrared wavelengths. Their emission dominated by their photosphere.

The evolutionary status could be obtained from their infrared excess color (See Fig. 1.4). The Class 0/I share the reddest part of the color-color (CC) diagram, whereas, Class II sources located in the medium IR excess zones. However, it 's hard to distinguish Class III sources and field population from their infrared excess emission. Based on the long wavelength excess with respect to the stellar blackbody radiation, Lada & Wilking (1984; see also Lada 1987, Lada et al. 1991) proposed three classes: I, II, III. Quantitatively, their spectral index is defined as:

$$\alpha_{IR} = -\frac{d\log(\lambda F_{\lambda})}{d\log(\lambda)} \quad (1.4)$$

whereas, Class I sources have very broad energy distribution with $0 < \alpha_{IR} < +3$, Class II sources have $-2 < \alpha_{IR} < 0$, whereas, Class III sources have $\alpha_{IR} < -2$. The large IR excess is attributed to the thermal emission from the thick circumstellar envelope.

Intermediate mass (2-8 M_{\odot}) PMS stars are called Herbig Ae/Be stars after their discovery by Herbig (1960). Their spectral type range between B0 and early F. Their strong emission line, high infrared excess make them unique type of PMS. Their study serves as an important link between low- to high-mass star formation. These stars are associated with much higher outflow rates and show jets. The Herbig Ae/Be are more massive analogs to T Tauri stars. They follow almost similar-long wavelength properties with low-mass T Tauri.

1.5 H-R Diagram

Our knowledge of intrinsic properties of YSOs relies almost entirely on theoretical stellar models. From this models ages, masses of YSOs are derived provided the distance, brightness and effective temperatures are known. The Hertzsprung-Russell (HR)-diagram is a valuable tool in

understanding stellar evolution. A relation between luminosity and effective temperature that traces a line in the HR-diagram for a specified stellar mass is called Hayashi track (Hayashi 1961) as shown in Fig. 1.5(*Top*) taken from ATNF ^{*}. The Hayashi track gives the location of protostars in the HR diagram. However, for this tracks, it is important that from the collapse of a gravitationally unstable and isothermal cloud is completely convective structure emerges. A protostar may be considered fully convective, and this is usually the starting point of Hayashi track. When the dust opacity drops down, the internal temperature rises and the convective zone decreases from the center. The evolutionary path of the star in the HR-diagram move towards left (higher effective temperatures and reaches to radiative track on time scales of 5-10 Myr. The end the evolutionary track happens when energy generation by nuclear reactions in the stellar core adequately compensates the energy losses due to radiation from the stellar photosphere. The star emerges into ZAMS, the end point of PMS evolution. Low-mass ($M < 2M_{\odot}$) PMS are considered convective, the progress in the HR diagram in terms of luminosity and T_{eff} is marginal. Massive PMS stars ($M > 8M_{\odot}$) shows a steep decline of time towards the ZAMS due to their extremely short contraction time scale.

When Class II sources can be placed on the color-magnitude (HR) diagram and compared with theoretical evolutionary tracks, the derived ages are mostly between 0.5 and 5 Myr (e.g., Fig. 1.5(*Bottom*)) although some stars retain CTT characteristics as long as ~ 15 Myr. Many WTTSs occupy the same region on the HR diagram as do CTTSs, although some are approaching the ZAMS.

1.6 Variable Signature of Young Stars

Since the pioneering work of Joy (1945), photometric variability is long investigated as defining characteristics of PMS. A long time monitoring program on young clusters having T Tauri association reveals that observed flux can change by few millimagnitude to few magnitudes on

^{*}Australia Telescope National Facility, [http : //www.atnf.csiro.au/outreach/education/senior/astrophysics/](http://www.atnf.csiro.au/outreach/education/senior/astrophysics/)

the timescales of minutes-days to years. CTTSs typically vary in irregular fashion up to few magnitudes, arises from a different source of modulations such as irregular accretion of materials on to star, flare like activity on the surface, temporal variation in circumstellar extinction (Herbst et al. 1994, Ménard & Bertout 1999, Carpenter et al. 2001). However, strong accreting CTTSs sometimes shows a periodic or quasi-periodic variation of the hot continuum emission (Hartmann 1998). For example, two light curves are presented in Fig. 1.6. These two stars show irregular as well as periodic variation during the different course of their photometric variation. The model that best explains this accretion process is magnetospheric accretion model. According to this models, the interaction of stellar magnetic field with accretion disc channelized the accretion onto specific location of star surface, an accretion shock (hot spot) develops at the bottom of accretion column (Camenzind 1990, Koenigl 1991, Calvet et al. 1994, Shu et al. 1994). These hot spots are few thousand Kelvin hotter than the unchanged photosphere and rotate into and out of view of an observer at the stellar rotation period (Bertout et al. 1988). Unlikely, WTTSs do not accrete matter from the circumstellar disc. They usually show periodic rotation in small amplitude (e.g., V magnitude amplitudes $\lesssim 0.75$ mag; Herbst et al. 2000) due to large solar-like cool spots on the stellar surface. Various types of photometric variation could be seen in PMS stars. In most cases, the variations are irregular over the different wavelength range. The most remarkable optical variations are:

- The outbursts in FU Ori type show a strong increase by up to 6 magnitudes within few months and decline on a time scale of years to decades. Such outbursts are believed to be originated from instabilities in circumstellar accretion disc in PMS stars.
- The strong emission line stars very often show P Cygni type characteristics, which are generated by stellar winds in T Tauri stars. Few T Tauri exhibit inverse P-Cygni profile, which is redward displacement absorption components, such profiles indicate mass infall into the stellar surface.
- The brightness of EX Lupi type variables increases up to few magnitudes but, unlike to FU-Ori decreases almost in the same timescale.

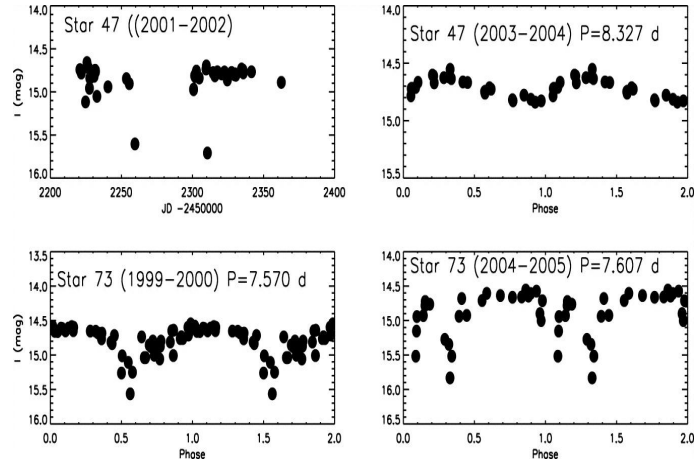


Figure 1.6: Example light curves and phase plots for the two periodic and irregular stars in IC 348 taken from Nordhagen et al. 2006. *Top* The star shows highly irregular behavior during 2001–2002 (left), but shows standard moderate-amplitude (0.25 mag) periodic behavior during 2004–2005 (right). *Bottom* The star shows good periodic behavior in 1999–2000 (left) but less definitively periodic variations in 2004–2005 (right).

- Some of the irregular variation show a small or moderate magnitude variation (~ 1 -2 mag) on a time scale to minutes to few hours due to flare like activity on their corona.
- Because of starspot on their surface, T Tauri stars sometimes show periodic/quasi-periodic variations on a time scale of less than 15 days, which is basically rotation rates of those stars.
- In a binary system of stars the components periodically eclipse one another results a change in the apparent brightness of the system. Their period of the eclipse could be determined from the light curves.

1.7 Motivation of the thesis

Stars form in the stellar clusters, and they are embedded and obscured in GMCs gas and dust. Multiwavelength (optical, particularly infrared) observations are the only way to understand the formation and early evolution of their members. Radio observations reveal the environment of the cluster including star-forming clumps and cores. The knowledge of star formation is directly

related to the fundamental problems of astrophysics. As the star formation is occurring in the present epoch in the Galactic environment and studies of such young clusters are also interesting for understanding the origin of the solar system. Moreover, such cluster members share the common heritage of being formed more or less simultaneously from the same progenitor and provide an opportunity to study different mass-spectrum of young stars. Massive star-forming, H II regions, are particular interest for this thesis work as several scientifically important cases as discussed below are still poorly known. Furthermore, the rich available database from several infrared space-based surveys like *Spitzer* and *WISE* as well as ground based Near-IR surveys using large telescope facilities provide ample opportunities to explore this scientific field. The star-formation and characterization of individual members are directly related to the understanding of GMCs, which are still poorly known.

- *Understanding of the star formation mechanism:* One of the primary goals of the present study is to understand the dominant star formation mechanism associated with a given star forming region and influence on its neighborhood. To understand how massive OB stars in H II environments have the influence to the star-formation processes.
- *Circumstellar disc properties in young stellar objects:* Planets form in circumstellar discs of gas and dust around young stars. Therefore, to understand the origin of our solar system, it is crucial to comprehend the range of processes that could affect the evolution of circumstellar discs. Hence, a comparative observational study of circumstellar disc properties of young clusters in different star forming environments is essential to address this issue.
- *Photometric variability in young T Tauri stars:* T Tauri stars show various types of complex profiles on their strong emission lines, strong flux variation due to spot signatures, stochastic outburst due to instabilities in the accretion disc. Thus, the characterization of photometric variation could be directly addressed brilliantly to the properties of these young stars, and also helps to pick up the young population in a cluster against the field population.

- *Age and mass spread in young clusters:* The age of a young embedded cluster member provides an effective lower limit to the age of the molecular cloud from which it formed. Most SFRs are found to contain only very young stars ($< 2\text{Myrs}$), whereas molecular clouds, from which those stars are born, are thought to have lifetimes of star forming molecular cloud is on the order of $\sim 10\text{ Myr}$. Thus, the age spread of a cluster gives the duration of star formation or the timescale for the cluster population. Studies of high to low mass stars within a star forming group offer distinct advantages over environmental influences on star formation.
- *Spatial distribution of YSOs:* The spatial distribution of YSOs in the H II region traces the history of star formation of the cloud. In particular, spatial distribution of stars with different mass and age in the various regions at different stages of evolution, we can portrait a general picture of how stars within those regions formed and the role of the birth environments may have played in this processes.

One of the most efficient methods of identifying high to low mass members of young stellar clusters and associations is through optical and near-infrared imaging surveys. Spectroscopy in such cluster search young stars in more reliable fashion. When photometric monitoring observations are available, PMS stars can also be identified through photometric variability caused by the presence of starspots. The principal scientific objectives of this investigation are to study the fundamental parameters of young clusters including distance, reddening, stellar density, young stellar population, age, mass, disc frequency, the mechanism involved in star formation in a given region. In this thesis work, we have chosen three young clusters associated with different H II environment. Studying of such young clusters, particularly those embedded in their natal clouds, requires multi-wavelength observations ranging from optical to radio. For this studies, we carried out deep optical *BVRI*, slitless and slit spectroscopic observing data and *I*-band monitoring data. The archival data sets from *Spitzer*-IRAC, WISE, WIRCAM, UKIDSS, 2MASS, MSX, IRAS, FCRAO, JCMT and NVSS are used to understand the stel-

lar population. The YSOs are estimated from infrared excession and global scenario of star formation in/around these young clusters.

1.8 Outline of the thesis

The thesis contains the following Chapters:

Chapter 1 provides a brief overview Giant molecular clouds and H II regions and star formation scenario in them. Different class of YSOs and their evolution are discussed. Finally, motivation of our study is also discussed.

Chapter 2 is devoted to the description of observing instruments including telescopes, filter systems, detectors used for observations, and data reduction techniques. The archival database used for studies are also described.

Chapter 3 discuss estimation of the fundamental parameters of the young cluster NGC 2282. We identified few new massive members from spectroscopy including the census of low-mass members from infrared excess, H_{α} emission properties. Finally, those YSOs are characterized using various CMDs.

Chapter 4 deals with the star-formation activity in the young H II region S149 and its associated molecular cloud complex. We identified massive-to-low mass members using spectroscopy, infrared and radio data. The star formation scenario in this region is discussed.

Chapter 5 is discussed to study the detection of variable stars in the young cluster NGC 2282. From multi-epoch I band observations, we identified several variable stars towards this cluster. We characterize those variable sources from their optical, infrared colors and CMDs.

Chapter 6 deals with the candidate variable stars in the Cygnus OB7 near by Lynds 1003 cloud. From I -band monitoring observations, we identified several candidate variable stars. They are characterized using optical and infrared color.

Chapter 7 presents the summary of the main results of this dissertation and the outline of the future research plan.

Chapter 2

Observations and Data Reduction

The chapter consists of brief description of the telescopes used for the present studies, the backend instruments on those telescopes used to obtain data, photometric reduction techniques and calibration methods, and spectroscopic data reduction methods for the data used in this thesis work. Different archival database in the multi-wavelength range optical to radio are used in the thesis work, and those are also described briefly.

2.1 Telescopes and backend instruments

In this thesis work, the optical data were collected from the Himalaya Faint Object Spectrograph and Camera instrument on 2m Himalayan Chandra Telescope (HCT) located at Indian Astrophysical Observatory (IAO), Hanle, Ladakh, operated by Indian Institute of Astrophysics, Bangalore; the Optical $2K \times 2K$ CCD imager on 1.30m Devasthal Fast Optical Telescope located at Devasthal Observatory, Nainital, operated by Aryabhata Research Institute of Observational sciences (ARIES), Nainital; the Optical $2K \times 2K$ CCD imager on 1.04 m Sampurnanand Telescope (ST) operated by ARIES. The Near-IR (NIR) data were taken from the Near-infrared Camera and Multi-Object Spectrometer (NICMOS) on the 1.2m infrared telescope, located at Mt. Abu IR Observatory operated by Physical Research Laboratory (PRL), Ahmedabad. Brief

parameters of those telescopes used for our observations are given in the Table 2.1 mentioned below.

The Himalaya Faint Object Spectrograph Camera (HFOSC) instrument at the Cassegrain focus of 2m HCT is an optical imager cum spectrograph. This is a focal reducer type instrument where the focal reduction helps relatively wide-field imaging for a given detector. Using collimator and camera optics, this instrument operates in both larger imaging and low-resolution spectroscopy mode. The switch over between the modes could be possible immediately during observing run in a night. In HFOSC, the reduction factor is 0.58, means one can have an enhanced field of view with factor ~ 1.7 . HFOSC instrument has several Bessell-Cousins UBVRI optical broadband as well as several narrow-band filters. For spectroscopy mode, it uses a set of nine slits with width ranging from 0.77 to 15.4 arcsec and length 2 to 11 arcmin and a set of 10 gratings covering spectral resolution, $R = 200$ to 4500. More detailed information on those components could be found at <https://www.iiap.res.in//iao/hfosc.html>. Few of the HFOSC parameters relevant for our observations are listed in the Table 2.2.

The 2K \times 2K CCD imagers at the 1.3m DFOT and 104cm ST are installed on the Cassegrain focus of those telescopes. The imager at the 1.3m DFOT has Bessell-Cousins UBVRI and SDSS ugriz and narrowband O[III], S[II], and H_{α} line filters. The optical imager at 104cm ST has Bessell-Cousins UBVRI broad-band filters. More details could be found at <http://aries.res.in/~1.3m/observation.html>. Some of those parameters are mentioned in the Table 2.2.

The Near-Infrared Multi-object Camera cum Spectrograph (NICMOS)-3 at the 1.2m Mt. Abu telescope has Near-IR HgCdTe detector, which is sensitive in the wavelength range ~ 0.95 to $2.4 \mu\text{m}$. NICMOS-3 has the capability of imaging and spectroscopy mode, which could be switched over immediately during observing run in a night. The imaging mode has two selectable FOVs of 2×2 or 4×4 arcmin. It has Near-IR $JHKK'$ broadband as well as several narrow-band filters. The spectroscopy mode covers individual single spectra over JHK band with spectral resolution 1000 -2000. Some of parameters are mentioned in the Table 2.2.

Table 2.1: Specifications of the telescopes used for our observations

Telescope Parameters	HCT	DFOT	ST	Mt. Abu
Primary mirror size (m)	2.01	1.30	1.04	1.2
Located at Altitude (m)	4500	2420	1955	1680
Effective focal ratio	f/9	f/4	f/13	f/13
Focus	Cassegrain & Nasmyth	Cassegrain	Cassegrain	Cassegrain
Plate Scale (arcsec/mm)	11.5	39.4	15.2	13.2
Mount	Alt-Azimuth	Equatorial	Equatorial	Equatorial

Table 2.2: Specifications of backend instruments, detectors and filters used for our observations

Instrument	On the telescope	Detector system (Pixel size, Gain & Readout noise)	Imaging scale & Field of View	Filters & ($\lambda/\Delta\lambda$)	Spectrograph
HFOSC	HCT	STTe 2048 \times 4096 pixels (Pixel size = 15 μ m, Gain=1.22 & Rdnoise=4.8)	0.296 arcsec/pixel 10 \times 10 arcmin on 2K \times 2K	Bessell UBVR _I , H $_{\alpha}$	Grism#7 (λ =3800-6840 \AA ; R = 1330) Grism#8 (λ =5800-8350 \AA ; R = 2190) Grism#5 (λ =5200-10300 \AA ; R = 870)
Optical Imager	DFOT	Andor e2v 2048 \times 2048 pixels (Pixel size = 13.5 μ m, Gain=2.0 & Rdnoise=6.5)	0.535 arcsec/pixel 18 \times 18 arcmin	Bessell UBVR _I	–
Optical Imager	ST	e2v 2048 \times 2048 pixels (Pixel size=24 μ m, Gain=10.0 & Rdnoise=5.3)	0.366 arcsec/pixel 12.5 \times 12.5 arcmin	Bessell/Cousins UBVR _c I _c	–
NICMOS3	Mt. Abu	HgCdTe 256 \times 256 pixels (Pixel size=40 μ m; Gain=10.0; & Rdnoise=53)	0.528 arcsec/pixel 2 \times 2 arcmin or 4 \times 4 arcmin (selectable)	JHKK'	–

2.1.1 Photometric Data Reduction

The raw images taken from the CCD and telescope have several instrumental signatures, which require cleaning. We used the software Image Reduction and Analysis Facility (IRAF^{*}), which is distributed by National Optical Astronomy Observatories (NOAO), USA. IRAF has several image cleaning tasks, and those have been used here.

- **Bias Subtraction:** The CCD has a dc offset voltage, which gets recorded along with the image. The bias frame is taken as an image frame with exposure time zero that contains information of dc offset in the CCD detector array. We require to subtract it from the raw image frames. Several bias frames are taken some interval during observing

^{*}<http://iraf.noao.edu/>

run over night and make an average bias frame from all the individual bias frames. We use ZEROCOMBINE task of IRAF package to produce a master bias image. The master-bias was subtracted from the raw images.

- **Flat Fielding:** Flat fielding correction remove the effect of the pixel-to-pixel sensitivity variations across the CCD arrays as well as any variation due to the optical system (e.g. dust or scratches on the CCD window, vignetting by the telescope or camera optics, etc.). The flat field frames are taken for each filter during each observing night or at-least for the same set-up during observing run. The flat-field frames for our observations are taken using sky frames during evening and morning twilight. To get good flat-field (high signal-to-noise ratio, SNR), the bright multiple frames in the linear response region of CCD are preferred, and always targeted during our observations. First, all flat-field images were bias subtracted, and then all flat-field images were combined to get a master flat. A normalized master flat was created by dividing its mean. These procedures were performed using FLATCOMBINE task of IRAF.
- **Dark correction** A significant amount of charge can accumulate in the CCD pixels due to thermal excitation during the long exposure. This is termed as the dark counts, which need to be subtracted from the images. The dark count problem could be minimized by cooling the CCD to a temperature near $\sim 100^{\circ}$ C at an evacuated dewar (to overcome condensation). Under this condition, the dark counts are negligible even with 20-30 min exposure time. So, the dark correction is not applied in our case.
- **Cosmic Ray Removal:** Cosmic rays due to ionizing radiation hit the CCD images randomly, and it spread over single or more pixels. Cosmic ray events appear like a few bright dots in addition to stars in the CCD frames. They have arbitrary shapes and sharp edges. The median combine technique of several frames is quite effective to remove these events. However, for a single exposure image or variability studies, the median combine technique could not be used. We have used IRAF based task L.A.-Cosmic based on the

variation of Laplacian edge detection, developed by van Dokkum (2001), which works satisfactorily with a single image.

NIR data reduction:

For NIR observations, it is critical to create the good sky frames from multiple dithered exposures around the target regions. The NIR sky varies due to mostly closed populated hydroxyl (OH) emission lines, O₂ at 1.27 μm and H₂O at red part of K-band (Ramsay et al. 1992). The NIR sky varies from few minutes to hour scale; it roughly varies about 10% level at 10 min. So, several short exposures (band dependent) dithering (few arcsecs) the telescope around the target regions are taken for our observations. The good sky-background image was obtained by median combining of several images from at-least five or more dithered positions. The dithering technique is also helpful to eliminate bad pixel of the detector. The resultant reduced images were obtained after sky-background subtraction from the dark-subtracted raw images. The target fields are then combined by shifting using several reference stars' positions in the frames to increase SNR on the resultant image. Finally, these combined images are used for photometric reduction.

Astrometry:

The world coordinate system (wcs) coordinates for the detected stars in the frame were determined using several (in our case ~ 20) isolated moderately bright stars with their positions taken from the Two Micron All Sky Survey (2MASS) point source catalogue (PSC) (Cutri et al. 2003). A position accuracy of better than 0.3'' has been achieved using IRAF tasks *ccfind*, *ccmap* and *ccsetwcs*. The world coordinates of a set of image coordinates of each source were extracted using *xy2sky* utility of WcsTools*.

*<http://tdc-www.harvard.edu/wcstools/>

Aperture Photometry:

All those cleaning processes on the raw images as mentioned in the above are done with one-go by IRAF task *ccdproc*. Finally, we have science frames for further photometric analysis. First, we need to detect the individual stars for their pixel positions (x, y) in the frames for photometry. But as the number of stars in one frame are quite large, it is not possible to detect manually the positions, which is done by different methods:

Source detection:

- IRAF based DAOFIND task: We use automatic star finder algorithm *DAOFIND* task of IRAF DAOPHOT package to detect stars or starlike objects above a certain detection threshold above the background. DAOFIND routine convolves a Gaussian profile of full width at half maximum (FWHM) of the objects as given by us. It tries to locate objects by going through each pixel and looking for locations of the good Gaussian profile. It keeps only those objects within certain roundness and sharpness limits to reject non-stellar objects (e.g. background galaxies, cosmic rays, etc.).
- **SExtractor:** Considering a large image and variety shape of objects, we sometimes used SExtractor (Source Extractor) software to detect objects from reduced images (Bertin & Arnouts 1996). Unlike IRAF, this software is involved with minimal human intervention and ability to distinguish stars and contaminants like unresolved knots, extragalactic objects, Active Galactic Nuclei (AGN) with better approach. An example of source extraction parameters in SExtractor are listed in Table 2.3. DETECT_MINAREA and SEEING_FWHM have been estimated individually for each frame. A Gaussian filter FILTER_NAME is used for objects detection. SExtractor parameter CLASS_AUTO is used to separate star and galaxies. The CLASS_AUTO output, which is a ratio between semimajor to semiminor axes, contains a value between 0 (more towards extended objects) to 1 (resembles towards point like sources) assigned for all objects (Keenan et al. 2010).

Table 2.3: SExtractor Parameters

Parameters	Settings
DETECT_TYPE	CCD
DETECT_MINAREA	2.0
DETECT_THRESHOLD	1.5
ANALYSIS_THRESHOLD	1.5
FILTER	Y
FILTER_NAME	gauss_2.0_5X5.conv
DEBLEND_NTHRESH	64
DEBLEND_MINCONT	0.00001
CLEAN	Y
CLEAN_PARAM	1.0
MASK_TYPE	CORRECT
PHOT_APERTURS	4, 6
SEEING_FWHM	2.0
STARNNW_NAME	default.nnw
BACK_SIZE	48
BACK_FILTERSIZE	8.0
BACKPHOTO_TYPE	LOCAL
WEIGHT_TYPE	MAP_WEIGHT
WEIGHT_THRESH	10

However, some of the point sources were not detected automatically due to the high background in a nebulous region. We identified these sources visually and added the coordinates in automated detection database to extract their magnitudes, and thus we made sure that photometry of every genuine source is derived.

Starlight spread over some pixels on CCD due to the seeing effect of the Earth atmosphere. To extract the brightness (or intensity) of a star from the image, we estimate the contribution of the star over all pixels illuminated by it and subtract the signal from the sky background using nearby pixels. In aperture photometry technique, it is usually chosen a circular region of the aperture within which starlight falls that is related to full-width half maxima (FWHM) of a particular star. Measured flux can be converted to the instrumental magnitude using the relation: $mag = constant - 2.5 \log F_\lambda$, where F_λ is the observed flux (as counts) of the star after background sky-subtraction. The constant defines the zero-point in the magnitude scale, which needs to be calibrated by observing standard stars as described later. The IRAF task *PHOT* is used to acquire instrumental magnitudes, which has options to include all

instrumental parameters (e.g. CCD gain, readout noise, Exposure time, FWHM, etc.). These instrumental parameters are listed in the *FITS* image header file, and some are estimated from the image. Measuring the starlight requires making an aperture large (few FWHM) enough to include all of the light from the star. However, large aperture introduces more uncertainties in measuring the sky background. Thus, the first step in our photometry calculation is to determine the optimal aperture radius. The usual approach to minimize these problems is to examine the curve-of-growth. The simple aperture photometry has an assumption of linearly-varying background in the aperture's vicinity. Thus aperture photometry technique can not provide precise photometry to the fainter end as well as stars in the crowded field (e.g., star-forming cluster, globular clusters or open clusters). In cases of photometry on crowded regions like our studies, we need to do Point Source Function (PSF) photometry, and PSF photometry also needs aperture photometry at first.

Point Source Function Photometry :

Point Source Function (PSF) Photometry is used to measure starlight in crowded (large population of stars) field regions in sky . This method is based on the principle that all star images have the same shape, with the only difference being the scaling factor, and all the image of a point source formed by a telescope and CCD system can be described by a same mathematical function. The light distribution in the CCD frame is modeled by assuming positions and brightness for the observed stars and knowing the PSF function. The PSF could be approximated using the following mathematical functions;

$$\text{Gaussian } G(r; a) \propto \exp(-r^2/2a^2),$$

$$\text{Modified Lorentzian } L(r; a, b) \propto 1/1 + (r^2/a^2)^b,$$

$$\text{and, Moffat } M(r; a, b) \propto 1/(1 + r^2/a^2)^b,$$

where, r is the distance from the center and a and b are the parameters to be fitted (Stetson 1987).

We first construct PSF by selecting few isolated stars free from bumps and wings. In PSF routine, an analytic function is fit to the observed stellar profiles and residuals are stored in a look-up table. The obtained model PSF is applied to all the detected stars in the field using *ALLSTAR* routine of IRAF. This technique uses deconvolution procedure for magnitude determination of overlapping stellar images. It is therefore effectively used for accurate photometry of stars in a cluster, where large number of stars are populated in the small region. In order to ascertain whether all the stars have been detected and measured, the measured stars were subtracted from the frame by *ALLSTAR*. If there were stars still left in the subtracted image, those stars need to detect manually and the whole procedures of photometry was repeated till we get a clean residual image after subtraction of all detected stars.

2.1.2 Photometric Calibration

The intensity of measured instrumental magnitudes are reduced due to absorption and scattering by the Earth atmosphere. The extinction effect and colour terms (filter effect) need to be corrected. These terms are corrected using the optical standard stars list from Landolt (1992) at the beginning, middle and end of our observations. If we consider an observations through the atmosphere, at any particular wavelength λ , we can relate $m_0(\lambda)$, the magnitude of the observed object outside the atmosphere, to $m(\lambda)$, the magnitude of the observed object at the earth by the relation, $m(\lambda) = m_0(\lambda) + K(\lambda)X(z)$, where $X(z)$ is the airmass, $K(\lambda)$ is the extinction coefficient at any wavelength λ and z is the the angular distance of the object from the zenith at the time of observations. The airmass at the zenith is one and for small zenith angles $X = \sec(z)$. To estimate atmospheric extinction and transformation coefficients, several optical standard (Landolt 1992) were observed. The instrumental magnitudes are calculated and compared with standard magnitudes. The transformation equations used for photometric calibrations are estimated from a fit between standard and observed magnitudes, given as follows:

$$(B - V) = m_{b-v}(b - v) + c_{b-v}$$

$$(V - R) = m_{v-r}(v - r) + c_{v-r}$$

$$(V - I) = m_{v-i}(v - i) + c_{v-i}$$

$$(V - v) = m_v(V - I) + c_v$$

where B, V, R, I are the standard magnitudes and b, v, r, i are the instrumental magnitudes corrected for the atmospheric extinctions. The m 's are the transformation coefficients and c 's are the zero points. Finally these transformations are applied to instrumental magnitudes of program stars.

For NIR observations of Mt. Abu data, we use the sky-subtracted images as described in earlier section for aperture photometry. We have used bright standard star list from the UKIRT website* for photometric calibration. No extinction and colour term corrections is required here as they are negligible, but airmass corrections are applied here.

2.2 Spectroscopic reduction

Spectroscopy is a powerful tool in astronomy, which often allows us to get information about the temperature, density, composition, radial velocities, and important physical processes of an astronomical object. The astronomical spectroscopy is performed using spectrograph instrument containing two basic elements, slit, collimator optics, disperser (usually a reflection/transmission grating), camera optics and detector system, which split and separate-out the flux information at different wavelengths and measure the relative amounts of radiation at each wavelength from a *spectrum* of the object.

*http://www.ukirt.hawaii.edu/astronomy/calib/phot_cal/ukirt_stds.html

Optical spectra of our target stars (bright stars in the clusters area) were obtained HFOSC on 2 m HCT, and the details of instrument are described in earlier section. To achieve optical coverage of spectroscopic observations, we used Grism#5, Grism#7 and Grism#8 as listed in the Table 2.2. We observed with the long slit of width 1.92 arcsec ($167\mu\text{m}$) for our observations to avoid any flux-loss. During observations, a series of bias frames, wavelength-calibration spectra using argon lamp, and flat frames using the halogen lamp were also taken. Flat fields and arc lamps were taken immediately following each target star observations. The standard flux calibrator stars from Massey et al. (1988) were also observed during the nights, whenever required. In the following sections, we describe the procedures to get the flux calibrated spectra from the raw spectra.

Long-slit Spectral data Reduction:

Cleaning of raw spectroscopic images is almost similar to that of photometry (see 2.1.1). In brief, this process involves to remove the artifacts using the IRAF tasks. The corrections for bias were made using the bias frame obtained with zero exposure just after program star observations. A composite flat field was created for each day of observations by combining the individual flat field calibration lamps. The flat field was normalized using the median value of the central dispersion row. Several steps are followed to get wavelength as well as flux calibrated spectra.

- **Spectrum Extraction :** The stellar spectrum is usually laid along columns, called dispersion axis. This can be found manually by examining or automatically by searching for strongest peak along rows (spatial axis). We first specified extraction window of the spatial profile of spectrum, and background window along spatial axis. The spectrum is not exactly perpendicular to spatial axis as we considered for theoretical dispersion axis. The center of the spatial profile will shift slightly along dispersion axis due to various reasons such as, distortions of camera optics, gratings location in the cells, differential atmospheric refraction. So, essentially we have to trace the center of spatial profile along

dispersion axis. At each point along the dispersion axis, the data within the traced aperture is summed and subtracted from sky background. All the above described steps for spectrum extraction have been consolidated in a single task *APALL* of IRAF. Now, we have extracted the 1-dimensional (1-d) spectrum from the 2-dimensional (2-d) images, and we can proceed now for calibration steps.

- **Wavelength calibration:** The extracted spectrum is in the pixel scale. We need to calibrate them in wavelength scale. The wavelength calibration is done with a series of process.

- We extract a 1-d spectrum from 2-d arc lamp spectral image using identical aperture and trace, used for object spectrum. This can be accomplished similar way by *APALL* task as discussed in above section.
- The dispersion solution is determined from the extracted 1-d arc spectrum interactively by the task *IDENTIFY*. This solution is linked with object spectrum by the task *REFSPEC*.
- In the final step, this solution is applied to object spectrum on linear scale by interpolating a constant wavelength per pixel using the task *DISPCOR*, and now we have wavelength-calibrated the object spectrum.

- **Flux Calibration:**

- The spectral wavelength-calibrated data is transformed to real flux unit using suitable standard star observations. The task creates observation-by-observation listing of the observed counts within each band-pass along with the standard star flux. The task *SENSFUNC* fit the sensitivity function as a function of wavelength using the output file from the task *STANDARD*. Now in final step, the sensitivity function is applied to data using the task *CALIBRATE* to get flux calibrated spectrum. The object spectrum are corrected for atmospheric extinction.

- In few cases, we normalize the spectrum to unit scale. This is performed by *CONTINUUM* task, which attempts to fit a smooth function through the continuum and normalize the spectrum by this fitting.

2.2.1 Slitless spectral data

The cluster regions were observed using a combination of Grism#5 or Grism#8 and the H_α broadband filter (6300-6740Å) using HFOSC instrument at 2.01m HCT. The slitless spectra are recorded without any slit. In this mode of observations, the stars are replaced by their spectra. The slitless spectra were used to identify the presence of any H_α emission line stars in the cluster region by visual inspection only, which appear as bright blobs on H_α emission stars only otherwise it is bright line on star position. The wavelength and flux calibration is quite tedious and challenging, and we have not tried here.

2.3 Archival Data sets

2.3.1 NIR data from WIRCam

WIRCam (Wide-field InfraRed Camera) is a NIR instrument, mounted at the prime focus of the 3.6m Canada-France-Hawaii Telescope (CFHT; Puget et al. 2004). The CFHT is located on Mauna Kea mountain in Hawaii at an altitude of 4,204 meters from the mean sea level. The WIRCam focal plane consists of four HAWAII2-RG detectors, each containing 2048×2048 pixels. In this set up each pixel corresponds to $0''.3$ and yields a FOV $\sim 20' \times 20'$. The available image frames on our targets are obtained from the CFHT Science Archive*.

The raw dithered images in *JHK* filters have been reduced using Interactive Data Language (IDL) based reduction pipeline-SIMPLE Imaging and Mosaicking PipeLine (SIMPLE; Wang

*<http://www.cadc-ccda.hia-ihp.nrc-cnrc.gc.ca/en/cfht/>

et al. 2010). This pipeline generates sky-flat from median combining of the dithered images. It provides excellent treatment to frame-to-frame sky background fluctuation and minimized artifacts from bright objects. Distortion corrections are achieved with all the objects detected in SExtractor command within the pipeline. Absolute astrometry solutions have been obtained with 2MASS reference catalog. The images were calibrated with the 2MASS catalog to get standard photometry magnitude. To avoid nonlinearity due to saturated stars in WIRCAM bright end, we considered stars only in 13-14.5 mag for K and 13-15 mag for H with good photometric accuracy (error < 0.1) for our photometric calibration. All reduced images are combined to create the larger mosaic with tangential projection. The most obvious brightest cosmic ray hits are removed from each exposure with a Sigma filter. Whereas the fainter cosmic rays are detected from same sky position in all dither exposures and removed with a sigma filter. The identification of point sources was performed with the DAOFIND task in IRAF. The photometry on the images was performed with PSF algorithm of DAOPHOT package (see section 2.1.1).

2.3.2 NIR data sets from UKIDSS

The United Kingdom Infrared Telescope (UKIRT) is a 3.8-m infrared telescope on Mauna Kea, Hawaii. The UKIRT Infrared Deep Sky Survey (UKIDSS) is an astronomical survey conducted using the Wide-field Camera (WFCAM) on the UKIRT. The WFCAM has four 2048×2048 Rockwell Hawaii II (HgCdTe) devices. The pixel scale of 0.4 arcsec gives an exposed solid angle of 0.21 square degrees (sq. degs.). The survey began in May 2005 and surveyed 7500 sq. degs. of the Northern sky, extending over both high and low Galactic latitudes, in NIR filters down to $K = 18.0$ (Lawrence et al. 2007). This depth is three magnitudes deeper than 2MASS. The UKIDSS consists of five surveys for separate goals covering a range of areas and depths, using various combinations of five NIR filters ($YJHKH_2$). These surveys are Large Area Survey (LAS), Galactic Plane Survey (GPS), Galactic Cluster Survey (GCS), Deep Extragalactic Survey (DXS), Ultra Deep Survey (UDS). We have acquired data sets on the

star-forming region from GPS. The GPS covers an area of 1800 square degrees in $JHKH_2$ of the northern and equatorial Galactic plane at Galactic latitudes $-5^0 < b < 5^0$, and additional 200 square degrees area of the Taurus-Auriga-Perseus molecular cloud complex also covered through a narrow-band H_2 filter (Lucas et al. 2008). The motivation for the GPS creation of a legacy database and 3-D atlas is to study of star formation and the IMF with environmental dependence, counterparts to X-ray sources, high-energy astrophysics, AGB stars and planetary nebulae, including detection of brief phases of stellar evolution, brown dwarfs. The observations comprise eight individual exposures of duration 10, 10 and 5 s employing a subpixel dithering strategy to sample the image profile fully, makes the total on-source integration times of 80, 80 and 40 s in the J , H and K filters, respectively. The photometric zero-points are taken from the 2MASS Point Source Catalog, which is believed to provide a reliable photometric calibration over the whole sky (Skrutskie et al. 2006). Observations of calibration fields were made at regular intervals. Photometric transformations are used to correct the zero-points. These transformations include extinction terms to correct for the fact that the colors of stars in the Galactic plane. The source magnitude depth in GPS are $J = 19.9$, $H = 19.0$, $K = 18.8$ mag. The saturation limits $J = 13.25$, $H = 12.75$, $K = 12.0$ mag.

2.3.3 NIR data from 2MASS

The Two Micron All Sky Survey (2MASS) has uniformly scanned the entire sky in three near-infrared bands J , H , K_s to detect and characterize point sources. 2MASS used two highly automated 1.3-m telescopes located one at Mt. Hopkins, AZ for the northern sky survey, and another at CTIO, Chile for the southern sky survey. Each telescope contains a three-channel camera, where each channel consisting of a 256×256 array of HgCdTe detectors. 2MASS observed each sky location in 7.8 s of integration time and, with a $2'' \times 2''$ pixel scale. This total integration time was divided into six 1.3 s exposures dithering position to reduce sky background. Photometry of standard stars in these fields was used to derive the photometric zero points in each of the three survey band passes as a function of time during each night

(Cutri et al. 2003). The 2MASS database provides photometry in the JHK_s to a limiting magnitude of 15.8, 15.1 and 14.3, respectively, with an S/N ratio greater than 10. There are several quality flags in the photometric catalog for the point sources to examine their quality.

2.3.4 Mid-infrared data from *Spitzer*

The *Spitzer* Space Telescope is an infrared space telescope launched in 2003 and was rotating along Earth-orbit (Werner et al. 2004). It is the fourth NASA Great Observatories program. *Spitzer* is equipped with an 85 cm telescope. In its cryogenic phase, the telescope was gradually cooled to ~ 5.5 K. *Spitzer* carries three instruments onboard: the Infrared Array Camera (IRAC, Fazio et al. 2004), the Infrared Spectrograph (IRS, Houck et al. 2004), and the Multiband Imaging Photometer for *Spitzer* (MIPS, Rieke et al. 2004). The IRAC operates simultaneously on four wavelengths ($3.6 \mu\text{m}$, $4.5 \mu\text{m}$, $5.8 \mu\text{m}$ and $8.0 \mu\text{m}$). The IRS operates at the wavelengths $5.3\text{-}14 \mu\text{m}$ (low resolution), $10\text{-}19.5 \mu\text{m}$ (high resolution), $14\text{-}40 \mu\text{m}$ (low resolution), and $19\text{-}37 \mu\text{m}$ (high resolution). MIPS works at far infrared ($24 \mu\text{m}$, $70 \mu\text{m}$, and $160 \mu\text{m}$). The cryogen was finally depleted on 15 May 2009. After the end of the cryogenic mission, the Warm *Spitzer* Mission began in late July 2009, and temperature increase to 27.5 K. *Spitzer* is operating with one of its instruments IRAC in $3.6\mu\text{m}$ and $4.5\mu\text{m}$. IRAC observes two FOVs simultaneously, each FOV is seen simultaneously by two detectors (one InSb and one Si: As detector). Each array has 256×256 pixels, with the same plate scale ($1''.2$ per pixel) whereas MIPS has a plate scale of $2''.45$ per pixel. The observed image products were taken from the *Spitzer* archive*. The IRAC and MIPS observations data files are generated by the data reduction pipelines at *Spitzer* Science Center (SSC).

The Basic Calibrated Data (BCD) is the calibrated, individual images generated by the SSC pipeline from a single raw image to a flux-calibrated image. The procedures are described below, starting the initial cleaning, which is taken care by the SSC pipeline. For more details, we refer to IRAC and MIPS Data Instrument Handbook (Reach et al. 2005).

*<http://archive.spitzer.caltech.edu/>

- **Cleaning:** The pipeline removes the bias, subtracts a dark sky image generated from observations of relatively empty sky near the ecliptic pole, flat-fields using a super-flat generated from the calibration observations of approximately 20 pre-selected blank fields near the ecliptic plane, and by co-adding and then normalizing the values in each pixel in each of the observations. The pipeline also analyzed for probable radiation hits and major artifacts.
- **Muxbleed:** When a bright source is read out in InSb arrays, the readout multiplexers in the cold electronics do not return to their quiescent state for a considerable length of time. Resultant pixel bleeds only as a result of the light falling onto it. The mux bleed flux is not real, so can be corrected by knowing the readout order of the pixels.
- **Bandwidth Effect:** The bandwidth effect in IRAC channels at 5.8 and 8.0 μm creates a decaying trail of pixels 4, 8, and 12 columns. Presently, there is no suitable correction for this effect. It is recommended to take small apertures (< 4 pixels) for photometry of bright objects at 5.8 and 8 μm .
- **Column Pull-down/Pull-up:** When a bright star or cosmic ray on the array reaches up to a level of 35,000 DN, there is a change in the intensity of the column carrying the signal. In channels at 3.6 μm and 4.5 μm , the intensity is reduced along the column. The pipeline estimates the true sky value for the affected pixels and fits a DC offset.

Mosaicking with MOPEX

The IRAC and MIPS data were mosaicked using the MOPEX (see Makovoz & Marleau 2005) software. MOPEX re-project the frames onto a tangent plane and correct for image distortions. It interpolates the background matched frames to a common grid. The frames are coadded to make one image by averaging the interpolated pixel values from each frame. MOPEX detects moving objects and radiation hits in the image while mosaicking the individual frames together in outlier detection process. It removes max bleed and column pulldown artifacts and finally

combines individual frames into one mosaic per each band (Makovoz & Khan 2005). Every mosaic is accompanied by an uncertainty mosaic, constructed from the individual uncertainty images provided by the SSC. Temporal outlier module of MOPEX removes cosmic rays, and other outliers have been removed.

Photometry using APEX:

The photometry of the point sources in the mosaic images were performed in the *Spitzer* Astronomical Point Source Extraction tool, i.e., APEX developed by SSC for all the IRAC and MIPS images. The software performs point source extraction in multi-frame and single-frame modes. We followed the multi-frame mode for IRAC data. In multi-frame point source extraction mode, the individual images were interpolated and co-added. Point sources were detected on this co-added images. The main components of point source detection are non-linear matched filtering and image segmentation. These components produce a detection list with the potential point sources; subsequent point source estimation was performed by Point Response Function (PRF) fitting of the potential point sources from the detection list. For MIPS data, we performed the source extraction by PRF fitting in single frame mode to increase the SNR. For single frame point source extraction, the detection and estimation were performed on a single input image. To convert the flux densities to magnitudes, we adopted the zero-points from IRAC Data Handbook, and the values of conversion factors are 280.9, 179.7, 115.0 and 64.1 Jys for the 3.6, 4.5, 5.8 and 8.0 μm bands, respectively. The zero-point value of 7.14 Jys from the MIPS Data Handbook was used to convert flux densities of MIPS 24 μm data to magnitudes.

2.3.5 Mid-infrared data from WISE

Wide-field Infrared Survey Explorer (WISE) is a NASA infrared space telescope launched in December 2009 (Wright et al. 2010). WISE performed an all-sky survey in four wavelengths;

3.4 (W1), 4.6 (W2), 12 (W3) and 22 (W4) μm with a 40 cm telescope (Cutri et al. 2012). The WISE short-wavelength channels employ HgCdTe arrays with 1024×1024 pixels each $18 \mu\text{m}$ square. For the long wavelength channels, the detectors are Si: As BIB arrays with the same 1024×1024 pixel format and pitch. Each 11 s cadence between two consecutive frames is divided into ten parts. The WISE filters provide an angular resolution of $6''.1$, $6''.4$, $6''.5$, $12''.0$, respectively. We used WISE images and photometric catalog to study the morphology of the regions.

2.3.6 Mid and far-infrared data from IRAS

The Infrared Astronomical Satellite (IRAS) was the first-ever space telescope to perform a sky survey of the entire sky at far-IR wavelengths. It carried a 57 cm IR telescope. It conducted three surveys of almost the entire sky during its ten months of life (Neugebauer et al. 1984). The mission performed all-sky mapping at 12, 25, 60 and $100 \mu\text{m}$. This study used the IRAS data reduced using High-Resolution Image Restoration (HIRES) at the IPAC, Caltech to obtain high-resolution photometry in all the four IRAS bands (Surace et al. 2004). The HIRES image reconstruction technique lead to achieving a spatial resolution ranging from $30''$ to $1'.5$. The HIRES maps have been used to obtain flux densities of the objects and to estimate the spatial distribution of warm dust (e.g., $25 \mu\text{m}$) and cold dust (e.g., $100 \mu\text{m}$) and optical depth.

2.3.7 $^{12}\text{CO}(1-0)$ data from FCRAO

The Five College Radio Astronomy Observatory (FCRAO) operates the 14-meter radio telescope located in New Salem, Massachusetts, United States. To trace molecular material of H II regions, we used the FCRAO Outer Galaxy Survey (OGS; Heyer et al. 1998). The OGS mapped $^{12}\text{CO} J = 1-0$ spectral line emission over the longitude range $102^{\circ}.5 \leq l \leq 141^{\circ}.5$ and latitudes $-3^{\circ} \leq b \leq 5^{\circ}.4$. The data were re-gridded from the FCRAO $50.22''$ pixel scale to

the CGPS 18'' pixel scale and from the FCRAO 0.812565 km/s velocity sampling to the CGPS 0.82446 km/s velocity sampling using DRAO program.

2.3.8 CO data from JCMT

The James Clerk Maxwell Telescope (JCMT) is the largest single-dish telescope in the world near the summit of Mauna Kea, Hawaii, US. Its 15-metre (50-foot) dish looks at the sky between the infrared and radio waves, observing at wavelengths between 1.4 and 0.4mm. Mainly two type of instrumentation is now operational at the JCMT: Continuum Instrumentation and Heterodyne Instrumentation. Submillimetre Common-User Bolometer Array 2 (SCUBA-2) is a JCMT's continuum bolometer camera operating simultaneously at 450 and 850 μm (Holland et al. 2013). The JCMT presently has two operational heterodyne receivers: Receiver A3 (RxA) and Heterodyne Array Receiver Program (HARP). RxA (or 230 GHz band receiver) covers the frequency range 212 to 274 GHz. HARP (or 350 GHz band receiver) can be tuned between 325 and 375 GHz (Buckle et al. 2009). The Auto Correlation Spectral Imaging System (ACSIS) is a digital autocorrelation spectrometer, used as the backend for the spectral line receivers. We have obtained JCMT molecular line observations from CFHT Science archive.

2.3.9 Radio data

The Very Large Array (VLA) of National Radio Astronomy Observatory (NRAO) is one of the world's leading astronomical radio observatories. It consists of 27 radio antennas each of them is 25 meters in diameter located on the plains of San Agustin, Socorro, New Mexico. Each of the VLA 25-meter parabolic dish antennas use 10 receivers: 74 MHz (Band 4), 327 MHz (P Band), 1.4 GHz (L-Band), 3 GHz (S-Band), 4.89 GHz (C Band), 8.4 GHz (X-Band), 15 GHz (Ku Band), 22 GHz (K-Band), 33 GHz (Ka-Band) and 43 GHz (Q Band). The NRAO VLA Sky Survey (NVSS) covers the sky north of J2000.0 $\delta = -40$ deg at 1.4 GHz (Condon et al. 1998). This survey covers almost 80% of the sky provides images with 45'' FWHM resolution

and nearly uniform sensitivity. We have obtained NVSS survey catalog, and all other available radio maps on our targets H II regions from VLA archive*.

*<https://science.nrao.edu/facilities/vla/archive/index>

Chapter 3

The young cluster NGC 2282 : a multi-wavelength perspective

3.1 Introduction

Embedded stellar clusters are very good platform to grow our knowledge about star-formation process and stellar evolution, as each cluster contains massive to low-mass pre-main sequence (PMS) stars with almost similar ages within a relatively small volume of space (Lada & Lada 2003). Young star clusters are born in giant molecular clouds (GMCs), mainly composed of molecular hydrogen (Lada et al. 1994; Lada & Lada 2003). Young stellar objects (YSOs) are formed and evolved in such dense molecular clouds. Multiwavelength studies of such regions provide census of YSOs, their fundamental parameters e.g. masses, ages, effective temperatures, circumstellar disks around them (if any) etc. (Carpenter et al. 2001; Kenyon S., & Hartman 1995). From such parameter space, broad pictures emerge on the young star-forming regions like star-formation history, star-formation efficiency, timescales etc. (e.g., Evans et al. 2009; Lada et al. 2010; Jose et al. 2012).

However, identifications of such member stars in a given young association is not very straightforward, because it is contaminated by the foreground and background stars projected on the given region of the sky. Particularly, studies at near-infrared (near-IR) and mid-infrared (mid-IR) wavelengths of such regions help us to distinguish the young members in those regions against the foreground and background populations. YSOs show excess emission in IR due to thermal emission from their circumstellar material. Such excess emission makes easier to distinguish YSOs from foreground and background stars (Allen et al. 2004; Flaherty et al. 2007). Such contamination could be further narrow down through spectroscopic observations in the optical and near-IR wavelengths (Briceno et al. 2002; Rebull et al. 2010; Herczeg & Hillenbrand 2014).

In this chapter^{*}, we focus on the observational prospect of PMS stars as well as the properties of the cluster. We selected to observe young cluster NGC 2282 ($\alpha_{2000} = 06^h46^m50.4^s$ $\delta_{2000} = +01^{\circ}18'50''$) to understand the timescales and kinematics of the gaseous material. NGC 2282 is a reflection nebula in the Monoceros constellation. It is located in an isolated molecular cloud of few thousand solar masses (Horner et al. 1997). The cluster is about 3° away on the sky from Mon OB2 and is probably associated with it. NGC 2282 has been listed in the several sky surveys of reflection nebulae (Van der Bergh 1966; Racine 1968; Kutner et al. 1980; Chini et al. 1984), and is also listed in the surveys of Galactic H II regions as BFS 54 (Blitz et al. 1982; Avedisova & Kondratenko 1984; Fich 1993; Kislyakov & Turner 1995). The distance of NGC 2282 was estimated to be 1.7 ± 0.4 kpc, which was mainly based on the spectral type (B2 V) of the brightest star HD 289120 in NGC 2282 (Racine 1968; Avedisova & Kondratenko 1984). So far three optical sources were classified towards NGC 2282, namely V507 Mon, HD 289120 and EQ 0644.3+0121, of which, V507 Mon was identified as a spectroscopic binary (Wachmann 1996), while HD 289120 as the illuminating source to the reflection nebula (Horner et al. 1997). EQ 0644.3+0121 was noticed as a faint nebulous source in the Palomar plates (Petrossian 1985).

^{*}This chapter is based on our published work in the Monthly Notices of Royal Astronomical Society (MNRAS) - Dutta et al. (2015)

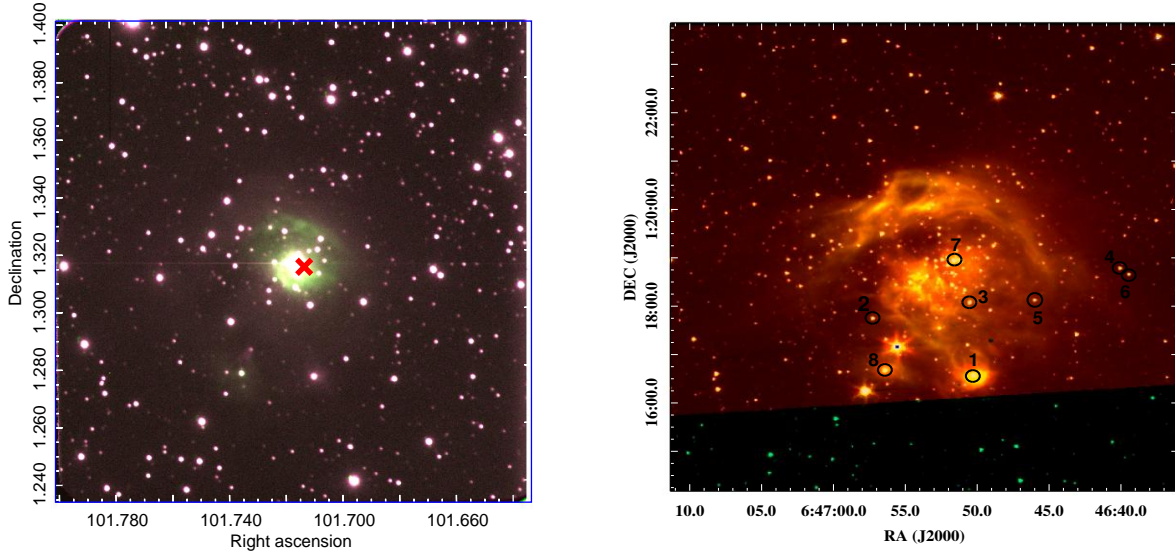


Figure 3.1: (a) Optical color composite image of NGC 2282 (blue: 5007 Å(O III); green: 6563 Å(H_{α}); red: 6724 Å[S II]) obtained using 2m HCT. The cluster centre is marked with red cross. (b) Near-IR Color composite image of NGC 2282 (blue: K band; green: 3.6 μm ; red: 4.5 μm). All the spectroscopically studied objects are numbered with black circles (see text for details).

The cluster properties of NGC 2282 were first studied using JHK -bands data by Horner et al. (1997). The authors estimated the cluster age as $\sim 5\text{--}10$ Myrs based on the fraction (9%) of infrared excess emission sources, and its association with the parent molecular cloud. Horner et al. (1997) found a core radius 0.19 pc and a cluster radius 1.6 pc at 1.7 kpc distance, by radial profile fitting of K -band data with different models. Following the method of Lada et al. (1994), the authors further estimated a variable interstellar extinction in the cluster region, which showed a maximum value of $A_V \sim 6.7 \pm 0.4$ mag towards South-East part of the cluster center, while quite low value of 1.6 ± 0.4 mag at the cluster center around HD 289120.

In this work, we have estimated the basic properties of the cluster using deep optical/IR imaging and optical spectroscopic observations. We have identified and classified YSOs based on their IR excess emission in near-IR and mid-IR data as well as their H_{α} emission line properties. We have characterized the YSOs based on various color-magnitude diagrams. Optical/IR colour composite image of NGC 2282 is shown in Fig. 3.1. These optical observations were taken by us using narrow-band filters at 5007 Å[O III] (blue), 6563 Å[H_{α}] (green) and 6724 Å[S II]

Table 3.1: Log of Observations.

ID	$\alpha_{(2000)}$ (h:m:s)	$\delta_{(2000)}$ (d:m:s)	Date of Observations	Grism/filter	Exp. time (s) \times no. frame	Airmass	SNR
optical photometry							
NGC 2282	06:46:50.4	+01:18:5	14.12.2007	B	600 \times 6, 30 \times 1	1.048	
NGC 2282	06:46:50.4	+01:18:5	14.12.2007	V	600 \times 6, 10 \times 1	1.242	
NGC 2282	06:46:50.4	+01:18:5	14.12.2007	I	300 \times 5, 10 \times 1	1.339	
slit spectroscopy							
1	06:46:50.3	+1:16:35.9	06.10.2014	Gr7	1500 \times 2	1.398	28
2	06:46:57.3	+1:17:45.5	05.01.2013	Gr7	1800 \times 1	1.286	25
3	06:46:50.5	+1:18:05.0	05.01.2013	Gr7	2500 \times 1	1.733	24
4	06:46:40.1	+1:18:47.4	05.01.2013	Gr7	2500 \times 1	1.212	25
5	06:46:46.0	+1:18:07.8	05.01.2013	Gr7	1500 \times 1	1.733	30
6	06:46:39.5	+1:18:38.5	05.01.2013	Gr7	1500 \times 1	1.212	36
7	06:46:51.6	+1:18:57.8	05.01.2013	Gr7	1500 \times 1	1.172	60
8	06:46:56.4	+1:16:40.9	05.01.2013	Gr7	2500 \times 1	2.250	18
slitless spectroscopy							
NGC 2282	06:46:49.4	+1:18:44.5	08.11.2013	Gr8/H α -Br	1800 \times 1	1.181	
NGC 2282	06:46:49.4	+1:18:44.5	25.01.2011	Gr5/H α -Br	1200 \times 1	1.532	

(red). While IR colour composite image is made using UKIDSS K -band (blue), *Spitzer* 3.6 μm (green) and 4.5 μm (red) images. Section 3.2 describes our observations and archival data sets used for the present study. Section 3.3 deals with our analyses and results that include spectroscopic study of 8 optical bright objects, identification and classification of the YSOs. In Section 3.4, we discuss the cluster properties such as ages, masses, spatial distribution etc. In section 3.5, we summarize our main results of the work.

3.2 Data Sets Used

3.2.1 Observations

Optical Photometry

The CCD *BVI* observations of the cluster were acquired using the 1.04m Sampurnanand telescope (ST; Sagar 1999) at Nainital, India during 2007 December 14. The log of optical observations is shown in Table 3.1. We used a 2048 \times 2048 CCD Camera having a pixel size of 24 μm and field-of-view (FOV) about 13' \times 13' with a plate scale of 0.37 arcsec pixel $^{-1}$. The gain and read out noise of the CCD are 10 e $^{-}$ /Analog to Digital Unit(ADU) and 5.3 e $^{-}$ respectively.

The observations were taken in 2×2 binning mode to improve the signal to noise ratio (SNR) and the average FWHM of the stars were $\sim 2''$. The observations were taken in short and long exposures to get a good dynamic coverage of the stellar brightness. Along with the NGC 2282 field, standard stars in the SA 92 field (Landolt 1992) were also observed at various airmasses on the same night.

The raw CCD images were cleaned using IRAF* software following bias subtraction, flat fielding and cosmic ray removal. The identification of point sources was performed with the DAOFIND task. Following Stetson (1987), we have used the roundness limits of -1 to $+1$ and sharpness limits of 0.2 to $+1$ to eliminate bad pixels brightness enhancements and the extended sources such as background galaxies from the point source catalog. The photometry by PSF fitting was done using ALLSTAR task of DAOPHOT package (Stetson 1992). The instrumental magnitudes were converted to standard magnitudes following the procedure outlined by Stetson (1987). A total of 13 stars of SA 92 field were used to estimate atmospheric extinction and transformation coefficients. The estimated extinction coefficients in B , V and I are 0.307 ± 0.014 , 0.185 ± 0.005 and 0.108 ± 0.008 , respectively. The final transformation equations used for photometric calibrations are

$$(V - I) = (0.971 \pm 0.008)(v - i) + (0.511 \pm 0.006) \quad (3.1)$$

$$(B - V) = (0.977 \pm 0.009)(b - v) - (0.29 \pm 0.010) \quad (3.2)$$

$$V = v + (0.089 \pm 0.001)(V - I) - (4.31 \pm 0.002) \quad (3.3)$$

where B , V , I are the standard magnitudes and b , v , i are the instrumental magnitudes corrected for the atmospheric extinctions for the airmass given in Table 3.1. The error of final magnitude measurements are obtained by propagating the uncertainties in extinction measurements, standard coefficients and profile-fitting photometry etc. The profile-fitting uncertainty

*Image Reduction and Analysys Facility (IRAF) is distributed by National Optical Astronomy Observatories (NOAO), USA (<http://iraf.noao.edu/>)

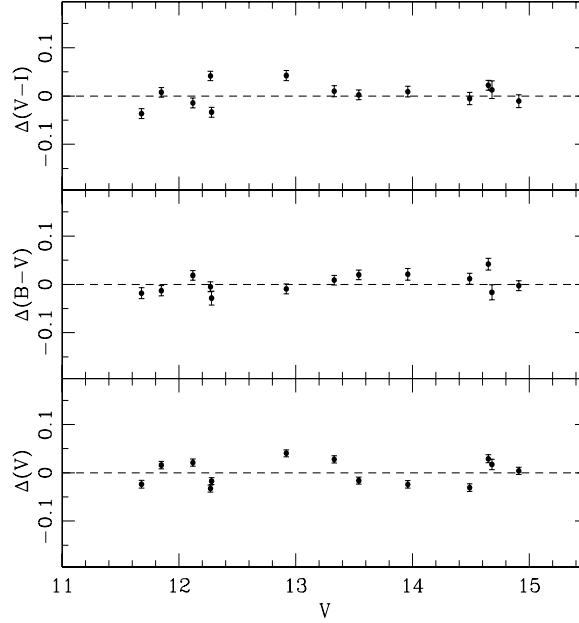


Figure 3.2: Residuals between standard and transformed magnitudes and colours of standard stars plotted against the Landolt standard magnitudes. The error bars are combined errors of Landolt (1992) and present measurements.

is estimated from the gain and read-out-noise of CCD camera, and background level of an image etc. Fig. 3.2 shows the standardization residuals (Δ) between standard and transformed V magnitudes, $(B - V)$ and $(V - I)$ colours of standard stars as function of V magnitudes. The standard deviations in ΔV , $\Delta(B - V)$ and $\Delta(V - I)$ are 0.024, 0.019 and 0.023 mag, respectively. Finally, we estimated optical magnitudes of 1379 objects, which are detected in two or more bands with a limiting magnitude of $V \sim 22$ mag.

The world coordinate system (wcs) coordinates for the detected stars in the frame were determined using 20 isolated moderately bright stars with their positions from the 2MASS point source catalogue (PSC) (Curti et al. 2003), and a position accuracy of better than $0.3''$ has been achieved. We used IRAF tasks *ccfind*, *ccmap* and *ccsetwcs* to achieve the above astrometric solution.

Slit Spectroscopy

We obtained optical spectroscopic observations of 8 bright sources within NGC 2282 using HFOSC of 2m Himalayan Chandra Telescope (HCT), India (Prabhu 2014). These observations were acquired using Grism 7 (3800- 6840 Å) with a resolving power of 1200 and a spectral dispersion of about 2.9 Å per two pixels. The FeAr arc lamp observations were taken immediately after the target observations. The spectrophotometric standard star G191B2B (Oke 1990) was also observed with an exposure time of 600s for the flux calibration. The log of spectroscopic observations is tabulated in Table 3.1.

After bias subtraction and flat field correction, the one-dimensional spectra were extracted using the optimal extraction method using APALL task in IRAF and wavelength calibrated using the FeAr arc lamp observations. The spectra were also corrected for the instrumental response using the sensitivity function generated from the standard star observations.

Slitless Spectroscopy

The grism slitless spectroscopic observations were obtained to identify H_α emission line stars using HFOSC of HCT on 2011 January 25 and 2013 November 08. The observations were carried out using a combination of Grism 5 (5200-10300 Å) or Grism 8 (5800-8350 Å) and the H_α broadband filter (6300-6740Å). The log of observations is shown in Table 3.1. The H_α emitting sources were identified by the presence of bright spot along the slitless spectra, while non-emitting H_α sources do not show any bright spot. Thus, we have identified 16 sources as H_α emission line sources which are discussed later in sect. 3.5.3.

Table 3.2: Photometric catalog of point sources towards NGC 2282. The complete table is available in the electronic form in online.

ID	RA (J2000) (deg)	Dec (J2000) (deg)	V (mag)	B - V (mag)	V - I (mag)	J (mag)	H (mag)	K (mag)	3.6 μ m (mag)	4.5 μ m (mag)
1	101.709618	1.276534	14.674 \pm 0.008	0.933 \pm 0.007	1.438 \pm 0.004	11.964 \pm 0.020	11.506 \pm 0.029	11.164 \pm 0.034	10.678 \pm 0.002	10.371 \pm 0.003
2	101.738704	1.295886	13.858 \pm 0.006	0.775 \pm 0.003	0.945 \pm 0.002	12.273 \pm 0.019	11.886 \pm 0.022	11.771 \pm 0.023	11.706 \pm 0.004	11.712 \pm 0.005
3	101.710595	1.301281	14.285 \pm 0.004	0.978 \pm 0.003	1.177 \pm 0.003	12.264 \pm 0.020	11.789 \pm 0.025	11.648 \pm 0.025	11.606 \pm 0.004	11.612 \pm 0.005
4	101.667052	1.313098	13.348 \pm 0.005	0.587 \pm 0.002	0.735 \pm 0.005	12.196 \pm 0.020	11.959 \pm 0.026	11.873 \pm 0.026	11.816 \pm 0.004	11.824 \pm 0.005
5	101.691841	1.302181	13.777 \pm 0.005	0.721 \pm 0.003	0.803 \pm 0.002	12.460 \pm 0.020	12.155 \pm 0.026	12.080 \pm 0.025	12.017 \pm 0.004	12.066 \pm 0.006
6	101.664463	1.311054	14.037 \pm 0.004	0.646 \pm 0.003	0.809 \pm 0.005	12.711 \pm 0.020	12.548 \pm 0.027	12.429 \pm 0.028	12.333 \pm 0.005	12.318 \pm 0.006
7	101.715141	1.315808	10.198 \pm 0.010	1.148 \pm 0.010	0.337 \pm 0.009	9.717 \pm 0.025	9.586 \pm 0.024	9.542 \pm 0.026	9.425 \pm 0.002	9.404 \pm 0.002
8	101.735121	1.277934	15.934 \pm 0.013	1.037 \pm 0.010	1.841 \pm 0.007	12.061 \pm 0.023	11.212 \pm 0.020	10.572 \pm 0.023	9.616 \pm 0.003	9.049 \pm 0.002
9	101.738965	1.208942	18.459 \pm 0.004	1.934 \pm 0.035	2.624 \pm 0.008	13.554 \pm 0.021	12.615 \pm 0.028	12.198 \pm 0.023	11.951 \pm 0.004	...
10	101.662814	1.214660	16.779 \pm 0.002	1.506 \pm 0.010	1.914 \pm 0.010	13.243 \pm 0.020	12.477 \pm 0.027	12.242 \pm 0.026	12.064 \pm 0.004	...
11	101.689942	1.216617	13.879 \pm 0.003	0.543 \pm 0.005	0.755 \pm 0.010	12.630 \pm 0.020	12.391 \pm 0.027	12.287 \pm 0.026	12.258 \pm 0.005	...
12	101.705790	1.222968	15.948 \pm 0.003	0.921 \pm 0.004	1.286 \pm 0.007	13.620 \pm 0.023	13.225 \pm 0.027	13.064 \pm 0.033	12.890 \pm 0.007	...
13	101.702240	1.224899	16.201 \pm 0.002	1.801 \pm 0.006	2.206 \pm 0.007	12.172 \pm 0.018	11.303 \pm 0.025	11.019 \pm 0.025	10.808 \pm 0.002	...
14	101.660364	1.219329	15.163 \pm 0.002	0.658 \pm 0.005	0.897 \pm 0.013	13.664 \pm 0.023	13.438 \pm 0.036	13.302 \pm 0.042	13.218 \pm 0.009	...
15	101.695928	1.240098	11.657 \pm 0.001	0.331 \pm 0.001	0.428 \pm 0.001	11.001 \pm 0.018	10.895 \pm 0.025	10.821 \pm 0.021	10.863 \pm 0.002	...
16	101.697027	1.251858	16.037 \pm 0.043	1.509 \pm 0.055	1.611 \pm 0.068	12.930 \pm 0.026	12.423 \pm 0.034	12.075 \pm 0.034	12.083 \pm 0.004	...
17	101.707273	1.250715	18.082 \pm 0.005	2.273 \pm 0.028	2.860 \pm 0.006	12.790 \pm 0.018	11.691 \pm 0.026	11.269 \pm 0.025	10.937 \pm 0.003	...
18	101.781223	1.227141	15.286 \pm 0.004	1.804 \pm 0.009	2.248 \pm 0.003	11.254 \pm 0.019	10.401 \pm 0.020	10.126 \pm 0.019	9.938 \pm 0.002	...
19	101.756836	1.248329	15.473 \pm 0.003	0.840 \pm 0.003	1.099 \pm 0.003	13.624 \pm 0.019	13.266 \pm 0.024	13.119 \pm 0.030	13.093 \pm 0.008	...
20	101.755078	1.237696	14.601 \pm 0.002	0.952 \pm 0.004	1.178 \pm 0.005	12.565 \pm 0.021	12.172 \pm 0.020	12.057 \pm 0.021	12.030 \pm 0.005	...
21	101.783209	1.238542	14.248 \pm 0.003	0.483 \pm 0.002	0.690 \pm 0.003	13.137 \pm 0.023	12.998 \pm 0.030	12.899 \pm 0.026	12.834 \pm 0.007	...
22	101.768600	1.242802	16.683 \pm 0.003	1.446 \pm 0.006	2.174 \pm 0.004	13.213 \pm 0.021	12.608 \pm 0.020	12.386 \pm 0.024	12.140 \pm 0.005	...
23	101.768194	1.248966	16.017 \pm 0.004	1.770 \pm 0.005	2.305 \pm 0.002	11.783 \pm 0.019	10.860 \pm 0.020	10.555 \pm 0.021	10.323 \pm 0.002	...
24	101.792152	1.249625	13.821 \pm 0.004	0.549 \pm 0.002	0.740 \pm 0.003	12.674 \pm 0.019	12.402 \pm 0.020	12.344 \pm 0.023	12.299 \pm 0.005	...
25	101.783535	1.271522	15.903 \pm 0.003	1.693 \pm 0.005	2.090 \pm 0.003	12.141 \pm 0.019	11.370 \pm 0.020	11.099 \pm 0.021	10.916 \pm 0.003	10.907 \pm 0.003
26	101.810802	1.277135	15.134 \pm 0.002	0.739 \pm 0.005	0.936 \pm 0.005	13.607 \pm 0.025	13.327 \pm 0.038	13.150 \pm 0.034	13.165 \pm 0.008	13.132 \pm 0.010
27	101.813572	1.282032	18.224 \pm 0.027	1.899 \pm 0.028	2.541 \pm 0.008	13.647 \pm 0.026	12.714 \pm 0.026	12.393 \pm 0.024	12.085 \pm 0.004	12.061 \pm 0.005
28	101.750326	1.247554	14.367 \pm 0.004	0.709 \pm 0.003	0.858 \pm 0.006	12.931 \pm 0.025	12.598 \pm 0.028	12.536 \pm 0.027	12.502 \pm 0.006	...
29	101.749411	1.261315	13.565 \pm 0.005	1.148 \pm 0.003	1.307 \pm 0.004	11.442 \pm 0.021	10.831 \pm 0.020	10.737 \pm 0.023	10.687 \pm 0.002	...
30	101.772527	1.267760	15.406 \pm 0.004	0.834 \pm 0.003	1.081 \pm 0.003	13.596 \pm 0.023	13.155 \pm 0.028	13.017 \pm 0.037	13.001 \pm 0.008	12.995 \pm 0.010
31	101.740814	1.270879	17.872 \pm 0.005	2.871 \pm 0.041	3.932 \pm 0.003	10.489 \pm 0.019	8.853 \pm 0.039	8.118 \pm 0.015	7.623 \pm 0.029	7.629 \pm 0.011
32	101.783952	1.276780	17.428 \pm 0.008	2.170 \pm 0.016	2.688 \pm 0.003	12.529 \pm 0.023	11.460 \pm 0.028	11.071 \pm 0.023	10.818 \pm 0.002	10.815 \pm 0.003
33	101.790469	1.288697	12.782 \pm 0.002	0.597 \pm 0.003	0.724 \pm 0.003	11.595 \pm 0.019	11.262 \pm 0.020	11.226 \pm 0.017	11.214 \pm 0.003	11.210 \pm 0.004
34	101.797372	1.315962	12.522 \pm 0.002	0.774 \pm 0.002	0.918 \pm 0.002	11.018 \pm 0.019	10.597 \pm 0.020	10.511 \pm 0.021	10.501 \pm 0.002	10.472 \pm 0.003
35	101.763612	1.311435	13.608 \pm 0.004	0.417 \pm 0.005	0.765 \pm 0.004	12.270 \pm 0.018	12.075 \pm 0.020	11.984 \pm 0.021	11.868 \pm 0.004	11.845 \pm 0.005

3.2.2 ARCHIVAL DATA SETS

Near-Infrared Data from UKIDSS and 2MASS

Near-IR *JHK* photometric data towards NGC 2282 were acquired from the UKIRT Infrared Deep Sky Survey (UKIDSS, Lawrence et al. 2007), which were taken during the UKIDSS Galactic Plane Survey (GPS) (Lucas et al. 2008; data release 6). The UKIDSS GPS has saturation limits at $J = 13.25$, $H = 12.75$ and $K = 12.0$ mag, respectively (Lucas et al. 2008). We therefore, replaced the saturated stars with the 2MASS PSC data. We set the 2MASS limit 0.5 magnitudes fainter than UKIDSS saturation limits following Alexander et al. (2013). In total, 150 saturated sources in UKIDSS catalog were replaced by 2MASS sources.

Spitzer-IRAC data from warm mission

The IRAC observations in 3.6 and 4.5 μm bands (channels 1 and 2) were available in the *Spitzer* archive program (Program ID: 61071; PI: Whitney, Barbara A). The data sets were taken towards NGC 2282 on May 25, 2011 at various dithered positions and with integration time of 0.4 and 10.4 sec per dither. The basic calibrated Data (version S18.18.0) were downloaded from Spitzer archive*. The raw data were processed and the final mosaic frames were created using MOPEX (version 18.5.0) with an image scale of 1.2 arcsec pixel⁻¹. We performed point response function (PRF) fitting method using APEX tool provided by *Spitzer* Science centre on all the *Spitzer* IRAC images to extract the magnitudes of point sources. The detailed procedure of source detection and magnitude extraction is described in Jose et al. (2013). We adopted zero point flux densities of 280.9 and 179.7 Jy for the 3.6 and 4.5 μm bands, respectively, following the Warm Spitzer Observer Manual. We finally detected 3049 and 2341 number of sources within 7' radius around the cluster in IRAC 3.6 and 4.5 μm bands, respectively. The

*<http://archive.spitzer.caltech.edu/>

Table 3.3: Details of the spectroscopically studied stars.

IDRA	(J2000) Dec	(J2000)	V	$V - I$	Spectroscopic	Photometric*	distance	** distance	Spectral	Remarks
	(h:m:s)	(d:m:s)	(mag)	(mag)	A_V (mag)	A_V (mag)	modulus	(pc)	Type	
1	06:46:50.3	+1:16:36.0	14.674	1.438	4.91 ± 0.20	4.69 ± 0.90	11.01 ± 0.20	1592 ± 147	B5V	member
2	06:46:57.3	+1:17:45.5	13.858	0.945	0.64 ± 0.15	...	7.96 ± 0.15	390 ± 30	G8V	foreground
3	06:46:50.5	+1:18:04.9	14.285	1.177	0.67 ± 0.20	...	7.71 ± 0.20	348 ± 32	K1V	foreground
4	06:46:40.1	+1:18:47.5	13.348	0.735	0.46 ± 0.16	...	9.20 ± 0.17	692 ± 50	F7V	foreground
5	06:46:46.0	+1:18:07.8	13.777	0.803	0.59 ± 0.17	...	9.21 ± 0.18	695 ± 55	F9V	foreground
6	06:46:39.5	+1:18:38.5	14.037	0.809	0.86 ± 0.21	...	10.33 ± 0.21	1165 ± 110	F0V	foreground
7	06:46:51.6	+1:18:57.8	10.198	0.337	1.66 ± 0.17	1.61 ± 0.71	11.18 ± 0.18	1722 ± 135	B2V	HD 289120; member
8	06:46:56.4	+1:16:40.9	15.934	1.841	8.82 ± 0.14	10.72 ± 0.62	B0.5Ve	Herbig Be; member

* Photometric A_V 's are calculated from extinction map. Foreground stars have not considered here.

** Distance moduli refers to the intrinsic distance moduli obtained from near-IR apparent distance moduli.

IRAC data of two bands were matched with a radial matching tolerance of 1.2 arcsec. Thus our final IRAC catalog contains 3304 sources, of which, 2085 sources are detected in both bands.

IPHAS data

INT Photometric H_α Survey of the Northern Galactic Plane (IPHAS) is a photometry survey using wide field camera (WFC) on the 2.5m Isaac Newton Telescope (INT) with Sloan r , i filters and H_α narrow-band filter (Drew et al. 2005; Gonzalez-Solares et al. 2008). The data for NGC 2282 were obtained in all three bands from the data release 2 (Barentsen et al. 2014).

Multiwavelength Catalog

The multiwavelength catalog was built by cross-matching all the catalogs described in the above sections except IPHAS data. The JHK and IRAC data were matched with a matching radius of $2''$. Before this, we performed several test matches by increasing the matching radius in step of $0.1''$ from $1.0''$ to $3.5''$. We found that the matching radius of $2''$ is sufficient for cross-matching two catalogs. In few cases, we got more than one matching sources, and we have taken the closest one as the best match. Following the same method, we adopted the matching radius of $2''$ to match between IR and optical catalog. Finally, the results of each match have been visually inspected in Optical, UKIDSS, 2MASS and *Spitzer* images. Our final catalog contains total 5601 number of sources within $7'$ radius around the cluster, but all of

them do not have detection in all wavelengths. The part of photometric catalog is presented in Table 3.2, The entire photometric catalog is available from the online site^{*}. But, those sources with uncertainty ≤ 0.1 mag have been taken for our study to ensure good photometric accuracy.

The completeness limits at various bands were estimated from histogram turn over method (e.g. Samal et al. 2015). We considered $\sim 90\%$ completeness of our data from the turning points of magnitudes at which cumulative logarithmic distribution of sources in the histograms deviate from linear distribution (figures are not shown). We found that the photometric data is complete down to $V = 21$ mag, $I = 20$ mag, $J = 18.5$ mag, $H = 18$ mag, $K = 17.5$ mag, $[3.6] = 15.5$ mag and $[4.5] = 15$ mag, respectively. However, completeness is limited by various factors such as, variable reddening, central luminous sources, stellar crowding across the region etc. Bright extended sources, variable nebulosity, significant saturation in *Spitzer*-IRAC bands also limits the point source detections. The modest sensitivity of UKIDSS and *Spitzer*-IRAC observations significantly limits our study.

For cross-checking, the completeness limits of V -band was also estimated by the method of inserting artificial stars of various magnitude bins into the image using IRAF (e.g. Jose et al. 2013). The frames were reduced using the same procedure used for original frame. The V -band photometry was 100% complete down to 18 mag, reduced to $\sim 90\%$ for 19-20 mag range, and 78% for the 21-21.5 mag range. The completeness limit obtained for V -band using artificial star injection method fairly matches with that of the histogram analysis.

3.3 Analysis and Results

3.3.1 Stellar density and cluster radius

The radial extent of the cluster has been estimated using K - band data ($K \leq 17.4$ mag having photometric accuracy of < 0.1). The cluster center was chosen as RA (J2000) = $06^h 46^m 51^s$ and

^{*}<http://vizier.cfa.harvard.edu/viz-bin/VizieR?-source=J/MNRAS/454/3597>

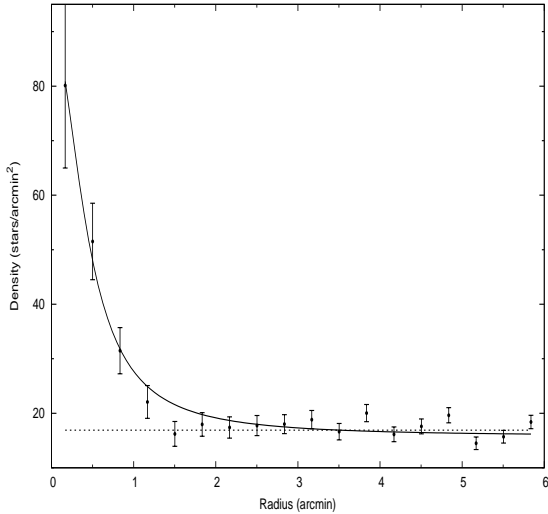


Figure 3.3: Radial density profile of the stars detected in NIR K- band towards the cluster NGC 2282. The continuous curve shows the least- square fit of the King (1962) profile to the data points. The dashed line indicates the field star density. The error bars represent $\pm\sqrt{N}$ in each bin.

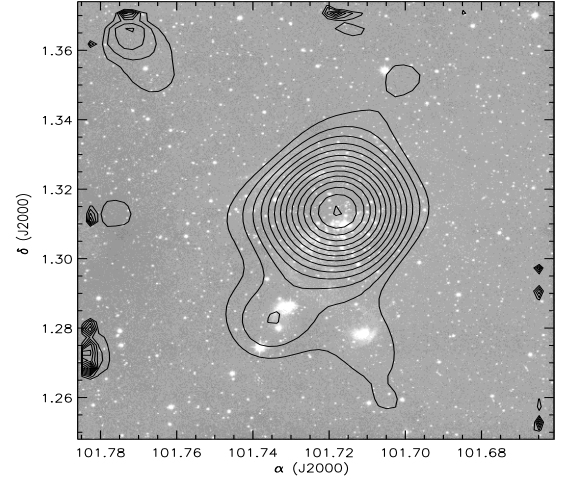


Figure 3.4: Stellar surface density map of sources detected in K-band towards NGC 2282 region overlaid on the UKIDSS *K*-band image. Stellar surface density was calculated using the nine nearest neighbors.

Dec (J2000) = $01^{\circ}18^m54^s$ from previous studies (Horner et al. 1997). We divided the cluster into a number of concentric circles. Radial stellar density in each concentric annular region was obtained from the ratio of the number of stars and the area of corresponding annulus. The densities thus obtained are plotted with the radial distance in Fig. 3.3. The horizontal dashed line indicates the density of field stars, which was obtained from a reference field of radius 3 arcmin located outside of the cluster area. We considered radius of the cluster ($r_{cluster}$) as the point at which radial density merges with field star density and become constant. The radial extent of the cluster thus obtained from near-IR data as $\sim 3.15'$, corresponds to 1.5 pc at the estimated distance of 1.65 kpc (see section 3.4). Our cluster radius estimation agrees well with the literature value of $\sim 3.33'$ (Horner et al. 1997).

We fitted the radial profile with the approach of King (1962), where the projected radial density $f(r)$ is given by $f(r) = f_0/[1 + (r/r_c)^2]$, where f_0 is the central surface density and r_c is a scale factor called core radius of the cluster. The King model fits well with a core radius of $r_c = 23.4''$ that corresponds to 0.19 pc.

In order to understand the spatial structure of the cluster, we generated the stellar surface density map using the nearest neighborhood technique and following the method introduced by Casertano & Hut (1985). Briefly, the stellar density $\sigma(i, j)$ inside a cell of an uniform grid with centre at the coordinates (i, j) is $\sigma(i, j) = \frac{N-1}{\pi r_N^2(i, j)}$ where, r_N is the distance from the centre of the cell to the N^{th} nearest source. Value of N is allowed to vary depending upon how smallest scale structures of the field are interested to study. In Fig. 3.4. we have shown the surface density map which is estimated using the K - band data ($K \leq 17.5$ mag with photometric uncertainty of < 0.1) for the stars towards NGC 2282 region overlaid on the UKIDSS K -band image. This map has been obtained using a grid size of $10'' \times 10''$ and $N=9$. As evident in the IR image of the cluster (see Fig. 3.1b), the surface density map shows a more or less centrally concentrated clustering with a slight elongation along the north-south direction. We obtained the peak stellar density as $418 \text{ stars}/pc^2$ ($96 \text{ stars}/arcmin^2$). The radius of the cluster can be considered as the semi-major axis of the outermost elliptical contour in Fig. 3.4. The cluster radius was thus estimated matches well with that of radial stellar density.

3.3.2 Spectral Classification of Optically Bright Sources

In this section we estimate the spectral types of 8 bright objects observed towards NGC 2282. The targets for low-resolution spectroscopy were selected on the basis of their brightness ($J < 13$ mag) around the cluster (see Fig. 3.1). The coordinates and optical magnitudes of these sources are given in Table 3.3, and the flux calibrated, normalized spectra are shown in Fig. 3.5.

We classified the observed spectra using different spectral libraries available in the literature (Walborn & Fitzpatrick 1990; Jacoby, Hunter & Christian 1984; Torres-Dodgen & Weaver 1993; Allen & Strom 1995). First, we determined a specific spectral range from strong conspicuous features. For e.g., the absence of He II 5411 Å, in a spectra constraints the spectral type as B0.5 or later. While the absence of He I 5876 Å, in a spectra limits the spectral type to A0 or later (Lundquist et al. 2014). Spectra of O- and B-type stars have the features of

hydrogen and helium along with other atomic lines (e.g. O II , C III , Si III , Si IV , Mg II). The He II line strength appears weaker for late O-type stars and He II 4686 is last visible in B0.5 (Walborn & Fitzpatrick 1990). If a spectrum shows He II line at 4200 Å along with the O II /C III blend at 4650 Å, we can classify them to be earlier than B1. The absence of He II 4200, He II 4686, Mg II 4481 and presence of weak features of silicon along with the weak O II /C III blends at 4070 and 4650 Å, indicates the spectral type in the range of B1–B2. For B2-type spectra, He I is in its maximum strength, but for later-type stars Si II 4128-4130 and Mg II gets stronger (Walborn & Fitzpatrick 1990). The presence of He I lines indicates that spectral type is earlier than B5–B7. The late-type sources are classified using the spectral lines TiO 5847-6058, Na I 5893, He I , H_{α} , Ca I 6122, 6162, Fe II 6456. A- and F- stars are identified comparing their H_{α} equivalent width. The G-band (CH λ 4300 Å) appears from F-type stars. G-type stars are classified in comparisons with the equivalent width of H_{α} and Mg I triplet ($\lambda\lambda$ 5167, 5172, 5183 Å). Finally, each source was compared visually to the standard library spectra from Jacoby et al. (1984). However, on the basis of the low-resolution spectroscopy of early type stars, it is difficult to distinguish the luminosity class between supergiants, giants, dwarfs and pre-main sequence stars.

Comparison with the standard spectral libraries of Jacoby et al. (1984) and Walborn & Fitzpatrick (1990), the star ID 1 is classified as B5 V as it has no features of He II 4200, weak features of He II 4541 and C II 4267. The star IDs 2, 3, 4, 5 and 6 are classified as G8 V, K1 V, F7 V, F9 V and F0 V, respectively, as these stars show presence of G-band (CH 4300 Å) and Mg III triplet ($\lambda\lambda$ 5167 Å, 5177 Å, 5183 Å), and their luminosity classes resemble better with main-sequence stars rather than super-giants or giants. The star ID 7 is classified as B2 V as it shows weak features of Si III 4552 along with blended C III /O II 4070 and C III /O II 4650, and absence of He II 4200, He II 4686, and Mg II 4481. The star ID 8 is classified as B0.5 Ve as it shows ionized helium lines at He II 4200, He II 4686, He II 5411, and He II 5720 including strong H_{α} , H_{β} and H_{γ} lines in emission. Based on low-resolution spectra of our targets, an un-

certainty of ± 1 or more in the sub-class estimation is expected. Photometric and spectroscopic details of all the 8 sources are given in Table 3.3.

3.3.3 Reddening towards the Region

The extinction in an embedded cluster is distributed non-uniformly. It is important to know the spatial variation of extinction of the cluster to characterize the cluster members. We estimated the K -band extinction towards NGC 2282 using 2MASS and UKIDSS data within an area $\sim 10' \times 10'$, to understand the local extinction towards the region. We measured the A_K value using $(H - K)$ colours of the stars. The sources without infrared excess (i.e., background dwarfs and non-excess sources within the field) were used to generate the extinction map. Following Gutermuth et al. (2005), we used the grid method to measure the mean value of A_K (see Jose et al. 2013 for details). Briefly, we divided the region of our interest into small grids of size $10'' \times 10''$. The mean value and standard deviation of $(H - K)$ colours of 5 nearest neighbor stars from the centre of each grid was measured. We rejected any sources deviating above 3σ to calculate the mean value of $(H - K)$ at each grid position. To eliminate foreground extinction, we took only those stars having $A_K > 0.12$ mag to generate the extinction map (Jose et al. 2013). The $(H - K)$ values were converted into A_K using the reddening law given by Falherty et al. (2007), i.e., $A_K = 1.82 \times (H - K)_{obs} - (H - K)_0$, where $(H - K)_0$ is the average intrinsic colour of stars, which is assumed to be 0.2 (Allen et al. 2008; Gutermuth et al. 2009). To improve the quality of the extinction map, we excluded the probable YSOs candidates (see sect. 3.5), which otherwise might show high extinction value due to near-IR excess from circumstellar disc emission. The derived extinction map is shown in Fig. 3.6. The extinction within NGC 2282 varies between $A_V = 1.6 - 8.7$ mag with an average extinction of $A_K \sim 0.35$, which corresponds to $A_V \sim 3.9$ mag considering the extinction ratio $A_K/A_V = 0.090$ given by Cohen et al. (1981). The south-eastern part of the cluster found to be at relatively high extinction (A_K is ~ 0.5 mag) compared to the average extinction of the cluster.

We also verified the extinction to each spectroscopically observed source from their photometry. According to the spectral types given in Table 3.3, we estimated the average interstellar extinction towards each star. We first calculated the IR colour excesses $E(J - H)$, $E(H - K)$, $E(J - K)$ for each sources using their observed colours. We transformed these colour excess into visual extinction according to the extinction law, $A_V = E(J - H)/0.11$, $A_V = E(H - K)/0.065$, $A_V = E(J - K)/0.175$ (Cohen et al. 1981). Finally, we took the average A_V values for each star and are given in Table 3.3. The extinction of HD 289120, which is the main illuminating stars of the cluster, is $A_V \sim 1.65$ mag.

3.3.4 Distance and Membership of the Bright Sources

The projected stars against NGC 2282 could be either the young members of the clusters, background stars or foreground stars. We estimated the membership of the candidates based on their spectral types, distance, and photometry. One can derive the distance to a star from estimated spectral type, apparent magnitudes and extinction. We calculated the optical intrinsic distance modulus ($V_0 - M_V$) and also the near-IR intrinsic distance modulus ($J_0 - M_J$), ($H_0 - M_H$) and ($K_0 - M_K$). We prefer near-IR intrinsic distance modulus over optical as it is relatively less uncertain on extinction and come from simultaneous three band measurements of 2MASS data. From near-IR intrinsic distance modulus, we estimated the distance to each spectroscopically observed stars and are given in Table 3.3. The intrinsic colours and absolute magnitudes are taken from Koorneef (1983), Schmidt-Kaler (1982) and Pecaut & Mamajek et al. (2013). The values of intrinsic distance modulus for star IDs 1 and 7 are found to be 11.01 ± 0.20 mag, 11.18 ± 0.18 mag, which corresponds to 1592 ± 147 pc and 1722 ± 135 pc, respectively. Three early B-type stars are adopted as members of the cluster. Thus, we measure the average distance to the cluster as $\sim 1650 \pm 100$ pc from our spectrophotometry observations. Our estimated distance agrees well with the published value in the literature (Racine 1968; Avedisova & Kondratenko 1984; Horner et al. 1997). Considering their distances, the star IDs 2, 3, 4, 5 and 6 seem to be foreground stars. The distance to the star ID 8 could

not be measured accurately, as it is an emission line star with large infrared excess due to the presence of circumstellar disc.

In Fig. 3.7, we show $V/(B - V)$ and $V/(V - I)$ colour-magnitude diagrams (CMDs) for all the stars detected in optical photometry towards NGC 2282. Spectroscopically classified stars are also marked with red circles. The solid blue curve is the zero-age main sequence (ZAMS) by Girardi et al. (2002) shifted for the distance 1.65 kpc and reddening $E(B - V) = 0.52$ mag and $E(V - I) = 0.65$ mag ($E(B - V)/E(V - I) = 1.25$; Cohen et al. 1981), respectively. Since the cluster reddening is highly variable, we used the extinction of the main-sequence (MS) member, HD 289120, located at the cluster centre for corrections of theoretical isochrones. HD 289120 lie on the ZAMS locus. The star IDs 1 and 8 are also high mass members of the cluster. Though the stars with IDs 2, 3, 4, 5 and 6 fall towards right side of the ZAMS, spectroscopic analysis reveals that these stars could be foreground towards NGC 2282. For more reliable membership analysis, we used various observable signature of youthfulness such as emission at H_{α} , excess emission due to presence of disc to identify the probable members of the cluster (see sect. 3.5).

3.3.5 Identification and Classification of YSOs

We identify and classify the YSOs towards NGC 2282 based on their IR colours. Following Gutermuth et al. (2008, 2009), we used IRAC 3.6 and 4.5 μm band data along with H and K data to identify and classify the YSOs. The main limitations for the identification of YSOs based on the IR colours arise from the contaminations of different non-stellar sources in IR detections such as, extragalactic objects like polycyclic aromatic hydrocarbon (PAH) emitting and star-forming galaxies, active galactic nuclei (AGN), unresolved knots of shock emission, PAH-emission contaminated apertures, etc. These sources have considerable IR colours, which could mimic the colours of YSOs in colour-colour (CC) diagram. A number of candidate YSOs could be missed in the mid-IR bands due to the limited sensitivity of IRAC observations. Hence, we identify more YSOs using their near-IR colours (UKIDSS and 2MASS) from the

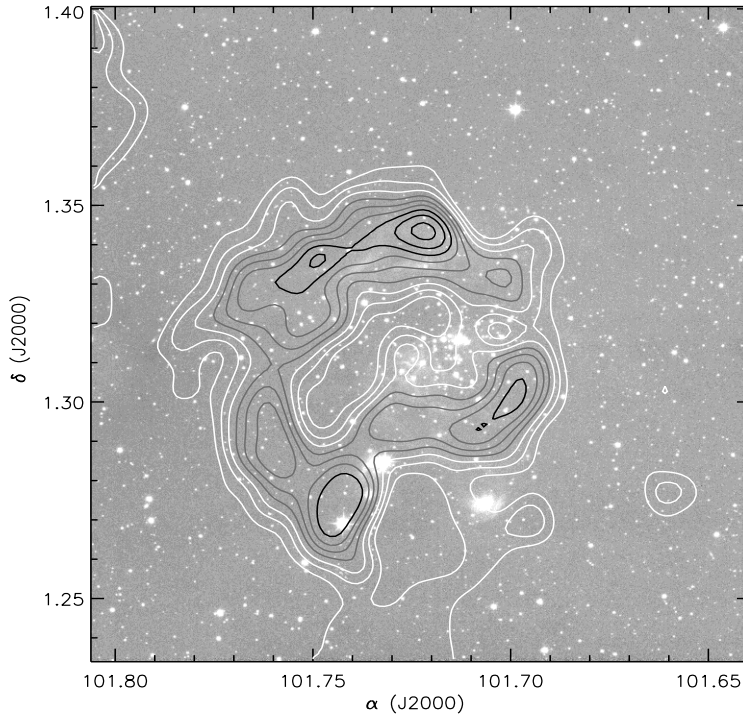


Figure 3.6: Extinction map over plotted on the UKIDSS K -band image. A_K values are estimated from the $(H - K)$ colours. The contour levels are for A_K values 0.32 - 0.42 (white), 0.47 - 0.57 (grey) and 0.62 - 0.82 mag (black), respectively.

master catalog given in Table 3.2. We used $(J - H)/(H - K)$ near-IR CC diagram to identify the additional YSOs, but we cannot classify them in to Class I or Class II category based on their near-IR colours alone. Similarly, the presence of H_α emission is considered as a significant characteristic of a YSO with ongoing disc accretion process (e.g. Dahm 2005). We identified the H_α emission line stars from our slitless spectroscopy data and IPHAS photometry survey (see sect. 3.5.3.). Below we explain the details about the various YSO selection processes.

Selection of YSOs from H , K , 3.6, 4.5 μm data

In order to classify the YSOs, we used IRAC 3.6 and 4.5 μm data from *Spitzer* and H and K near-IR data. The detection of YSOs based on the *Spitzer* data is limited here because NGC 2282 was observed during the *Spitzer* warm mission, which does not provide observations beyond 4.5 μm . Hence we missed the longer wavelength IRAC data at 5.6, 8.0 μm and MIPS

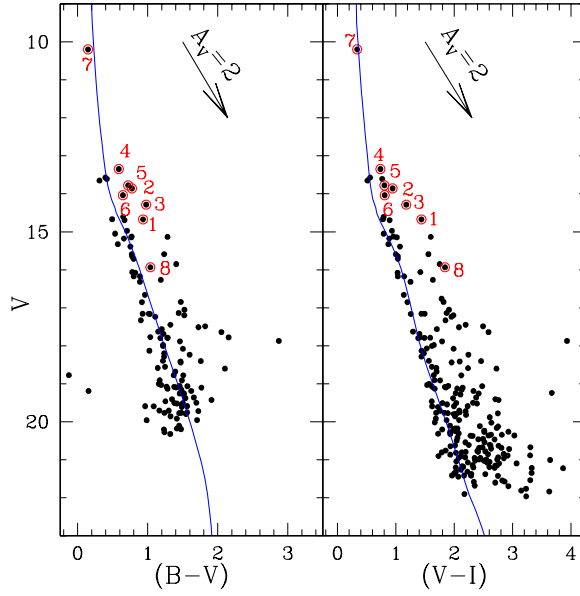


Figure 3.7: Optical CMDs for all the stars within $3.15'$ radius of the cluster. The solid blue curve is the ZAMS from Girardi et al. (2002), corrected for the distance of 1.65 kpc and reddening $E(B - V) = 0.52$ mag. The reddening vector $A_V = 2$ mag is also shown. The sources marked with red circles are the spectroscopically studied stars towards NGC 2282.

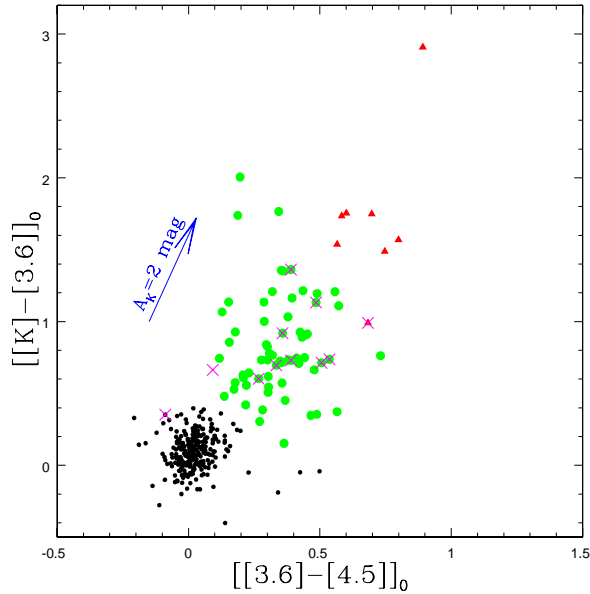


Figure 3.8: Dereddened $[K - 3.6]_0$ vs $[3.6 - 4.5]_0$ CC diagram for all the sources within the cluster radius of $3.15'$ after removing contaminants. The reddening vector $A_K = 2$ mag is plotted by using the reddening law from Flaherty et al. 2007. The sources in green and red are candidate Class II and Class I sources, respectively. The H_α emission sources detected from slitless spectroscopy are marked as magenta crosses.

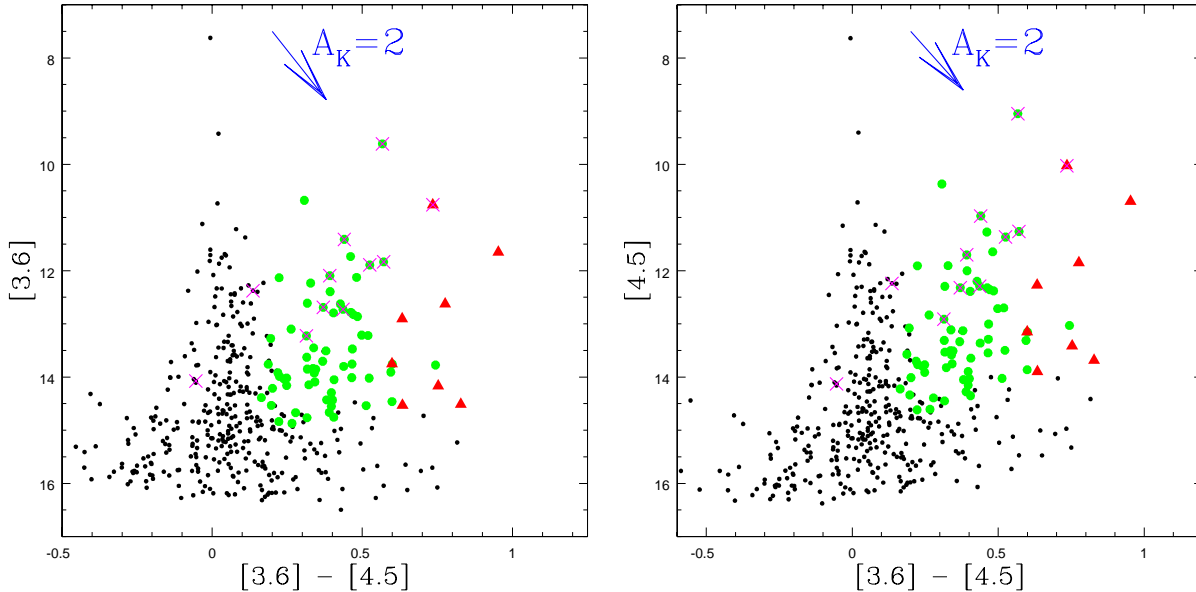


Figure 3.9: Colour-magnitude diagrams using IRAC bands along with the candidate YSOs identified. The symbols are same as Fig. 3.8.

at $24 \mu\text{m}$ bands for improved YSO classification. Here we classify only Class I and II objects and we do not account for Class III objects as they are indistinguishable from field stars based on the data sets used in this study.

We adopted the source classification scheme introduced by Gutermuth et al. (2008, 2009) based on the IR colours. We first dereddened the data using our K -band extinction map (see sect. 3.3). We minimized the inclusion of extragalactic contamination by applying a simple brightness cut in the dereddened $3.6 \mu\text{m}$ photometry, i.e, all the Class I YSOs essentially have $[3.6]_0 \leq 15$ mag and all the Class II YSOs essentially have $[3.6]_0 \leq 14.5$ mag (Gutermuth et al. 2009). After removing the contaminants, we identified YSOs from $([[K] - [3.6]]_0, [[3.6] - [4.5]]_0)$ CC diagram shown in Fig. 3.8. Thus we identified 84 candidate YSOs, which includes 9 Class I and 75 Class II sources with IR excess emission. In Fig. 3.8, the Class I and Class II sources are shown as the red triangles and green circles, respectively, and a reddening vector for $A_K = 2$ mag is also plotted by using the reddening law from Flaherty et al. (2007). The H_α emission line sources from slitless spectroscopy are marked with magenta crosses (discussed later). Fig. 3.9 shows the CMDs in mid-IR bands for all the uncontaminated sources along

with the candidate YSOs. Our present YSO selection is incomplete as many sources in high nebulous region might have not detected at 3.6 and 4.5 μm bands as well as due to the detection limits of IRAC observations.

YSOs from Near-IR Colour-Colour Diagram

Near-IR colour-colour diagram is shown in Fig. 3.10a. The black solid and long dashed green line represent the locus of the intrinsic colours of dwarf and giant stars, taken from Bessel & Brett (1988). The dashed black line represents the locus of the classical T Tauri stars (CTTSs) (Meyer et al. 1997). All the intrinsic locus and photometric data points are transformed in to the CIT (California Institute of Technology) system (Elias et al. 1982) using the relations given by Carpenter et al. (2001). The parallel dashed lines represent the interstellar reddening vectors. The slope of the reddening vectors (i.e., $A_J/A_V = 0.265$, $A_H/A_V = 0.155$ and $A_K/A_V = 0.090$) are taken from Cohen et al. (1981).

We divide the JHK near-IR space into three regions- F, T, and P. The near-IR emission of stars in ‘F’ region originate from their discless photosphere. These stars are located between the upper and middle reddening vectors in the near-IR CC diagram and they are considered to be either field stars or weak-line T Tauri stars (WTTSs)/Class III sources with no or small near-IR excess. However, it is very difficult to distinguish between WTTSs with small near-IR excess and field stars from only near-IR CC diagram (Ojha et al. 2004). The near-IR emission of ‘T’ region stars arise from both photosphere and circumstellar disc (Lada & Adams 1992). Majority of these stars are considered to be classical T Tauri stars (CTTSs). All such sources possess accreting optically thick disc (Meyer et al. 1997). The ‘P’ region stars have more near-IR colour excess at K-band, and these stars are thought to have accreting disc. Some of them might have envelope around them and they are protostellar in nature (Rice et al. 2012).

We also plotted the CC diagram for the reference field sources in Fig. 3.10b. The reference field region was chosen for the same area as that of the cluster (radius = 3.15') and at similar

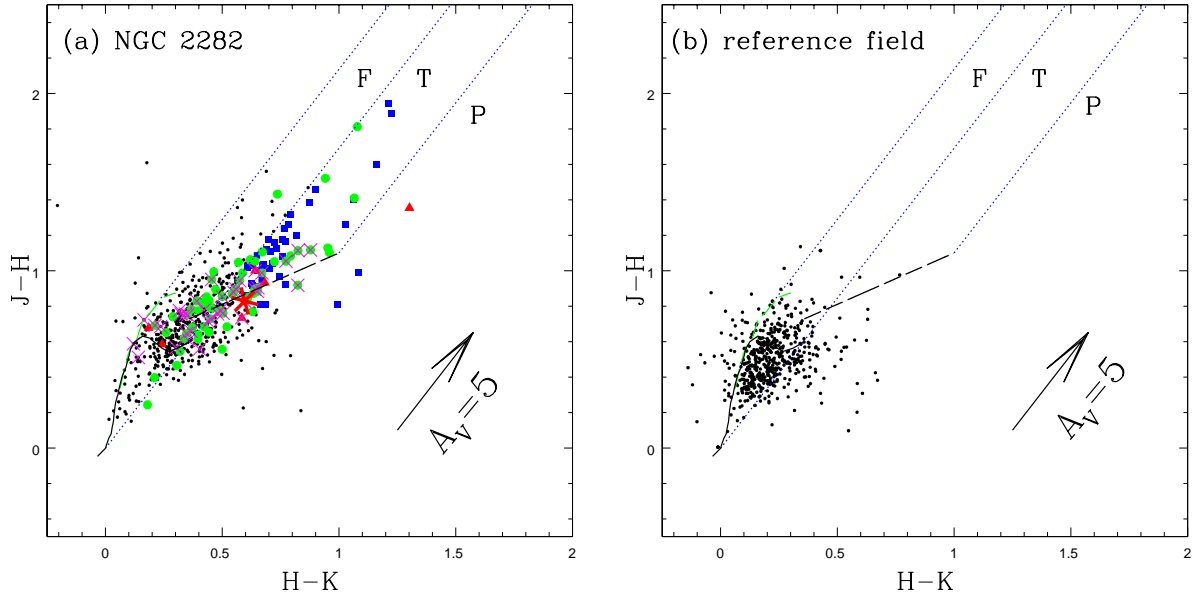


Figure 3.10: $J - H/H - K$ CC diagram of (a) NGC 2282 within $3.15'$ radius and (b) the reference field of same area. The locus for dwarfs (solid black) and giants (green dashed line) are taken from Bessel & Brett (1988). The long dashed black line represents the CTTs locus (Meyer et al. 1997) and the small dashed blue lines represent the reddening vectors (Cohen et al. 1981). The reddening vector of visual extinction $A_V = 5$ mag is also shown. All the Class I and Class II sources are represented with red triangles and green circles, respectively. The blue solid squares are the candidate YSOs identified from JHK colours. The asterisk mark is the location of Herbig Ae/Be star. The magenta crosses are the H_α emitting objects detected from slitless spectroscopy and IPHAS photometry (see text).

photometric depth. The reference field was selected $\sim 10'$ towards the North of NGC 2282 ($\alpha_{2000} = 06^h46^m51.06^s$ $\delta_{2000} = +01^{\circ}29^m29.9^s$), to avoid any superposition with the cluster region. A comparison of the reference field with our cluster region shows that almost all the stars in the reference field are confined below $(J - H) \sim 0.8$ mag and to the left of the middle reddening vector from $(H - K) \sim 0.6$ mag. Thus we assume that the ‘T’ and ‘P’ region stars are not contaminated by the field stars. Hence those sources fall in the ‘T’ and ‘P’ regions of the target field could be considered as candidate YSOs. From near-IR colour, we have selected 45 additional YSOs, which are not included in the previous YSO list (sect. 3.5.1). Only from JHK data it is not possible to distinguish Class I and Class II objects, hence we consider them as candidate YSO sources.

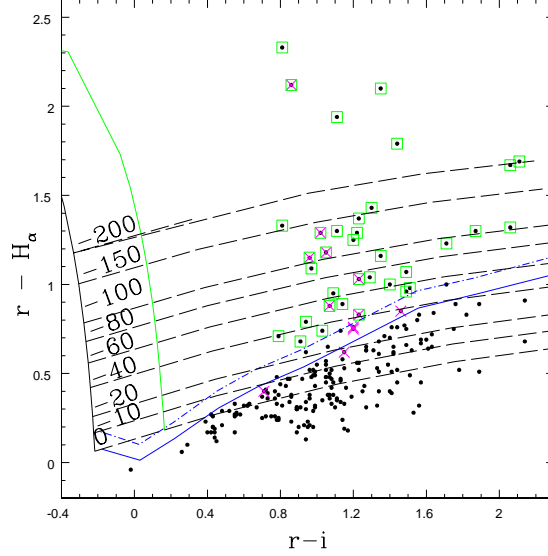


Figure 3.11: $r-i/r-H_\alpha$ CC diagram for all the sources detected in IPHAS photometry towards NGC 2282. The magenta crosses and green boxes are the H_α emission sources detected from slitless spectroscopy and IPHAS photometry, respectively. See text for increasing levels of H_α emission tracks, unreddened continuum and locus of main-sequence.

Selection of H_α Emission Stars from Slitless Spectroscopy and IPHAS Photometry

Using slitless spectroscopy, H_α emission-line stars were visually identified from their enhancement over the continuum. We identified 16 H_α emitting sources and they are listed in Table 3.4. Of the 16, 14 sources have JHK data sets. Ten H_α emission stars are detected as YSOs from H , K , 3.6 and 4.5 μm colours (1 Class I, 9 Class II). All the H_α emission stars are plotted in the near-IR colour-colour diagram shown in 3.10a. The star ID 8 (see Table 3.3), which is classified as a B0.5 Ve star in the optical slit-spectroscopy with strong H_α emission, is also detected with the slitless spectroscopy and falling in the ‘P’ region of JHK CC diagram (See Fig. 3.10a).

Fig. 3.11 presents the IPHAS ($r-i/r-H_\alpha$) CC diagram towards NGC 2282. Black filled circles are the sources brighter than $r < 20$ with photometric uncertainty of < 0.1 mag in IPHAS DR2. The identified sources are marked in Fig. 3.11. Two nearly vertical black and green lines represent the trend for an unreddened Rayleigh-Jeans continuum and the case of an unreddened optically thick disc accretion continuum, respectively (Barentsen et al. 2014). The

black broken lines are the predicted lines of constant net emission EW. The solid and broken blue lines indicate the locus of unreddened main-sequence and that of the main-sequence stars having an H_α emission-line strength of -10 \AA EW, respectively. The main-sequence emission line with EW -10 \AA is chosen as CTTS threshold for H_α emission stars. However, it is difficult to confirm CTTSs solely on the basis of IPHAS photometry (Barentsen et al. 2014). Other possible H_α emission objects are evolved massive stars (e.g. Be stars, Wolf-Rayet stars, luminous blue variables), evolved intermediate-mass stars (e.g. Mira Variables, unresolved planetary nebulae) and interacting binaries (e.g. cataclysmic variables, symbiotic stars). (Barentsen et al. 2011; Corradi et al. 2008).

We selected 44 sources as H_α emitting stars, which are located above the 3σ confidence level from CTTSs threshold as mentioned above. Out of 16 H_α emitting sources detected from slitless spectroscopy, 15 have IPHAS photometry, but only 10 satisfy the conditions for H_α emitting stars using IPHAS photometry. This difference could be due to the variable H_α emission activities in PMS sources as well as due to the different detection limits for these two observations. Thus we have selected 50 H_α emitting sources from slitless spectroscopy and IPHAS photometry. Among those 50 H_α emitting sources, 24 are classified as Class II and 3 are classified as Class I sources. Including these H_α emission sources, and the YSOs selected from mid-IR and near-IR colours in sect. 3.5.1 and sect. 3.5.2, we have 152 candidate YSOs in NGC 2282 region, and the details are presented in Table 3.4.

3.4 Discussion

3.4.1 Near-IR Colour-Magnitude Diagram

The near-IR CMD is a useful tool for understanding the nature of YSOs in the embedded star-forming regions. The near-IR CMD (K vs $(H - K)$) for all the stars detected towards NGC 2282 cluster is shown in Fig. 3.12a. The identified all sources are marked. A reference

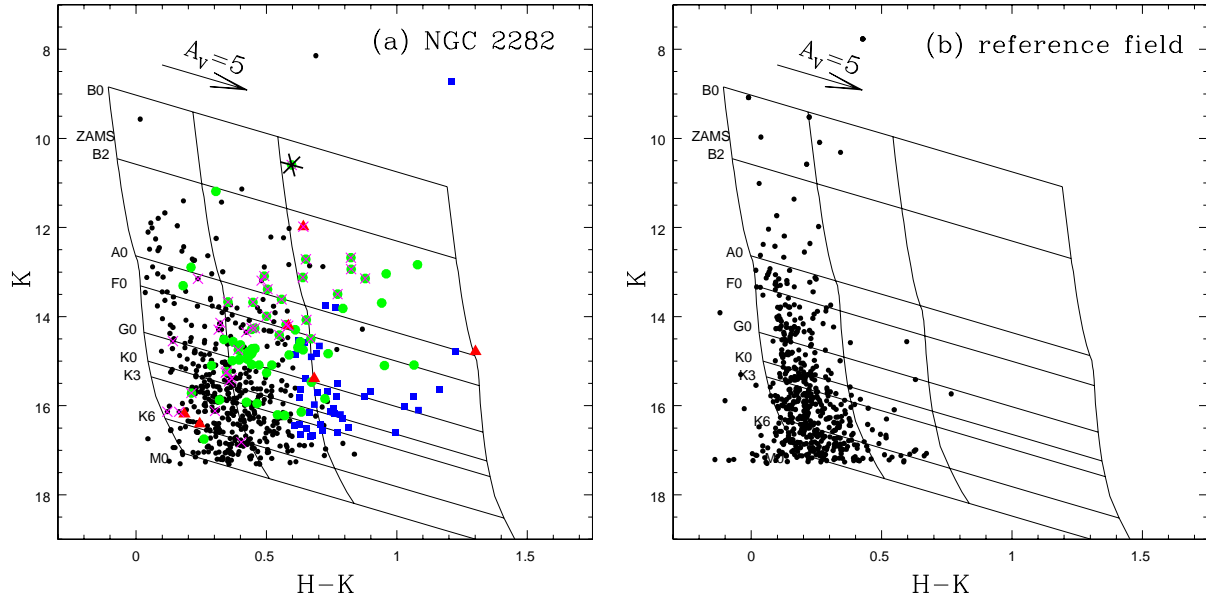


Figure 3.12: (a) Near-IR CM diagram of the stars within $3.15'$ radius of NGC 2282. The nearly vertical solid lines are the loci of ZAMS stars at 1.65 kpc reddened by $A_V = 0, 5, 10, 20$ mag. The slanting horizontal lines are the reddening vectors for corresponding spectral classes. All the Class I and Class II sources determined from the $H, K, 3.6$ and $4.5 \mu\text{m}$ data are represented with red triangles and green circles, respectively. The blue solid squares are the candidate YSOs selected from JHK colours. The magenta crosses are the H_α emitting objects detected from the slitless spectroscopy and IPHAS photometry. The asterisk is the location of Herbig Ae/Be star. The (b) CM diagram for the reference field.

field of same area and at similar photometric depth is also shown in Fig. 3.12b. The nearly vertical solid lines are the loci of ZAMS reddened by visual extinction of $A_V = 0, 5, 10, 20$ magnitude, respectively and corrected for cluster distance of 1.65 kpc. The slanting horizontal lines represent the reddening vectors of the corresponding spectral type made from Flaherty et al. (2007). The membership of any YSO relies on the fact that they are mainly found in the cluster area rather than in the surrounding field. We considered only those YSOs within the cluster area (radius = $3.15'$) to determine the cluster parameters. In the CMD given in Fig. 3.12a, we can see that majority of the YSOs are located within B2 to K6 spectral type. Majority of H_α emission objects fall within B0 to F0 spectral type. A Herbig Ae/Be type star, determined as B0.5 from spectroscopic observations, falls close to B0 vector with $A_V \sim 10$ mag. This estimate matches well with the spectroscopic observations (sect. 3.2). The YSOs, determined from IR CC diagrams, share IR space with many unclassified sources marked as

black dots. These might be the background sources or the weak line T Tauri sources, which are not included in our YSO survey. Spectroscopic observations are necessary for the confirmation of their membership.

3.4.2 Optical Colour-Magnitude Diagram of YSOs

An Optical CMD, V vs $(V - I)$ of YSOs is plotted in Fig. 3.13. It is an important tool to estimate the approximate ages and masses of YSOs. The solid curve in Fig. 3.13 represents the ZAMS, taken from Girardi et al. (2002) corrected for the cluster distance 1.65 kpc and reddening of $E(B - V) = 0.52$ mag ($E(V - I) = 0.65$ mag) (see sect. 3.3 & 3.4). We have used the PMS isochrone and evolutionary tracks of Bressan et al.(2012) to determine the ages and masses of the YSOs. The PMS isochrones for Siess et al. (2000) is also plotted for comparison. The ages and masses of YSOs have been estimated by comparing their locations on the CMD with PMS isochrones of various ages after correcting for the distance and extinction. Since the reddening vector is nearly parallel to the isochrones, a small extinction variation would not have much effect on the age estimation of YSOs.

We have compiled VI photometry for the YSOs, and compare their positions on the CMD to theoretical model isochrones. The CMD positions of YSOs seem to be adequately fit between 1–10 Myr. Different models at low-mass end differs significantly as we can see in Fig. 3.13. The average age of the YSOs seem to be $\sim 2-5$ Myr, which we considered as the average age of the cluster.

3.4.3 Mass Distribution

Since YSOs show excess emission at longer wavelengths, $K/H - K$ CM diagram is not a suitable tool to understand the mass distribution of YSOs. We used J vs $(J - H)$ CM diagram to reduce the effect of excess emission. Fig. 3.14 shows the $J/(J - H)$ CM diagram for all the YSOs detected from IR colour-colour diagrams (Fig. 3.8, 3.10a, 3.11). The ZAMS of Girardi

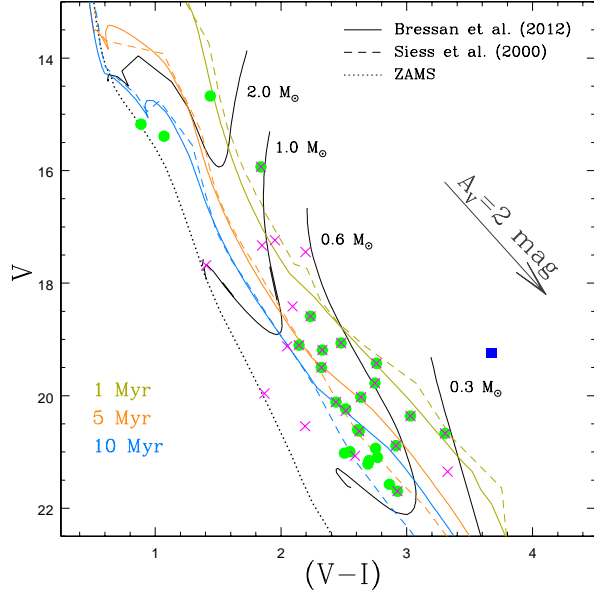


Figure 3.13: $V/(V-I)$ CMD for the Class II sources, candidate YSOs from JHK colours and H_α emitting sources within NGC 2282 cluster. All the symbols are same as in Fig. 3.10. The dotted curve is the locus of ZAMS from Girardi et al. (2002), solid curves are the PMS isochrones of age 1.0, 5.0 and 10.0 Myr, respectively, and the thin black solid curves are the evolutionary tracks for various mass bins from Bressan et al. (2012). The long dashed curves are PMS isochrones of age 1.0, 5.0 and 10.0 Myr taken from Siess et al. (2000). All the isochrones and tracks are corrected for the distance and reddening.

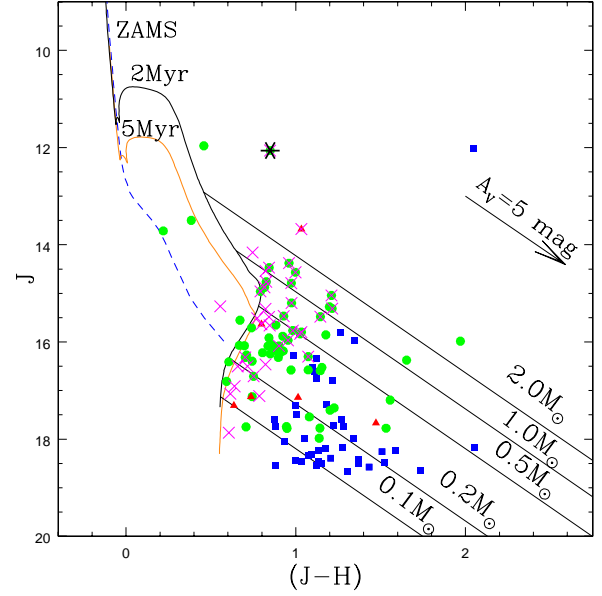


Figure 3.14: J vs $(J-H)$ diagram for Class I, Class II sources, candidate YSOs detected from JHK colours and the H_α emitting sources. All the symbols are same as in Fig. 3.10. Herbig AeBe star (asterisk mark) is also shown. The blue dashed curve is the locus of the ZAMS from Girardi et al. (2002). The solid curves are the PMS isochrones of age 2.0 and 5.0 Myr, respectively, from Bressan et al. (2012). The slanting solid lines are the reddening vectors corresponding to 0.1, 0.2, 0.5, 1.0 and 2.0 M_\odot .

et al. (2002) corrected for the cluster distance of 1.65 kpc is used for comparison in Fig. 3.14. The PMS isochrones for 2.0 Myr and 5.0 Myr are taken from Bressan et al. (2012).

It is apparent from Fig. 3.14 that majority of the candidate YSOs have masses $\sim 0.1-2 M_\odot$. Few candidate YSOs (e.g. ID = 8, asterisk mark) seem to be apparently more massive and we can not determine their parameters properly as they are highly embedded. Since the low-mass end of the isochrones are very close to each other, a change of $\sim 1-2$ Myr in age would not change the masses drastically. Thus we used a representative age of those YSOs as 2 Myr.

However, such mass estimation could be associated with several errors such as presence of binary companions, circumstellar envelope, variable stars and other unknown excess emissions etc. (Samal et al. 2014).

3.4.4 Spatial Distribution of YSOs

Spatial distribution of YSOs in the young clusters traces the star-forming history of that cloud. Fig. 3.15 shows the spatial distribution of the candidate YSOs within NGC 2282 (red triangles: Class I; green circles: Class II; Blue squares: candidate PMS stars and magenta crosses: H_α emission sources) overlaid on the IRAC 3.6 μm mosaic image. From Fig. 3.15, it is apparent that majority of YSOs are concentrated at the core region of the cluster (see sect. 3.1). Majority ($\sim 70\%$) of the H_α emitters including IR excess emitters are located in the core region, and some are scattered in the northern side of the cloud. A secondary peak is seen towards the South-Eastern part of the cluster, which harbors a Herbig B0.5 Ve star. An interesting arc is visible from East to West through North. No significant population of YSOs are seen in the Western part of the cloud. While a significant and scattered population towards North-East part of the cloud, particularly Class II, are visible. The extinction map is overplotted in Fig. 3.15 and it shows that majority of the YSOs are crowded mainly in the central (low extinction) areas of the region.

3.4.5 Disc Fraction and Age of the Cluster

YSOs are surrounded by circumstellar disc of gas and dust and the Near-IR excess emission originates from the disc (Lada & Adams 1992). The fraction of sources with excess over the entire number of sources would give an approximate age of the cluster. The disc fraction remains very high ($\geq 80\%$) at early stages (~ 0.3 Myr) of the clusters and decreases with the increasing age (Haisch et al. 2001). The disc lasts for small time scale of about $\sim 3\text{--}15$ Myr (Strom et al. 1989; Lada & Lada 1995; Haisch et al. 2001; Hillenbrand 2002; Hernández et

al. 2007) and disc fraction reaches to one-half in ≤ 3 Myr time scale (Haisch et al. 2001). The NGC 2282 cluster is physically associated with molecular cloud, which indicates that the cluster has an age of < 10 Myr (Leisawitz et al. 1989).

We have detected total 1050 objects from our observations within 3.15 arcmin of the cluster radius. While in similar depth of observations and area on reference field, we have detected 856 stars. After removing the field star contribution, the number of objects associated the cluster area would be ~ 203 . The number of candidate YSOs from H , K , 3.6, 4.5 μm data is 72 in the cluster area, while from J , H , K data the number is 40. All disc bearing H_α stars are detected as the IR excesses sources. Hence, the total number of IR excess sources within NGC 2282 is 112. Thus we estimated the disc fraction of NGC 2282 as $\sim 58\% \pm 6\%$. If we consider the IR excess sources from mid-IR data only, the disc fraction is $\sim 37\% \pm 5\%$. This disc fraction estimated in NGC 2282 is significantly larger than that of Horner et al. (1997). This is mainly because the detection limit of current study is much deeper than the former one. From disc-fraction, the age of the cluster could be in the range $\sim 2\text{--}5$ Myr, which is in agreement with the CMD analysis.

3.5 Summary and Conclusions

In this chapter, we have presented multiwavelength studies of a young cluster NGC 2282 in Monoceros constellation, using deep optical BVI observations complimented with the archival data sets from IPHAS, UKIDSS, 2MASS and mid-IR data from *Spitzer* 3.6 and 4.5 μm . We have also used the spectroscopy observations of 8 bright sources in the cluster region. The main results are summarized as follows:

1. We have analysed the stellar surface density distribution of K -band data using nearest neighborhood technique. The radius of the cluster has been estimated to be $\sim 3.15'$ from the semi-major axis of the outer most elliptical contour.

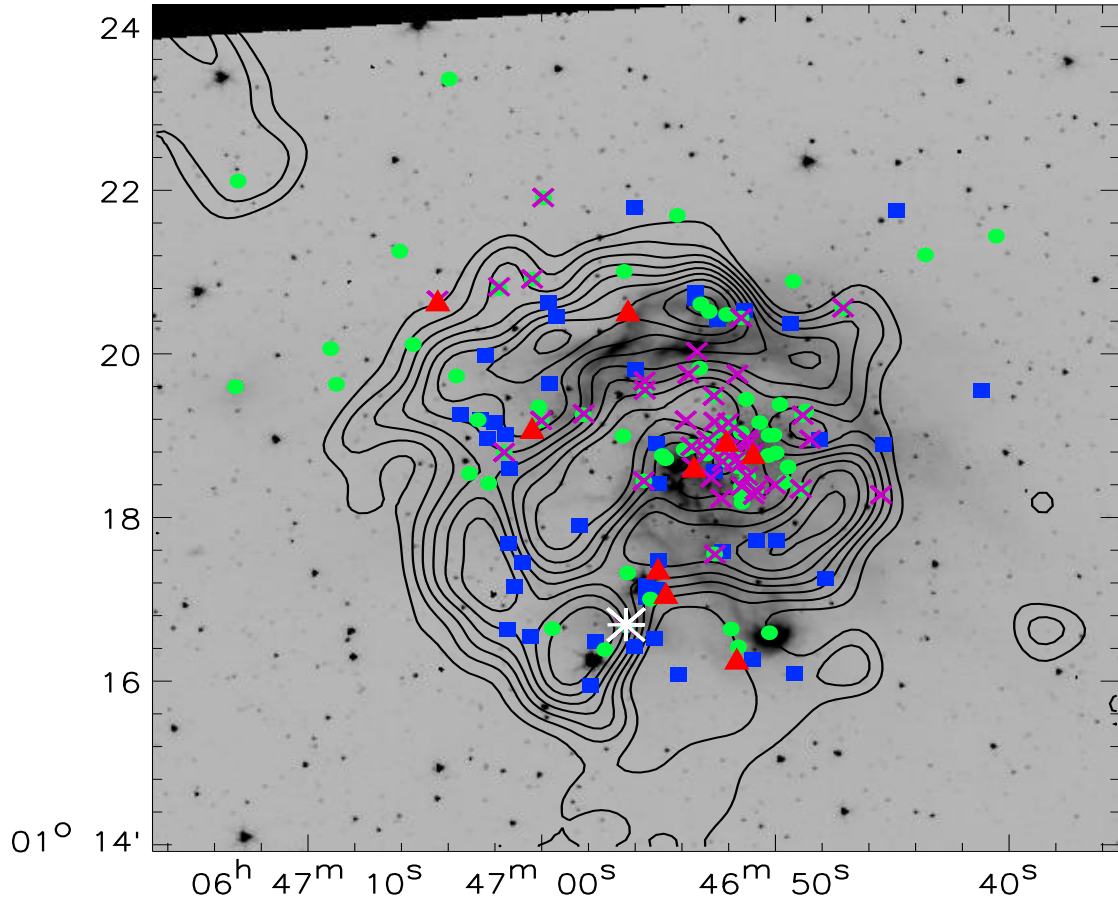


Figure 3.15: Spatial distribution of Class I (red triangles), Class II (green circles), candidate YSOs from JHK colours (blue squares) overlaid on IRAC $3.6 \mu\text{m}$ image. The magenta crosses indicate the H_α emission line sources. The location of Herbig Ae/Be star (white asterisk) is also shown. The contours are plotted for different A_K values from 0.32 to 0.87 mag.

2. We have estimated the spectral types and membership status of 8 bright sources located inside the cluster area using conspicuous lines and comparison of equivalent widths. We have identified three early B-type members in the cluster. Among these B-type massive members, HD 289120, a B2V type star was classified earlier, and two stars (a Herbig Ae/Be star and a B5 V) are classified for the first time in this work. We have estimated the distance to the cluster as ~ 1.65 kpc from spectrophotometric analysis of those massive members.

3. The K -band extinction map is estimated from $(H-K)$ colours using nearest neighborhood technique, and the mean extinction within the cluster area is found to be $A_V \sim 3.9$ mag. The extinction within the cluster region seem to be non-uniform.
4. From slitless spectroscopy, we have identified 16 H_α emission line stars. Another 34 H_α emission line stars are identified from IPHAS data, totaling 50 H_α emission line stars towards the region.
5. Using Gutermuth et al. (2008; 2009) scheme, we have classified 9 Class I and 75 Class II objects from mid-IR data. Other candidate YSOs are identified from near-IR $(J-H)/(H-K)$ CC diagram. We have identified 152 candidate YSOs from IR excess and H_α emission towards the region.
6. We characterized these YSOs from various colour-magnitude diagrams. From $V/(V-I)$ CMD, we have estimated the cluster age which is in the range of $\sim 2-5$ Myr. From mid-IR data, we have estimated the disc fraction of $\sim 58\%$, which corresponds to an age of $\sim 2-5$ Myr. The masses of the candidate YSOs are found to be in the range ~ 0.1 to $2.0 M_\odot$ in the $J/(J-H)$ CMD.
7. The morphology of the region has been studied from spatial distribution of YSOs, stellar density distribution, signature of dust in various optical-infrared images along with the extinction map.

Table 3.4: catalog of YSOs (Class I, Class II, other PMS stars and H $_{\alpha}$ sources).

id	α_{2000} (deg)	δ_{2000} (deg)	V mag	B-V mag	V-I mag	J mag	H mag	K mag	3.6 μ m mag	4.5 μ m mag	H $_{\alpha}$ emission (YES/NO)
Class I sources											
54	101.723024	1.310400	17.447 \pm 0.005	1.323 \pm 0.018	2.195 \pm 0.005	13.677 \pm 0.026	12.644 \pm 0.026	11.958 \pm 0.027	10.761 \pm 0.003	10.026 \pm 0.002	YES
310	101.715435	1.271265	21.316 \pm 0.039	1.434 \pm 0.248	2.224 \pm 0.046	17.144 \pm 0.024	16.131 \pm 0.016	15.420 \pm 0.017	13.749 \pm 0.013	13.150 \pm 0.011	NO
313	101.728048	1.284664	20.794 \pm 0.033	1.692 \pm 0.188	2.195 \pm 0.036	17.129 \pm 0.024	16.393 \pm 0.021	16.200 \pm 0.034	14.514 \pm 0.021	13.686 \pm 0.015	NO
644	101.768647	1.344268	18.882 \pm 0.008	1.331 \pm 0.026	1.844 \pm 0.010	16.088 \pm 0.010	14.724 \pm 0.005	13.497 \pm 0.003	12.051 \pm 0.004	11.494 \pm 0.004	YES
1873	101.729427	1.289632	17.665 \pm 0.038	16.193 \pm 0.017	14.837 \pm 0.010	12.903 \pm 0.008	12.270 \pm 0.006	NO
1972	101.751821	1.318276	17.810 \pm 0.076	16.137 \pm 0.033	14.167 \pm 0.013	13.414 \pm 0.012	NO
2304	101.717280	1.315665	17.309 \pm 0.028	16.674 \pm 0.027	16.420 \pm 0.043	14.532 \pm 0.046	13.898 \pm 0.019	NO
2329	101.712510	1.313155	15.636 \pm 0.007	14.838 \pm 0.005	14.230 \pm 0.006	12.626 \pm 0.007	11.850 \pm 0.005	YES
2493	101.734794	1.342232	19.570 \pm 0.220	16.985 \pm 0.036	14.804 \pm 0.010	11.650 \pm 0.004	10.697 \pm 0.003	NO
Class II sources											
1	101.709618	1.276534	14.674 \pm 0.008	0.933 \pm 0.007	1.438 \pm 0.004	11.964 \pm 0.020	11.506 \pm 0.029	11.164 \pm 0.034	10.678 \pm 0.002	10.371 \pm 0.003	NO
8	101.735121	1.277934	15.934 \pm 0.013	1.037 \pm 0.010	1.841 \pm 0.007	12.061 \pm 0.023	11.212 \pm 0.020	10.572 \pm 0.023	9.616 \pm 0.003	9.049 \pm 0.002	YES
71	101.705376	1.348143	15.176 \pm 0.003	0.660 \pm 0.003	0.887 \pm 0.005	13.715 \pm 0.026	13.496 \pm 0.035	13.283 \pm 0.033	12.863 \pm 0.006	12.379 \pm 0.007	NO
72	101.726013	1.361580	15.389 \pm 0.003	0.752 \pm 0.004	1.070 \pm 0.003	13.498 \pm 0.021	13.114 \pm 0.032	12.870 \pm 0.034	12.233 \pm 0.005	11.905 \pm 0.005	NO
97	101.804643	1.326651	13.103 \pm 0.005	0.461 \pm 0.005	0.878 \pm 0.004	11.618 \pm 0.019	11.209 \pm 0.020	10.952 \pm 0.021	10.420 \pm 0.002	10.225 \pm 0.003	NO
101	101.775393	1.354269	15.659 \pm 0.003	1.161 \pm 0.004	1.501 \pm 0.004	13.017 \pm 0.023	12.240 \pm 0.024	11.840 \pm 0.023	11.168 \pm 0.003	10.974 \pm 0.003	NO
289	101.748231	1.277375	20.235 \pm 0.018	1.594 \pm 0.123	2.514 \pm 0.014	15.275 \pm 0.005	14.077 \pm 0.003	13.078 \pm 0.002	12.126 \pm 0.005	11.645 \pm 0.005	NO
298	101.715135	1.273663	20.994 \pm 0.037	1.632 \pm 0.217	2.548 \pm 0.031	16.182 \pm 0.010	15.294 \pm 0.008	14.851 \pm 0.010	14.212 \pm 0.018	14.011 \pm 0.018	NO
307	101.716418	1.277292	21.022 \pm 0.034	1.443 \pm 0.182	2.505 \pm 0.030	16.320 \pm 0.012	15.423 \pm 0.009	14.978 \pm 0.012	14.387 \pm 0.020	14.223 \pm 0.021	NO
321	101.719373	1.292577	19.190 \pm 0.013	1.621 \pm 0.050	2.329 \pm 0.009	15.042 \pm 0.004	13.832 \pm 0.002	12.973 \pm 0.002	11.412 \pm 0.003	10.972 \pm 0.003	YES
363	101.759568	1.306980	21.575 \pm 0.061	...	2.862 \pm 0.046	15.855 \pm 0.008	14.678 \pm 0.005	13.852 \pm 0.005	12.626 \pm 0.006	12.199 \pm 0.006	NO
364	101.762999	1.308987	20.603 \pm 0.056	...	2.610 \pm 0.029	15.653 \pm 0.007	14.770 \pm 0.005	14.308 \pm 0.007	13.212 \pm 0.009	12.714 \pm 0.008	NO
374	101.756814	1.313292	20.670 \pm 0.033	1.323 \pm 0.153	3.304 \pm 0.012	14.960 \pm 0.004	14.168 \pm 0.003	13.701 \pm 0.004	13.098 \pm 0.007	12.835 \pm 0.008	YES
375	101.750214	1.319768	20.361 \pm 0.027	1.395 \pm 0.115	3.029 \pm 0.039	15.966 \pm 0.009	15.012 \pm 0.006	14.440 \pm 0.007	13.472 \pm 0.012	13.005 \pm 0.010	YES
382	101.786648	1.327160	19.114 \pm 0.008	1.668 \pm 0.042	2.150 \pm 0.008	15.316 \pm 0.005	14.490 \pm 0.004	14.120 \pm 0.006	13.472 \pm 0.010	13.221 \pm 0.011	NO
390	101.772999	1.335246	20.532 \pm 0.018	1.978 \pm 0.176	2.828 \pm 0.015	15.742 \pm 0.007	14.563 \pm 0.004	13.678 \pm 0.004	12.428 \pm 0.005	12.068 \pm 0.006	NO
395	101.761466	1.319915	21.154 \pm 0.052	1.540 \pm 0.245	2.700 \pm 0.056	16.577 \pm 0.015	15.605 \pm 0.010	15.114 \pm 0.013	14.092 \pm 0.017	13.750 \pm 0.015	NO
571	101.720487	1.315683	18.589 \pm 0.035	1.934 \pm 0.133	2.235 \pm 0.011	14.790 \pm 0.003	13.816 \pm 0.002	13.150 \pm 0.003	12.095 \pm 0.005	11.703 \pm 0.005	YES
572	101.714483	1.303121	21.096 \pm 0.060	...	2.767 \pm 0.026	16.230 \pm 0.011	15.324 \pm 0.008	14.864 \pm 0.011	14.021 \pm 0.019	13.498 \pm 0.015	NO
574	101.703997	1.305660	20.026 \pm 0.018	2.020 \pm 0.150	2.635 \pm 0.012	15.467 \pm 0.006	14.538 \pm 0.004	14.017 \pm 0.005	13.226 \pm 0.008	12.912 \pm 0.010	YES
575	101.720311	1.313621	19.778 \pm 0.078	...	2.747 \pm 0.035	15.311 \pm 0.005	14.097 \pm 0.003	13.182 \pm 0.003	11.892 \pm 0.004	11.367 \pm 0.004	YES
578	101.712067	1.305554	19.425 \pm 0.026	1.910 \pm 0.091	2.759 \pm 0.019	14.470 \pm 0.003	13.627 \pm 0.002	13.115 \pm 0.003	12.394 \pm 0.006	12.001 \pm 0.006	YES
603	101.703739	1.320896	19.063 \pm 0.011	1.565 \pm 0.048	2.478 \pm 0.014	14.567 \pm 0.003	13.569 \pm 0.002	12.711 \pm 0.002	11.835 \pm 0.003	11.264 \pm 0.004	YES
616	101.731768	1.325989	20.632 \pm 0.066	0.829 \pm 0.150	2.622 \pm 0.025	15.832 \pm 0.008	14.806 \pm 0.005	14.207 \pm 0.006	13.451 \pm 0.010	13.113 \pm 0.011	YES
620	101.719523	1.324788	19.101 \pm 0.017	1.766 \pm 0.076	2.143 \pm 0.015	14.761 \pm 0.003	13.935 \pm 0.002	13.410 \pm 0.003	12.611 \pm 0.006	12.294 \pm 0.007	YES
625	101.731974	1.307462	20.889 \pm 0.055	1.496 \pm 0.184	2.914 \pm 0.020	15.766 \pm 0.007	14.784 \pm 0.005	14.104 \pm 0.006	12.784 \pm 0.007	12.322 \pm 0.007	YES

Continued on next page

Table 3.4 – continued from previous page

id	α_{2000} (deg)	δ_{2000} (deg)	V mag	B-V mag	V-I mag	J mag	H mag	K mag	3.6 μ m mag	4.5 μ m mag	H α emission (YES/NO)
626	101.728691	1.312648	20.935 ± 0.086	...	2.752 ± 0.039	16.246 ± 0.011	15.396 ± 0.009	15.012 ± 0.012	13.921 ± 0.014	13.702 ± 0.016	NO
629	101.742782	1.320963	19.498 ± 0.013	1.693 ± 0.071	2.321 ± 0.015	15.197 ± 0.005	14.222 ± 0.003	13.641 ± 0.004	12.728 ± 0.007	12.292 ± 0.006	YES
645	101.757760	1.346685	19.675 ± 0.010	1.417 ± 0.053	1.964 ± 0.016	16.067 ± 0.009	15.239 ± 0.007	14.766 ± 0.010	14.049 ± 0.015	13.672 ± 0.012	YES
646	101.751829	1.348607	21.697 ± 0.067	1.409 ± 0.322	2.926 ± 0.035	16.302 ± 0.012	15.229 ± 0.007	14.531 ± 0.008	13.855 ± 0.013	13.510 ± 0.011	YES
654	101.720359	1.341991	21.212 ± 0.054	...	2.691 ± 0.034	16.591 ± 0.015	15.447 ± 0.009	14.780 ± 0.010	13.759 ± 0.014	13.572 ± 0.014	NO
665	101.696564	1.342525	20.114 ± 0.015	1.621 ± 0.120	2.437 ± 0.014	15.480 ± 0.006	14.335 ± 0.003	13.530 ± 0.004	12.690 ± 0.006	12.320 ± 0.007	YES
677	101.749821	1.365127	19.616 ± 0.013	1.442 ± 0.061	2.687 ± 0.015	14.849 ± 0.004	13.930 ± 0.002	13.246 ± 0.003	12.288 ± 0.005	11.854 ± 0.005	YES
999	101.757683	1.334398	20.614 ± 0.028	1.146 ± 0.088	2.454 ± 0.033	16.114 ± 0.010	15.148 ± 0.007	14.393 ± 0.007	13.635 ± 0.010	13.151 ± 0.010	YES
1060	101.804179	1.368557	19.016 ± 0.009	1.452 ± 0.033	2.176 ± 0.012	15.299 ± 0.005	14.453 ± 0.004	13.958 ± 0.005	13.398 ± 0.010	13.189 ± 0.010	NO
1853	101.734849	1.288707	15.983 ± 0.009	14.013 ± 0.003	12.889 ± 0.002	12.132 ± 0.005	11.909 ± 0.005	NO
1864	101.738908	1.273076	16.526 ± 0.014	15.372 ± 0.008	14.726 ± 0.009	13.704 ± 0.012	13.336 ± 0.011	NO
1865	101.730782	1.283392	17.196 ± 0.025	15.640 ± 0.010	14.873 ± 0.011	13.627 ± 0.012	13.312 ± 0.012	NO
1999	101.765280	1.328838	17.034 ± 0.022	15.947 ± 0.014	15.217 ± 0.014	14.491 ± 0.022	14.233 ± 0.019	NO
2287	101.715277	1.312198	16.222 ± 0.011	15.418 ± 0.009	15.117 ± 0.013	14.549 ± 0.027	14.152 ± 0.023	NO
2288	101.708434	1.313170	17.747 ± 0.042	17.040 ± 0.038	16.769 ± 0.058	14.756 ± 0.032	14.351 ± 0.025	NO
2289	101.708814	1.316813	16.575 ± 0.015	15.502 ± 0.009	14.891 ± 0.011	14.051 ± 0.017	13.645 ± 0.015	NO
2290	101.718250	1.317385	16.074 ± 0.010	15.208 ± 0.007	14.744 ± 0.010	13.756 ± 0.015	13.290 ± 0.012	NO
2300	101.716899	1.311380	16.071 ± 0.009	15.404 ± 0.009	14.992 ± 0.012	14.537 ± 0.027	14.024 ± 0.021	NO
2301	101.718028	1.314145	16.079 ± 0.010	15.382 ± 0.008	14.969 ± 0.012	14.462 ± 0.026	13.863 ± 0.018	NO
2302	101.720772	1.312962	17.125 ± 0.024	16.382 ± 0.021	15.941 ± 0.028	14.432 ± 0.025	14.031 ± 0.020	NO
2303	101.716874	1.314099	14.379 ± 0.003	13.419 ± 0.002	12.741 ± 0.002	11.734 ± 0.004	11.273 ± 0.004	YES
2305	101.716936	1.319362	16.080 ± 0.010	15.179 ± 0.007	14.771 ± 0.010	13.924 ± 0.013	13.584 ± 0.014	YES
2314	101.713513	1.308412	16.316 ± 0.012	15.614 ± 0.010	15.252 ± 0.015	14.765 ± 0.032	14.449 ± 0.027	YES
2316	101.706296	1.310313	17.406 ± 0.031	16.204 ± 0.018	15.504 ± 0.019	14.670 ± 0.028	14.392 ± 0.026	NO
2317	101.717317	1.312118	15.708 ± 0.007	14.969 ± 0.006	14.582 ± 0.008	14.295 ± 0.022	13.898 ± 0.019	NO
2326	101.706908	1.307239	16.408 ± 0.013	15.803 ± 0.012	15.282 ± 0.015	14.146 ± 0.019	13.824 ± 0.017	NO
2328	101.715204	1.310334	15.882 ± 0.008	14.959 ± 0.006	14.323 ± 0.007	13.508 ± 0.012	13.129 ± 0.011	NO
2330	101.709699	1.316759	16.270 ± 0.011	15.560 ± 0.010	15.098 ± 0.013	14.011 ± 0.017	13.546 ± 0.014	NO
2331	101.714601	1.317233	15.553 ± 0.006	14.882 ± 0.005	14.531 ± 0.008	13.219 ± 0.009	12.700 ± 0.008	NO
2336	101.714767	1.304984	17.777 ± 0.043	16.829 ± 0.031	16.169 ± 0.034	14.665 ± 0.029	14.275 ± 0.026	NO
2337	101.714569	1.306385	14.876 ± 0.004	14.060 ± 0.003	13.693 ± 0.004	12.827 ± 0.008	12.356 ± 0.007	YES
2340	101.709810	1.312652	16.810 ± 0.018	16.218 ± 0.018	15.885 ± 0.026	14.429 ± 0.024	14.048 ± 0.020	NO
2345	101.711362	1.319353	16.185 ± 0.010	15.259 ± 0.008	14.808 ± 0.010	13.839 ± 0.011	13.503 ± 0.013	NO
2416	101.707737	1.323049	16.068 ± 0.009	15.215 ± 0.007	14.740 ± 0.010	13.849 ± 0.015	13.532 ± 0.014	NO
2418	101.703176	1.321699	16.083 ± 0.010	15.247 ± 0.008	14.591 ± 0.008	13.775 ± 0.009	13.031 ± 0.010	NO
2425	101.713752	1.324094	16.190 ± 0.011	15.291 ± 0.008	14.828 ± 0.010	14.160 ± 0.018	13.912 ± 0.018	NO
2430	101.724791	1.313832	17.741 ± 0.041	16.796 ± 0.030	16.231 ± 0.036	14.019 ± 0.018	13.771 ± 0.017	NO
2439	101.735680	1.316618	15.916 ± 0.008	15.074 ± 0.006	14.657 ± 0.009	13.989 ± 0.015	13.765 ± 0.015	NO

Continued on next page

Table 3.4 – continued from previous page

id	α_{2000} (deg)	δ_{2000} (deg)	V mag	B-V mag	V-I mag	J mag	H mag	K mag	3.6 μm mag	4.5 μm mag	H α emission (YES/NO)
2441	101.750685	1.322554	16.375 ± 0.012	14.722 ± 0.005	13.741 ± 0.004	12.794 ± 0.007	12.390 ± 0.007	NO
2444	101.722041	1.330434	17.357 ± 0.029	16.131 ± 0.017	15.139 ± 0.014	13.800 ± 0.015	13.362 ± 0.013	NO
2445	101.728063	1.311994	17.542 ± 0.034	16.462 ± 0.022	15.979 ± 0.029	14.034 ± 0.015	13.795 ± 0.017	NO
2447	101.723477	1.314508	15.795 ± 0.008	14.762 ± 0.005	14.288 ± 0.007	13.275 ± 0.010	13.080 ± 0.011	YES
2514	101.717229	1.341390	17.981 ± 0.052	16.843 ± 0.032	16.250 ± 0.037	14.837 ± 0.032	14.615 ± 0.031	NO
2534	101.714663	1.340683	16.707 ± 0.017	15.956 ± 0.014	15.735 ± 0.023	14.871 ± 0.035	14.605 ± 0.033	YES
2541	101.721826	1.343510	17.773 ± 0.043	16.631 ± 0.026	15.877 ± 0.026	14.533 ± 0.025	14.336 ± 0.025	NO
2551	101.735458	1.350155	17.775 ± 0.043	16.243 ± 0.018	15.133 ± 0.014	13.755 ± 0.013	13.155 ± 0.007	NO
2636	101.669244	1.357335	15.716 ± 0.007	15.058 ± 0.006	14.551 ± 0.008	13.839 ± 0.013	13.443 ± 0.012	NO
2748	101.681845	1.353512	16.396 ± 0.013	15.653 ± 0.011	15.111 ± 0.013	13.908 ± 0.014	13.313 ± 0.011	NO
3045	101.766597	1.389371	16.066 ± 0.009	15.305 ± 0.008	14.721 ± 0.009	14.095 ± 0.016	13.785 ± 0.014	NO
Other YSOs selected from <i>JHK</i>											
1144	101.731542	1.286178	19.240 ± 0.062	2.452 ± 0.118	3.670 ± 0.037	12.027 ± 0.035	9.979 ± 0.028	8.709 ± 0.021	NO
1786	101.756172	1.277104	18.213 ± 0.062	16.794 ± 0.030	15.975 ± 0.028	15.393 ± 0.034	15.203 ± 0.039	NO
1797	101.741440	1.265756	17.659 ± 0.038	16.483 ± 0.022	15.745 ± 0.023	15.209 ± 0.038	...	NO
1803	101.755068	1.286005	18.258 ± 0.065	16.750 ± 0.028	15.838 ± 0.025	14.961 ± 0.026	14.429 ± 0.022	NO
1807	101.752168	1.275818	17.579 ± 0.035	16.504 ± 0.023	15.769 ± 0.023	15.549 ± 0.053	15.198 ± 0.034	NO
1821	101.725786	1.268031	18.343 ± 0.070	17.269 ± 0.046	16.141 ± 0.033	13.253 ± 0.008	...	NO
1822	101.705098	1.268233	17.713 ± 0.040	16.490 ± 0.022	15.726 ± 0.022	15.239 ± 0.039	...	NO
1849	101.730069	1.275450	17.286 ± 0.027	16.106 ± 0.016	15.430 ± 0.017	14.237 ± 0.019	14.385 ± 0.022	NO
1855	101.729343	1.291282	17.600 ± 0.036	16.332 ± 0.020	15.529 ± 0.019	15.010 ± 0.032	14.778 ± 0.033	NO
1953	101.756050	1.294627	18.448 ± 0.078	17.416 ± 0.052	16.719 ± 0.055	16.046 ± 0.067	16.157 ± 0.081	NO
1977	101.743445	1.298413	18.173 ± 0.061	16.120 ± 0.016	14.843 ± 0.010	14.191 ± 0.017	14.076 ± 0.019	NO
1980	101.755812	1.310042	18.430 ± 0.077	17.430 ± 0.053	16.627 ± 0.051	15.719 ± 0.053	15.766 ± 0.065	NO
1981	101.756634	1.316957	15.807 ± 0.008	14.546 ± 0.004	13.790 ± 0.004	13.392 ± 0.007	13.197 ± 0.011	NO
1982	101.758462	1.319349	18.454 ± 0.079	17.323 ± 0.049	16.578 ± 0.049	16.817 ± 0.133	16.233 ± 0.094	NO
1984	101.753593	1.290810	18.547 ± 0.085	17.668 ± 0.066	16.633 ± 0.051	15.849 ± 0.068	16.048 ± 0.073	NO
1988	101.759838	1.316056	17.743 ± 0.041	16.464 ± 0.022	15.738 ± 0.023	15.241 ± 0.037	14.878 ± 0.031	NO
2033	101.764510	1.320904	17.314 ± 0.028	16.315 ± 0.019	15.658 ± 0.021	15.172 ± 0.039	15.016 ± 0.032	NO
2264	101.699716	1.287557	18.473 ± 0.080	16.952 ± 0.034	15.845 ± 0.025	14.936 ± 0.028	14.733 ± 0.030	NO
2279	101.711955	1.295338	18.507 ± 0.082	17.138 ± 0.041	16.065 ± 0.031	15.249 ± 0.041	14.755 ± 0.037	NO
2296	101.708325	1.295349	17.594 ± 0.036	16.717 ± 0.028	16.005 ± 0.029	15.850 ± 0.072	15.993 ± 0.095	NO
2315	101.719380	1.309391	16.270 ± 0.011	15.282 ± 0.008	14.611 ± 0.009	12.983 ± 0.009	13.036 ± 0.010	NO
2321	101.718022	1.293170	18.424 ± 0.076	17.053 ± 0.038	16.237 ± 0.036	14.762 ± 0.033	14.965 ± 0.040	NO
2402	101.689245	1.314965	16.333 ± 0.012	15.214 ± 0.007	14.564 ± 0.008	13.608 ± 0.012	13.699 ± 0.014	NO
2403	101.700792	1.315831	18.538 ± 0.085	17.416 ± 0.053	16.712 ± 0.056	16.076 ± 0.075	15.326 ± 0.045	NO
2412	101.671871	1.325880	18.183 ± 0.062	17.011 ± 0.037	16.220 ± 0.036	15.253 ± 0.042	14.926 ± 0.032	NO
2426	101.748797	1.327326	18.575 ± 0.088	17.143 ± 0.041	16.317 ± 0.039	15.278 ± 0.044	15.421 ± 0.051	NO

Continued on next page

Table 3.4 – continued from previous page

id	α_{2000} (deg)	δ_{2000} (deg)	V mag	B-V mag	V-I mag	J mag	H mag	K mag	3.6 μm mag	4.5 μm mag	H α emission (YES/NO)
2463	101.733396	1.330173	17.496 \pm 0.033	16.490 \pm 0.023	15.837 \pm 0.025	14.695 \pm 0.029	14.674 \pm 0.035	NO
2474	101.747575	1.341025	18.240 \pm 0.065	16.655 \pm 0.027	15.717 \pm 0.023	15.178 \pm 0.036	15.765 \pm 0.069	NO
2484	101.760195	1.330335	16.795 \pm 0.018	15.579 \pm 0.010	14.859 \pm 0.011	14.241 \pm 0.018	14.126 \pm 0.018	NO
2495	101.748947	1.343741	16.524 \pm 0.014	15.425 \pm 0.009	14.693 \pm 0.009	14.232 \pm 0.018	14.246 \pm 0.021	NO
2529	101.705876	1.339501	18.164 \pm 0.061	16.889 \pm 0.033	16.100 \pm 0.032	15.212 \pm 0.046	15.105 \pm 0.045	NO
2530	101.722820	1.345824	16.756 \pm 0.017	15.637 \pm 0.011	14.937 \pm 0.011	14.710 \pm 0.029	14.412 \pm 0.026	NO
2535	101.713981	1.342169	15.969 \pm 0.009	14.624 \pm 0.004	13.827 \pm 0.004	13.231 \pm 0.010	13.049 \pm 0.011	NO
2540	101.718916	1.340296	18.498 \pm 0.083	17.345 \pm 0.050	16.688 \pm 0.055	16.833 \pm 0.189	15.841 \pm 0.090	NO
2561	101.733705	1.363192	17.991 \pm 0.052	16.940 \pm 0.034	16.164 \pm 0.034	15.491 \pm 0.037	15.562 \pm 0.048	NO
2730	101.687074	1.362596	18.293 \pm 0.068	17.294 \pm 0.048	16.218 \pm 0.036	15.373 \pm 0.041	14.987 \pm 0.031	NO
3598	101.712660	1.271039	18.225 \pm 0.063	17.094 \pm 0.039	16.443 \pm 0.043	NO
3649	101.729638	1.285287	18.641 \pm 0.092	16.904 \pm 0.033	15.693 \pm 0.022	NO
3674	101.740656	1.274678	18.675 \pm 0.095	17.373 \pm 0.050	16.523 \pm 0.046	NO
3682	101.733633	1.273637	18.393 \pm 0.073	17.187 \pm 0.042	16.451 \pm 0.043	NO
3685	101.731529	1.283687	17.984 \pm 0.051	16.641 \pm 0.026	15.841 \pm 0.025	NO
3781	101.761094	1.319910	16.614 \pm 0.015	15.505 \pm 0.009	14.870 \pm 0.011	NO
4142	101.729409	1.306852	18.046 \pm 0.054	17.113 \pm 0.040	16.480 \pm 0.045	NO
4231	101.729732	1.315159	17.746 \pm 0.041	16.866 \pm 0.032	16.173 \pm 0.034	NO
4296	101.722840	1.344536	18.323 \pm 0.070	17.232 \pm 0.045	16.552 \pm 0.048	NO

All the H α emission sources detected from various methods

Detected from both slitless spectroscopy and IPHAS photometry											
8	101.735121	1.277934	15.934 \pm 0.013	1.037 \pm 0.010	1.841 \pm 0.007	12.061 \pm 0.023	11.212 \pm 0.020	10.572 \pm 0.023	9.616 \pm 0.003	9.049 \pm 0.002	YES
54	101.723024	1.310400	17.447 \pm 0.005	1.323 \pm 0.018	2.195 \pm 0.005	13.677 \pm 0.026	12.644 \pm 0.026	11.958 \pm 0.027	10.761 \pm 0.003	10.026 \pm 0.002	YES
571	101.720487	1.315683	18.589 \pm 0.035	1.934 \pm 0.133	2.235 \pm 0.011	14.79 \pm 0.003	13.816 \pm 0.002	13.15 \pm 0.003	12.095 \pm 0.005	11.703 \pm 0.005	YES
575	101.720311	1.313621	19.778 \pm 0.078	...	2.747 \pm 0.035	15.311 \pm 0.005	14.097 \pm 0.003	13.182 \pm 0.003	11.892 \pm 0.004	11.367 \pm 0.004	YES
603	101.703739	1.320896	19.063 \pm 0.011	1.565 \pm 0.048	2.478 \pm 0.014	14.567 \pm 0.003	13.569 \pm 0.002	12.711 \pm 0.002	11.835 \pm 0.003	11.264 \pm 0.004	YES
629	101.742782	1.320963	19.498 \pm 0.013	1.693 \pm 0.071	2.321 \pm 0.015	15.197 \pm 0.005	14.222 \pm 0.003	13.641 \pm 0.004	12.728 \pm 0.007	12.292 \pm 0.006	YES
645	101.757760	1.346685	19.675 \pm 0.010	1.417 \pm 0.053	1.964 \pm 0.016	16.067 \pm 0.009	15.239 \pm 0.007	14.766 \pm 0.010	14.049 \pm 0.015	13.672 \pm 0.012	YES
677	101.749821	1.365127	19.616 \pm 0.013	1.442 \pm 0.061	2.687 \pm 0.015	14.849 \pm 0.004	13.930 \pm 0.002	13.246 \pm 0.003	12.288 \pm 0.005	11.854 \pm 0.005	YES
1007	101.791586	1.354167	19.996 \pm 0.012	1.526 \pm 0.076	2.419 \pm 0.012	15.921 \pm 0.008	15.165 \pm 0.007	14.887 \pm 0.011	14.570 \pm 0.022	14.516 \pm 0.023	YES
3109	101.657578	1.26854	13.198 \pm 0.0197	12.187 \pm 0.0245	11.86 \pm 0.0246	...	YES
Detected from slitless spectroscopy only											
321	101.719373	1.292577	19.190 \pm 0.013	1.621 \pm 0.050	2.329 \pm 0.009	15.042 \pm 0.004	13.832 \pm 0.002	12.973 \pm 0.002	11.412 \pm 0.003	10.972 \pm 0.003	YES

Continued on next page

Table 3.4 – continued from previous page

id	α_{2000} (deg)	δ_{2000} (deg)	V mag	B-V mag	V-I mag	J mag	H mag	K mag	3.6 μm mag	4.5 μm mag	H α emission (YES/NO)
574	101.703997	1.305660	20.026 ± 0.018	2.020 ± 0.150	2.635 ± 0.012	15.467 ± 0.006	14.538 ± 0.004	14.017 ± 0.005	13.226 ± 0.008	12.912 ± 0.010	YES
624	101.731694	1.328054	17.684 ± 0.007	1.224 ± 0.013	1.405 ± 0.008	15.267 ± 0.005	14.712 ± 0.005	14.565 ± 0.008	14.075 ± 0.015	14.129 ± 0.022	YES
652	101.722476	1.333859	18.414 ± 0.008	1.468 ± 0.024	2.092 ± 0.008	14.538 ± 0.003	13.716 ± 0.002	13.215 ± 0.003	12.376 ± 0.006	12.240 ± 0.007	YES
665	101.696564	1.342525	20.114 ± 0.015	1.621 ± 0.120	2.437 ± 0.014	15.480 ± 0.006	14.335 ± 0.003	13.530 ± 0.004	12.690 ± 0.006	12.320 ± 0.007	YES
1365	101.713708	1.316122	11.571 ± ...	11.224 ± ...	12.349 ± 0.050	11.373 ± 0.005	10.940 ± 0.003	YES
Detected from IPHAS photometry only											
115	101.715745	1.311569	17.237 ± 0.037	1.107 ± 0.075	1.951 ± 0.022	13.414 ± ...	12.601 ± ...	12.695 ± 0.072	12.468 ± 0.006	12.334 ± 0.007	YES
374	101.756814	1.313292	20.670 ± 0.033	1.323 ± 0.153	3.304 ± 0.012	14.960 ± 0.004	14.168 ± 0.003	13.701 ± 0.004	13.098 ± 0.007	12.835 ± 0.008	YES
375	101.750214	1.319768	20.361 ± 0.027	1.395 ± 0.115	3.029 ± 0.039	15.966 ± 0.009	15.012 ± 0.006	14.440 ± 0.007	13.472 ± 0.012	13.005 ± 0.010	YES
553	101.689779	1.304655	20.543 ± 0.029	1.784 ± 0.192	2.191 ± 0.039	17.112 ± 0.023	16.327 ± 0.020	16.155 ± 0.033	15.912 ± 0.080	16.109 ± 0.089	YES
569	101.708629	1.306686	21.348 ± 0.055	0.432 ± 0.180	3.325 ± 0.022	15.659 ± 0.007	14.813 ± 0.005	14.373 ± 0.007	13.918 ± 0.016	13.802 ± 0.017	YES
570	101.719982	1.308091	19.124 ± 0.055	0.587 ± 0.111	2.049 ± 0.020	15.321 ± 0.005	14.500 ± 0.004	14.163 ± 0.006	13.224 ± 0.010	13.169 ± 0.012	YES
576	101.702357	1.315923	21.068 ± 0.041	1.457 ± 0.251	2.588 ± 0.032	17.067 ± 0.023	16.452 ± 0.022	16.137 ± 0.033	15.648 ± 0.056	15.004 ± 0.039	YES
578	101.712067	1.305554	19.425 ± 0.026	1.910 ± 0.091	2.759 ± 0.019	14.470 ± 0.003	13.627 ± 0.002	13.115 ± 0.003	12.394 ± 0.006	12.001 ± 0.006	YES
581	101.714753	1.311102	17.330 ± 0.029	0.902 ± 0.074	1.849 ± 0.018	14.159 ± 0.002	13.414 ± 0.002	13.167 ± 0.003	12.902 ± 0.008	12.763 ± 0.009	YES
614	101.724490	1.319838	19.960 ± 0.039	0.984 ± 0.099	1.869 ± 0.034	16.912 ± 0.020	16.273 ± 0.019	16.148 ± 0.033	16.687 ± 0.107	17.297 ± 0.283	YES
616	101.731768	1.325989	20.632 ± 0.066	0.829 ± 0.150	2.622 ± 0.025	15.832 ± 0.008	14.806 ± 0.005	14.207 ± 0.006	13.451 ± 0.010	13.113 ± 0.011	YES
620	101.719523	1.324788	19.101 ± 0.017	1.766 ± 0.076	2.143 ± 0.015	14.761 ± 0.003	13.935 ± 0.002	13.410 ± 0.003	12.611 ± 0.006	12.294 ± 0.007	YES
621	101.719392	1.319557	20.268 ± 0.066	...	2.515 ± 0.066	16.461 ± 0.013	15.640 ± 0.011	15.282 ± 0.015	14.759 ± 0.022	14.628 ± 0.030	YES
625	101.731974	1.307462	20.889 ± 0.055	1.496 ± 0.184	2.914 ± 0.020	15.766 ± 0.007	14.784 ± 0.005	14.104 ± 0.006	12.784 ± 0.007	12.322 ± 0.007	YES
644	101.708647	1.344268	18.882 ± 0.008	1.331 ± 0.026	1.844 ± 0.010	16.088 ± 0.010	14.724 ± 0.005	13.497 ± 0.003	12.051 ± 0.004	11.494 ± 0.004	YES
646	101.751829	1.348607	21.697 ± 0.067	1.409 ± 0.322	2.926 ± 0.035	16.302 ± 0.012	15.229 ± 0.007	14.531 ± 0.008	13.855 ± 0.013	13.510 ± 0.011	YES
999	101.787683	1.334398	20.614 ± 0.028	1.146 ± 0.088	2.454 ± 0.033	16.114 ± 0.010	15.148 ± 0.007	14.393 ± 0.007	13.635 ± 0.010	13.151 ± 0.010	YES
1019	101.807941	1.367194	20.851 ± 0.026	1.480 ± 0.167	1.816 ± 0.051	17.764 ± 0.042	17.169 ± 0.042	16.978 ± 0.070	16.645 ± 0.127	16.501 ± 0.097	YES
1301	101.778282	1.411728	15.771 ± 0.004	0.661 ± 0.003	1.048 ± 0.014	13.930 ± 0.002	13.696 ± 0.002	13.480 ± 0.003	YES
1366	101.717136	1.316972	13.402 ± ...	13.019 ± 0.068	12.412 ± ...	12.411 ± 0.006	12.176 ± 0.006	YES
2089	101.646048	1.244118	17.575 ± 0.033	16.796 ± 0.030	16.520 ± 0.049	16.569 ± 0.087	...	YES
2286	101.717945	1.311399	15.486 ± 0.006	14.644 ± 0.004	14.314 ± 0.007	13.950 ± 0.016	13.830 ± 0.018	YES
2303	101.716874	1.314099	14.379 ± 0.003	13.419 ± 0.002	12.741 ± 0.002	11.734 ± 0.004	11.273 ± 0.004	YES
2305	101.716936	1.319362	16.080 ± 0.010	15.179 ± 0.007	14.771 ± 0.010	13.924 ± 0.013	13.584 ± 0.014	YES
2311	101.712369	1.304588	15.509 ± 0.006	14.737 ± 0.005	14.276 ± 0.006	13.710 ± 0.014	13.650 ± 0.016	YES
2314	101.713513	1.308412	16.316 ± 0.012	15.614 ± 0.010	15.252 ± 0.015	14.765 ± 0.032	14.449 ± 0.027	YES
2329	101.712510	1.313155	15.636 ± 0.007	14.838 ± 0.005	14.230 ± 0.006	12.626 ± 0.007	11.850 ± 0.005	YES
2337	101.714569	1.306385	14.876 ± 0.004	14.060 ± 0.003	13.693 ± 0.004	12.827 ± 0.008	12.356 ± 0.007	YES
2427	101.724016	1.329207	16.502 ± 0.014	15.844 ± 0.013	15.473 ± 0.018	16.680 ± 0.171	15.401 ± 0.056	YES
2447	101.723477	1.314508	15.795 ± 0.008	14.762 ± 0.005	14.288 ± 0.007	13.275 ± 0.010	13.080 ± 0.011	YES
2534	101.714663	1.340683	16.707 ± 0.017	15.956 ± 0.014	15.735 ± 0.023	14.871 ± 0.035	14.605 ± 0.033	YES
4087	101.718185	1.303909	16.501 ± 0.014	15.785 ± 0.012	15.403 ± 0.017	YES

Continued on next page

Table 3.4 – continued from previous page

id	α_{2000} (deg)	δ_{2000} (deg)	V mag	B-V mag	V-I mag	J mag	H mag	K mag	3.6 μm mag	4.5 μm mag	H α emission (YES/NO)
4318	101.715302	1.329219	17.865 ± 0.046	17.259 ± 0.046	16.839 ± 0.063	YES
5595	101.6128077	1.3901412	20.117 ± 0.013	1.203 ± 0.067	1.62 ± 0.032	YES

Chapter 4

Active star formation at Galactic H II regions: the complex associated with Sh 2-149

4.1 Introduction

Embedded clusters are associated with H II regions, where there is sufficient amount of gas and dust to form stars. Therefore, the study of Galactic H II regions could trace active star formations in our galaxy. H II regions and associated molecular clouds provide us crucial information about the fragmentation of molecular clouds, star formation process, stellar evolution and stellar structure. Numerous surveys are now available allowing a better understanding star formation in the vicinity of H II regions (e.g., Kirsanova et al. 2008, Kerton et al. 2008, Anderson et al. 2012). Statistically, most luminous stars forms in molecular clouds associated with H II regions (Dobashi et al. 2001), specifically a significant fraction of stars originate at the peripheries of H II regions (e.g., Zavagno et al. 2006, Deharveng et al. 2008).

The massive stars (O, early B) and their associated H II regions inherently concern the nature of massive star formation and their impact on their ambient environment. Any OB star emits a huge amount of ultraviolet (UV) radiation and ionizes the surrounding medium of a molecular cloud to form H II region. Due to the difference in pressure of between hot H II region ($\sim 10^4$ K) and the cold natal molecular cloud (~ 30 K) the ionization front expands into the molecular cloud (Anderson et al. 2009). As discussed in chapter 1, in the collect and collapse process (Elmegreen & Lada 1977, Whitworth et al. 1994), a thin layer of neutral material accumulated between the ionization front (IF) and shock front (SF). This compressed shocked layer might become gravitationally unstable with a long timescale and become dense, massive cores. The appearance of pillars, filaments, shells, and rings are seen from such swept up materials. The filaments and pillars are overdensity of material and believed to be new and future star-forming regions (SFRs). The shells and rings render the end of H II regions, may contain young embedded objects (Zavagno et al. 2006). The knowledge of young stellar objects (YSOs) within H II regions and their natal molecular clouds delineate the star-formation process within it; their spatial distribution reflects the history of a given region.

In this chapter, we study the dense gas properties as well as the star formation processes associated with the H II complex S149. We explore the ionizing massive stars within H II regions with optical spectroscopy of optically bright objects and ionized dust emissions. The distribution of ionized and cold neutral material was investigated with optical, IR and radio continuum data sets. The protostellar objects were identified and characterized from high-resolution WIRCAM *HK* data and *Spitzer*-IRAC observations. We organized this work as follows. In the Section 4.2 we present a brief overview of the H II region S149 complex. Section 4.3 describes our observational details. Section 4.4 deals with the morphology of associated region, which contains identification of massive sources, multi-wavelength view of the cloud complex, properties of the ionized gas, young stellar content search and their spatial distribution. Section 4.5 is devoted to general discussion of our understanding of star-formation in Sh2-149 complex. We present the main conclusions in Section 4.6.

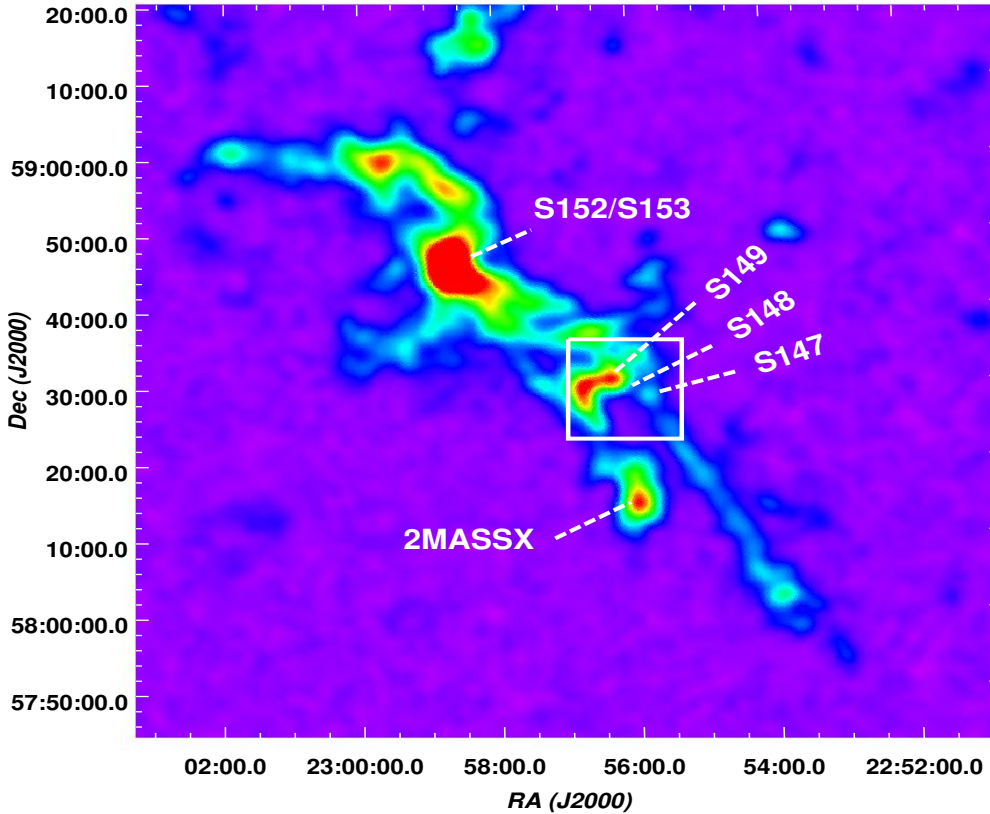


Figure 4.1: A low resolution FCRAO OGS $^{12}\text{CO}(1-0)$ map integrated over -49 km s^{-1} to -53 km s^{-1} . The abscissa (RA) and ordinate (Dec) are in J2000 epoch. The various H II regions associated with the cloud complex are marked, and the white box represents the area considered in this study. We considered the area covered by WIRCAM for the analysis. The H II region discussed in the text is marked in the white rectangular box (the corresponding optical and NIR image is shown in Figure 4.2 and 4.3, respectively).

4.2 Overview of the complex associated with Sh 2-149

The H II regions associated with S149 cloud complex is located in Perseus arm in our Milky Way Galaxy. CO studies and spectroscopic studies of a few bright sources have been performed on this region by several authors (e.g., Bergeat et al. 1975; Glushkov et al. 1975; Russell 1978; Blitz 1979; Tatematsu 1985; Caplan et al. 2000; Azimlu et al. 2011). A low resolution $^{12}\text{CO}(1-0)$ velocity integrated map taken from the 14-m Five College Radio Astronomy Observatory (FCRAO) Outer Galaxy Survey (OGS; Heyer et al. 1998) showed a dense molecular distri-

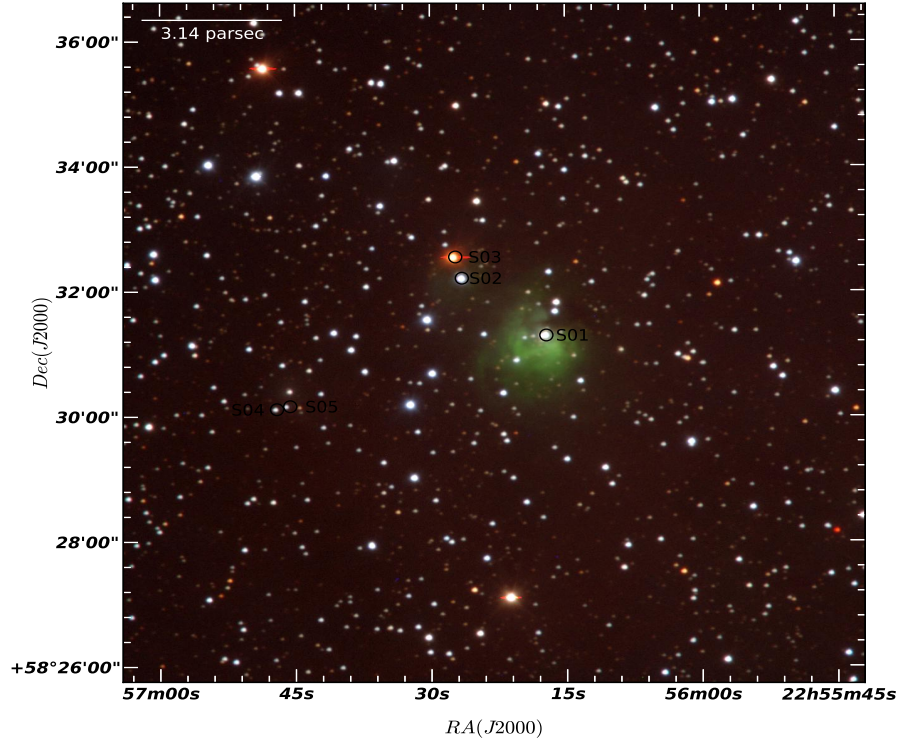


Figure 4.2: Optical color composite image of S149 complex (blue: V; green: R; red: I) obtained using 1.3m HCT. The spectroscopically observed stars are marked.

bution of gas and its apparent association with another complex as shown in Fig. 4.1. The molecular cloud complex are associated with several sub regions namely, S149, S148, S147 and extended Eastern border (marked in the white box) in Fig.4.1. An optically visible nebula are seen around Sh2-149 region as in Fig.4.2. The massive stellar content, their influence in the surrounding molecular clouds and the young stellar population of the complex have not been studied in detail in the past. The present study focus on the stellar content and the understanding of global star formation activity around S149 complex.

A recent analysis of molecular gas around S149 from CO observations (Azimlu et al. 2011) is shown several clumps, and their physical properties are derived. An average CO velocity of -55 kms^{-1} were found for the cloud complex. The highest column density was estimated to be $3.62 \times 10^{23} \text{ cm}^{-2}$. The integrated mass of massive clump is $\sim 1400 \pm 290 M_{\odot}$, whereas the total mass of all clumps in S148/S149 was estimated $\sim 8000 \pm 325 M_{\odot}$. Tatematsu et al. (1985) suggested that S147/S152 complex is an association of two group of clouds in the Perseus arm.

Table 4.1: Details of the IRAS sources.

ID	Name	RA (J2000) deg	Dec (J2000) deg	F_{12} Jy	F_{25} Jy	F_{60} Jy	F_{100} Jy	L^* L_{\odot}
IR1	IRAS 22535+5811	343.891144	58.450661	0.84	1.05	38.61	172.50	4613.43
IR2	IRAS 22536+5811	343.924652	58.466263	1.03	2.15	29.19	860.90	15453.50
IR3	IRAS 22542+5815	344.070923	58.520351	12.55	43.96	504.90	860.90	40584.00
IR4	IRAS 22544+5808	344.131470	58.414597	0.49	1.15	3.91	21.45	697.70
IR5	IRAS 22546+5814	344.186035	58.502727	2.21	4.14	43.92	860.90	16453.90
IR6	IRAS 22535+5813	343.890503	58.497051	0.97	0.44	29.02	860.90	15296.40

* FIR luminosity of the IRAS sources are estimated from the IRAS fluxes using the relation given by, Casoli et al. (1986).

One group of H II regions consists of S147, S148, and S149, while other group consists of S152 and S153. The spectroscopic distances for the ionizing stars of S148, S149, S152, and S153 were estimated as 5.5, 5.4, 3.6 and 4.0 *kpc*, respectively, by Crampton et al. (1978). Tatematsu et al. (1985) also predicted that the cloud complex might be interacting to supernova remnant SNR G109.10-1.0, which is located at a distance 4.1 *kpc* (Sofue et al. 1983). The complex is located at galactocentric distance ~ 12.8 *kpc* (Biltz 1979). Herczeg et al. (2016) reported an outburst of ASASSN-15qi (2MASS J22560882+5831040), which is probably associated with a young stellar object in the complex.

The S149 molecular cloud complex contains several IRAS sources (see Table 4.1). The fluxes of the IRAS sources have been obtained from IRAS point source catalog, Version 2.0 (Helou & Walker 1988). We estimated FIR luminosity of the IRAS sources following Casoli et al. (1986). The source IRAS 22542+5815 (luminosity $\sim 40584 L_{\odot}$) is located at the center of S148, whereas, IRAS 22536+5811 (luminosity $\sim 15453 L_{\odot}$) is located at central part of S147, $\sim 6''$ S-W of S148. The IRAS 22535+5811 with luminosity $\sim 4613 L_{\odot}$ and IRAS 22535+5813 with luminosity $\sim 15296 L_{\odot}$ are in close proximity of S147 ($\sim 1''$ and $\sim 2.''4$ away, respectively). IRAS 22546+5814 (luminosity $\sim 16453 L_{\odot}$) and IRAS 22544+5808 (luminosity $\sim 697.70 L_{\odot}$) sources are located in the S-E edge of the molecular cloud; the IRAS 22546+5814 is located near most massive clump in S-E to S148. The position of IRAS sources are marked in Fig.4.3.

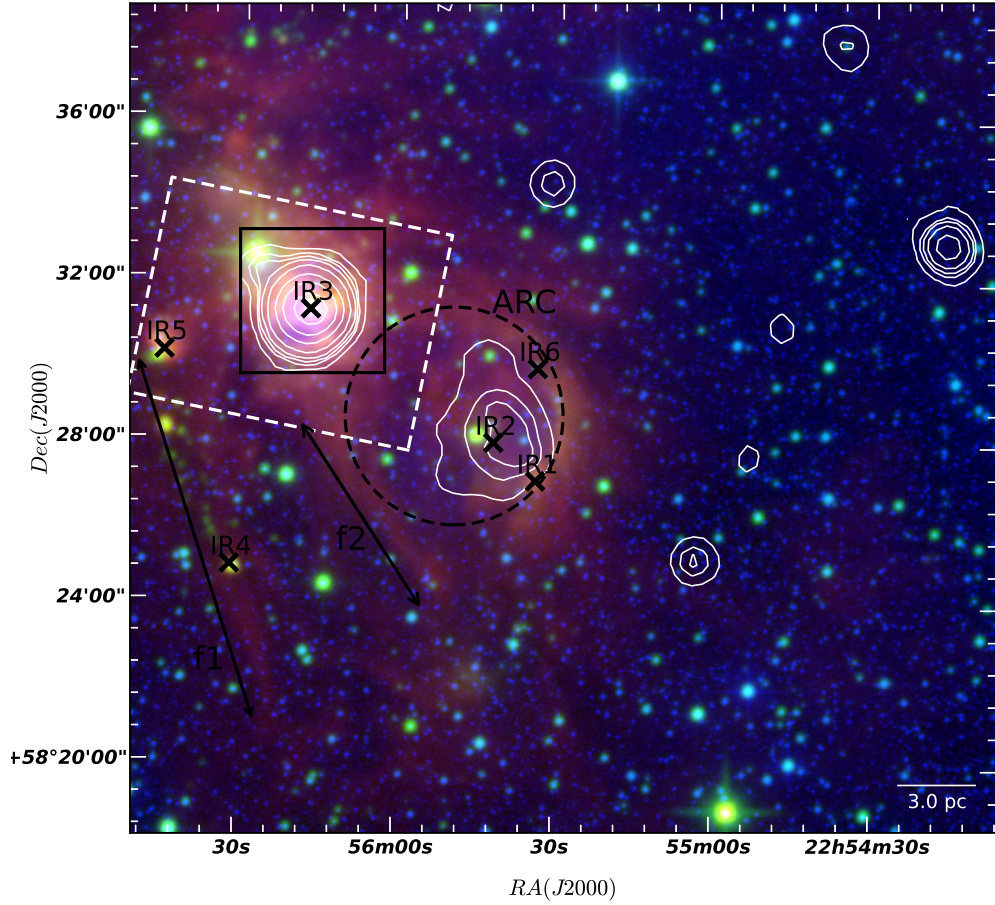


Figure 4.3: Color composite image of S149 complex obtained using optical emission (blue; from DSS2 survey), WISE 4.6 (green), and $12 \mu\text{m}$ (red). The 1.4 GHz contours are over plotted, contour levels are at 1.5, 4.0, 6.0, 10.0, 20.0, 50.0, 100.0, 200.0 mJy beam^{-1} . All the IRAS sources are marked (see text for details). A semi circular ‘ARC’ and two filament like structure are also marked. The black box region is core region of S149 (A close-up view of box region is shown in Figure 4.4). The white dash box is region of *spitzer*-IRAC coverage (see section 4.4.6).

4.3 Data Accumulations

4.3.1 Spectroscopic Observations

We obtained optical spectroscopic observations of 5 bright sources towards S149 complex using HFOSC of 2m Himalayan Chandra Telescope (HCT), India (Prabhu 2014). The observations were performed using Grism 7 (3800- 6840 \AA) with a resolving power of 1200 and Grism 8

Table 4.2: Log of spectroscopic observations.

ID	$\alpha_{(2000)}$ (h:m:s)	$\delta_{(2000)}$ (d:m:s)	Date of Observations	Grism (Gr7/Gr8)	Exp. time (s)	Airmass	SNR
1	22:56:17.17	+58:31:17.98	11.07.2016	Gr7	1200	1.367	24
				Gr8	1200	1.310	25
2	22:56:26.52	+58:32:12.17	11.07.2016	Gr7	1200	1.231	26
				Gr8	1200	1.196	26
3	22:56:27.24	+58:33.13	11.07.2016	Gr7	1200	1.957	22
				Gr8	1200	1.487	23
4	22:56:47.07	+58:30:07.07	02.11.2016	Gr7	2400	1.396	30
				Gr8	2400	1.545	33
5	22:56:45.60	+58:30:10.0	02.11.2016	Gr7	3000	2.100	35
				Gr8	2700	2.312	31

(5800- 8350 Å) with a resolving power of 2190. Arc lamp and bias frame observations were taken immediately after the target. The spectroscopic standard star G191B2B (Oke 1990) was also observed with an exposure time of 600s for the flux calibration. The log of spectroscopic observations is tabulated in Table 4.2.

After bias subtraction and flat field correction, the one-dimensional spectra were extracted using the optimal extraction method using APALL task in IRAF and wavelength calibrated using the arc lamp observations. The spectra were also corrected for the instrumental response using the sensitivity function generated from the standard star observations. More about spectroscopic observations could be found in chapter 3 of this thesis and Dutta et al. (2015).

4.3.2 NIR Imaging

Deep Near-IR (NIR) observations towards S149 complex (centered on $\alpha_{2000} = 22^h55^m31.53^s$ $\delta_{2000} = +58^{\circ}26'14.0''$) were obtained in H (1.63 μm), K (2.14 μm) bands from CFHT data archive observed using WIRCAM camera at CFHT 3.6 m telescope during 2007 July 31. In this set up each pixel corresponds to $0''.3$ and yields a FOV $\sim 20' \times 20'$. The average FWHM during the observing period was $\sim 0'.69$. The data were reduced using Interactive Data Language (IDL) based reduction pipeline-SIMPLE Imaging and Mosaicking PipeLine (SIMPLE; Wang et al. 2010). This pipeline generates sky-flat from median combining of the dithered images.

It provides good treatment to sky background fluctuation and minimized artifacts from bright objects. Absolute astrometry solution was obtained with 2MASS reference catalog. The images were calibrated with the 2MASS catalog. To avoid nonlinearity due to saturated stars in WIRCAM bright end, we considered only stars in 13-14.5 mag for K and 13-15 mag for H with good photometric accuracy ($\text{err} \leq 0.1$) for our photometric calibration. The identification of point sources was performed with the DAOFIND task in IRAF*. Following Stetson (1987), we have used the roundness limits of -1 to $+1$ and sharpness limits of 0.2 to $+1$ to eliminate bad pixels brightness enhancements and the extended sources such as background galaxies from the point source catalog. The photometry on the images was performed with PSF algorithm of DAOPHOT package (Stetson 1992).

To avoid the saturated sources in our list, those sources with $H < 13.75$ and $K < 13.5$ were replaced with the 2MASS catalog. We include all J-band detections from 2MASS in our final catalog. Following Keenan et al. (2010), the magnitudes of the sources of uncertainty ≤ 0.05 mag have been taken for our study to ensure good photometric accuracy.

The completeness limits at various bands were estimated from histogram turn over method (e.g. Dutta et al. 2015). We considered $\sim 90\%$ completeness of our data from the turning points of magnitudes at which cumulative logarithmic distribution of sources in the histograms deviate from linear distribution (figures are not shown). We found that the photometric data is complete down to $H = 18$ mag, $K = 18.5$ mag, respectively.

4.3.3 *Spitzer*-IRAC data

The *Spitzer*-IRAC observations at 3.6, 4.5, 5.8 and 8.0 μm bands were available in the *Spitzer* archive program (Program ID: 30734; PI: Figer, Donald F). The data sets were taken towards S149 complex during 2006-2007 at various dithered positions and with an effective integration time of 1.2 s per pixel at 3.6 and 4.5 μm , and 10.4 s at 5.8, 8.0 μm . The basic calibrated Data

*Image Reduction and Analysis Facility (IRAF) is distributed by National Optical Astronomy Observatories (NOAO), USA (<http://iraf.noao.edu/>)

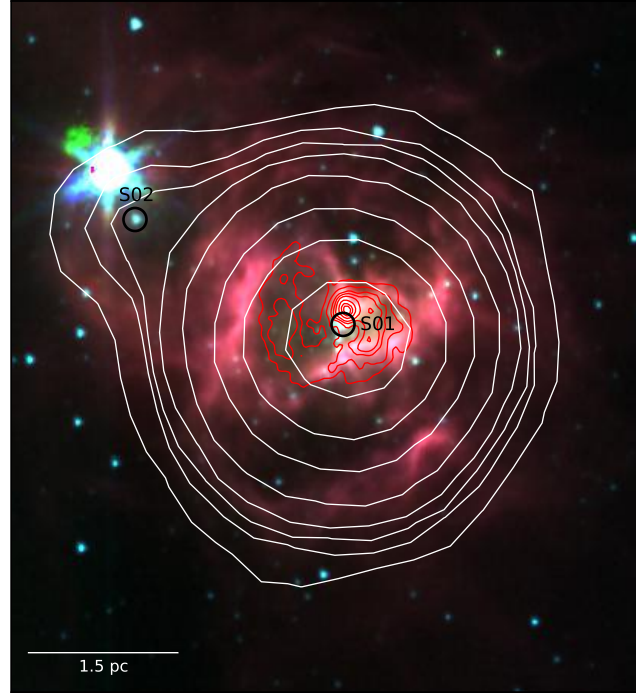


Figure 4.4: A close-up view of S149 subregion (marked with black box in Figure 4.3) is shown in IRAC 3.6, 4.5, 8.0 μm color composite image. The massive ionizing sources are marked. The white contours are as depicted in Figure 4.3. The 4.8 GHz contours (red) levels are at 2, 3, 4, 5, 7, 10, 13, 15 mJy beam^{-1} .

(version S18.18.0) were downloaded from *Spitzer* archive*. The images were processed, and the final mosaic frames were created using MOPEX (version 18.5.0) with an image scale of 1.2 arcsec pixel $^{-1}$. We performed point response function (PRF) fitting method using APEX tool provided by *Spitzer* Science center on all the *Spitzer* IRAC images to extract the magnitudes of point sources. The detailed procedure of source detection and magnitude extraction can be found in Dutta et al. (2015).

We finally extracted the photometry of 490, 474, 350 and 297 number of sources around the cluster at IRAC 3.6, 4.5, 5.8 & 8.0 μm bands, respectively within an area $5.5' \times 7.0'$ (see Fig. 4.1, and Fig. 4.3). The IRAC data were matched with a radial matching tolerance of 1.2 arcsec. Thus our final IRAC catalog contains 553 sources detected in one or more than one band with uncertainty ≤ 0.2 mag to ensure good photometric accuracy. All the sources were matched following the method of Dutta et al. 2015.

*<http://archive.spitzer.caltech.edu/>

To trace the molecular material towards Sh 2-149 complex, we made use of the FCRAO Outer Galaxy Survey (OGS; Heyer et al. 1998) in $^{12}\text{CO}(1-0)$ (115 GHz). The 1.4 GHz continuum survey, and 4.8 GHz continuum survey were obtained from the National Radio Astronomy Observatory (NRAO) VLA Sky Survey (NVSS; Condon et al. 1998). The WISE survey (Cutri et al. 2012) provides photometry at four wavelengths; 3.4, 4.6, 12 and 22 μm , with an angular resolution of $6''.1$, $6''.4$, $6''.5$, $12''.0$, respectively. We used WISE images and photometric catalog to study the morphology of the region. This study also made use of IRAS images and IRAS-PSC, and James Clerk Maxwell Telescope (JCMT) HARP $^{13}\text{CO}(3-2)$ (330 GHz) observations (Buckle et al. 2009).

4.4 Morphology of the region

4.4.1 Identifying Massive stars from spectroscopic study

We estimated the spectral types of 5 bright objects observed towards S149 complex in search for exciting stars of the region. We observed only those stars that have a higher probability of cluster membership. The targets for low-resolution spectroscopy were selected by their brightness and visually inspected location around the bright nebulosity (see Fig. 4.2). The coordinates and J magnitudes of these sources are given in Table 4.3, and the flux calibrated, normalized spectra are shown in Fig. 4.5. We classified the observed spectra using different spectral libraries available in the literature (Walborn & Fitzpatrick 1990; Jacoby, Hunter & Christian 1984; Torres-Dodgen & Weaver 1993; Allen & Strom 1995). First, we determined a specific spectral range from strong conspicuous features. The method of spectral classification is discussed in more details in Dutta et al. 2015. Based on low-resolution spectra of our targets, an uncertainty of ± 1 or more in the sub-class estimation is expected. Photometric and spectroscopic details of all the five sources are given in Table 4.3. Finally, each source was compared visually to the standard library spectra from Jacoby et al. (1984). However, by the

low-resolution spectroscopy of early type stars, it's hard to distinguish the luminosity class between supergiants, giants, dwarfs, and pre-main sequence stars.

S01: The star S01 appears to lie within strong nebulosity of S148. It is classifiable from hydrogen and helium lines. Presence of He II lines ($\lambda\lambda$ 4686, 5411 Å) and He II+I ($\lambda\lambda$ 4026 Å) limits the spectral type to O-type. Prominent absorption bands occur at hydrogen ($\lambda\lambda$ 3970, 4101, 4340, 4861, 6563 Å), He I ($\lambda\lambda$ 4144, 4387, 4471, 4713 Å), Si IV ($\lambda\lambda$ 4089, 4116 Å), blended C II + O III ($\lambda\lambda$ 4070, 4650 Å), N III ($\lambda\lambda$ 4379, 4641 Å). Moderate nitrogen enhancement indicate a later O-type spectrum. The ratio of He II ($\lambda\lambda$ 4686 Å) to He I ($\lambda\lambda$ 4713), the line ratios Si IV ($\lambda\lambda$ 4089 Å)-to-He I ($\lambda\lambda$ 4144, 4387, 4471, 4713 Å) and Si IV ($\lambda\lambda$ 4116 Å)-to-He I ($\lambda\lambda$ 4144 Å) are revealing the star more than towards O8-O9 V. Significant P-cyg profile is seen at H_α , which indicates a strong accretion of matter onto the star. Our classification matches well with Crampton et al. (1978), they estimated this star as O8 V.

S02: The absence of prominent H II lines and presence of He I ($\lambda\lambda$ 4009, 4026, 4121, 4144, 4387, 4471, 4713, 5876 Å) limits the star S02 in the between B0.5 to A0-type. The spectrum shows absorption at N III ($\lambda\lambda$ 4511 – 15, 4641 Å), C II ($\lambda\lambda$ 4216 Å), O III ($\lambda\lambda$ 4415 – 4417 Å), C II + O III ($\lambda\lambda$ 4070, 4650 Å), Si IV ($\lambda\lambda$ 4089, 4116, 4128 Å), Si II ($\lambda\lambda$ 4552-4568 Å). The ratio of Si II ($\lambda\lambda$ 4552 Å) / Si IV ($\lambda\lambda$ 4128 Å), and comparison of He I strength suggests the S02 is more similar to B1 V spectrum. Crampton et al. (1978) found this star as B0 V in their study, which is within our error limits.

S03: The main conspicuous features obtained in spectrum of S03 are absorption lines Fe I at $\lambda\lambda$ 7749, 7834 Å, Ca I at $\lambda\lambda$ 6162 Å, H_α , blended Fe I , Ti I , Cr I at $\lambda\lambda$ 6362 Å, blended Ba I , Fe I , Ca I , Mn I , Ti I and Ti II at $\lambda\lambda$ 6497 Å, Ti O band at $\lambda\lambda$ 5847-6058, 6080-6390 Å. These stellar lines and features identified in spectrum of S03 explain its trends, both with spectral type and luminosity class as K6 III.

S04: The presence of G band in its spectrum indicating it as after F2 type. The discernible absorption features are Ca I ($\lambda\lambda$ 4226 Å), Fe I ($\lambda\lambda$ 4326 Å), Ca I ($\lambda\lambda$ 4226 Å), Na I ($\lambda\lambda$ 5890 Å),

Table 4.3: Details of the spectroscopically studied stars.

ID	RA (J2000) (h:m:s)	Dec (J2000) (d:m:s)	J (mag)	$J - H$ (mag)	Spectroscopic A_V (mag)	distance modulus	** distance (pc)	Spectral Type	Remarks
S01	22:56:17.17	+58:31:17.98	10.572	0.348	4.78 ± 0.20	13.70 ± 0.20	5400 ± 150	O9V	Member
S02	22:56:26.52	+58:32:12.76	11.179	0.205	3.00 ± 0.15	13.10 ± 0.15	5100 ± 140	B1V	Member
S03	22:56:27.24	+58:32:33.13	6.099	1.432	K6 III	foreground
S04	22:56:47.07	+58:30:07.07	13.832	0.428	G9-K0V	foreground
S05	22:56:45.600	+58:30:09.90	14.410	0.437	2.154 ± 0.2	10.43 ± 0.18	1200 ± 105	F3-F5V	foreground

* Photometric A_V 's are calculated from extinction map. Foreground stars have not considered here.

** Distance moduli refers to the intrinsic distance moduli obtained from near-IR apparent distance moduli.

(Ba II, Fe I, Ca I ($\lambda\lambda 6497 \text{ \AA}$), H_α , Ca I ($\lambda\lambda 8498, 8542, 8662 \text{ \AA}$), CaH ($\lambda\lambda 6386 \text{ \AA}$). Literature comparison of these mentioned features along with line strength of H_α and Na I makes S04 more similar to G9-K0 V.

S05: Based on the late-type absorption features at G band ($\lambda\lambda 4300 \text{ \AA}$), Fe I ($\lambda\lambda 4383 \text{ \AA}$), Mn I ($\lambda\lambda 4030 \text{ \AA}$), Fe I ($\lambda\lambda 4046 \text{ \AA}$), Ca I ($\lambda\lambda 6162 \text{ \AA}$), Fe II ($\lambda\lambda 6242, 6456 \text{ \AA}$), Fe I + Ca I ($\lambda\lambda 6497 \text{ \AA}$) in this objects, we agree with the spectral range F3-F7 V.

Physical parameters of spectroscopically observed stars

All the spectroscopically observed stars are shown in (J-H)/(H-K) color-color (CC) diagram and J/(J-H) color-magnitude diagram (CMD) in Fig. 4.6 and Fig. 4.7, respectively. The 2MASS and WIRCAM magnitudes and colors were converted to the CIT system using the relations given by Carpenter et al. (2001). The sources towards the right of the reddening vector at 'T' are assumed to be the location of classical T-Tauri stars (Ojha et al. 2004). The star S01 falls in zones of highly extinct massive young stars. The S02 is moderately extinct massive members. However, S04 and S05 are close to the main-sequence branch and agree well our spectral classification. In the case of S03, the location is shifted along 'F' region, which is believed to be the location of field-stars. The observed photometric flux in a nebulous region is highly affected by emission from the ambient H II environment, circumstellar dust envelope

cluster. Our estimated distance agrees well with the published value in the literature (see 4.2). Considering the estimated distances, the star IDs 3, 4 and 5 seem to be foreground stars.

4.4.2 Optical and Infrared view

Fig. 4.2 displays the optical (*VRI*) view of the complex. The *R* and *I* images shows emission around massive stars (S01, S02; see section 4.4.1). The molecular clouds absorbed UV photons from ionizing stars and re-emitted. So, the interface of the H II region is seen even in optical wavelengths. However, the cold molecular environment could not be traced in optical. Therefore, we need IR or longer wavelengths to perceive the star formation activity behind the neutral molecular clouds. In Fig. 4.3 (optical DSS2, WISE 3.4, 12 μm), the emission at WISE 3.4 μm band has contribution from a weak, diffuse Polycyclic aromatic hydrocarbon (PAH) feature at 3.3 μm , whereas 12 μm band is contaminated from 11.3 μm and 12.7 μm PAH band. The 12 μm emission trace the compressed dense structure like, finger tip, filament, bright rim produced by dust or PAH molecules on the interface of H II region. The WISE color composite image reveals the expanded dust shell in S148 region with radius 1.5' ($\sim 2.35\text{pc}$ at a distance 5.4 kpc, see section 4.4.1 cluster distance). An extended distribution of the shell is seen towards N-E to S148, which also coincides with S149 sub region of radius 30'' (0.8 pc at cluster distance). The presence of a semi circular structure of radius $\sim 2.5'$ (~ 4.0 pc at cluster distance), from North to South-East via West (Marked Circle 'ARC'). In the Eastern part of the cloud, a pillar like structure (filament 'f1') populated with infrared excess stars (see section 4.4.6) is seen. Filament 'f1' is 5' (~ 8.0 pc at cluster distance) in length. Another prominent structure is 'f2' of length 3.5' (~ 5.5 pc at cluster distance). Apart from those dominant structures, several dense molecular structures are also seen. Such dense structure is believed to be possible sites for future or ongoing star formation. They are possibly attached with strong radiation of exciting sources.

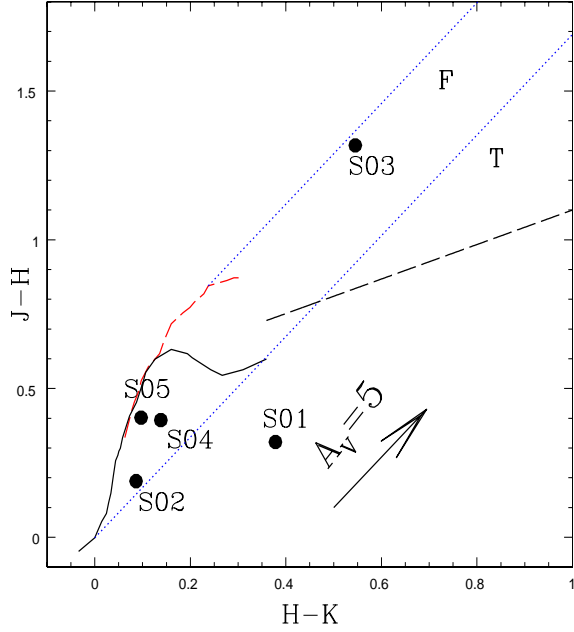


Figure 4.6: $(J-H)/(H-K)$ CC diagram of the spectroscopically classified stars in S149 Complex. Their IDs are as given in Table 2. The sequences for dwarfs (solid black) and giants (red dashed line) are taken from Bessel & Brett (1988). The long dashed black line represents the CTTs locus (Meyer et al. 1997). The dotted blue lines represent the reddening vectors (Cohen et al. 1981). The arrow indicates a visual extinction of $A_V = 5$ mag.

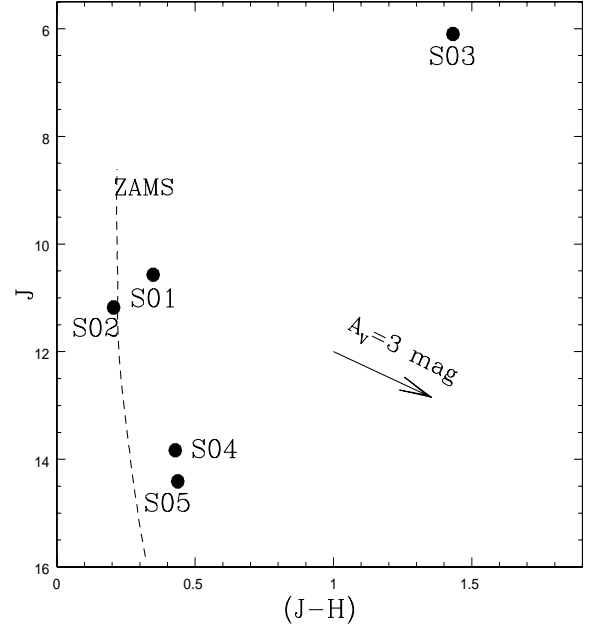


Figure 4.7: $J/(J-H)$ CMD for all spectroscopically classified stars in S149 complex. The solid dash curve is the ZAMS from Girardi et al (2002), corrected for the distance of 5.4 kpc and average reddening $E(B-V) = 1.0$ mag.

We reproduced a close-up color composite image of *Spitzer* 3.6, 4.5 and 8 μm in Fig.4.4) emphasizing the bright diffuse nebular emission. Several wisps in this nebula coincide with the position of this massive ionizing sources. The emission at the 3.6 μm might have a small contribution from weak PAH features at 3.3 μm , whereas, the 8.0 IRAC band contains emission from 7.7 and 8.6 μm PAH molecules. PAH are generally found in the interaction zone of molecular cloud and H II region, they are believed to be destroyed in the ionized gas, though they are excited in the photo-dissociation region (PDR) by absorption of ionizing photons at the H II region interface (Deharveng et al. 2010, Samal et al. 2014).

4.4.3 Molecular gas

The morphology from low resolution $^{12}\text{CO}(1-0)$ map (Fig. 4.1) shows that our target S147-S148-S149 complex is possibly attached with S152/S153, including a stream line flow of length $\sim 40'$ (63 pc at cluster distance) towards South-West. The complex is extended towards South-East, which is also attached with 2MASX J22555978+5814424 to the West via an ionized layer of length $\sim 18'$ (28 pc at cluster distance). The location of the nebula coincides with the position where the molecular gas peaks. Azimlu et al. (2011) estimated the distribution of clumps in S149/S148 from $^{12}\text{CO}(2-1)$ and $^{13}\text{CO}(2-1)$, and the most massive clump is located at the extended part in South-East. Thus, CO maps describe the distribution of molecular material in the region. However, we shall refer to NIR and radio emission to trace the young stars in cold dust distribution.

Fig. 4.3, 4.4 show the radio continuum view of the S149 complex overplotted on IR images. This map shows the non-uniform distribution of ionized gas. The radio contour encompasses the dust ridge of the ionized layer. The 1.4 GHz map allows us to identify a compact radio emission at ($\alpha_{2000} = 22^{\text{h}}56^{\text{m}}17.17^{\text{s}}$ $\delta_{2000} = +58^{\circ}31^{\text{m}}18.0^{\text{s}}$), which is also coincide with massive ionizing star S01 (see section 4.4.1). A ‘pin’ type of structure is prominent towards North-West, around the location of S02 stars. Such structure occurs possibly due to swept out ionized gas excited by S02 star. These compact structures possibly represent the heated dust distribution around massive source(s). Considering the structure of the boundary between radio contour and half circle structure, suggest a probable expanding IF, and circular structure as a consequence of collect and collapse process. The 4.8 GHz shows a ‘comet’ like distribution. The head of the complex cometary structure is located around S01 source, which is extended towards North via. S-E direction. The H II region shows a complex morphology with diffuse patchy, irregular shape emission. An absorption lane is seen at the center of the nebula. It traces the swept up central cavity between IF and ionizing sources.

The half circular ‘ARC’ of molecular material is probably created by collecting material during expansion of H II region. It is presently fragmented; few fragmentations are present along the ring. However, NIR images could not detect any massive sources at its central region, but from 1.4 GHz map, it is evident that there are at least two massive sources (see section 4.4.4).

4.4.4 Others ionizing sources

The main ionizing star of the sub region S148 is 08-09 V, located at the center of the region. This source is also coincident with IRAS 22542+5815. Another, B1 V star is ionizing it’s surrounding molecular cloud in S149. However, the distribution of molecular gas over a large area, significantly describes that this region is possibly ionized by many other massive sources, which is most likely embedded by cold neutral material and, the UV radiation from them exciting local surrounding cloud creating a small compact H II region. In agreement with our view to other massive sources are, 1) many compact IR structures at a various location well beyond the core region. 2) The WISE 22 μm image shows many strong peaks around, emphasizing many dust heating sources might be present at other location. 3) Considering the location of ‘ARC’ in S147 and massive ionizing sources in S148/S149, it might be created by another ionizing source(s). 4) The CO peaks at a different location, emphasizing fragmentation of massive structures, which also coincides with 22 μm peaks.

Properties of ionized gas

Radio continuum observations from archival VLA data were used to estimate various physical parameters which characterize an H II region e.g., total Lyman photons emitted by ionizing source(s), electron density, emission measure. Assuming a homogeneous and spherically symmetric nature for the H II region, the Lyman continuum photon required to maintain ionization

of the nebula is given by (Kurtz et al. 1994),

$$N_* > 8.04 \times 10^{46} T_e^{-0.85} U^3 \quad (4.1)$$

where the excitation parameter, $U = rn_e^{3/2}$ pc cm⁻². The numerical coefficient is appropriate for T_e in kelvins and gives N_* in s⁻¹. The value of U could be obtained from measured integrated flux density,

$$U = 4.553 \left[\left(\frac{1}{a(\nu, T_e)} \right) \left(\frac{\nu}{GHz} \right)^{0.1} \left(\frac{T_e}{K} \right) \left(\frac{S_\nu}{Jy} \right) \left(\frac{D}{Kpc} \right)^2 \right]^{1/3} \quad (4.2)$$

For our calculation, we set $a(\nu, T_e)$ as 0.99 (obtained from Merzer & Henderson 1967), and T_e to 10⁴ K (Panagia & Felli 1975). We estimated an integrated flux value (0.782 Jy) at 4.8 GHz radio peak at the center of S148 (see Figure 4.4), which also coincides with star S01. Considering a distance 5.4 kpc, we obtained the value of N_* as 1.8×10^{48} photons s⁻¹ (hence log(N_*) is 48.2663). Assuming a class V luminosity for star S01, a comparison of log(N_*) with Panagia (1973) yields a spectral type O8-O9 V, which is consistent with our spectroscopic study.

We further used 1.4 GHz flux density tabulated in NVSS catalog to estimate properties of ionized sources of the region. Following the above approach, we estimated the value of N_* for four sources, hence their spectral types. The estimated parameters are presented in Table 4.4. The spectral classification of S01 and S02 consistent with our spectroscopy. Another two 1.4 GHz radio peak (S06, S07) are possibly coming from massive ionizing sources at central part of S147. Non-detection of these two sources in optical/NIR suggests their very early stage of evolution. However, angular resolution of the NVSS survey prevents a definitive conclusion on this issue. The location of S07 coincide with IRAS 22536+5811, suggest that we are in right direction of identifying atleast one probable massive young source in this location.

Evolutionary status of the H II region

The region S149 contain a B1 V star (S02), whereas S148 is most likely powered by a O8-O9 V star (S01). The dynamical the age of the region could be 1-2 Myr. The early-type stars

Table 4.4: Physical Parameters of the massive sources.

ID	$\alpha_{(2000)}$ (h:m:s)	$\delta_{(2000)}$ (d:m:s)	Flux (mJy)	U	N_*	Spectral Type
1	22:56:17.17	+58:31:17.98	575.0±19.4	33.8085	48.0923	O8-09 V
2	22:56:26.52	+58:32:12.17	7.1± 0.6	7.81429	46.1839	B0.5-B1 V
6	22:55:41.14	+58:29:02.10	19.1±3.4	10.849	46.6114	B0-B0.5 V
7	22:55:40.93	+58:27:53.00	34.2±4.3	13.1971	46.8667	B0-B0.5 V

usually form in dense core of a molecular cloud, and the presence of compact radio emissions (see Figure 4.3), and dust emission at $25 \mu m$ and $100 \mu m$ (see figure 4.8) suggest that associated H II regions are probably in their early stage of evolution. The presence of relatively less intense dust emission at $25 \mu m$ and $100 \mu m$ and, radio emission at 1.4 GHz suggest S147 is relatively evolved. However, non-detection of two ionizing sources in optical, relatively deep WIRCAM H , K , *spitzer*-IRAC, WISE four bands at the radio peak in S147 suggest the sources to be their very younger stage (≤ 0.5 Myr). The intense dust emission at $25 \mu m$ and $100 \mu m$ and, non-detection of radio emission at the ‘A’ subregion are indicative to absence of or till embedded ionizing sources in their ambient environment. Thus, ‘f1’ structure is possibly at relatively younger age as compared to S148/S149 and S147.

4.4.5 Reddening towards the complex

The light coming from distant objects of embedded cluster is strongly extinguished on a process of absorbing and scattering by the dust and gas, thus essentially reducing observed flux reaching us and making the objects appear redder than they really are. The extinction is generally distributed non-uniformly in an embedded cluster. It is important to know the spatial variation of extinction of the cluster to characterize the cluster members. In order to quantify the amount of extinction effected each part of the S149 complex, we estimated the K -band extinction map using 2MASS and WIRCAM data within an area $\sim 20' \times 20'$, to understand the local extinction towards the region. We measured the A_K value using $(H - K)$ colors of the stars. The sources without infrared excess (i.e., background dwarfs and non-excess sources within the field) were

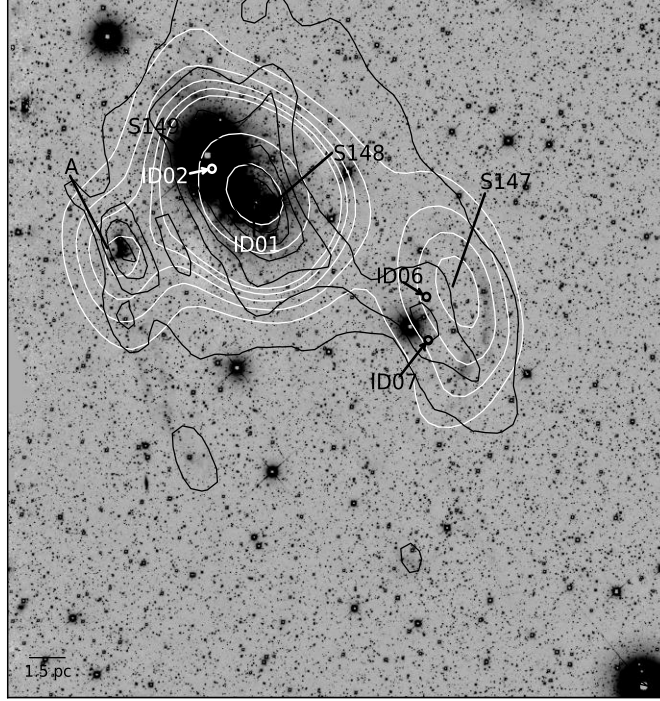


Figure 4.8: Location of two confirmed (ID01, ID02) and two probable (ID06, ID07) massive sources are shown in WIRCAM K -band image. The warm dust contours (black) at $25 \mu\text{m}$ and cold dust contours (white) at $100 \mu\text{m}$ are taken from IRAS images. The $25 \mu\text{m}$ contour levels are at 2%, 3%, 7%, 15%, 30%, 50%, 75% of the peak value 670 MJy st^{-1} and the $100 \mu\text{m}$ contours are at 7%, 9%, 11%, 13%, 15%, 35%, 55%, 75% of the peak value 2650 MJy st^{-1} . The location of individual H II subregions (S149, S148, S147 & A) are marked.

used to generate the extinction map. Following Gutermuth et al. (2005), we used the grid method to measure the mean value of A_K (see Dutta et al. 2015 for details).

Briefly, we divided the region of our interest into small grids of size $5'' \times 5''$. The mean value and standard deviation of $(H - K)$ colors of 20 nearest neighbor stars from the center of each grid was measured. We rejected any sources deviating above 3σ to calculate the mean value of $(H - K)$ at each grid position. To eliminate foreground extinction, we took only those stars having $A_K > 0.12$ mag to generate the extinction map. This much of A_K value corresponds to minimum value of a B1 V stars (S02, see section 4.4.1) to be present at a distance beyond 4.0 kpc towards the S149 cloud complex. The $(H - K)$ values were converted into A_K using the reddening law given by Flaherty et al. (2007), i.e., $A_K = 1.82 \times (H - K)_{obs} - (H - K)_0$, where $(H - K)_0$ is the average intrinsic color of stars, which is assumed to be 0.2 (Allen et

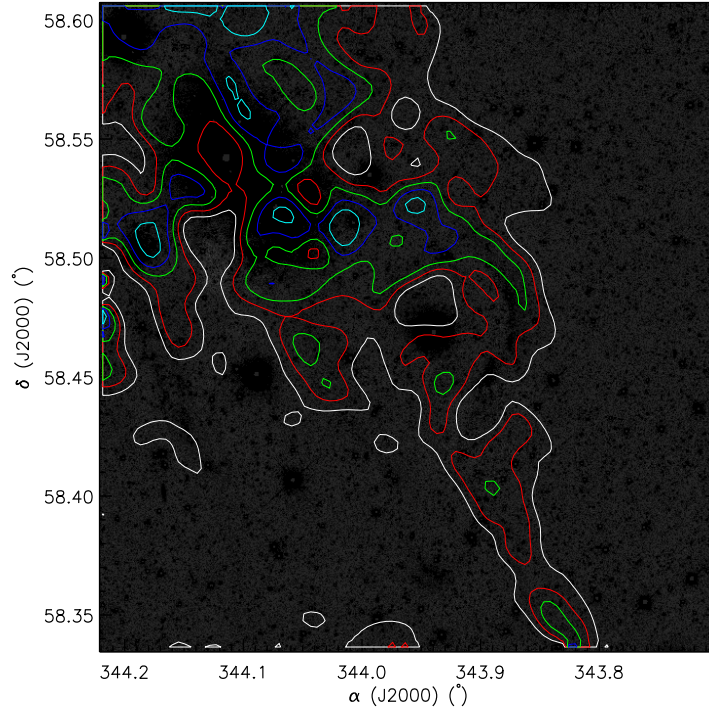


Figure 4.9: Extinction map over plotted on the WIRCAM K -band image. A_K values are estimated from the $(H - K)$ colors. The contour levels are for A_K values 0.40-0.45 (white), 0.50-0.55 (red), 0.60-0.70 (green), 0.75-0.85 (blue), 0.9-1.0 (cyan), respectively.

al. 2008; Gutermuth et al. 2009). To improve the quality of the extinction map, we excluded the probable YSOs candidates (see section 4.4.6), which otherwise might show high extinction value due to NIR excess from circumstellar disc emission. The derived extinction map is shown in Fig. 4.9. The extinction within S149 varies between $A_V = 4.5-15$ mag with an average extinction of $A_K \sim 0.54$ mag, which corresponds to $A_V \sim 6$ mag considering the extinction ratio $A_K/A_V = 0.090$ given by Cohen et al. (1981). The extinction peaks up at subregion ‘A’, filamentary (‘f1’) head at Eastern border, with a A_K value 1.4 mag ($A_V \sim 15.5$ mag). As a whole the extinction contours show nicely correlated with column density of CO map and, the extinction is higher at the location of molecular condensation.

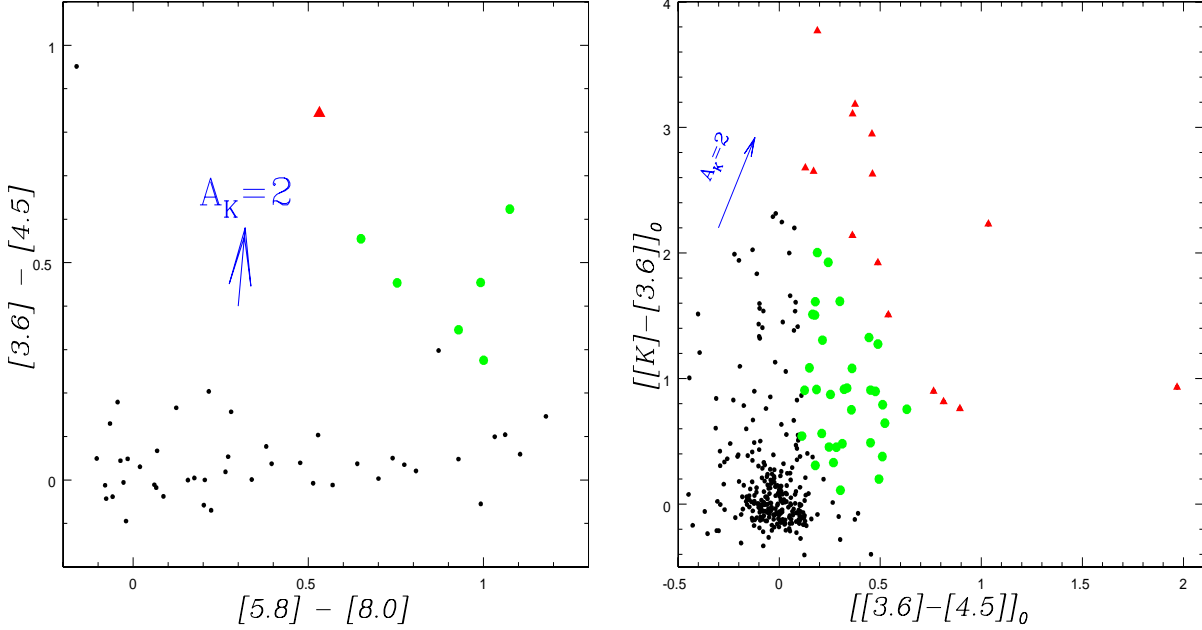


Figure 4.10: *Left*: IRAC CC diagram of all the uncontaminated sources identified within the region shown in Figure 4.3. *Right*: Dereddened $[K - 3.6]_0$ vs $[3.6 - 4.5]_0$ CC diagram for all the sources within the coverage area. The YSOs classified as candidate Class I and Class II, based on Gutermuth et al. (2009) color criteria, are shown in red triangles and green circles, respectively. The reddening vector $A_K=2$ mag is plotted by using the reddening law from Flaherty et al. (2007).

4.4.6 Young stars in the complex

Crucial to our young star search is the ability to distinguish luminous pre-main sequence stars, and background-foreground stars. Dust in the molecular cloud core averts YSOs observable at radio, submillimeter, and infrared wavelengths because of thick dust cocoon enshrouding it. We identified probable YSOs in the S149 complex following the color criterion proposed by Gutermuth et al. (2008, 2009) based on *spitzer*-IRAC, 2MASS & WIRCAM data. We excluded the possible contaminations of different non-stellar sources in IR detections such as, extragalactic objects like PAH emitting and star-forming galaxies, active galactic nuclei (AGN), unresolved knots of shock emission, PAH-emission contaminated apertures, etc. We minimized the inclusion of extragalactic contamination by applying a simple brightness cut in the dereddened photometric data.

From our multiwavelength catalog, we identified and classified the Class I (protostars with ambient thick envelope), Class II (pre-main sequence stars with optically thick disk) using $[3.6] - [4.5]$ vs. $[5.8] - [8.0]$ (Allen et al. 2004) as shown in Figure 4.4.5(*left*). Out of 215 sources detected in all IRAC bands, 154 are found to be contaminants. The remaining sample is used to identify Class I and Class II sources. We found 8 sources with IR excess, of which one is class I and 7 are class II, the rest could be Class III/field stars, which we could not classify reliably on the basis of IRAC four color criteria.

The detection and classification of YSOs based on solely IRAC colors is limited by lower sensitivity of Telescope and high nebulosity. In order to estimate more YSOs, we used $H, K, [3.6], [4.5]\mu m$ data sets. We dereddened the data set using our K-band extinction map. The inclusion of extragalactic contamination is minimized by applying brightness cut in the dereddened $3.6 \mu m$ photometry. All the class I YSOs essentially have $[3.6]_0 \leq 15$ mag and all the class II YSOs essentially have $[3.6]_0 \leq 14.5$ mag (Gutermuth et al. 2009). After removing the contaminants, we identified YSOs from $([[K] - [3.6]]_0, [[3.6] - [4.5]]_0)$ CC diagram shown in Figure 4.10. Thus in addition to IRAC 4 band search, we identified more candidate YSOs including 15 class I and 33 class II with IR excess emission. In Figure 4.10(*right*), the class I and class II sources are shown as the red triangles and green circles, respectively, and a reddening vector $A_K = 2$ mag is also plotted by using the reddening law from Flaherty et al. (2007). Our present YSO selection is incomplete as many sources in high nebulous region might have not detected in low-sensitive observations towards S149 cloud complex, and small area coverage.

The NIR CMD is a useful tool for identification of excess sources and understanding the nature of YSOs in the embedded SFRs as well. K vs $(H-K)$ CMD for all the stars detected towards S149 complex are shown in Figure 4.11(*left*). a relative reference field (between RA(J2000) 343.82507-to-343.53528 & Dec(J2000) 58.62993-to-58.325) at similar photometric depth is also shown in Figure 4.11(*right*), which does not show NIR H, K as well as optical R, I nebulosity. In Figure 4.11(*left*), the YSOs, identified from IRAC 4-band color and $([[K] - [3.6]]_0 / [[3.6] - [4.5]]_0)$ CC diagram are shown as red triangles (class I) and green circle (class II), respectively. A

careful comparison with control field shows an apparent limit of $H - K \sim 0.55$ mag of field stars, thereby indicating that the stars with $H - K < 0.55$ are most likely foreground stars. The stars below to $K = 9.0$ mag are too luminous to be members of the star-forming cluster. They are most likely foreground giants. Thus, after removing possible foreground contaminants, we consider additional 520 sources with possible NIR excess sources with $H - K > 0.55$ mag. The YSOs selected in this method may contain a few number of unresolved galaxy contaminations. We visually inspected in our high resolution HK images to reject all most-likely extended unresolved non-YSO objects lying in the selected YSO list. However, if we further accept that our YSOs sample is still contaminated by non-YSO sample from control field selected zones, then it should be less than 10%. We suggest that spectroscopic observations are necessary for the confirmation of their membership.

From CMD we can see that majority of the YSOs are located within B0 to G0 spectral type. Spectroscopically studied stars are marked with magenta ‘asterisk’ in Figure 4.11(*left*). S01 and S02 show their location in CMD to be massive stars, though exact classification does not match with spectroscopy, as they are located at the center of high nebulous and high stellar density region, their photometric measurement could be effected from emission of near by young stars.

In total, we have identified 575 YSOs in the target region with IR emission. Of these 16 have excess consistent with Class I, 39 are class II, and 520 are termed as NIR-excess sources. A list of YSOs is presented in Table 4.6. We did not report Class III sources as with present catalog they are indistinguishable from field stars.

4.4.7 Spatial Distribution of YSOs

The spatial distribution of YSOs on the column density map is shown in Figure 4.12. Majority of candidate YSOs are preferentially concentrated along the high column density, and high extinction region (see Figure 4.4.5). Overall distribution of YSOs display an important correlation between dense structure of molecular gas e.g., at H II region boundary near S148/S149, along

semi circular boundary near S147 and high density pillar structure at Eastern edge boundary ('A'). We discuss possible star formation process in these sub structures in section 4.5. Large YSOs concentration near radio compact sources indicate a possible influence of expanding H II region in star-formation. We note that most of the Class 0/I sources are distributed near massive ionizing source in S148/S149, except a few at 'f1' filamentary head 'A'. However, the NIR excess sources are show slightly scattered distribution, although in general they follow the molecular density distribution in our CO map. The S147 cluster does not seem to have many YSOs in NIR emission. But, their spatial location along semi circular boundary nicely correlate collecting material with star-formation. Since Class II sources are more evolved compared to Class I, the ratio ClassI/II most likely indicate the relative age of a star-forming region. The Class I/II ratios obtained at S148/S147 and Substructure 'A' are 0.6 and 0.3, respectively. These high concentration of Class I towards S148/S147 indicates that the youngest population is located in proximity massive ionizing sources.

4.5 Discussion

4.5.1 Star formation scenario

In our studied molecular cloud complex, Azimlu et al. (2011) found 13 dense compact molecular structure around S148/S149 and subregion 'A'. Such dense structure are at their early stage of possible massive star formation. However, all of them don't seem to have impact on local star formation, as they are yet to be radiate strong UV photons cutting through ambient dust cocoon. Tatematsu et al. (1985) shows that the whole cloud complex has two sub-groups. One group is consist of S147, S148 and S149, whereas other consists of S152 and S153. They found the northern part is probably interacting with supernova remnant SNR G109.1-1.0, However, the scenario of triggering the birth of northern complex is ruled out considering their age distribution. The location of massive sources around YSOs distribution suggest a

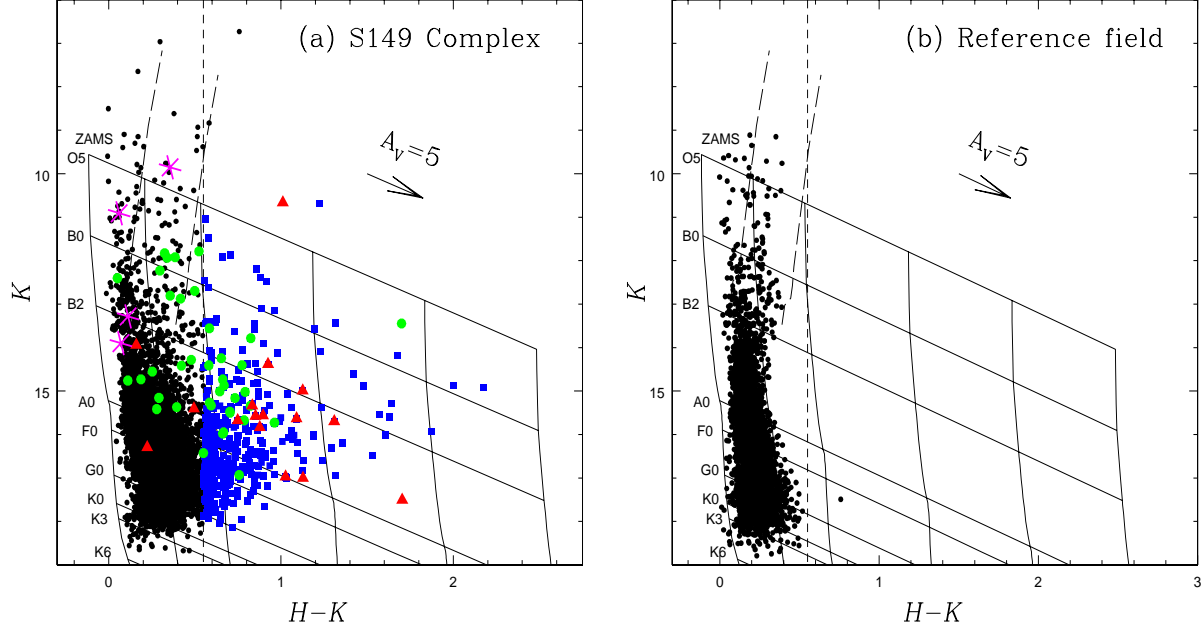


Figure 4.11: *Left*: $K/(H - K)$ CM diagram of all stars within our target area (see Figure 4.3) towards S149 cloud complex. The nearly vertical solid lines are the loci of ZAMS stars at 5.4 kpc reddened by $A_V = 0, 5, 10, 20, 30$ mag. The slanting horizontal lines represent the reddening vectors of the corresponding spectral type, taken from Flaherty et al. (2007). The thick solid lines represent the loci of giants reddened by $A_V = 0$ and 5 mag, respectively. The $H - K$ cutoff at 0.55 has been marked with a dashed vertical line. All the Class I and Class II sources determined from *spitzer*-IRAC, H and K data are represented with red triangles and green circles, respectively. The blue solid squares are the candidate YSOs selected from $(H - K) > 0.55$ cutoff. *Right*: CM diagram for the control field.

probable interaction of H II region in the local star-formation. Considering the large area of the complex, it is suggested that whole H II region is not created by the expansion of H II region, rather it is influenced nearby to exciting stars and producing compressed dense structure like filament, bright rim. We observed multi-location on-going star formation around the region. The molecular material is seemed to be fragmented at various location.

S149: S149 of the subregion is excited by a B1 V source. The radio emission shows a possible expansion of ionized gas, and creates a pin-type structure in radio contours (e.g., Figure 4.4). Moderate concentration of Class I and Class II sources and their proximity to massive ionizing source suggest a possible triggering star formation.

S148: A ionizing source O8-O9 V is probably formed in massive clumps of mass $960 \pm 196 M_{\odot}$ the large extended molecular filament. Once it formed, continue to eject UV radiation and excite the nearby cloud in S148. Thus, overall excitation of S148/S149 region is dominated by a this ionizing star. This exciting star is emitting $10^{48.09}$ photons s^{-1} . Considering the sound speed 11×10^5 cm s^{-1} , present observed radius 2.35 pc of the H II region and our estimated density of medium as 4100 cm^{-3} , the dynamic age of the ionizing star is ~ 1 Myr.

S147: It is really difficult to explain the origin of the half circular ‘ARC’, of molecular material, which shows brightest NIR emission in S147. If we admit the possible detection of massive sources two massive B0-B0.5 stars, their non-detection in optical, deep NIR images suggest their very younger phase. So, influence of these sources on dense ring formation is quit questionable. It is possibly created by collecting material of expanding H II region due to influence of any other means. A $22 \mu m$ emission shows at least three large fragmentation in the ring. Two possible condensations are detected at IRAS observations (IRAS 22535+5811, IRAS 22535+5813). The star-formation in this ring is triggered by expansion of H II region, via. collect and collapse process. Also, few lower-mass YSOs have formed in the collected material as explained in Figure 4.12.

subregion ‘A’: Out of total accumulated condensed mass of S148/S149 ($8 \times 10^3 M_{\odot}$), the most of it concentrated in the Eastern ‘A’ subregion ($2.6 \times 10^3 M_{\odot}$, Azimlu et al. 2011). Considering high extinction and non-detection of massive sources suggest this part of the region is most young compared to other sub regions.

4.6 Conclusion

In this chapter we have presented deep WIRCAM HK, *Spitzer*-IRAC, radio continuum observations of the S149 complex. We explore its stellar and interstellar content, as well as star-formation history of the region. Based on the observations our results can be summarized as follows:

- The S149 cloud complex associated with subregions S149, S148, S147 and the region is extended towards S-E border. There are few IRAS sources at various locations. S148 has relatively large H II region boundary with large fraction of on-going star formation. The half circular ring of S147 could be due to collection of material at the H II interface, which might be a good example of collect and collapse processes.
- Out of 5 bright spectroscopically studied stars, two are massive ionizing sources located in central region of S149, and S148. Further, we suggest the presence of another two massive sources at the central cavity of S147 using observational evidence in 1.4GHz and IRAS observations, along with molecular distribution in half circular shape.
- Using the IRAC and NIR CC diagrams, we identified 575 candidate YSOs, which include 16 Class I, 39 Class II, 520 NIR excess sources. We observed spatial distribution of YSOs along high column density, with clustering around ionizing sources, indicating recent star-formation at multiple sites.

In summary, it seems to be multi-generation star formation is going on though out the molecular cloud complex. Observational evidence suggest that triggering star formation is possibly taking place at the immediate periphery of S149 complex. Whereas, the massive ionizing sources could have been formed spontaneously or by some other process.

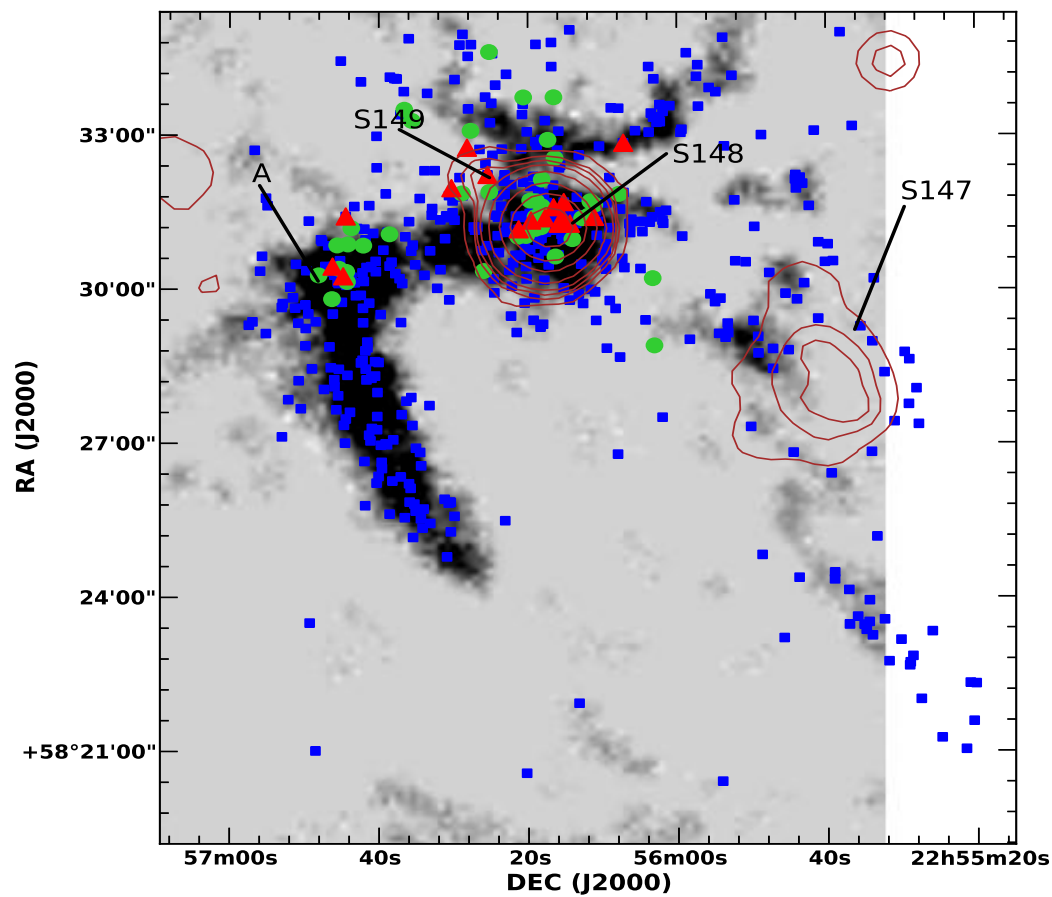


Figure 4.12: Spatial distribution of YSOs in S149 complex overplotted on the $^{13}\text{CO}(3-2)$ image. The candidate Class I, Class II and IR excess sources are shown by the red triangles, green circles and blue squares, respectively. The main sub-regions are marked in the figure. The level of brown 1.4 GHz contours are same as Figure 4.3.

Table 4.5: Catalog of YSOs (Class I and Class II)

ID	α_{2000} (deg)	δ_{2000} (deg)	J (mag)	H (mag)	K (mag)	[3.6] (mag)	[4.5] (mag)	[5.8] (mag)	[8.0] (mag)	Remarks *
Class I sources										
187	344.11736	58.54593	14.279±0.175	14.108±0.028	13.916±0.016	12.824±0.015	10.816±0.006	11.240±0.017	10.666±0.015	b
202	344.05987	58.52124	16.244±0.190	15.334±0.025	14.357±0.022	12.184±0.007	11.634±0.008	9.715±0.004	...	b
461	344.10590	58.53710	...	16.740±0.039	15.812±0.026	14.148±0.035	13.569±0.035	b
514	344.18662	58.50423	...	16.451±0.024	15.549±0.015	12.686±0.022	12.510±0.030	9.601±0.008	9.729±0.007	b
529	344.08853	58.51944	...	16.192±0.023	15.309±0.021	14.243±0.033	13.437±0.030	13.836±0.147	10.297±0.023	b
531	344.08158	58.52227	...	15.917±0.015	15.381±0.019	14.335±0.039	13.464±0.030	b
535	344.18519	58.52365	...	18.030±0.041	16.949±0.018	14.150±0.061	13.646±0.070	b
548	344.03005	58.54747	...	16.978±0.017	15.267±0.020	12.551±0.010	11.707±0.008	10.642±0.007	10.111±0.007	a
578	344.04635	58.52343	...	19.256±0.098	17.480±0.027	13.528±0.018	13.293±0.024	10.211±0.006	9.099±0.003	b
580	344.06329	58.52825	...	16.150±0.022	14.967±0.023	14.009±0.029	13.066±0.022	b
582	344.12606	58.53281	...	16.531±0.019	16.273±0.017	13.992±0.029	13.594±0.035	11.050±0.011	9.365±0.005	b
596	344.19254	58.50738	...	16.487±0.018	15.540±0.012	12.629±0.022	12.394±0.029	9.575±0.008	10.003±0.008	b
601	344.06392	58.52328	...	16.756±0.019	15.609±0.025	12.267±0.008	11.845±0.009	b
603	344.06903	58.52661	...	18.164±0.070	16.979±0.040	14.536±0.045	13.447±0.030	10.925±0.020	...	b
610	344.06616	58.52123	...	16.448±0.020	15.652±0.019	12.411±0.009	11.879±0.009	9.906±0.005	...	b
616	344.07378	58.52301	...	17.046±0.030	15.675±0.040	12.261±0.008	11.828±0.009	b
Class II sources										
112	344.03252	58.53086	16.804±0.160	15.417±0.015	14.710±0.019	13.584±0.023	13.404±0.032	11.875±0.023	9.665±0.008	b
142	344.06890	58.56226	15.883±0.077	14.777±0.016	14.257±0.022	13.598±0.023	13.300±0.028	13.216±0.058	12.344±0.068	b
183	344.14821	58.55464	15.378±0.067	14.876±0.030	14.734±0.031	14.429±0.075	14.078±0.101	...	11.104±0.026	b
201	344.05850	58.51622	14.167±0.036	13.210±0.049	12.670±0.046	11.513±0.005	11.268±0.006	10.230±0.007	...	b

Continued on next page

Table 4.5 – continued from previous page

ID	α_{2000} (deg)	δ_{2000} (deg)	J (mag)	H (mag)	K (mag)	[3.6] (mag)	[4.5] (mag)	[5.8] (mag)	[8.0] (mag)	Remarks
203	344.04843	58.52848	15.754±0.067	14.926±0.030	14.706±0.035	14.014±0.026	13.771±0.034	11.493±0.016	...	b
204	344.05307	58.52301	16.168±0.126	14.632±0.016	13.758±0.016	11.933±0.006	11.581±0.007	9.380±0.003	...	b
217	344.10491	58.53153	15.982±0.081	14.921±0.021	14.222±0.017	13.678±0.023	13.127±0.023	b
223	344.08205	58.52876	15.505±0.074	14.816±0.017	14.528±0.024	13.884±0.025	13.532±0.031	11.662±0.022	9.482±0.005	b
227	344.07594	58.52010	15.497±0.123	14.852±0.021	14.391±0.028	13.081±0.014	12.663±0.016	...	10.868±0.034	b
228	344.07923	58.51956	16.634±0.169	15.008±0.015	14.384±0.022	13.919±0.027	13.359±0.028	b
239	344.18899	58.50666	13.113±0.033	12.537±0.045	12.204±0.046	11.616±0.011	11.283±0.014	9.529±0.008	9.943±0.008	b
240	344.18425	58.51460	15.270±0.056	14.047±0.017	13.385±0.040	12.444±0.021	12.169±0.024	11.808±0.034	10.807±0.016	a
248	344.19286	58.49681	16.635±0.129	15.672±0.012	14.983±0.015	14.041±0.059	13.363±0.057	b
249	344.18448	58.50239	13.994±0.036	13.178±0.041	12.784±0.038	12.056±0.015	11.896±0.019	9.673±0.008	9.785±0.007	b
255	344.18226	58.51987	16.328±0.106	15.197±0.015	14.344±0.009	12.944±0.025	12.321±0.027	11.898±0.035	10.822±0.016	a
258	344.16061	58.51783	12.627±0.021	12.145±0.028	12.050±0.019	12.739±0.148	12.285±0.036	11.908±0.036	10.916±0.020	a
267	344.12021	58.53109	16.546±0.129	15.460±0.011	15.133±0.019	14.095±0.029	13.800±0.041	10.993±0.012	10.078±0.013	b
318	344.06811	58.51061	15.921±0.086	14.826±0.016	13.878±0.020	13.014±0.014	12.460±0.015	12.380±0.041	11.729±0.063	a
434	344.20030	58.50453	...	15.948±0.012	15.310±0.012	14.399±0.065	14.002±0.080	13.301±0.184	...	b
446	344.17534	58.51418	...	16.200±0.014	15.450±0.013	14.314±0.070	13.926±0.075	12.880±0.078	11.490±0.030	b
455	344.04934	58.52387	...	15.195±0.017	13.423±0.064	11.729±0.005	11.519±0.007	9.357±0.003	...	b
459	344.07560	58.53558	...	15.203±0.014	14.381±0.020	13.671±0.024	13.164±0.025	b
478	344.11535	58.55142	...	14.162±0.014	13.534±0.019	13.100±0.017	12.890±0.023	12.968±0.059	...	b
480	344.15241	58.55826	...	15.834±0.022	14.994±0.016	13.932±0.052	13.415±0.060	13.275±0.099	...	b
497	344.01279	58.48168	...	15.872±0.019	15.243±0.013	14.459±0.044	13.902±0.048	13.574±0.069	12.559±0.089	b
512	344.01377	58.50352	...	15.068±0.020	14.486±0.017	13.652±0.023	13.306±0.028	12.851±0.039	11.922±0.042	a
516	344.18492	58.50565	...	15.917±0.015	15.137±0.015	13.375±0.035	13.134±0.047	10.445±0.013	9.855±0.007	b

Continued on next page

Table 4.5 – continued from previous page

ID	α_{2000} (deg)	δ_{2000} (deg)	J (mag)	H (mag)	K (mag)	[3.6] (mag)	[4.5] (mag)	[5.8] (mag)	[8.0] (mag)	Remarks
517	344.10808	58.50591	...	15.777±0.018	15.344±0.019	14.724±0.047	14.400±0.060	12.834±0.039	10.557±0.011	b
526	344.19017	58.51425	...	15.299±0.016	14.496±0.012	12.781±0.022	12.327±0.027	11.762±0.031	11.008±0.018	a
527	344.08438	58.51727	...	16.994±0.019	16.402±0.019	14.868±0.062	14.372±0.064	...	9.828±0.008	b
536	344.07555	58.52688	...	16.222±0.036	15.471±0.029	14.034±0.031	13.506±0.031	12.466±0.043	10.942±0.034	b
540	344.07867	58.52851	...	15.705±0.018	15.391±0.026	14.144±0.032	13.954±0.042	11.740±0.023	9.582±0.005	b
549	344.07226	58.54845	...	16.188±0.019	15.316±0.017	14.354±0.034	13.800±0.037	13.117±0.058	12.238±0.050	b
560	344.10499	58.57696	...	15.564±0.080	14.849±0.089	13.721±0.043	13.346±0.039	...	11.272±0.022	b
588	344.08584	58.56222	...	16.717±0.023	15.702±0.013	14.617±0.047	14.120±0.055	13.671±0.093	11.495±0.033	b
599	344.08881	58.51704	...	16.660±0.018	15.953±0.025	13.820±0.025	13.526±0.032	10.999±0.012	9.114±0.018	b
606	344.06836	58.54254	...	17.713±0.055	16.908±0.018	14.684±0.049	14.440±0.063	11.679±0.018	10.546±0.020	b
611	344.07908	58.52345	...	16.639±0.028	15.927±0.028	14.391±0.041	14.120±0.050	b
613	344.04616	58.52740	...	16.485±0.036	15.650±0.029	13.909±0.025	13.698±0.033	10.985±0.010	9.125±0.004	b

* 'a': The YSOs are estimated using IRAC 4 color criteria,

'b': The YSOs are estimated using H , K , [3.6] and [4.5] color criteria.

Chapter 5

Optical Photometric Variable Stars

towards Galactic H II region NGC 2282

5.1 Introduction

Infrared excess emission from optically thick disk allows us to detect young stars (Lada & Adams 1992; Lada et al. 2000). The photometric variability is also a ubiquitous characteristic of young stars (Joy 1945; Herbig 1962). Thus, the potential of variability studies helps also to pick out the young stars among the field population. However, variability alone is not sufficient evidence to identify young members, and sometimes might be false positive. Thus, additional constraining tools are highly needed, such as location on a color-magnitude diagram, infrared excess, H_α emission, spatial location, etc. Photometric variability is proposed to be the result of rotational modulation by hot or cool stellar spots on the star's surface with observed period ranges from hours to 15 days (Herbst et al. 1994; Carpenter et al. 2001; Briceno et al. 2005). The variability is also a useful tool to estimate the rotation period of those spotted stars. Various temporal phenomena such as flare like activity on the Corona, circumstellar disk extinction due to disk asymmetry, eclipsing binarity may lead to aperiodic variability of stars. PMS variable census has allowed recent studies to probe rotation rates spanning over several

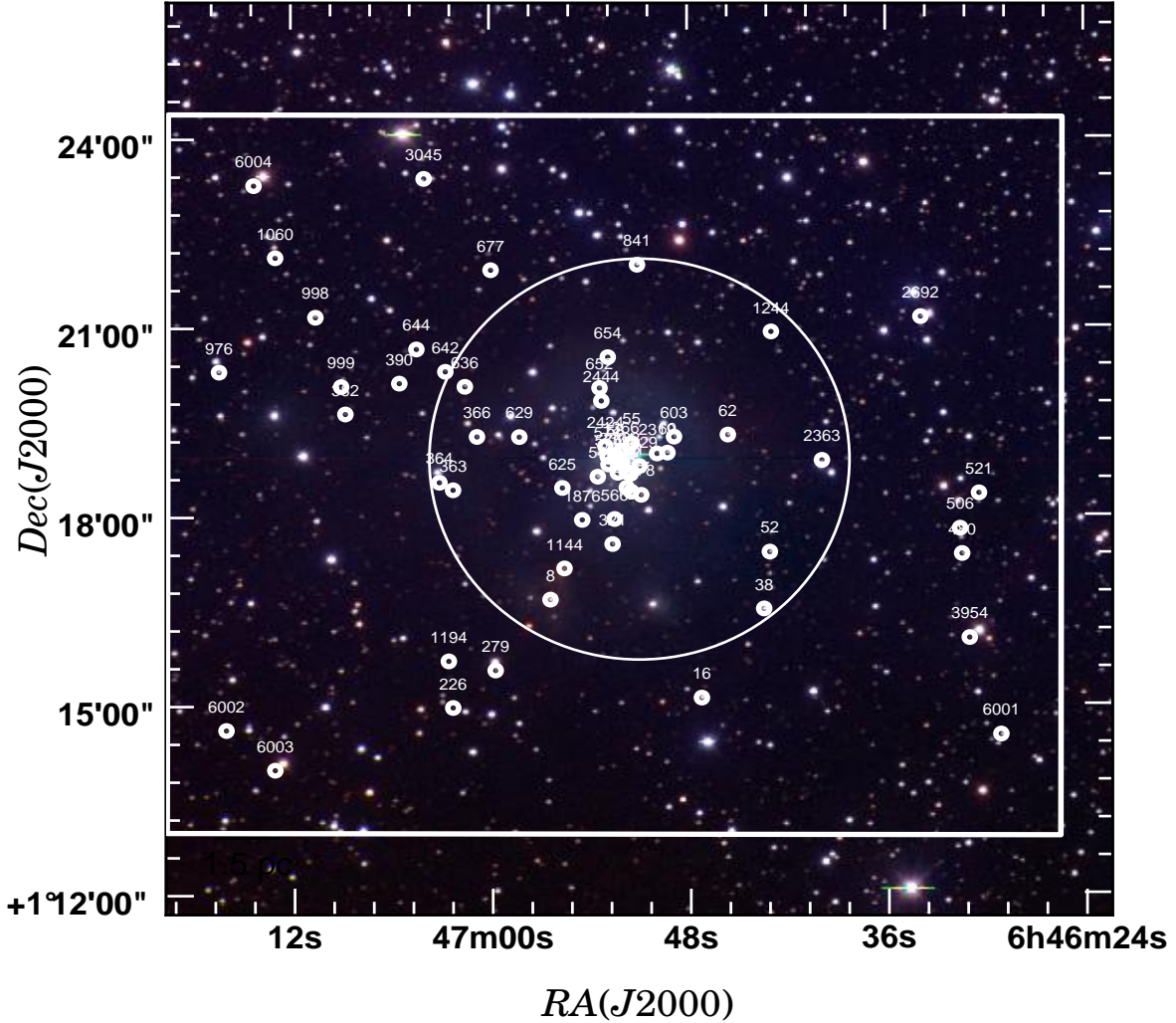


Figure 5.1: Optical color composite image of NGC 2282 (blue: V; green: R; red: I) obtained at 1.3m DFOT (Up is North, left is East). The cluster area is marked with white circle. Our combined monitoring observations were done at the white box region. The variable candidates are marked (see text for details).

Myrs young and old clusters, including Chamaeleon I (Joergens et al. 2003), IC 348 (Cohen et al. 2004), Taurus (Nguyen et al. 2009), the Orion Nebula Cluster (Stassun et al. 1999; Herbst et al. 2002; Rodriguez-Ledesma et al. 2010), σ Orionis (Scholz & Eisloffel 2004; Cody & Hillenbrand 2010), NGC 2362 (Irwin et al. 2008), and NGC 2264 (Makidon et al. 2004; Lamm et al. 2005).

Our principal focus of monitoring young cluster programs has been the discovery of rotation periods in PMS stars and characterizing their variability characteristics. Photometric method

to study variable stars is a useful tool to pick up memberships for young clusters (e.g. Briceno et al. 2001). It could also be treated as an effective tool to detect Weak-line T Tauri Stars (WTTSs) even they are very challenging to be distinguished from field stars using their small infrared excess. Observational evidence of period distribution at ages of few Myr shows periods between 1 and 10 days and extends up to ~ 25 days for slower rotators (Cody & Hillenbrand 2010). Additionally, the rotation period distribution show bimodal, split between fast rotators peaks 1-2 days and slower peaks greater than 3-4 days (Herbst et al. 2002; Lamm et al. 2005; Coker et al. 2016). Star-disk connection might play significant role here and their interaction might be effectively coupled with the rotation rate as stellar angular momentum evolution models are predicted (Konigl 1991; Shu et al. 1994). The disk locking mechanism was verified by observations on several young clusters from any correlation between rotation period and disk indicators e.g. $\Delta(I-K)$, $\Delta(H-K_s)$; $[3.6]-[8.0]$ and H_α (Edwards et al. 1993; Stassun et al. 1999; Herbst et al. 2002; Makidon et al. 2004; Lamm et al. 2005; Rebull et al. 2006; Cieza & Baliber 2007; Rodriguez-Ledesma et al. 2010; Cody & Hillenbrand 2010; Lata et al. 2015;). However, no conclusive evidence was found that slowly rotating stars have disks or faster rotating stars are diskless (Cieza & Baliber 2007). Review works in this subject area have explored rotation-disk connection in low and very low mass star in Herbst et al. (2007) and Bouvier (2007). Mass-rotation connection shows a clear mass-dependent morphology, which evolves with ages with relatively fast rotation seen in the low mass end (Irwin et al. 2008; Coker et al. 2016 and reference therein).

NGC 2282 ($\alpha_{2000} = 06^h46^m50.4^s$; $\delta_{2000} = +01^{\circ}18^m50^s$) is a reflection nebula in the Monoceros constellation, may be associated with 3° away Mon OB2. The cluster parameters of NGC 2282 were first studied by Horner et al. (1997) using Near-IR data. Subsequently, recently Dutta et al. (2015) (hereafter Paper I) studied more elaborately the pre-main sequence (PMS) member candidates and cluster parameters of NGC 2282 using deep optical $BVIH_\alpha$, UKIDSS JHK and *Spitzer*-IRAC data. Using Near-IR to mid-IR color-color (CC) criteria and H_α -emission properties, the authors have identified an abundant population of 152 PMS member

candidates, which include 75 Class II and 9 Class I sources. The majority of cluster members are concentrated within the radius of $\sim 3.15'$, and the minimum extinction was found to be $A_V \sim 1.65$ mag. Based on the optical and near-IR color-magnitude diagram (CMD) analyses and disc fraction ($\sim 58\%$), the cluster age had been estimated to be in the range of 2 – 5 Myr. Spectroscopic study of bright stars finds that the region contains at least three B-type stars. Thus, it is one of the best targets for detailed variability study, as it is relatively populous within a small region, sufficiently nearby with a younger cluster age. From optical spectroscopic studies, the authors also confirmed the previously known main-illuminating source B2V type star, HD 289120, and found two more high mass stars, a Herbig Ae/Be star (B0.5 Ve) and a B5 V star, and established the distance to the cluster as ~ 1.65 kpc. Thus, it is one of the best targets for detailed variability study that we have undertaken here.

In this chapter, we present long time-series photometric studies of NGC 2282 to understand and characterize the variable properties of PMS stars. Section 5.2 contains details of our observations and archival data sets used for the present study. Section 5.3 provides our result and discussion on photometric light curve analyses, identifications of the variable stars, and our analyses of a sample of 62 periodic/apperiodic variables. We estimate in this section their infrared excess, and how they are related to rotation rates, variability amplitude, and masses. Finally, in section 5.4, we summarize our main results of this work.

5.2 Data Sets Used

5.2.1 Observations

Optical Photometry

The *RI* photometric and *I*-band time-series observations of the cluster NGC 2282 were carried out over 25 epochs during 15 Oct 2013 to 18 Feb 2016 using two different Indian telescopes. We

Table 5.1: Log of Observations.

Date of Observations	Telescope	I Exp.(s) × N	R Exp.(s) × N	Avg. seeing (arcsec)
2m HCT				
15.10.2013	2.0m HCT	60×1, 120×30	200×1	2.5
07.11.2013	2.0m HCT	120×20, 300×1	200×1	2.5
08.11.2013	2.0m HCT	120×3, 300×1	300×1	2.5
05.01.2014	1.3m DFOT	150×46	250×1	1.8
06.01.2014	1.3m DFOT	150×56	...	1.9
29.03.2014	1.3m DFOT	150×49	250×1	1.75
31.03.2014	1.3m DFOT	150×16, 60×1	250×2, 150×1	1.8
05.10.2014	2.0m HCT	90×2	...	1.5
06.10.2014	2.0m HCT	120×2, 90×4, 60×5	...	3.2
29.10.2014	2.0m HCT	120×2, 90×5, 60×5	...	2.5
30.10.2014	2.0m HCT	120×6, 90×8, 60×3	...	2.5
12.11.2014	1.3m DFOT	150×40, 90×27, 60×30	250×2	2.0
13.11.2014	1.3m DFOT	150×25, 90×21, 60×20	250×2	2.0
14.11.2014	1.3m DFOT	150×35, 90×25, 60×25	250×2	2.0
30.11.2014	1.3m DFOT	150×60, 90×41, 60×40	250×2	2.0
01.12.2014	1.3m DFOT	180×60, 90×20, 60×20	250×2	2.0
10.12.2014	1.3m DFOT	180×45, 90×10, 60×10	250×2	2.0
11.12.2014	1.3m DFOT	180×60, 90×15, 60×15	250×2	2.0
12.12.2014	1.3m DFOT	180×50, 90×40, 60×20	250×2	2.0
15.01.2015	2.0m HCT	180×3, 120×4, 60×5	250×2	2.5
16.01.2015	2.0m HCT	120×3, 60×3	200×1	2.5
17.01.2015	2.0m HCT	120×2, 60×2	200×1	2.5
05.10.2015	2.0m HCT	150×2, 60×2	200×1	2.5
07.10.2015	2.0m HCT	300×2, 60×3	200×2	2.5
18.02.2016	2.0m HCT	200×5, 90×6	200×1, 90×1	2.5

performed photometric observations using the 1.3m Devasthal Fast Optical Telescope (DFOT) operated by Aryabhata Research Institute of Observational Sciences (ARIES), Nainital, India (Sagar 2011). We have used a backend instrument 2048 × 2048 Andor CCD camera on the DFOT for this studies. The 2K×2K CCD camera having a pixel size of 13.5 μm provides a field-of-view (FOV) of about 18' × 18' on the CCD with a plate scale of 0.535 arcsec pixel⁻¹ for F/4 optics of the DFOT. The gain and readout noise of the CCD are 6.5 e⁻/Analog to Digital Unit(ADU) and 2 e⁻ respectively. The DFOT observations were taken in 2×2 binning mode to improve the signal to noise ratio (SNR), and the average FWHM of the stars were ~ 2". We also carried out photometric observations using Himalaya Faint Object Spectrograph

Camera (HFOSC) backend instrument on 2m Himalayan Chandra Telescope (HCT), operated by Indian Institute of Astrophysics (IIA), India (Prabhu 2014). The HFOSC imaging CCD 2048×2048 pixels with pixel size $15 \mu\text{m}$ provides a FOV of about $10'$ on a side of the CCD with a plate scale of $0.296 \text{ arcsec pixel}^{-1}$ for F/9 optics of the HCT. The gain and read out noise of the CCD are $1.22 \text{ e}^-/\text{Analog to Digital Unit(ADU)}$ and 4.8 e^- respectively. The HCT observations were taken in 2×2 binning mode, and the average FWHM of the stars were $\sim 1.5\text{-}3.2''$. The observations were taken in short and long exposures to get a good dynamic coverage of the stellar brightness. The log of optical observations is shown in Table 5.1. The Optical color composite image of NGC 2282 is shown in Fig. 5.1, which was taken by the DFOT CCD camera having $18' \times 18'$ FOV, and the HFOSC CCD FOV of $10' \times 10'$ is marked for our overlapping monitoring program.

The raw CCD images were cleaned using IRAF* software following bias subtraction, flat fielding and cosmic ray removal. The identification of point sources was performed with the DAOFIND task. Following Stetson (1987), we have used the roundness limits of -1 to $+1$ and sharpness limits of 0.2 to $+1$ to eliminate bad pixels brightness enhancements and the extended sources such as background galaxies from the point source catalog. The photometry by PSF fitting was done using ALLSTAR task of DAOPHOT package (Stetson 1992). The astrometry on CCD frames were determined using IRAF tasks *ccfind*, *ccmap* and *ccsetwcs*, and we have taken 20 isolated moderately bright stars with their positions from the 2MASS point source catalogue (PSC) (Curti et al. 2003), and a position accuracy of better than $0.3''$ has been achieved.

We have used available archival optical to mid-IR data for characterizing PMS stars of NGC 2282 such as (i) NIR *JHK* photometric data from the UKIRT Infrared Deep Sky Survey (UKIDSS, Lawrence et al. 2007), which were taken during the UKIDSS Galactic Plane Survey (GPS) (Lucas et al. 2008; data release 6); (ii) the *JHK_s* photometric data from 2MASS PSC (Cutri et al. 2003) for bright end; (iii) the *Spitzer* IRAC observations in 3.6 and $4.5 \mu\text{m}$ bands (channels 1 and 2) (Program ID: 61071; PI: Whitney, Barbara A); (iv) mid-IR data on 3.4 , 4.6 ,

*Image Reduction, and Analysis Facility (IRAF) is distributed by National Optical Astronomy Observatories (NOAO), USA (<http://iraf.noao.edu/>)

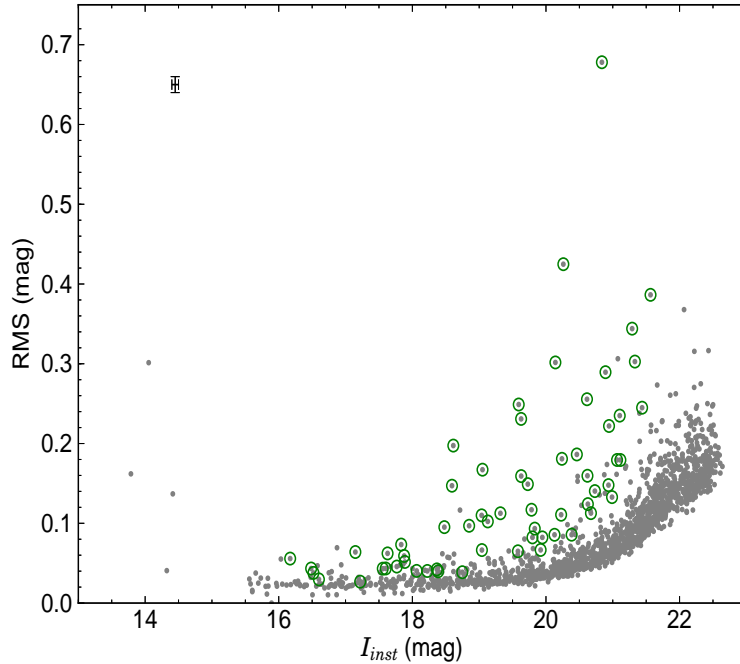


Figure 5.2: RMS of the I -band light curves of 1627 stars towards NGC 2282. The green circles marks are detected variables. The average error bars for magnitudes and rms value are also shown on the top left corner (see text for details).

12, and 22 μm from Wide-field Infrared Survey Explorer (WISE) All-sky Survey Data Release (Wright et al. 2010); (v) the optical data were obtained from INT Photometric H_α Survey of the Northern Galactic Plane (IPHAS), which is a photometry survey using wide field camera (WFC) on the 2.5m Isaac Newton Telescope (INT) with Sloan r , i filters and H_α narrow-band filters (Drew et al. 2005; Gonzalez-Solares et al. 2008; Barentsen et al. 2014).

5.3 Results and discussion

5.3.1 Identification of variable stars

Considering a large number of sample, we have employed several techniques to select variable stars quantitatively. These tools were developed using *Python*. Particularly, we performed root-mean-square (RMS) deviation of magnitudes for each star over the whole span of observations

for the different telescopes. Following Carpenter et al. (2001), RMS of all data sets for each star was estimated using

$$\sigma_{mag}^2 = \frac{n \sum_{k=1}^n w_k (I_k - \bar{I})^2}{(n-1) \sum_{k=1}^n w_k}, \quad (5.1)$$

where I_k 's are the individual magnitudes associated with photometric uncertainty σ_k 's and weightage $w_k = 1.0/\sigma_k^2$ for each observation. The rms noise was also considered as

$$\sigma_{noise}^2 = \frac{n}{\sum_{k=1}^n 1.0/\sigma_k^2}. \quad (5.2)$$

The mean magnitude and RMS of time-series data for each star were estimated using all the observations. Fig. 5.2 displays the RMS of each star as a function of instrumental magnitudes. RMS of majority stars increases with fainter magnitudes as signal-to-noise ratio (SNR) decrease accordingly towards the fainter limit. The observed RMS values of normal stars follow an expected nearly exponential trend; RMS values range from ~ 0.01 mag for a brighter end to ~ 0.2 mag towards completeness limit. However, a few stars are scattered from the normal trend. Such type of deviation could be due to photometric noise or intrinsic variability. We restricted our analysis that a star is variable having equal or more than a 3σ RMS scatter. From rms deviation, we have peaked up 69 variable stars from criterion as mentioned above. Considering location on the edge of CCD few of them are rejected from variable list. The variability signature was also cross-checked by the visual inspection of the individual light curve. Finally, we have 62 variable candidates for further analysis. The spatial distribution of variable candidates in the young clusters traces the star-forming history of that cloud. Fig. 5.1 shows the spatial distribution of the candidate variables within NGC 2282 (white circles). From Fig. 5.1, it is apparent that majority of variables are concentrated at the core region of the cluster. A significant and scattered population towards north-east part of the cloud, which suggests that the cluster might be extended towards that direction as predicted by Horner et al. (1997).

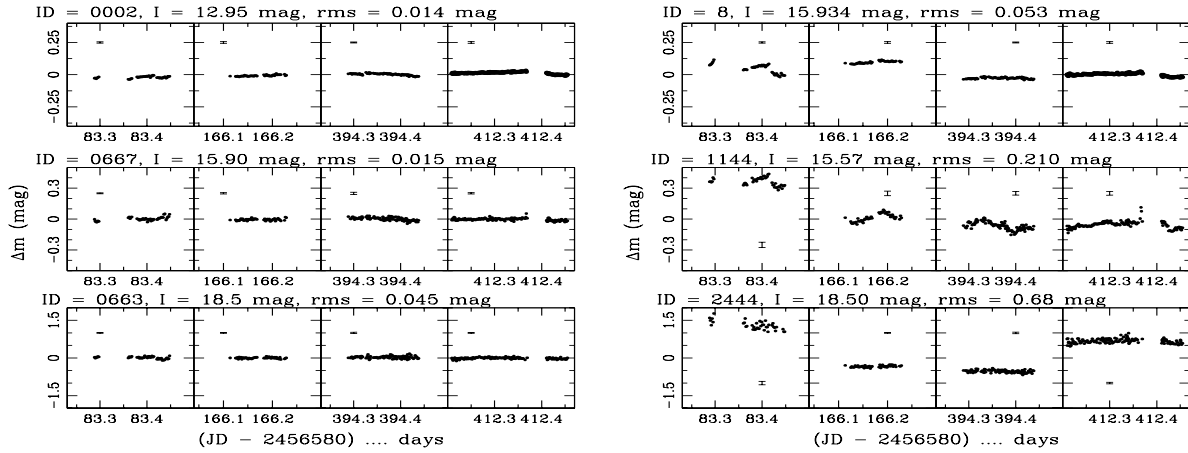


Figure 5.3: Example light curves for few apparently non variable stars of different magnitude range (left three panels) and few candidate variable stars (right three panels). The Δm represents the relative magnitude with respect to comparison star. Star identifications, I magnitude and RMS value are mentioned. Average error corresponding to each day data is plotted. (see text for details).

Differential Light Curves

For those peaked-up 62 variable candidates from RMS analysis, we have performed differential photometry to clean the light curves from sky variability, instrument signatures, airmass, etc. We have considered a few reference stars in the same CCD frame of the targets, which showed a stable behavior on the basis of RMS scatter in the observed light curve and visual inspection. To obtain relative photometry, we subtract each target star magnitude from those of the reference stars in each frame. The technique of differential photometry provides excellent photometric precision, even in the crowded nebulous region of the cluster. The light curves of few non-variables and variable stars are shown in Fig. 5.3, where one can find high-precision light curves for non-variables. The catalog of detected variable stars from our analysis are listed in Table 5.2.

From the differential light curve, we found ID 366 as an eclipsing binary star (Fig. 5.4), where the two components periodically eclipse one another, hence decrease in the apparent brightness of the system as seen by the observer. Another star ID 2692 shows fast stochastic variability,

could be a classical T Tauri candidate as a typical manifestation of the underlying variable accretion processes. This is a kind of aperiodic variable in this analysis.

Period Analysis

To estimate periods of those variable candidates, we used the Lomb-Scargle (LS) periodogram analysis (Lomb 1976; Scargle 1982), the LS algorithm publicly available at the Starlink* software database. The LS method is used to find out significant periodicity even with unevenly sampled data and verified successfully in several cases to determine periods from such sparse data sets (Lamm et al. 2004; Mondal et al. 2010; Lata et al. 2012). The periods were also verified from other software like PERIOD04** (Lenz & Breger 2005) and NASA Exoplanet Archive Periodogram Service***. Out of 62 variable candidates, 42 stars are periodic in nature. The LS power spectrum of two variable candidates having an identification number of ID 364 and ID 55 are shown as an example in Fig. 5.5, which show significant periods of 0.546 and 2.309 days, respectively. The periods of variable candidates exhibit in the range 0.233 to 7.143 days, and those are listed in Table 5.3. Considering those estimated periods, we have generated the phased light curves of variable candidates, which are shown in Fig. 5.6.

5.3.2 Characterization of variable stars

H_α Emission property of Variable candidates

H_α emission are activity indicators of stars in T Tauri phase, and hence those are bonafide members in the cluster NGC 2282. Here we have used IPHAS archive data as described in section 2, and our observed slitless spectroscopy (Paper I) to identify H_α emission-line stars among variable candidates. Fig. 5.7 presents the IPHAS ($r - i/r - H_\alpha$) CC diagram of all

*<http://www.starlink.uk>

**<http://www.univie.ac.at/tops/Period04>

***<http://exoplanetarchive.ipac.caltech.edu/cgi-bin/Periodogram/nph-simpleupload>

the candidate variable stars detected in IPHAS DR2. Two nearly vertical black and green lines represent the trend for an unreddened Rayleigh-Jeans continuum and the case of an unreddened optically thick disc accretion continuum, respectively (Barentsen et al. 2014). The black broken lines are the predicted lines of constant net emission EW. The solid and broken blue lines indicate the locus of unreddened main-sequence and that of the main-sequence stars having an H_α emission-line strength of -10 \AA EW, respectively. The main-sequence emission line with EW -10 \AA is chosen as Classical T Tauri Stars (CTTSs) threshold for H_α emission stars. However, it is difficult to confirm CTTSs solely on the basis of IPHAS photometry (Barentsen et al. 2014, Paper I)

We identified 21 variable sources as H_α emitting stars from IPHAS photometry which are located above the 3σ confidence level from CTTSs threshold as mentioned above. We also compared H_α emission properties from IPHAS photometry to that of slitless spectroscopy (Paper I). Rest of the variable stars could be WTTSs with small H_α or no H_α emission. However, those stars could have strong H_α emission but not detected in the present study due to the variable H_α emission activities in PMS sources. The details of all the variable candidates with H_α emission properties in NGC 2282 region are presented in Table 5.3.

Near-IR Color-Color Diagram

Like H_α emission, the Near-IR excess is one of useful tool to pick-up PMS stars, we have used this technique to identify variable candidates as PMS objects. Near-IR $(J - H)/(H - K)$ CC diagram of variable candidates is shown in Fig. 5.8. The black solid and long dashed green line represent the locus of the intrinsic colors of dwarf and giant stars, taken from Bessel & Brett (1988). The dashed black line represents the locus of the CTTSs (Meyer et al. 1997). All the intrinsic locus and photometric data points are transformed into the CIT (California Institute of Technology) system (Elias et al. 1982) using the relations given by Carpenter et al. (2001). The parallel dashed lines represent the different interstellar reddening vectors. The slope of the reddening vectors (i.e., $A_J/A_V = 0.265$, $A_H/A_V = 0.155$ and $A_K/A_V = 0.090$) are taken from

Cohen et al. (1981). We divide the JHK near-IR space into three regions- F, T, and P. The near-IR emission of stars in ‘F’ region originate mainly from their disc-less photosphere, they may be either field stars or WTTSs/Class III sources with no or small near-IR excess. However, it is very difficult task to distinguish between WTTSs with small near-IR excess and field stars from only near-IR CC diagram (Ojha et al. 2004). The near-IR emission of ‘T’ region stars arise from both photosphere and circumstellar disk (Lada & Adams 1992), and the majority of these stars are considered to be CTTSs. All such sources possess accreting optically thick disk (Meyer et al. 1997). The ‘P’ region stars have more near-IR color excess at K-band, and these stars are thought to have an accreting disk, and might have envelope around them like a protostellar (Rice et al. 2012).

From Fig. 5.8, we find that majority of variable stars follow the CTTSs locus. Among 62 variable stars, 39 stars are located within 3.15 ' radius of the cluster (Paper I). Out of 62 stars, 30 stars (47%) were previously identified as young stars from either infrared excess, H_{α} -emission or both activities, and in those 30, 25 have infrared excess. The ‘F’ region stars might be WTTSs with less infrared excess or field stars. The rest of 33 variables might be WTTSs with less IR excess or field stars. But spectroscopy follow up is needed to distinguish them from field stars. However, YSOs selection in Paper I was incomplete as many sources in the high nebulous region might not have been detected in near-infrared bands and due to unavailability of *Spitzer* data in longer wavelengths.

Optical Color-Magnitude Diagram of YSOs

An Optical CMD, V vs $(V - I)$ of YSOs is plotted in Fig. 5.9. It is an important tool to estimate the approximate ages and masses of variable candidates. The solid curve in Fig. 5.9 represents the ZAMS, taken from Girardi et al. (2002) corrected for the cluster distance 1.65 kpc and reddening of $E(B - V) = 0.52$ mag ($E(V - I) = 0.65$ mag) (see sect. 3.3 & 3.4 of Paper I). We have used the PMS isochrone and evolutionary tracks of Bressan et al.(2012) to determine the ages and masses of the YSOs. The PMS isochrones for Siess et al. (2000) is also plotted for

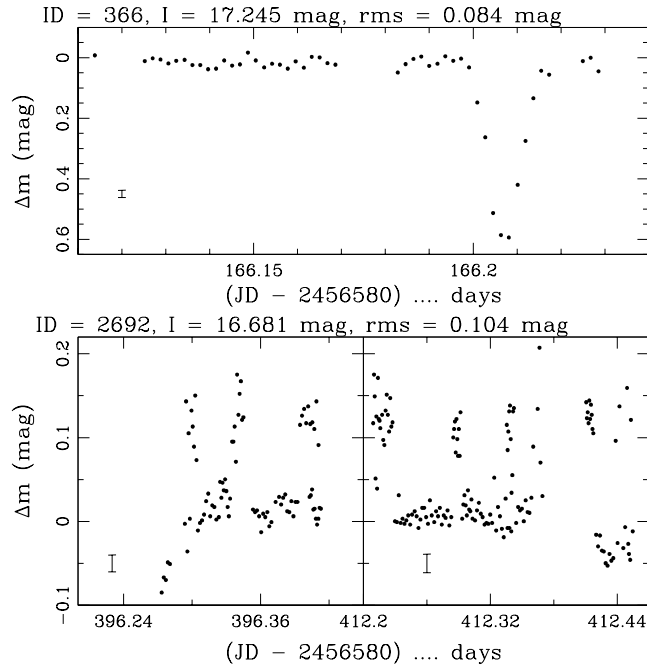


Figure 5.4: Example light curves of a eclipsing binary (upper panel) and probably fast stochastic variable (lower panel). All the marks are as Fig. 5.3 (see text for details).

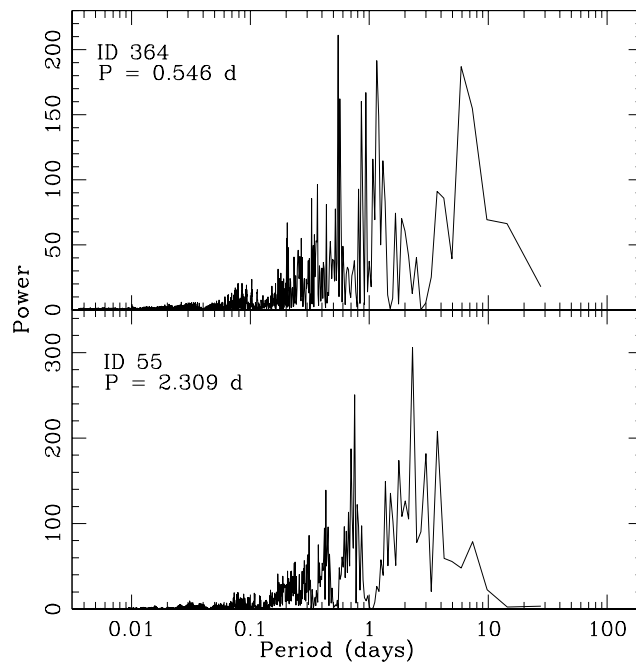


Figure 5.5: Example LS power spectrum of selected stars. The highest peaks are marked with red dashed lines (See text for details).

comparison. The ages and masses of YSOs have been estimated by comparing their locations on the CMD with PMS isochrones of various ages after correcting for the distance and extinction.

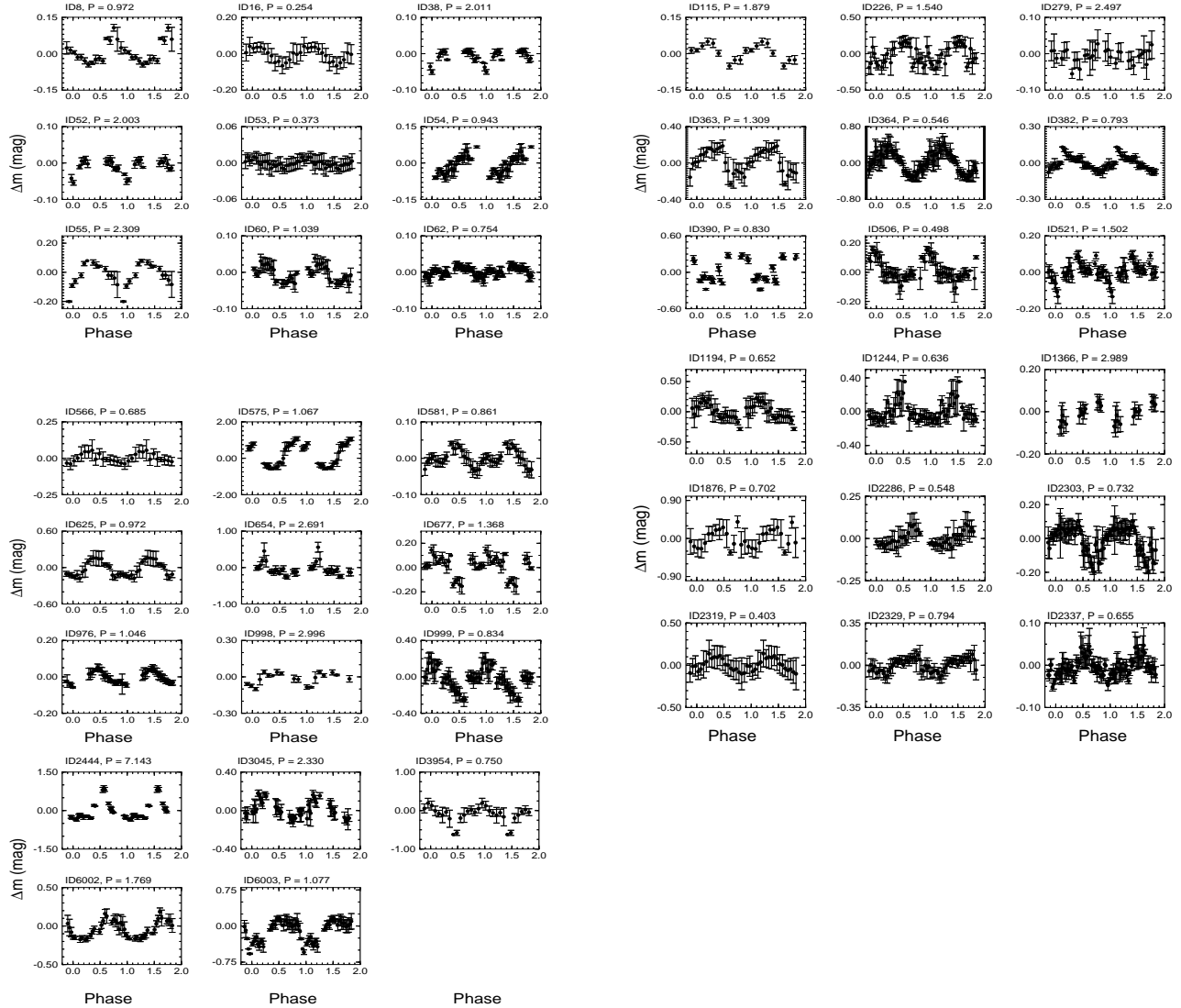


Figure 5.6: The phase I -band light curve of variables are shown here. Period of variables are taken from Table 5.3, and details of variable IDs are listed in Table 5.2 (see text for details).

Since the reddening vector is nearly parallel to the isochrones, a small extinction variation would not have much effect on the age estimation of YSOs.

We have compiled VI photometry for the YSOs, and compare their positions on the CMD to theoretical model isochrones. We estimated mass and age of a few variable stars using interpolation methods of Siess et al. (2000) isochrones in the CMD. However, our estimation is limited due to the absence of V measurements of all variable stars. The CMD positions of

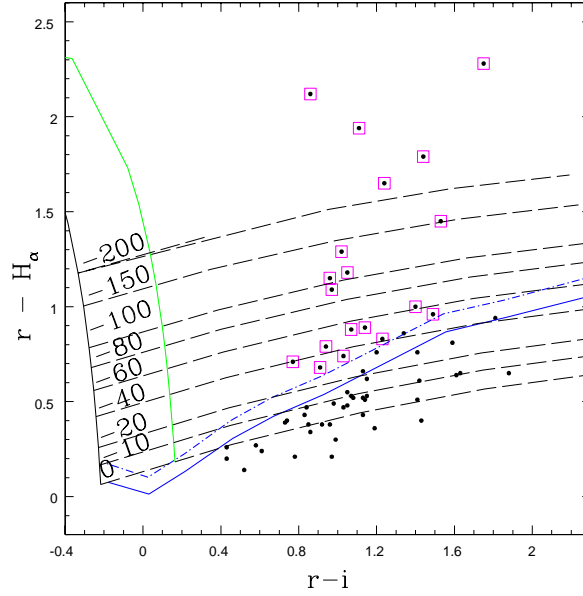


Figure 5.7: $(r-i)$ versus $(r-H_\alpha)$ CC diagram for all the sources detected in IPHAS photometry towards NGC 2282. The magenta crosses and green boxes are the H_α emission sources detected from slitless spectroscopy and IPHAS photometry, respectively. See text for increasing levels of H_α emission tracks, unreddened continuum and locus of main-sequence.

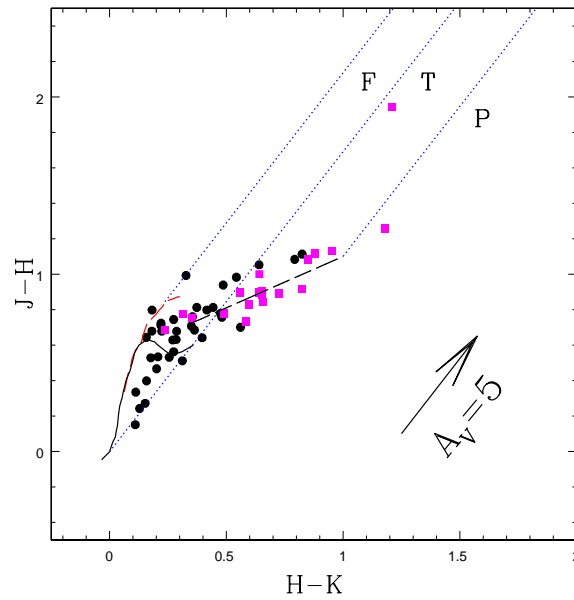


Figure 5.8: $(J-H)$ versus $(H-K)$ CC diagram of variable stars within $3.15'$ radius. The locus for dwarfs (solid black) and giants (green dashed line) are taken from Bessel & Brett (1988). The long dashed black line represents the CTTS locus (Meyer et al. 1997) and the small dashed blue lines represent the reddening vectors (Cohen et al. 1981). The reddening vector of visual extinction $A_V = 5$ mag is also shown (see text).

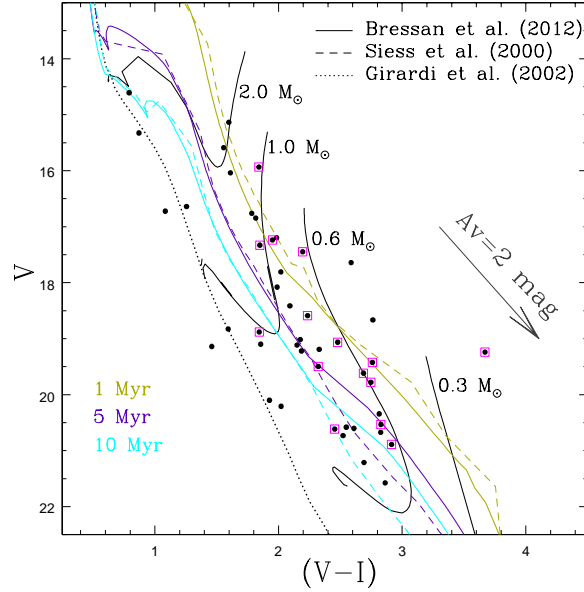


Figure 5.9: $V/(V - I)$ CMD for variable stars towards NGC 2282. All symbols are same as in Fig. 5.7. The thick solid curve is the locus of ZAMS from Girardi et al. (2002), dashed curves are the PMS isochrones of age 1.0, 2.0 and 5.0 Myr, respectively, and the thin solid curves are the evolutionary tracks for various mass bins from Siess et al. (2000). All the isochrones and tracks are corrected for the distance and reddening.

YSOs seem to be adequately fit between 1–10 Myr. Different models at the low-mass end differ significantly as we can see in Fig. 5.9. The average mass of the YSOs seems to be ~ 0.3 – $2.5 M_{\odot}$.

Spectral Energy distribution

The study of circumstellar environment of YSOs is important to understand the pre main-sequence evolution of stars. We constructed spectral energy distributions (SEDs) using the grid of models and fitting tools of Robitaille et al. (2006, 2007) for characterizing and understanding the nature of YSOs in NGC 2282 cluster. The grid consists of 20,000 YSO models at 10 viewing angles for each model, resulting in a total of 200,000 SEDs. The SED fitting tool fits multiwavelength data with those precomputed models and provides the evolutionary stage and physical parameters such as disc mass, disc accretion rate and stellar temperature of YSOs. Figure 5.4 displays sample SED for a variable source using the SED fitting tools. We obtained

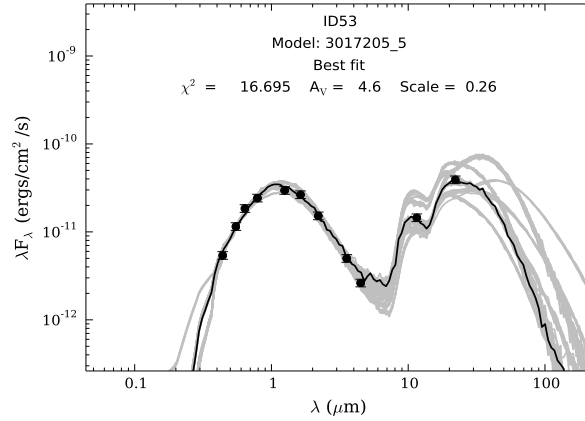


Figure 5.10: A sample SED for a variable source using the SED fitting tools of Robitaille et al. (2007). The solid black line shows the best fit and the grey lines show the subsequent well fits. The filled circles denote the input flux values.

the physical parameters of YSOs using the relative probability distribution for the stages of all the good-fit models. The well-fit models of each source are defined by $\chi^2 - \chi_{min}^2 \leq 3N_{data}$, where χ_{min} is the goodness of fit parameter for the best-fitting model and N_{data} is the number of input observational data points. From the well-fit models for each source derived from the SED fitting tool, we calculated the χ^2 weighted model parameters such as the average extinction (A_v), stellar mass (MASS), temperature (TEMP), stellar age (TIME), disc accretion rate (\dot{M}), mass of the disc (Mdisc), etc. The error in each parameter is calculated from the standard deviation of all well-fit parameters. The parameters and the corresponding errors of all the candidate variables are listed in Table 5.4. For some of the sources, the errors associated with few parameters (Table 5.4) are quite large because we are dealing with a large number of parameter space, with limited number of observational data points. Additional observational data points in longer wavelengths would help constrain these parameters more precisely. We compared mass and age estimations with V/(V-I) CMD, we found a notable difference. These could be due to unavailability of all complete all band measurements (See also section 3.3).

5.3.3 Period distribution

All variable stars are searched for periodicity; however, we were managed to estimate periods of $\sim 66\%$ stars. Figure 5.11 showed frequency distribution of rotation periods in NGC 2282 and compared with Orion nebula cluster (ONC) stars and NGC 2264 stars with the mass more than $0.25 M_{\odot}$. Herbst et al. (2000, 2002) found a bimodal distribution of periods persists for stars $> 0.25 M_{\odot}$ in ONC. But no such conclusive evidence was found for NGC 2264 cluster (Makidon et al. 2004). However, their study reaches fewer faint, low-mass stars as NGC 2264 is farther away than ONC. For NGC 2282 stars, the period distribution is unimodal, where fast rotators are peaking up at ~ 0.5 -1 days. Hartmann (2002) suggests that protostellar disk locking should leave the star in a rapidly rotating state, gradually spinning down during the T Tauri phase over the disk braking timescale. This implies that young stars may not be locked to their discs at early stages of their life. Herbst et al. (2002), performed a detailed study on ONC, argued that stars are released from their disk locking after ~ 1 Myr of age. However, Matt & Pudritz (2005) argued that the time taken to lock a star to its disk should be $< 4 \times 10^4$ yr. After a comparative study on ONC, Orion Flanking Fields and IC 348, Littlefair et al. (2005) concluded that disk locking takes effect at ~ 1 Myr, and at the age of ~ 3 Myr (IC 348) disk locking further removed fast rotator. However, the disk-locking theory could not explain the notable difference of period distribution for NGC 2264 and IC 348. The period distribution of NGC 2282 is strongly biased towards fast rotation side, and the lack of slow rotators is quite significant. Our sample mainly consists of stars with periods below four days. This contradiction can be explained by the fact that the phases of rapid accretion can dramatically increase the size and luminosity of a young star (e.g. Hartmann & Kenyon 1996; Kley & Lin 1999). Hence, a star would look much younger in a CMD than a non-accreting counterpart with the same initial mass and radius (Littlefair et al. 2011). However, some of the results of such period distribution may be effected from cluster environments like variability, extinction, and binarity, etc. (Littlefair et al. 2005, 2011).

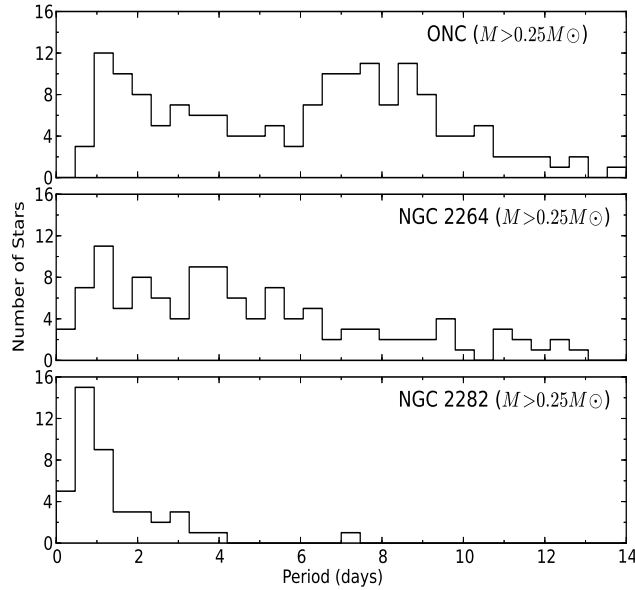


Figure 5.11: Distribution of periods in NGC 2282 are compared with the distributions for the ONC (Herbst et al. 2002) and NGC 2264 (Makidson et al. 2004). The bi-modal period distribution is seen in ONC and NGC 2264, while the distribution for NGC 2282 is uni-modal.

5.3.4 Correlation between IR excess and rotation periods and variability amplitude

From time-series photometric observational data on young (1-5 Myrs.) star-forming regions, several authors have investigated any possible correlations between rotation periods of PMS stars and the presence of circumstellar disks using IR excess and H_{α} emissions. Results show compelling evidence for significant differences in rotation periods between stars with circumstellar disks and those lacking disks and others studies do not have any conclusive evidence (e.g. Rebull 2001; Herbst et al. 2002; Carpenter et al. 2002; Makidon 2004; Lamm et al. 2005; Rebull et al. 2006; Cieza & Baliber 2007; Biazzo et al. 2009; Nguyen et al. 2009; Rodriguez-Ledesma et al. 2010; Rice et al. 2015; Cody & Hillenbrand et al. 2010).

For understanding the correlation of NIR excess and rotation rates of our periodic/aproperiodic variables, we have used an index (I-K) as defined by Hillendrand et al. (1998) and used by several authors (e.g. Herbst et al. 2002 Makidon 2004; Rodriguez-Ledesma et al. 2010). I-

band fluxes are thought to be dominated by pure photospheric emission, while K-band fluxes can have additional fluxes from circumstellar disk, if any (Hillenbrand et al. 1998; Rodriguez-Ledesma et al. 2010). The (I-K) index being longer wavelength base provides more pronounced excess compared to other NIR indices (e.g. (J-H) or (H-K)). The NIR excess from (I-K) color defined by Hillenbrand et al. (1998) and same used by others (e.g. Herbst et al. 2002; Makidon et al. 2004; Rodriguez-Ledesma et al. 2010), could be written as,

$$\Delta(I - K) = (I - K)_{obs} - (A_I - A_K) - (I - K)_o \quad (5.3)$$

Where $(I-K)_{obs}$ is the observed magnitudes; A_I and A_K are interstellar extinctions in I and K-bands respectively. $(I-K)_o$ is the intrinsic color of a star. Without knowledge of spectral types, the intrinsic color is difficult to measure and this is the case for our variables. However, it could be estimated from photometric measurements, extinction, and theoretical isochrones. Following Rodriguez-Ledesma et al. 2010, first, we have measured the intrinsic colors $(I-J)_o$ as it is expected to be originating from photospheric emission from observed $(I - J)$ colors corrected by the average extinction of $A_v = 1.65$ mag as estimated in Paper I. Using the Baraffe et al. (1998) color information of NGC 2282 and mean age of 3 Myrs (Paper I), we estimated the intrinsic color $(I-K)_o$ from $(I-J)_o$. The NIR excess $\Delta(I - K)$ are calculated using Eqn. 5.3 for individual variables.

To search possible correlation between rotation rates and NIR excess we have plotted period versus disk indicator as an NIR excess $\Delta(I - K)$. As in previous authors (e.g. Herbst et al. 2002; Makidon et al. 2004; Rodriguez-Ledesma et al. 2010), the value of $\Delta(I - K) = 0.3$ mag is adopted here for separating disk and disk-less stars. Out of total 41 periodic variables, we don't have any K-band measurements for two objects. We have plotted data for 39 periodic variables in the upper panel of Fig.5.12 (upper panel), where 16 objects show NIR excess for the adopted criterion above for $\Delta(I - K)$. We have 15 H_α emitting periodic variables that marked in Fig 5.12. These H_α emitting sources are picked up from slitless spectroscopy and IPHAS

photometry, which is described elsewhere (Sec. 3.2.1). NIR excess is used for the presence of near-photospheric circumstellar dust, while H_{α} emission is commonly used as an indicator of accretion in T-Tauri stars. A remarkable correlation between accretion indicators as H_{α} emission and NIR excess are visible in Fig.5.12, where out of 16 NIR excess sources, majority 10 objects show H_{α} emission. The similar correlation between H_{α} emission line widths and NIR excess has been reported earlier in the literature (e.g. Sicilia-Aguilar et al. 2005, 2006; Bazio et al. 2009). These H_{α} emitting sources with NIR excess could be CTTSs candidates, while others diskless WTTS candidates. We found the disk fraction of about 41% among periodic variables from NIR excess analysis. Since we have longer wavelengths Spitzer data on IRAC bands 3.6 and 4.5 μm on NGC 2282 as mentioned before, these could be used for probing better disk indicator than NIR wavelengths (Lada et al. 2000; Rodgriguez-Ledesma et al. 2010). However, nebular PAH emission on the central part of the cluster might be problematic sometimes at IRAC bands (Gutermuth et al. 2009). Among 41 periodic variables, 33 variables have mid-IR data. In lower panel of Fig.5.12, we have plotted the period versus Spitzer IRAC color [3.6]-[4.5] for all 33 variables; and as we see population of variables close to [3.6]-[4.5] ≈ 0 indicating diskless bare photospheric color (Patten et al. 2006). The color of [3.6]-[4.5] > 0.7 and > 0.15 indicates Class 1 and Class II sources respectively (Gutermuth et al. 2008; 2009). We adopt conservatively here the color of [3.6]-[4.5] > 0.25 criterion for the disked stars as shown in Fig.5.12 (lower panel). We found relatively higher disk fraction of $\sim 51\%$ from mid-IR data. This is somewhat less than with earlier estimation of $\sim 58\%$ for all PMS stars (Paper I). For our sample in Fig.5.12, we do not have any conclusive evidence of relatively longer periods for disked stars compared to that of diskless stars, which is an indicator of the disk-locking system as studied before in the literature. This finding could be related to the age of NGC 2282, as it is relatively old (2–3 Myrs), and such disk-locking systems may be efficient at the young age of ~ 1 Myr. or less as suggested by several authors and already described in earlier section 3.3. Here we have analyzed whether there is any correlation between variability amplitude of the periodic/aproperiodic variables and IR excess using $\Delta(I - K)$ and [3.6]-[4.5] as stated in the above

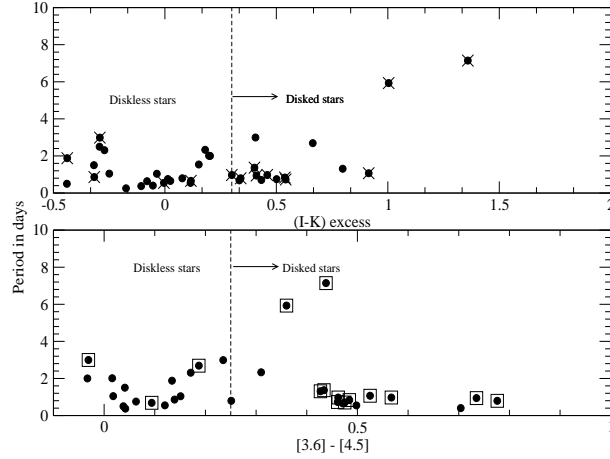


Figure 5.12: Periods are plotted as a function of disk indicator NIR excess $\Delta(I - K)$ (upper panel) and mid-IR excess $[3.6] - [4.5]$ (lower panel) for periodic variables. The vertical solid lines of $\Delta(I - K) = 0.3$ and $[3.6]-[4.5]=0.25$ are adopted for the boundary of diskless and disked stars. No conclusive trends are seen for disk-locking mechanism.

section. We have total 62 variables, and 51 have both $[3.6]$ and $[4.5]$ measurements. In Fig. 5.13, we have plotted the variability amplitude from the light curve RMS versus NIR excess $\Delta(I - K)$ (upper panel) and mid-IR excess $[3.6]-[4.5]$ (lower panel). It seems that there is a clear trend of increasing variability amplitude with IR excess seen in Fig.5.13.

5.3.5 Correlation between periods and masses

To investigate any correlation between rotation periods and masses, we analyzed here the rotation periods as a function of stellar masses for periodic variables in NGC 2282 in Fig.5.14. To estimate masses from I-band magnitudes and mean cluster extinction ($A_v=1.65$ mag), we have used 3 Myr theoretical isochrones from Baraffe et al. (1998). The estimated masses range from $0.1 M_{\odot}$ to $2.5 M_{\odot}$. The mass determination is quite uncertain at these young ages. Furthermore, the lower mass limit of $0.1 M_{\odot}$ lies near to $I \sim 20.5$ mag, where the light curves lose enough sensitivity to detect any variability from our dataset. For comparison, we have plotted the period distribution with masses in NGC 2362 (~ 5 Myr), taken from Irwin et al. (2008). From Fig.5.14, it is apparent that the period distribution of masses shows a sloping mass dependence of the rotation periods in NGC 2282 (~ 3 Myr). However, our periodic variables

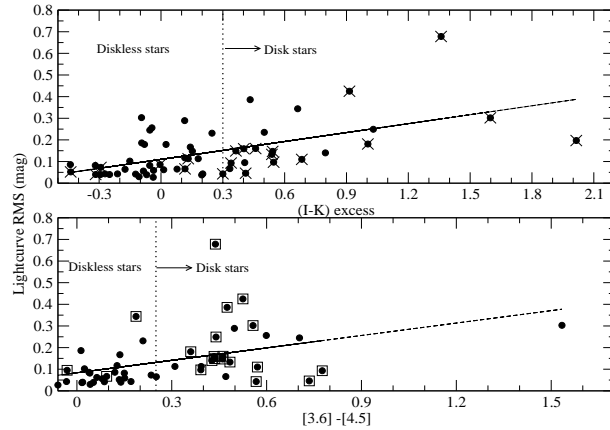


Figure 5.13: The light curves RMS (variability amplitude) are plotted as a function of disk indicator NIR excess $\Delta(I - K)$ (upper panel) and mid-IR excess $[3.6]-[4.5]$ (lower panel) for periodic and aperiodic variables. The vertical solid lines of $\Delta(I - K) = 0.3$ and $[3.6]-[4.5]=0.25$ are adopted for the boundary of diskless and disked stars. The grey line shows the clear increasing trend of RMS with infrared excess.

detection did not enough sensitive at the lower mass close to $0.3 M_{\odot}$, and the result has to be taken with caution.

Our result agrees with the findings in the literature (e.g. Irwin et al. 2008; Coker et al. 2016 and reference therein). These authors found that an age evolutionary sequence of the mass dependence of the rotation periods. Fig. 12 of Irwin et al. (2008) shows a flat mass dependence of the rotation periods in the ONC (~ 1 Myr), while a sloping relation at the lower mass-end in NGC 2264 (~ 2 Myr) and 2362 (~ 5 Myr), and a more increasingly slope at the more older ages of NGC 2547 (~ 40 Myr) and NGC 2516 (~ 150 Myr). The picture brings out that the low-mass stars have a relatively long timescale for angular momentum evolution (Coker et al. 2016).

5.4 Summary and Conclusions

In this chapter, we present deep I -band (~ 20.5 mag) monitoring studies of stars towards a young (2–5 Myr) cluster NGC 2282 in Monoceros constellation to understand variability

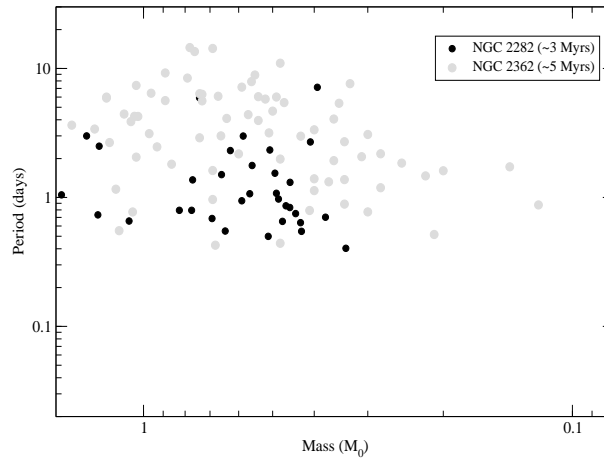


Figure 5.14: Mass versus period is plotted for periodic variables. From our detection limit, periodic variables are identified upto low mass limit of $> 0.25 M_{\odot}$, and a systematic trend for fast rotators at low mass-end might be real feature as seen in other few regions (see Irwin et al. 2008.)

characteristics of towards the low-mass end of PMS stars. Our main results are summarized as follows:

1. From differential photometry light curves of 1627 stars, we have identified 62 new photometric variable stars. Out of 62 variables, 41 are periodic variables and show the rotation periods from 0.2 to 7 days.
2. From H_{α} emission activities, J–H/H–K CC diagram, IR excess, and paper I, we found majority variable stars are members of the cluster. Spatial distribution of variables shows that majority of them located at the NGC 2282 region clustering around the core.
3. The period distribution shows a median period around ~ 1 day as seen in other young clusters (e.g. NGC 2264, ONC, etc.). It shows a unimodal distribution like others; but younger like ONC has a bimodal distribution with slow rotators peaking at ~ 6 –8 days.
4. To understand disk-locking hypothesis in young PMS though rotation-disk connection, we have derived NIR excess from $\Delta(I-K)$ and mid-IR excess from *Spitzer* $[3.6] - [4.5] \mu\text{m}$ data. No conclusive evidence of slow rotation with disk stars and fast rotation for diskless stars is seen from the periodic variables in NGC 2282.

5. Furthermore, to investigate variability-disk connection, we have studied near-infrared (NIR) excess, and mid-IR excess from *Spitzer* data with variability amplitude (RMS) derived from the light curves. A clear increasing trend of variability amplitude with IR excess is seen for all periodic/aproperiodic variables.
6. Disk fraction among periodic variables are studied using NIR and mid-IR excess as discussed, we estimated disk fraction of $\sim 51\%$ for all periodic/aproperiodic variables, while $\sim 41\%$ for periodic variables. This estimation is slightly less than 58% of whole cluster population as studied by us before (Paper I).
7. To understand fast rotation in the lower mass end of PMS stars, the period-mass correlation in the mass range $0.3\text{--}1.6 M_{\odot}$ are studied. It is apparent from our analysis that there is an evidence of relatively fast rotation with decreasing masses (sloping relation) as seen in the literature (Irwin et al. 2008; Coker et al. 2016). However, our periodic variables detection is not sensitive enough at lower mass beyond $0.3 M_{\odot}$, the result needs to be taken with caution.
8. We estimated different parameters of the candidate variable stars from V/V-I CMD and SED analysis.

Table 5.2: Catalog of the identified variable stars adopted from Paper I

ID	α_{2000} (deg)	δ_{2000} (deg)	B (mag)	V (mag)	R (mag)	I (mag)	J (mag)	H (mag)	K (mag)	3.6 μm (mag)	4.5 μm (mag)	W1 (mag)	W2 (mag)
8	101.735121	1.277934	16.971 ± 0.012	15.934 ± 0.013	14.935 ± 0.007	14.189 ± 0.003	12.061 ± 0.023	11.212 ± 0.020	10.572 ± 0.023	9.616 ± 0.003	9.049 ± 0.002	4.189 ± 0.015	1.079 ± 0.021
16	101.697027	1.251858	17.546 ± 0.049	16.037 ± 0.043	15.260 ± 0.039	14.314 ± 0.046	12.930 ± 0.026	12.423 ± 0.034	12.075 ± 0.034	12.083 ± 0.004	99.999 ± 99.999	10.109 ± 0.092	7.073 ± 0.160
38	101.681203	1.275360	15.257 ± 0.007	14.608 ± 0.008	14.147 ± 0.009	13.876 ± 0.005	13.306 ± 0.030	12.956 ± 0.001	12.952 ± 0.044	12.842 ± 0.008	12.826 ± 0.009	9.541 ± 0.093	7.619 ± 0.203
52	101.679695	1.290380	19.691 ± 0.020	17.640 ± 0.004	16.207 ± 0.009	14.898 ± 0.006	12.795 ± 0.020	11.770 ± 0.026	11.406 ± 0.023	11.121 ± 0.003	11.154 ± 0.004	11.955 ± 99.999	8.283 ± 99.999
53	101.715712	1.307466	16.823 ± 0.008	15.588 ± 0.004	14.729 ± 0.007	13.999 ± 0.003	12.775 ± 0.026	12.126 ± 0.028	11.936 ± 0.030	11.688 ± 0.004	11.646 ± 0.005	6.786 ± 99.999	3.643 ± 0.119
54	101.723024	1.310400	18.770 ± 0.013	17.447 ± 0.005	16.363 ± 0.009	17.674 ± 0.009	13.677 ± 0.026	12.644 ± 0.026	11.958 ± 0.027	10.761 ± 0.003	10.026 ± 0.002	99.999 ± 99.999	99.999 ± 99.999
55	101.714484	1.319228	99.999 ± 99.999	16.760 ± 0.072	16.161 ± 0.008	17.549 ± 0.020	13.439 ± 0.036	12.624 ± 0.027	12.409 ± 0.033	12.229 ± 0.004	12.058 ± 0.006	99.999 ± 99.999	99.999 ± 99.999
58	101.718528	1.316127	16.417 ± 0.014	15.134 ± 0.011	14.292 ± 0.012	13.575 ± 0.004	12.280 ± 0.029	11.593 ± 0.033	11.379 ± 0.033	11.219 ± 0.003	11.139 ± 0.004	99.999 ± 99.999	99.999 ± 99.999
60	101.705423	1.316671	18.720 ± 0.007	17.198 ± 0.003	16.228 ± 0.008	15.274 ± 0.005	13.677 ± 0.028	12.919 ± 0.034	12.609 ± 0.035	12.398 ± 0.009	12.247 ± 0.007	7.873 ± 0.154	4.513 ± 0.073
62	101.690142	1.321381	18.318 ± 0.007	16.846 ± 0.005	15.825 ± 0.008	14.979 ± 0.004	13.703 ± 0.026	12.968 ± 0.027	12.714 ± 0.032	12.581 ± 0.005	12.518 ± 0.007	99.999 ± 99.999	99.999 ± 99.999
115	101.715745	1.311569	18.344 ± 0.059	17.237 ± 0.037	16.215 ± 0.010	15.270 ± 0.008	13.781 ± 0.002	13.028 ± 0.001	12.695 ± 0.072	12.468 ± 0.006	12.334 ± 0.007	99.999 ± 99.999	99.999 ± 99.999
226	101.759810	1.249410	22.631 ± 0.165	20.581 ± 0.049	19.614 ± 0.050	18.026 ± 0.058	16.222 ± 0.011	15.355 ± 0.008	14.921 ± 0.011	14.421 ± 0.020	99.999 ± 99.999	11.465 ± 0.224	8.700 ± 99.999
279	101.749052	1.259269	20.304 ± 0.030	18.666 ± 0.016	17.328 ± 0.014	15.965 ± 0.009	14.230 ± 0.002	13.653 ± 0.002	13.387 ± 0.003	13.056 ± 0.008	99.999 ± 99.999	99.999 ± 99.999	99.999 ± 99.999
321	101.719373	1.292577	20.811 ± 0.037	19.190 ± 0.013	17.365 ± 0.008	16.448 ± 0.008	15.042 ± 0.004	13.832 ± 0.002	12.973 ± 0.002	11.412 ± 0.003	10.972 ± 0.003	6.696 ± 0.061	5.079 ± 0.143
363	101.759568	1.306980	99.999 ± 99.999	21.575 ± 0.061	19.667 ± 0.056	18.182 ± 0.025	15.855 ± 0.008	14.678 ± 0.005	13.852 ± 0.005	12.626 ± 0.006	12.199 ± 0.006	99.999 ± 99.999	99.999 ± 99.999
364	101.762999	1.308987	99.999 ± 99.999	20.603 ± 0.056	19.877 ± 0.062	18.299 ± 0.044	15.653 ± 0.007	14.770 ± 0.005	14.308 ± 0.007	13.212 ± 0.009	12.714 ± 0.008	99.999 ± 99.999	99.999 ± 99.999
366	101.753455	1.321061	20.504 ± 0.022	19.099 ± 0.008	17.974 ± 0.012	17.170 ± 0.015	15.797 ± 0.008	15.060 ± 0.006	14.827 ± 0.010	14.755 ± 0.029	14.605 ± 0.023	99.999 ± 99.999	99.999 ± 99.999
382	101.786648	1.327160	20.782 ± 0.030	19.114 ± 0.008	17.921 ± 0.012	16.968 ± 0.012	15.316 ± 0.005	14.490 ± 0.004	14.120 ± 0.006	13.472 ± 0.010	13.221 ± 0.011	10.354 ± 0.172	8.302 ± 99.999
390	101.772999	1.335246	22.510 ± 0.125	20.532 ± 0.018	18.557 ± 0.019	17.202 ± 0.013	15.742 ± 0.007	14.563 ± 0.004	13.678 ± 0.004	12.428 ± 0.005	12.068 ± 0.006	9.943 ± 0.114	7.116 ± 0.197
480	101.631159	1.289772	17.534 ± 0.004	16.723 ± 0.003	16.144 ± 0.011	15.747 ± 0.007	14.899 ± 0.003	14.536 ± 0.004	14.419 ± 0.008	14.390 ± 0.019	14.303 ± 0.020	11.852 ± 99.999	8.826 ± 99.999
506	101.631642	1.296466	20.213 ± 0.021	19.140 ± 0.008	18.408 ± 0.016	17.956 ± 0.028	16.553 ± 0.013	16.120 ± 0.016	15.955 ± 0.029	15.823 ± 0.064	15.785 ± 0.054	99.999 ± 99.999	99.999 ± 99.999
521	101.626837	1.305785	20.003 ± 0.017	18.828 ± 0.005	18.082 ± 0.019	17.451 ± 0.020	16.053 ± 0.009	15.546 ± 0.010	15.336 ± 0.017	15.236 ± 0.035	15.195 ± 0.042	99.999 ± 99.999	99.999 ± 99.999
566	101.718819	1.299192	21.513 ± 0.104	20.343 ± 0.059	18.755 ± 0.021	17.345 ± 0.021	15.169 ± 0.005	14.149 ± 0.003	13.642 ± 0.004	13.000 ± 0.009	12.906 ± 0.010	99.999 ± 99.999	99.999 ± 99.999
571	101.720487	1.315683	20.523 ± 0.097	18.589 ± 0.035	99.999 ± 99.999	16.354 ± 0.008	14.790 ± 0.003	13.816 ± 0.002	13.150 ± 0.003	12.095 ± 0.005	11.703 ± 0.005	99.999 ± 99.999	99.999 ± 99.999
575	101.720311	1.313621	99.999 ± 99.999	19.778 ± 0.078	99.999 ± 99.999	17.76 ± 0.021	15.311 ± 0.005	14.097 ± 0.003	13.182 ± 0.003	11.892 ± 0.004	11.367 ± 0.004	99.999 ± 99.999	99.999 ± 99.999
578	101.712067	1.305554	21.335 ± 0.067	19.425 ± 0.026	18.137 ± 0.012	19.061 ± 0.026	14.470 ± 0.003	13.627 ± 0.002	13.115 ± 0.003	12.394 ± 0.006	12.001 ± 0.006	6.478 ± 0.064	3.536 ± 0.039
581	101.714753	1.311102	18.232 ± 0.056	17.330 ± 0.029	16.641 ± 0.009	18.140 ± 0.016	14.159 ± 0.002	13.414 ± 0.002	13.167 ± 0.003	12.902 ± 0.008	12.763 ± 0.009	99.999 ± 99.999	99.999 ± 99.999
603	101.703739	1.320896	20.628 ± 0.035	19.063 ± 0.011	17.607 ± 0.011	16.540 ± 0.009	14.567 ± 0.003	13.569 ± 0.002	12.711 ± 0.002	11.835 ± 0.003	11.264 ± 0.004	7.860 ± 99.999	4.835 ± 0.062
625	101.731974	1.307462	22.385 ± 0.136	20.889 ± 0.055	19.250 ± 0.034	18.063 ± 0.028	15.766 ± 0.007	14.784 ± 0.005	14.104 ± 0.006	12.784 ± 0.007	12.322 ± 0.007	99.999 ± 99.999	99.999 ± 99.999
629	101.742782	1.320963	21.191 ± 0.051	19.498 ± 0.013	18.645 ± 0.018	17.367 ± 0.018	15.197 ± 0.005	14.222 ± 0.003	13.641 ± 0.004	12.728 ± 0.007	12.292 ± 0.006	99.999 ± 99.999	99.999 ± 99.999

N.B. The value '99.999' represent the absence of the particular magnitude.

ID	α_{2000} (deg)	δ_{2000} (deg)	<i>B</i> (mag)	<i>V</i> (mag)	<i>R</i> (mag)	<i>I</i> (mag)	<i>J</i> (mag)	<i>H</i> (mag)	<i>K</i> (mag)	3.6 μ m (mag)	4.5 μ m (mag)	W2 (mag)	W3 (mag)
636	101.756456	1.334327	19.582 \pm 0.012	18.079 \pm 0.004	17.101 \pm 0.007	16.062 \pm 0.009	14.622 \pm 0.003	13.936 \pm 0.002	13.639 \pm 0.004	13.338 \pm 0.010	13.286 \pm 0.009	99.999 \pm 99.999	99.999 \pm 99.999
642	101.761370	1.338316	20.979 \pm 0.034	19.220 \pm 0.008	18.257 \pm 0.014	17.178 \pm 0.013	15.326 \pm 0.005	14.443 \pm 0.004	14.054 \pm 0.005	13.613 \pm 0.011	13.486 \pm 0.012	9.251 \pm 0.047	6.040 \pm 0.072
644	101.768647	1.344268	20.213 \pm 0.019	18.882 \pm 0.008	18.374 \pm 0.018	17.396 \pm 0.018	16.088 \pm 0.010	14.724 \pm 0.005	13.497 \pm 0.003	12.051 \pm 0.004	11.494 \pm 0.004	8.587 \pm 0.032	6.507 \pm 0.059
652	101.722476	1.333859	19.882 \pm 0.018	18.414 \pm 0.008	17.855 \pm 0.012	16.584 \pm 0.010	14.538 \pm 0.003	13.716 \pm 0.002	13.215 \pm 0.003	12.376 \pm 0.006	12.240 \pm 0.007	99.999 \pm 99.999	99.999 \pm 99.999
654	101.720359	1.341991	99.999 \pm 99.999	21.212 \pm 0.054	20.040 \pm 0.067	18.388 \pm 0.025	16.591 \pm 0.015	15.447 \pm 0.009	14.780 \pm 0.010	13.759 \pm 0.014	13.572 \pm 0.014	99.999 \pm 99.999	99.999 \pm 99.999
677	101.749821	1.365127	21.058 \pm 0.044	19.616 \pm 0.013	18.549 \pm 0.020	17.123 \pm 0.015	14.849 \pm 0.004	13.930 \pm 0.002	13.246 \pm 0.003	12.288 \pm 0.005	11.854 \pm 0.005	9.620 \pm 0.059	7.737 \pm 0.185
841	101.712858	1.366399	15.900 \pm 0.004	15.326 \pm 0.002	14.911 \pm 0.007	14.575 \pm 0.004	13.919 \pm 0.002	13.755 \pm 0.002	13.640 \pm 0.004	13.489 \pm 0.010	13.549 \pm 0.012	9.887 \pm 0.097	7.177 \pm 0.124
976	101.818492	1.338385	17.431 \pm 0.004	16.640 \pm 0.003	15.993 \pm 0.008	15.449 \pm 0.007	14.515 \pm 0.003	14.220 \pm 0.003	14.061 \pm 0.005	13.909 \pm 0.014	13.891 \pm 0.016	99.999 \pm 99.999	99.999 \pm 99.999
998	101.794092	1.352774	19.320 \pm 0.028	17.809 \pm 0.025	16.803 \pm 0.031	15.796 \pm 0.020	14.982 \pm 0.004	14.299 \pm 0.003	14.017 \pm 0.005	13.300 \pm 0.009	13.331 \pm 0.011	12.321 \pm 99.999	8.917 \pm 99.999
999	101.787683	1.334398	21.760 \pm 0.065	20.614 \pm 0.028	19.691 \pm 0.048	18.180 \pm 0.040	16.114 \pm 0.010	15.148 \pm 0.007	14.393 \pm 0.007	13.635 \pm 0.010	13.151 \pm 0.010	10.064 \pm 0.071	7.569 \pm 0.241
1060	101.804179	1.368557	20.468 \pm 0.024	19.016 \pm 0.009	17.942 \pm 0.012	16.859 \pm 0.013	15.299 \pm 0.005	14.453 \pm 0.004	13.958 \pm 0.005	13.398 \pm 0.010	13.189 \pm 0.010	11.431 \pm 0.404	8.209 \pm 0.335
1144	101.731542	1.286178	21.692 \pm 0.094	19.240 \pm 0.062	17.941 \pm 0.048	16.113 \pm 0.037	12.027 \pm 0.035	9.979 \pm 0.028	8.709 \pm 0.021	99.999 \pm 99.999	99.999 \pm 99.999	4.028 \pm 0.016	1.666 \pm 0.021
1194	101.760852	1.261733	22.247 \pm 0.102	20.732 \pm 0.038	19.509 \pm 0.050	18.104 \pm 0.062	16.759 \pm 0.017	16.022 \pm 0.015	15.723 \pm 0.022	99.999 \pm 99.999	99.999 \pm 99.999	99.999 \pm 99.999	99.999 \pm 99.999
1244	101.679135	1.348597	21.549 \pm 0.070	20.101 \pm 0.033	19.194 \pm 0.061	18.289 \pm 0.047	17.166 \pm 0.025	16.586 \pm 0.025	16.370 \pm 0.041	99.999 \pm 99.999	99.999 \pm 99.999	99.999 \pm 99.999	99.999 \pm 99.999
1366	101.717136	1.316972	99.999 \pm 99.999	99.999 \pm 99.999	16.097 \pm 0.025	17.689 \pm 0.045	13.767 \pm 0.002	13.040 \pm 0.001	12.412 \pm 0.002	12.757 \pm 0.006	12.176 \pm 0.006	99.999 \pm 99.999	99.999 \pm 99.999
1876	101.726996	1.298998	99.999 \pm 99.999	99.999 \pm 99.999	20.101 \pm 0.063	18.539 \pm 0.048	16.262 \pm 0.011	15.194 \pm 0.007	14.628 \pm 0.009	14.477 \pm 0.026	14.002 \pm 0.021	99.999 \pm 99.999	99.999 \pm 99.999
2286	101.717945	1.311399	99.999 \pm 99.999	99.999 \pm 99.999	19.066 \pm 0.047	17.492 \pm 0.032	15.486 \pm 0.006	14.644 \pm 0.004	14.314 \pm 0.007	13.950 \pm 0.016	13.830 \pm 0.018	99.999 \pm 99.999	99.999 \pm 99.999
2301	101.718028	1.314145	99.999 \pm 99.999	99.999 \pm 99.999	99.999 \pm 99.999	17.914 \pm 0.04	16.079 \pm 0.010	15.382 \pm 0.008	14.969 \pm 0.012	14.462 \pm 0.026	13.863 \pm 0.018	99.999 \pm 99.999	99.999 \pm 99.999
2303	101.716874	1.314099	99.999 \pm 99.999	99.999 \pm 99.999	16.809 \pm 0.052	15.948 \pm 0.047	14.379 \pm 0.003	13.419 \pm 0.002	12.741 \pm 0.002	11.734 \pm 0.004	11.273 \pm 0.004	99.999 \pm 99.999	99.999 \pm 99.999
2319	101.708042	1.316467	99.999 \pm 99.999	99.999 \pm 99.999	99.999 \pm 99.999	18.739 \pm 0.045	16.729 \pm 0.017	15.985 \pm 0.014	15.606 \pm 0.020	14.729 \pm 0.031	14.025 \pm 0.022	99.999 \pm 99.999	99.999 \pm 99.999
2329	101.712510	1.313155	99.999 \pm 99.999	99.999 \pm 99.999	18.231 \pm 0.040	17.112 \pm 0.028	15.636 \pm 0.007	14.838 \pm 0.005	14.230 \pm 0.006	12.626 \pm 0.007	11.850 \pm 0.005	99.999 \pm 99.999	99.999 \pm 99.999
2337	101.714569	1.306385	99.999 \pm 99.999	99.999 \pm 99.999	17.418 \pm 0.010	16.353 \pm 0.007	14.876 \pm 0.004	14.060 \pm 0.003	13.693 \pm 0.004	12.827 \pm 0.008	12.356 \pm 0.007	99.999 \pm 99.999	99.999 \pm 99.999
2363	101.666431	1.314573	99.999 \pm 99.999	99.999 \pm 99.999	99.999 \pm 99.999	17.762 \pm 99.999	16.459 \pm 0.013	15.848 \pm 0.013	15.562 \pm 0.020	15.342 \pm 0.040	15.329 \pm 0.041	99.999 \pm 99.999	99.999 \pm 99.999
2424	101.721067	1.318456	99.999 \pm 99.999	99.999 \pm 99.999	20.380 \pm 0.093	19.398 \pm 0.143	16.772 \pm 0.017	16.003 \pm 0.015	15.638 \pm 0.021	16.573 \pm 0.138	15.039 \pm 0.040	99.999 \pm 99.999	99.999 \pm 99.999
2444	101.722041	1.330434	99.999 \pm 99.999	99.999 \pm 99.999	19.980 \pm 0.070	18.458 \pm 0.041	17.357 \pm 0.029	16.131 \pm 0.017	15.139 \pm 0.014	13.800 \pm 0.015	13.362 \pm 0.013	99.999 \pm 99.999	99.999 \pm 99.999
2692	101.641386	1.352463	99.999 \pm 99.999	99.999 \pm 99.999	17.099 \pm 0.021	16.681 \pm 0.019	15.512 \pm 0.006	14.938 \pm 0.006	14.754 \pm 0.010	14.516 \pm 0.021	14.492 \pm 0.023	99.999 \pm 99.999	99.999 \pm 99.999
3045	101.766597	1.389371	99.999 \pm 99.999	99.999 \pm 99.999	99.999 \pm 99.999	17.973 \pm 0.01	16.066 \pm 0.009	15.305 \pm 0.008	14.721 \pm 0.009	14.095 \pm 0.016	13.785 \pm 0.014	99.999 \pm 99.999	99.999 \pm 99.999
3954	101.629350	1.267540	99.999 \pm 99.999	99.999 \pm 99.999	19.171 \pm 0.083	18.239 \pm 0.088	17.466 \pm 0.030	16.692 \pm 0.027	16.463 \pm 0.046	99.999 \pm 99.999	99.999 \pm 99.999	99.999 \pm 99.999	99.999 \pm 99.999
4753	101.658233	1.394522	99.999 \pm 99.999	99.999 \pm 99.999	18.791 \pm 0.030	17.948 \pm 0.049	16.845 \pm 0.017	16.286 \pm 0.019	15.945 \pm 0.029	99.999 \pm 99.999	99.999 \pm 99.999	99.999 \pm 99.999	99.999 \pm 99.999
6001	101.621500	1.241976	99.999 \pm 99.999	99.999 \pm 99.999	15.731 \pm 0.012	15.348 \pm 0.008	14.496 \pm 0.003	14.233 \pm 0.003	14.099 \pm 0.006	99.999 \pm 99.999	99.999 \pm 99.999	11.463 \pm 99.999	8.470 \pm 0.404
6002	101.817056	1.243599	99.999 \pm 99.999	99.999 \pm 99.999	18.481 \pm 0.021	17.785 \pm 0.026	15.990 \pm 0.009	15.400 \pm 0.008	15.122 \pm 0.013	15.066 \pm 0.035	99.999 \pm 99.999	12.480 \pm 99.999	8.960 \pm 99.999
6003	101.804790	1.233050	21.879 \pm 0.106	20.208 \pm 0.029	19.153 \pm 0.043	18.041 \pm 0.067	17.134 \pm 0.022	16.545 \pm 0.021	16.219 \pm 0.034	99.999 \pm 99.999	99.999 \pm 99.999	99.999 \pm 99.999	99.999 \pm 99.999
6004	101.809540	1.387650	22.231 \pm 0.097	20.674 \pm 0.042	19.002 \pm 0.050	17.744 \pm 0.046	16.892 \pm 0.019	16.171 \pm 0.017	15.923 \pm 0.027	99.999 \pm 99.999	99.999 \pm 99.999	99.999 \pm 99.999	99.999 \pm 99.999

Table 5.3: Result of our analysis : periods, membership characteristics, IR excess, masses of the identified variable stars.

ID	I* (mag)	I _{err} (mag)	RMS (mag)	H _α ** (emission Y/N)	Period (days)	PMS from Paper I (Yes/No)	Δ(I-K) (mag)	[3.6]-[4.5] (mag)	mass*** (M _⊙)
8	14.189	0.003	0.043	Y	0.972	Yes	0.300	0.567	2.43
16	14.314	0.046	0.064	N	0.254	No	-0.174	...	2.33
38	13.876	0.005	0.038	N	...	No	0.197	0.016	2.69
52	14.898	0.006	0.043	N	...	No	0.202	-0.033	1.90
53	13.999	0.003	0.03	N	0.373	No	-0.106	0.042	2.58
54	17.674	0.009	0.046	Y	0.942	Yes	0.410	0.735	0.59
55	17.549	0.02	0.043	N	2.309	No	-0.271	0.171	0.63
58	13.575	0.004	0.056	N	...	No	-0.085	0.08	2.96
60	15.274	0.005	0.059	N	1.039	No	-0.036	0.151	1.66
62	14.979	0.004	0.062	N	0.754	No	0.013	0.063	1.84
115	15.27	0.008	0.052	Y	1.879	Yes	-0.438	0.134	1.66
226	18.026	0.058	0.148	N	1.54	No	0.152	...	0.49
279	15.965	0.009	0.04	N	2.497	No	-0.293	...	1.27
321	16.448	0.008	0.249	N	...	Yes	1.030	0.44	1.04
363	18.182	0.025	0.14	N	1.309	Yes	0.797	0.427	0.45
364	18.299	0.044	0.289	N	0.546	Yes	0.114	0.498	0.43
366	17.17	0.015	0.082	N	...	No	-0.054	0.15	0.75
382	16.968	0.012	0.065	N	0.794	Yes	0.077	0.251	0.82
390	17.202	0.013	0.181	Y	...	Yes	1.003	0.36	0.74
480	15.747	0.007	0.042	N	...	No	-0.122	0.087	1.38
506	17.956	0.028	0.086	N	0.499	No	-0.439	0.038	0.51
521	17.451	0.02	0.082	N	1.502	No	-0.318	0.041	0.65
566	17.345	0.021	0.067	N	0.686	No	0.333	0.094	0.69
571	16.35	0.01	0.097	Y	3.754	Yes	0.546	0.392	1.08
575	17.76	0.021	0.425	Y	1.066	Yes	0.914	0.525	0.56
578	19.061	0.026	0.113	Y	...	Yes	0.132	0.393	0.28
581	18.14	0.016	0.04	Y	0.861	Yes	-0.317	0.139	0.46
603	16.54	0.009	0.11	Y	...	Yes	0.683	0.571	0.99
625	18.063	0.028	0.16	Y	0.972	Yes	0.459	0.462	0.48
629	17.367	0.018	0.149	Y	...	Yes	0.363	0.436	0.68
636	16.062	0.009	0.039	N	...	No	-0.069	0.052	1.22
642	17.178	0.013	0.117	N	...	No	0.115	0.127	0.75
644	17.396	0.018	0.302	Y	...	Yes	1.597	0.557	0.67
652	16.584	0.01	0.167	N	...	Yes	0.142	0.136	0.98
654	18.388	0.025	0.344	N	2.69	Yes	0.663	0.187	0.41
677	17.123	0.015	0.159	Y	1.368	Yes	0.401	0.434	0.77
841	14.575	0.004	0.027	N	3.326	No	-0.037	-0.06	2.13
976	15.449	0.007	0.04	N	1.046	No	-0.249	0.018	1.55
998	15.796	0.02	0.095	N	2.996	No	0.406	-0.031	1.35
999	18.18	0.04	0.133	Y	0.835	Yes	0.538	0.484	0.45
1060	16.859	0.013	0.231	N	...	Yes	0.247	0.209	0.86
1144	16.113	0.037	0.197	Y	...	Yes	2.014	...	1.19
1194	18.104	0.062	0.179	N	0.652	No	0.024	...	0.47
1244	18.289	0.047	0.179	N	0.637	No	-0.080	...	0.43
1366	17.689	0.045	0.073	Y	2.989	Yes	-0.292	0.235	0.58
1876	18.539	0.048	0.386	N	0.702	No	0.432	0.475	0.37
2286	17.492	0.032	0.086	Y	0.549	Yes	-0.004	0.12	0.64
2301	17.914	0.04	0.256	N	0.238	Yes	-0.043	0.599	0.52
2303	15.948	0.047	0.147	Y	0.732	Yes	0.541	0.461	1.27
2319	18.739	0.045	0.245	N	0.403	No	-0.053	0.704	0.34
2329	17.112	0.028	0.093	Y	0.794	Yes	0.339	0.776	0.77
2337	16.353	0.007	0.066	Y	0.656	Yes	0.116	0.471	1.08
2363	17.762	0.01	0.186	N	...	No	-0.093	0.013	0.56
2424	19.398	0.143	0.303	N	...	No	-0.094	1.534	0.23
2444	18.458	0.041	0.678	Y	7.143	Yes	1.359	0.438	0.39
2692	16.681	0.019	0.102	N	2.989	No	-0.151	0.024	0.94
3045	17.973	0.033	0.113	N	2.331	Yes	0.180	0.31	0.51
3954	18.239	0.088	0.235	N	0.749	No	0.501	...	0.44
6001	15.348	0.008	0.043	N	...	No	-0.210	...	1.61
6002	17.785	0.026	0.111	N	1.769	No	0.56
6003	18.041	0.067	0.222	N	1.077	No	0.49
6004	17.744	0.046	0.124	N	0.233	No	0.57

* Mean I magnitude from the light curve.

** From IPHAS photometry. See text for details.

*** From I magnitude, mean extinction 1.88 and theoretical isochrones of 3 Myr from Baraffe et al. (1998)

Table 5.4: Parameters of the candidate variable stars (see text for details)

ID	A_v^* (mag)	Age* (Myr)	MASS* (M_\odot)	RAD* (R_\odot)	TEMP* (K)	M/yr^* ($10^{-6}M_\odot$)	M_{disk}^* ($10^{-3}M_\odot$)
8	4.91	3.68	5.57	4.69	15946	22.23	7.75
	± 1.39	± 1.84	± 1.40	± 3.78	± 5352	± 65.76	± 23.28
16	1.95	2.18	2.16	3.40	5025	0.05	0.33
	± 0.31	± 1.11	± 0.24	± 0.37	± 297	± 0.18	± 1.30
38	1.93	7.05	2.42	1.86	10208	0.00	0.00
	± 0.17	± 0.72	± 0.21	± 0.04	± 712	± 0.00	± 0.00
52	4.05	0.99	2.55	4.72	4934	0.07	0.02
	± 0.44	± 0.36	± 0.68	± 0.29	± 305	± 0.09	± 0.01
53	4.11	3.84	3.88	2.89	12983	0.10	2.91
	± 0.74	± 2.49	± 1.19	± 0.45	± 4144	± 0.45	± 7.14
54	3.70	0.59	6.91	3.94	19406	1.25	131.14
	± 0.54	± 0.17	± 0.77	± 0.91	± 2839	± 0.88	± 93.84
55	2.71	1.45	4.17	3.82	12000	2.33	83.25
	± 0.83	± 1.53	± 1.81	± 0.97	± 5062	± 3.19	± 110.75
58	2.16	1.83	2.80	4.62	5755	0.17	3.18
	± 0.69	± 1.09	± 0.46	± 1.00	± 1805	± 1.10	± 13.24
60	4.41	4.11	2.38	2.55	8943	0.46	24.65
	± 1.30	± 2.44	± 0.88	± 0.75	± 3151	± 0.87	± 22.90
62	2.06	2.73	1.85	2.77	5107	0.70	1.46
	± 0.66	± 1.91	± 0.34	± 0.72	± 1207	± 38.00	± 5.81
115	2.78	3.05	1.94	2.82	5971	0.79	2.27
	± 1.19	± 2.44	± 0.60	± 0.83	± 2459	± 34.40	± 8.23
226	2.73	5.69	0.80	1.33	4063	0.02	4.17
	± 0.50	± 2.07	± 0.26	± 0.31	± 264	± 0.32	± 4.59
279	2.77	2.80	1.37	2.44	4808	2.88	1.87
	± 0.99	± 2.18	± 0.60	± 1.43	± 1346	± 54.10	± 8.21
321	4.66	4.29	2.04	3.51	8202	42.38	4.58
	± 2.07	± 3.08	± 0.76	± 2.24	± 3031	± 78.68	± 13.63
363	3.68	0.94	1.86	7.55	4392	74.73	16.25
	± 1.38	± 1.92	± 1.45	± 6.34	± 774	± 224.40	± 43.24
364	3.29	1.90	1.52	5.34	4302	75.39	12.98
	± 1.08	± 2.63	± 1.35	± 6.06	± 1301	± 240.92	± 32.42
366	1.69	7.45	1.21	2.20	4355	40.69	3.86
	± 0.20	± 2.58	± 0.67	± 3.50	± 198	± 194.57	± 13.00
382	2.48	3.95	1.37	1.96	4548	0.00	8.32
	± 0.41	± 1.69	± 0.33	± 0.45	± 266	± 0.00	± 13.99
390	2.58	0.33	1.26	5.08	4199	3.84	4.44
	± 0.90	± 0.12	± 0.87	± 1.24	± 313	± 4.69	± 8.95
480	1.60	9.16	1.50	1.77	5247	0.00	0.01
	± 0.00	± 0.00	± 0.00	± 0.00	± 0	± 0.00	± 0.00
506	2.10	0.43	2.00	5.44	4544	1.02	36.31
	± 0.58	± 0.09	± 1.05	± 1.58	± 253	± 0.78	± 19.61
521	1.82	4.09	1.01	2.26	4071	0.38	13.37
	± 0.55	± 2.05	± 1.00	± 2.32	± 394	± 0.76	± 19.52
566	2.73	2.05	0.81	2.40	4322	4.07	4.37
	± 1.48	± 2.42	± 0.72	± 1.51	± 1722	± 56.32	± 13.65
571	3.01	2.43	2.65	7.69	5407	77.34	13.77
	± 1.35	± 3.14	± 1.56	± 8.58	± 1787	± 224.19	± 41.19
575	2.69	1.30	2.19	8.76	4956	54.29	22.69
	± 1.23	± 2.45	± 1.50	± 8.22	± 1710	± 167.40	± 54.36
578	2.69	1.46	1.27	4.30	5881	3.35	15.76
	± 1.45	± 1.94	± 0.98	± 1.47	± 2987	± 2.86	± 10.63
581	2.41	0.32	1.51	3.23	6055	10.17	20.41
	± 0.86	± 0.26	± 2.04	± 0.86	± 4529	± 5.49	± 14.84
603	1.94	0.25	1.46	5.52	4249	27.87	9.30
	± 0.36	± 0.17	± 0.89	± 1.23	± 381	± 55.46	± 18.96
625	2.74	0.91	2.20	8.91	4476	96.81	22.49
	± 0.98	± 1.82	± 1.57	± 6.88	± 930	± 219.64	± 50.00
629	2.91	2.33	1.95	5.32	4891	51.72	16.24
	± 1.14	± 2.75	± 1.30	± 5.65	± 1587	± 177.80	± 37.73

* Estimated from SED analyses.

ID	A_v^* (mag)	Age* (Myr)	MASS* (M_\odot)	RAD* (R_\odot)	TEMP* (K)	\dot{M}/yr^* ($10^{-6}M_\odot$)	M_{disk}^* ($10^{-3}M_\odot$)
636	2.05	4.59	1.38	1.96	4711	2.10	1.08
	± 0.54	± 2.36	± 0.30	± 0.94	± 646	± 49.47	± 5.24
642	2.92	1.59	2.10	4.41	5652	8.72	17.02
	± 1.40	± 1.72	± 0.83	± 1.81	± 2030	± 23.43	± 19.54
644	2.48	3.89	2.57	3.77	7710	0.02	17.09
	± 0.80	± 3.25	± 0.92	± 2.76	± 2745	± 0.03	± 26.56
652	3.35	4.38	1.79	2.75	6085	11.64	7.66
	± 1.46	± 3.26	± 0.84	± 2.40	± 2437	± 109.42	± 19.33
654	3.00	2.45	1.47	5.46	4188	103.68	12.21
	± 0.80	± 2.77	± 1.24	± 6.22	± 501	± 264.96	± 32.98
677	3.25	2.48	0.95	2.34	4287	0.49	10.30
	± 1.01	± 2.74	± 0.62	± 0.72	± 1090	± 1.81	± 9.20
841	2.29	8.42	2.14	1.74	9424	0.00	0.02
	± 0.04	± 0.00	± 0.00	± 0.00	± 0	± 0.00	± 0.00
976	2.42	0.96	4.39	9.65	6188	2.43	85.28
	± 0.55	± 1.38	± 0.86	± 3.44	± 1470	± 2.79	± 63.97
998	1.65	3.76	1.34	1.92	4543	0.00	0.88
	± 0.14	± 1.63	± 0.12	± 0.14	± 156	± 0.00	± 1.26
999	2.81	4.95	0.78	1.67	4063	1.95	7.91
	± 0.66	± 3.23	± 0.61	± 0.85	± 1016	± 5.16	± 5.13
1060	2.00	2.21	1.56	2.84	4630	0.22	1.65
	± 0.37	± 1.52	± 0.35	± 0.83	± 273	± 0.54	± 2.85
1144	8.74	2.77	5.38	2.90	17065	0.04	11.48
	± 0.28	± 1.77	± 0.54	± 0.37	± 1351	± 0.11	± 26.70
1194	1.79	5.87	1.00	3.39	4002	80.12	6.63
	± 0.49	± 3.46	± 0.98	± 5.43	± 477	± 260.45	± 22.21
1244	2.97	0.54	2.28	6.04	4917	31.95	26.99
	± 1.15	± 0.24	± 1.37	± 3.23	± 1123	± 219.22	± 39.58
1366	3.34	1.23	1.73	3.50	4624	5.97	3.49
	± 0.55	± 0.59	± 0.56	± 2.12	± 308	± 84.17	± 13.37
1876	3.14	3.85	0.65	1.61	3823	5.50	1.17
	± 0.91	± 2.39	± 0.43	± 1.47	± 432	± 68.58	± 6.29
2286	2.56	3.23	0.75	1.69	3983	1.74	0.86
	± 0.75	± 2.06	± 0.39	± 0.91	± 390	± 39.60	± 4.64
2301	2.34	2.04	0.39	1.90	3347	10.84	1.45
	± 0.88	± 2.14	± 0.54	± 2.06	± 469	± 92.92	± 8.16
2303	3.24	4.47	2.31	4.58	6742	32.73	11.76
	± 1.30	± 3.63	± 1.13	± 6.14	± 2459	± 184.10	± 37.87
2319	3.21	1.77	0.44	2.54	3292	37.64	3.49
	± 1.09	± 1.96	± 0.79	± 3.68	± 478	± 178.57	± 16.62
2329	2.11	0.82	3.13	13.38	4816	271.87	54.13
	± 0.71	± 2.10	± 1.83	± 10.10	± 1165	± 433.17	± 103.37
2337	2.36	3.29	1.75	4.07	4754	60.16	9.74
	± 0.66	± 2.70	± 1.11	± 5.81	± 1014	± 243.07	± 31.87
2363	1.70	5.03	0.39	1.18	3517	3.18	0.61
	± 0.42	± 2.52	± 0.26	± 1.00	± 319	± 49.45	± 4.30
2424	4.18	0.30	1.17	4.64	4149	2.00	12.66
	± 1.44	± 0.13	± 0.80	± 0.95	± 374	± 1.75	± 27.60
2444	2.34	0.66	2.32	10.63	4311	187.92	32.64
	± 0.82	± 1.88	± 1.63	± 7.91	± 358	± 310.39	± 53.01
2692	1.68	7.06	1.47	2.59	4567	44.69	5.81
	± 0.39	± 2.96	± 0.86	± 3.96	± 210	± 280.03	± 20.50
3045	2.63	1.29	0.29	1.83	3203	4.20	1.06
	± 0.94	± 1.61	± 0.37	± 1.23	± 415	± 56.74	± 5.89
3954	2.51	0.64	1.86	5.55	4727	43.63	16.62
	± 0.92	± 0.87	± 1.39	± 5.76	± 1316	± 403.98	± 28.65
6001	1.80	6.44	1.65	1.91	5418	0.00	0.06
	± 0.63	± 2.35	± 0.24	± 0.21	± 1442	± 0.00	± 0.07
6002	1.86	0.99	1.14	4.07	4287	2.18	4.89
	± 0.21	± 2.08	± 0.28	± 0.87	± 174	± 1.49	± 5.63
6003	2.27	2.68	2.32	8.27	5178	160.48	36.41
	± 1.03	± 3.30	± 2.29	± 8.29	± 4224	± 363.51	± 64.20
6004	2.99	2.82	1.75	4.08	5577	22.97	12.03
	± 1.62	± 2.75	± 2.82	± 5.80	± 5080	± 121.08	± 44.55

Chapter 6

Photometric Variability in Young Stars towards Cygnus OB7 region

6.1 Introduction

Pre-main sequence (PMS) stars first came to spotlight due to their photometric variable characteristics (Joy 1945; Herbig 1962). Since then, numerous observational studies have been performed on exploring variability in young stars and the role of angular momentum in stellar evolution (Herbst et al. 2000; Carpenter et al. 2001; Lamm et al. 2004; Makidon et al. 2004; Littlefair et al. 2005; Briceño et al. 2005; Cody et al. 2017). The variation in the observed flux of a young star may arise from various mechanisms such as cool star spots, magnetically channeled variable accretion flows generating hot spots on star surface, flare-like activity, eclipsing binarity, non-uniform dust opacity, etc. (Stassun et al. 1999; Herbst et al. 2002). Each of these individual components is dynamic, and experience various types of phenomena at a different wavelength and timescale. These young stars in star-forming regions are variable over all wavelengths from x-ray to radio. Each wavelength domain provides a different aspect of characteristics in those young stars and their circumstellar materials. Compilation of the variable nature in various wavelength domain could be efficiently used to characterize their temporal

properties and physical characteristics (e.g., Kenyon et al. 1994, Yudin 2000; Carpenter et al. 2001; Rice et al. 2012). In general, Classical T Tauri Stars (CTTSs), having stronger emission lines & high infrared excess, show irregular variability, whereas variation in observed flux in Weak line T Tauri Stars (WTTSs) is periodic. Thus, studies of optical variability in young stars at a variety of masses and ages, directly allow us to explore the evolution of disc structure.

The Cygnus rift consists of several young star-forming regions (SFRs; Reipurth & Schneider 2008). The Cygnus OB7 (Cyg OB7) is the nearest of all recognized Cygnus OB association based on the observed distance of 740 pc (Hilter 1965; Schmidt 1958). The near-IR J, H, K monitoring of the dark clouds Lynds (LDN) 1003/1004 in the Cyg OB7 SFRs were carried by Rice et al. (2012) and Wolk et al. (2013) in search for disc-bearing young stars. A number of young embedded sources, Herbig Ae/Be and H_α emission stars were identified in the cloud complexes of Cygnus (e.g., Cohen 1980, Herbig & Bell 1988, Devine et al 1997, Movsessian et al. 2006, Melikian & Karapetian 2003, Magakian et al. 2013, Melikian et al. 2016). A significant number of IRAS sources, outflows from young massive stars and disc were found in this direction (Dobashi et al. 1996, Bernard et al. 1999). Despite the large populations of high to low-mass young stars, the cloud complex is not well explored, deserves detailed study.

In this chapter, we present an analysis of optical I time-series photometry over an area $16'' \times 16''$ centred on $\alpha_{2000} = 20^h 58^m 47^s$ $\delta_{2000} = +52^{\circ} 16' 17''$) of Lynds 1003 cloud in Cyg OB7. A small part of our observing field coincides with earlier JHK variability studies in Rice et al. (2012). Section 6.2.1 describes our observations for this study and the data reduction procedures. Section 6.3 deals with the identification of variable stars from their differential photometric light curves and properties of those observed variability. Section 6.3 analyzes the characteristics of variable stars. Finally, the conclusions of the present studies are summarized in section 6.5.

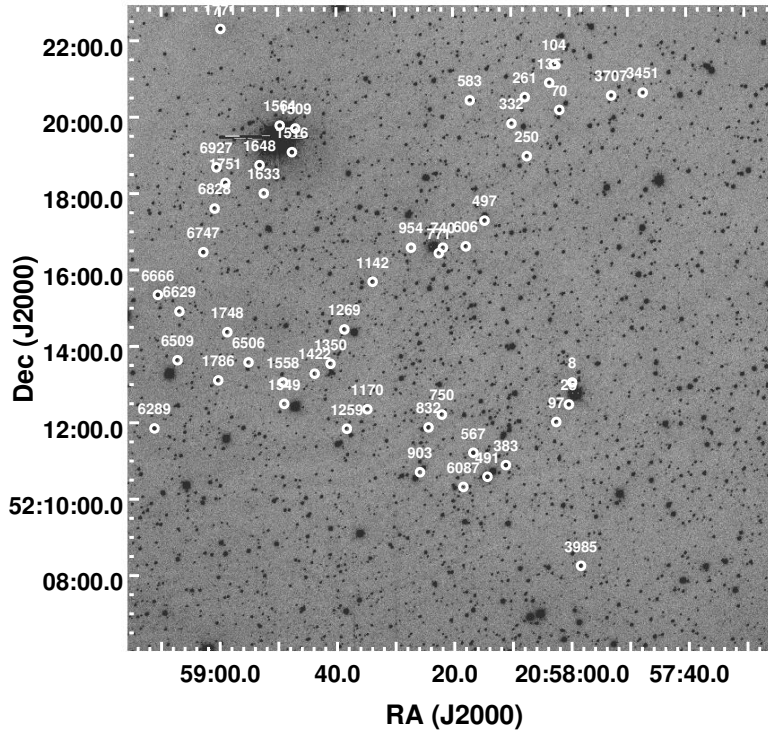


Figure 6.1: The observed region of Cyg OB7 (Lynds 1003). The I -band image is taken at 1.3m DFOT. The circles show the location of candidate variable stars estimated in the present work (see text for details).

6.2 Data

6.2.1 Observations and data reduction

The VRI deep photometric and I -band monitoring observations towards Cyg OB7 were carried out on 17 nights during 2014-2016 at three different Indian telescopes, and a log of our observations is mentioned in Table 6.1. We performed observations using $2K \times 2K$ CCD imager on the 1.3m Devasthal Fast Optical Telescope (DFOT) operated by Aryabhata Research Institute of Observational Sciences (ARIES), Nainital, India (Sagar 2011). The field-of-view (FOV) was about $18' \times 18'$ with a plate scale of $0.535 \text{ arcsec pixel}^{-1}$. The telescope specification used and observations technique are described in chapter 2 of this thesis work. We carried out

Table 6.1: Log of Observations.

Date of Observations	Telescope	I Exp.(s) × N	R Exp.(s) × N	V Exp.(s) × N	Avg. seeing (arcsec)
31.03.2014	1.3m DFOT	120×22, 60×1	250×2, 150×1	300×1, 100×1	1.8
13.11.2014	1.3m DFOT	150×42, 90×20, 60×25	1.8
14.11.2014	1.3m DFOT	150×15, 90×1, 60×8	1.8
29.11.2014	1.3m DFOT	150×4, 90×3, 30×3	2.2
10.12.2014	1.3m DFOT	150×13, 90×10, 20×5	1.8
11.12.2014	1.3m DFOT	150×7, 60×5, 20×6	1.8
21.05.2014	2.0m HCT	120×21	2.2
19.08.2014	2.0m HCT	120×10, 90×6, 60×8	1.0
29.10.2014	2.0m HCT	120×3, 90×3, 60×5	2.5
30.10.2014	2.0m HCT	120×5, 60×3	2.5
05.10.2015	2.0m HCT	300×2, 150×4	300×1, 60×1, 10×1	...	2.5
06.10.2015	2.0m HCT	300×2, 150×2, 150×2, 60×4	300×1, 30×1	...	2.5
07.10.2015	2.0m HCT	300×2, 150×3, 60×2	300×1, 30×2	...	2.5
28.05.2014	1.04m ST	150×12, 90×3, 30×2	2.5
29.05.2014	1.04m ST	150×26	2.5
03.06.2014	1.04m ST	150×18, 30×3	200×1, 90×1	250×1	2.5
05.06.2014	1.04m ST	200×5, 150×31, 60×4	2.5

further *I*-band monitoring observations using HFOSC on the 2m Himalayan Chandra Telescope (HCT), India (Prabhu 2014), which has an FOV $10' \times 10'$ with a pixel scale of 0.296 arcsec pixel⁻¹. We also took *I*-band monitoring observations with 1K × 1K CCD imager on the 1.04m Sampurnanand Telescope (ST) operated by ARIES. This telescope has an FOV about $13' \times 13'$ with a plate scale of 0.37 arcsec pixel⁻¹ (see chapter 2). The observations were taken in 2×2 binning mode, and the average FWHM of the stars were $\sim 1.0 - 2.5''$. The observations were made in short and long exposures to get a good dynamic coverage of the stellar brightness.

The raw CCD images were cleaned using IRAF* software following bias subtraction, flat-fielding, and cosmic ray removal. The identification of point sources was performed with the DAOFIND task. Following Stetson (1987), we have used the roundness limits of -1 to +1 and sharpness limits of 0.2 to +1 to eliminate bad pixels brightness enhancements and the extended sources such as background galaxies from the point source catalog. The photometry by PSF fitting was done using ALLSTAR task of DAOPHOT package (Stetson 1992). The standard magnitudes were obtained from instrumental magnitudes following the procedure outlined by Stetson (1987). A total of 8 stars of RU 149 field were used to estimate atmospheric extinc-

*Image Reduction, and Analysis Facility (IRAF) is distributed by National Optical Astronomy Observatories (NOAO), USA (<http://iraf.noao.edu/>)

tion and transformation coefficients. The final transformation equations used for photometric calibrations are

$$(V - I) = (-0.931 \pm 0.007)(v - i) + (-0.477 \pm 0.006) \quad (6.1)$$

$$(R - I) = (0.916 \pm 0.008)(r - i) + (0.296 \pm 0.010) \quad (6.2)$$

$$I = i + (0.00624 \pm 0.001)(R - I) - (-2.678 \pm 0.002) \quad (6.3)$$

where V , R and I are the standard magnitudes and v , r , i are the instrumental magnitudes corrected for the atmospheric extinctions. The error of final magnitude measurements is obtained by propagating the uncertainties in extinction measurements, standard coefficients, and profile-fitting photometry etc. The profile-fitting uncertainty is estimated from the gain and read-out-noise of CCD camera, and background level of an image etc. Fig. 6.2 shows the standardization residuals (Δ) between standard and transformed I magnitudes, $(R - I)$ and $(V - I)$ colors of standard stars as function of I magnitudes. The standard deviations in ΔV , $\Delta(R - I)$ and $\Delta(V - I)$ are 0.020, 0.018 and 0.020 mag, respectively. Finally, we estimated optical magnitudes of 7009 objects, which are detected in at least R and I bands. However, we consider variability studies for 1809 star, which have magnitude measurement more than 140.

The completeness limits at various bands were estimated from histogram turn over method (e.g. Dutta et al. 2015). We considered $\sim 90\%$ completeness of our data from the turning points of magnitudes at which cumulative logarithmic distribution of sources in the histograms deviates from the linear distribution. We found the photometric data are complete down to $V=21$ mag, $R=21$ mag, $I=20.5$ mag, respectively.

The world coordinate system (wcs) coordinates for the detected stars in the frame were determined using 20 isolated moderately bright stars with their positions from the 2MASS point source catalog (PSC) (Curti et al. 2003), and a position accuracy of better than $0.3''$ has been achieved. We used IRAF tasks *ccmap* and *ccsetwcs* to achieve the above astrometric solution.

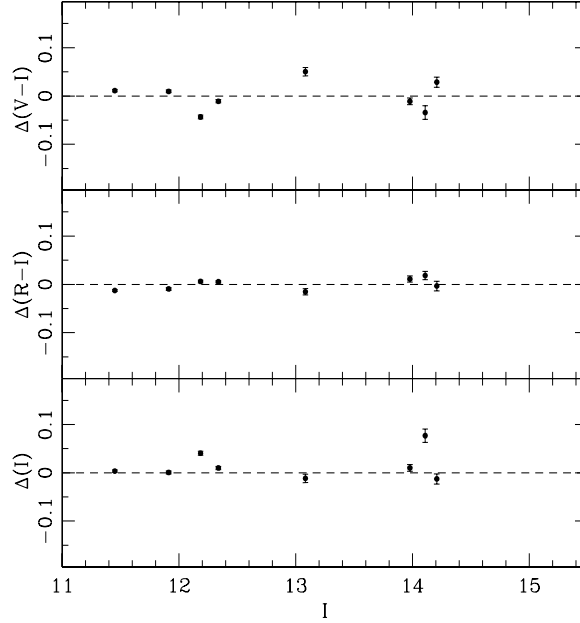


Figure 6.2: Residuals between standard and transformed magnitudes and colors of standard stars plotted against the Landolt standard magnitudes. The error bars are combined errors of Landolt (1992) and present measurements.

6.2.2 Archival NIR and MIR data sets

Deep Near-IR (NIR) observations towards Cyg OB7 (centered on $\alpha_{2000} = 20^h58^m47^s$ $\delta_{2000} = +52^{\circ}16'17.0''$) were obtained in *JHK* bands from UKIDSS data archive observed using WFCAM camera of the 3.8m UKIRT telescope. In this set up each pixel corresponds to $0''.3$ and yields a FOV $\sim 20' \times 20'$. The average FWHM during the observing period was $\sim 1''.2$. The identification of point sources and photometry were performed in IRAF in the same method described in section 6.2.1.

To avoid the inclusion of UKIRT saturated sources we replaced all the sources in our catalog having 2MASS magnitudes $J = 13.25$, $H = 12.75$ and $K = 12.0$ mag, respectively (Lucas et al. 2008). The magnitudes of the sources of uncertainty ≤ 0.1 mag have been taken for our study to ensure good photometric accuracy. We found the photometric data are complete down to $J=19$ mag, $H=18$ mag, $K=17.5$ mag, respectively.

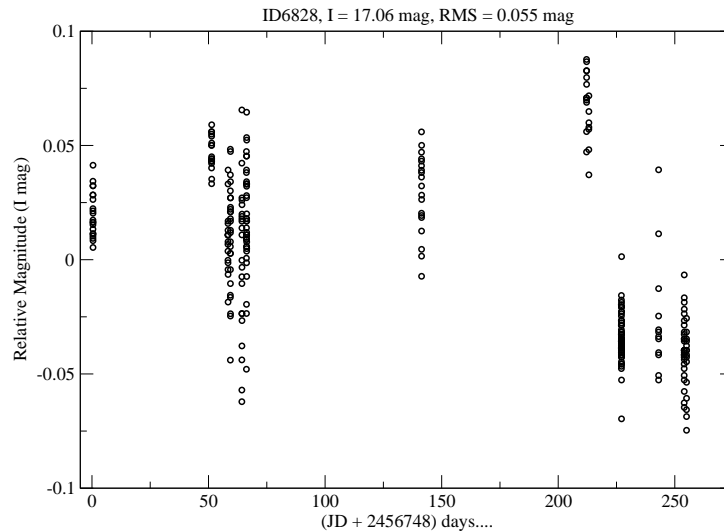


Figure 6.3: The observed light curve of ID6828, mean magnitude and RMS is also mentioned (see text for details).

The WISE survey (Cutri et al. 2012) provides photometry at four wavelengths; 3.4, 4.6, 12 and 22 μm , with an angular resolution of $6''.1$, $6''.4$, $6''.5$, $12''.0$, respectively. We used WISE photometric catalog with good quality photometry (uncertainty better than 20%) in this study.

6.3 Identificatio of variable stars

The estimation of variable stars using ground based telescopes could be biased towards high limiting magnitude and also led to misidentification in a crowded field. The reason arises from the fact that the contemporary CCDs are very sensitive and small. Thus, only a few percent of variable stars could be accessible to ground-based photometry. However, a vast majority of candidate variable could be studied from careful inspection of flux variation. Considering a large number of sample, various techniques are employed in the increasing search for variable stars, each having their own merits and limitations.

6.3.1 Differential photometry

We have performed differential photometry to clean the light curves from sky variability, instrument signatures, airmass, etc. Advantages of such technique provide a very good photometric precision, even in the crowded nebulous region of the cluster. We considered a set of 5 non-variable reference stars, which showed a stable behavior by σ_{mag} scattered on the observed light curves. To obtain the differential photometry, we subtract each target star magnitude by the average of five reference stars magnitude in each frame. The procedure is repeated for all the stars detected in a frame. An example differential light curve of a variable star in time frame is shown in Fig. 6.3.

To identify the variable stars from a large number of datasets, we performed root-mean-square (RMS; σ_{mag}) deviation of magnitudes for the differential photometric light curve on each star over the whole span of our observations with the different telescopes (e.g. Dutta et al. 2017). The σ_{mag} deviation of all data sets for each star was estimated quantitatively following Carpenter et al. (2002) and is given as,

$$\sigma_{mag}^2 = \frac{n \sum_{k=1}^n w_k (I_k - \bar{I})^2}{(n-1) \sum_{k=1}^n w_k}, \quad (6.4)$$

where I_k 's are the individual magnitudes associated with photometric uncertainty σ_k 's and weightage $w_k = 1.0/\sigma_k^2$ for each observation. The rms noise was also considered as

$$\sigma_{noise}^2 = \frac{n}{\sum_{k=1}^n 1.0/\sigma_k^2}. \quad (6.5)$$

We estimated σ_{mag} scatter using all data from 2m HCT, 1.04 m ST and 1.30m Devasthal Telescopes.

Fig. 6.4 shows the RMS (σ_{mag}) of the *I*-band differential photometric light curves of 1809 stars towards Cyg OB7. A close inspection to σ_{mag} deviation as a function of instrumental magnitudes, I_{inst} reveals that majority stars flow an expected trend of increment σ_{mag}^2 with I_{inst}

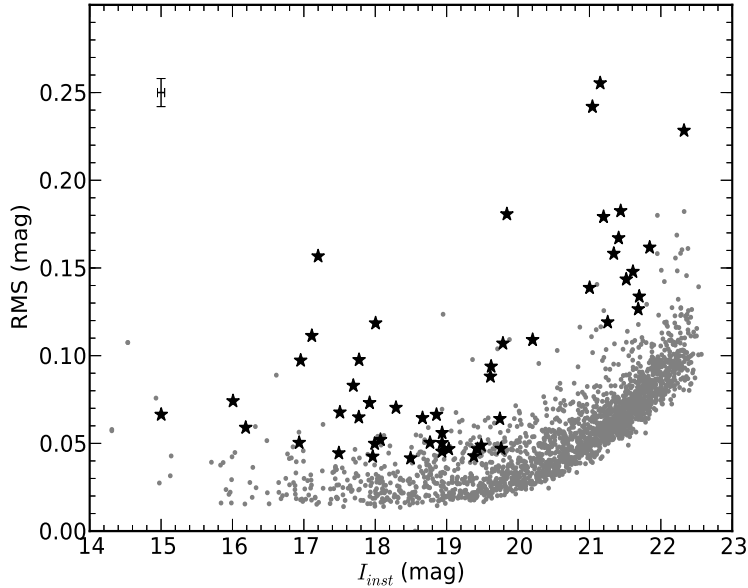


Figure 6.4: RMS of the I -band differential photometric light curves of 1809 stars towards Cyg OB7 are shown in grey circles. The black star marks are detected variables in the outliers. The average error bars for magnitudes and rms value are also shown on the top left corner (see text for details).

magnitudes as S/N ratio decrease accordingly. Scattering of magnitudes may arise from several facts, e.g., intrinsic variability of the star, photometric noise, variation in sky signal. But, few of them are scattered from the normal trend. We considered a star is variable with more than 3σ scatter sitting an outlier from that normal trend. We found 105 stars from the criterion mentioned above. However, visual inspection of the light curves (see sec. 6.3.1) indicate that 55 stars show large RMS values because of abrupt flux change over only a few data points. Such spurious identifications from false positive were rejected as variable stars considering their location on the edge of CCD, an effect of bad pixels or cosmic-rays hits. *Finally, we selected 50 sources as variable candidates.* However, estimation of confirmed variable stars demands further treatment of visual inspection of their light curves and phase light curves. Such exercises pass those all 50 variable candidates. A catalog of all candidate variable stars is presented in Table 6.2.

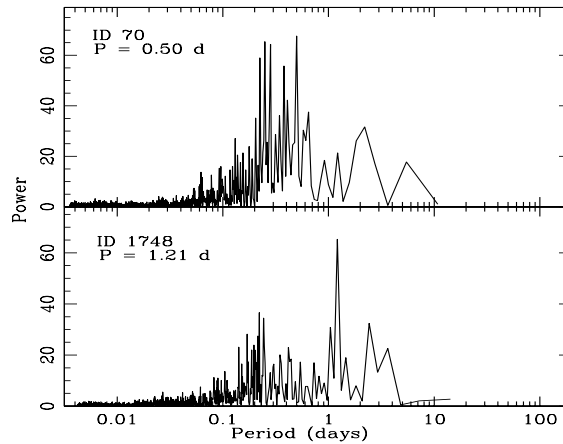


Figure 6.5: Example LS power spectrum of selected stars. The highest peaks are marked with red dashed lines (See text for details).

6.3.2 Period Estimation

We aim to check the periodicity of those candidate variables. We made use of Lomb-scargle (LS) periodogram analysis technique in our unevenly sampled data of variable stars in search for periodicity (Lomb 1976). This method calculates the normalized power for a given angular frequency and locates the highest peak in the estimated periodogram for each star. The light curve of each star is phased to the period according to the frequency of the highest peak (e.g., Lamm et al. 2004, Dutta et al. 2017). We used LS algorithm available at the starlink* software package. The periods were verified with period04** and NASA Exoplanet Archive Periodogram Service***. Fig. 6.5 displays an example LS power spectrum of ID70 and ID1748, and the estimated periods using Starlink package are 0.50 and 1.21 days, respectively. We estimate the periodicity of 44 candidate variables, rest six are considered as the irregular variables. The periods of all the stars are listed in Table 6.4. The visual light curves are folded with their estimated periods to generate the phase light curves. The phase light curves of all periodic or quasi-periodic variables are shown in Fig. 6.6.

* <http://www.starlink.ac.uk/>

** <https://www.univie.ac.at/tops/Period04/>

*** <http://exoplanetarchive.ipac.caltech.edu/cgi-bin/Periodogram/nph-simpleupload>

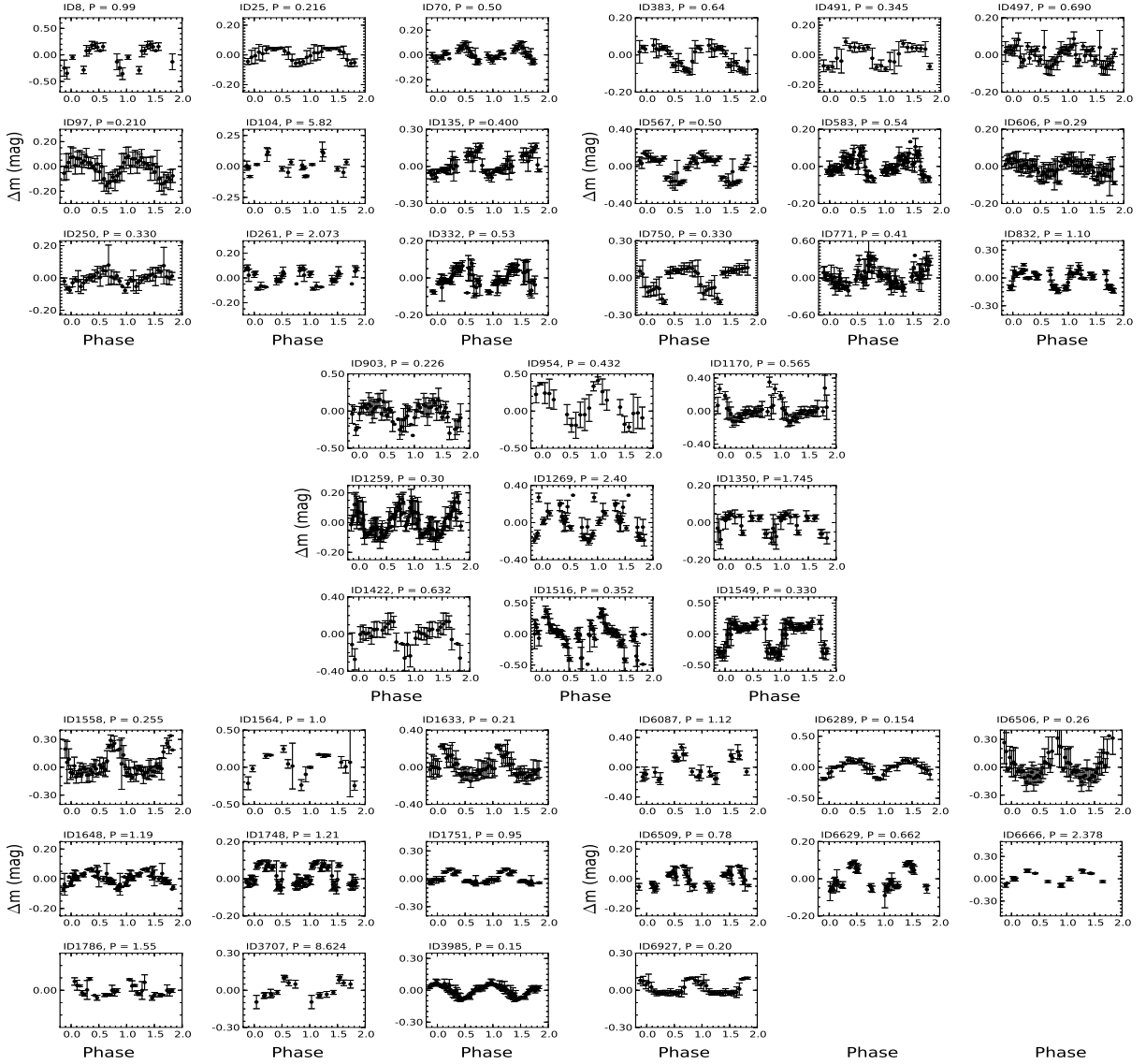


Figure 6.6: Phase light curves of periodic variables (see text for details).

6.3.3 Previously Known variables

The near-IR J, H, K monitoring of the dark clouds Lynds 1003 in the Cyg OB7 detected 30 variable young stars and all of them are disc-bearing young stars (CTTS and class I) (Rice et al. 2012). A small part of our observing FOV coincides with FOV of Rice et al. (2012) and Wolk et al. (2013). They estimated 13 variable stars from NIR JHK variability studies in that direction of Cygnus OB7. Of these, 6 stars are optically detected and studied by us from I-band observations, and only one star, ID 70, is optically variable from our present analysis.

We estimated a period of 0.30 day for ID 70, which is slightly smaller (0.50 day) than Wolk et al. (2013). Rice et al. (2012) estimated ID 1564 and ID 1771 as periodic variables with period measurement 4.84 and 6.35 days, respectively. Our present data suggest a period of 1.0 day for ID1564, and ID1771 is an irregular variable. ID 1648 and ID 6666 are listed in American Association of Variable Star Observers (AAVSO) Photometric All Sky Survey (APASS) DR9 (Henden 2016). This is the newest release of this database contains about 100 million datasets taken over both northern and southern hemispheres during the last six years.

6.3.4 New variables

Out of 50 candidate variables, 45 are new variables detected from our studies. Among 45 new candidate variables, 40 show periodic or quasi-periodic variations. The phase light curves of those periodic variables are shown in Fig. 6.6). Their periods of variable candidates exhibit in the range 0.14 to 8.62 days. In next section, we characterize those candidate variables.

Spatial distribution of all our variables is shown in Fig. 6.1. Interestingly, they might trace the star-forming cloud in active star-forming region LDN 1003 of CyG OB7. The LDN 1003 is going through an active phase of star formation (Khanzadyan et al. 2012).

6.4 Discussions

6.4.1 NIR Color-Color Diagram

NIR color-color (CC) diagram is shown in Figure 6.7. All the intrinsic locus and photometric data points are transformed into the CIT (California Institute of Technology) system (Elias et al. 1982) using the relations given by Carpenter et al. (2001). The parallel dashed lines represent the interstellar reddening vectors. The slope of the reddening vectors (i.e., $A_J/A_V = 0.265$, $A_H/A_V = 0.155$ and $A_K/A_V = 0.090$) are taken from Cohen et al. (1981).

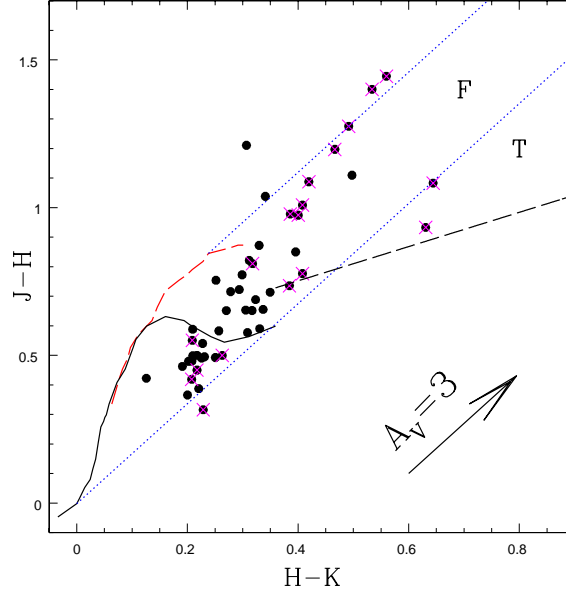


Figure 6.7: $J - H/H - K$ CC diagram of candidate variable stars in Cyg OB7. The magenta crosses are the probable CTTSs. The locus for dwarfs (solid black) and giants (red dashed line) are taken from Bessel & Brett (1988). The long dashed black line represents the CTTS locus (Meyer et al. 1997) and the small dashed blue lines represent the reddening vectors (Cohen et al. 1981). The reddening vector of visual extinction $A_V = 3$ mag is also shown (see text).

The NIR emission of ‘T’ region stars arise from both photosphere and circumstellar disc (Lada & Adams 1992). The majority of these stars in ‘T’ region are considered to be CTTSs. All such sources possess accreting optically thick disc (Meyer et al. 1997). The stars ID 1564 and ID 1771 are CTTSs, located at ‘T’ region. $(r - i)/(r - H_\alpha)$ CC diagram (e.g. Dutta et al. 2017) based on IPHAS photometry data reveals that these two stars are H_α emitting (Figures are not shown) with an equivalent width (EW) $> 10 \text{ \AA}$. The NIR emission of stars in ‘F’ region is thought to originate from their discless photosphere. These stars are located between the upper and middle reddening vectors in the NIR CC diagram, and they are considered to be either field stars or WTTSs/Class III sources with no or small NIR excess. However, CTTSs with relatively small excess could share this location around the CTTS locus or near the middle reddening vector (e.g. Dutta et al. 2015).

6.4.2 Spectral index for identifying T Tauri stars

The evolutionary stages of the YSO could be studied from the spectral index (α), the slope of the SED calculated between near-IR and mid-IR fluxes (Lada 1987). We estimated spectral index ($\alpha = d \log(\lambda F_\lambda) / d \log(\lambda)$) of the variable sources from 2MASS and WISE fluxes. Following Lada et al. (2006), objects with $\alpha \geq +0.3$ are considered as class I, $+0.3 > \alpha \geq -0.3$ flat spectrum, $-0.3 > \alpha \geq -1.8$ as Class II and $\alpha < -1.8$ as Class III sources. Out of 50 variable stars, 3 have all WISE band measurements. We estimated α for these sources from a least-square fit to the fluxes in the range 3.4 to 24 μm . The α indices of 17 sources are obtained from available K to 11.56 μm , and another 15 sources are considered from K to 4.6 μm . All the estimated α indices are listed in Table 6.5. Using the above approach, we find that 19 sources have $\alpha > -1.8$, which might be CTTSs. There are not any well-defined boundary of WTTS and main-sequence (MS). Considering their location on $J - H / H - K$ CC diagram, we considered 5 stars with $-2.5 < \alpha < -1.8$ stars as WTTS. Rest 26 stars could be either WTTS, MS or other field stars.

6.4.3 Optical Color-Magnitude Diagram

An Optical Color-Magnitude Diagram (CMD), V vs $(V - I)$ of variable stars is plotted in Fig. 6.8. It is an important tool to estimate the approximate ages and masses of variable candidates. The solid curve in Fig. 6.8 represents the ZAMS, taken from Girardi et al. (2002) corrected for the cluster distance 740 pc. The background stars are fitted well with a reddening of $E(B - V) = 0.30$ mag, which is considered as background extinction of the studied region. We have used the PMS isochrone and evolutionary tracks of Bressan et al. (2012) to determine the ages and masses of the candidate variables. The PMS isochrones for Siess et al. (2000) is also plotted for comparison. The ages and masses of YSOs have been estimated by comparing their locations on the CMD with PMS isochrones of various ages after correcting for the distance and

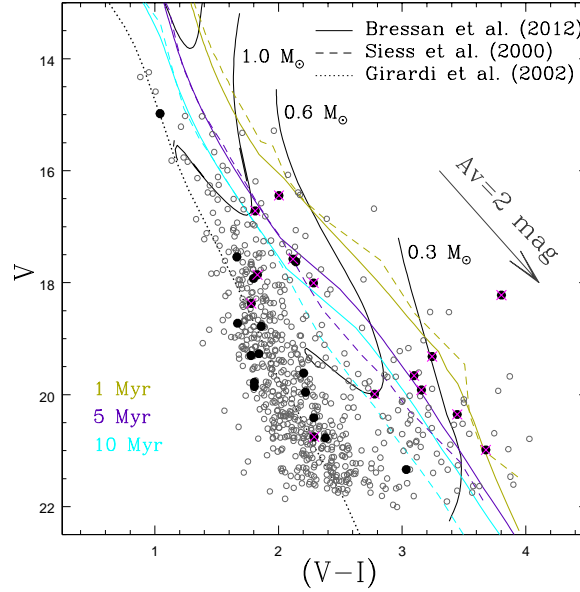


Figure 6.8: $V/(V-I)$ CMD for all the sources of studied region. The magenta box is candidate variable sources. The dotted curve is the locus of ZAMS from Girardi et al. (2002), solid curves are the PMS isochrones of age 1.0, 5.0 and 10.0 Myr, respectively, and the thin black solid curves are the evolutionary tracks for various mass bins from Bressan et al. (2012). The long dashed curves are PMS isochrones of age 1.0, 5.0 and 10.0 Myr taken from Siess et al. (2000). All the isochrones and tracks are corrected for the distance and reddening.

extinction. Since the reddening vector is nearly parallel to the isochrones, a small extinction variation would not have much effect on the age estimation of variable stars.

We have compiled VI photometry for the Variable stars, and compare their positions on the CMD to theoretical model isochrones. We estimated mass and age of few variable stars using interpolation methods of Siess et al. (2000) isochrones in the CMD. However, our estimation is limited due to an absence of V measurement of all variable stars. The CMD positions of candidate variables seem to be adequately fit ages between 1–10 Myr. Different models at low-mass end differ significantly as we can see in Fig. 6.8. The average mass of the YSOs seems to be $\sim 0.2-1.0 M_{\odot}$. The stars located around ZAMS are not considered for mass and age estimation in the above approach. The estimated ages and masses of variable stars are listed in Table 6.5. However, such measurement will lead to 50%-60% error in case of eclipsing binary stars. The presence of unresolved binary will brighten a star from its actual measurement, hence a lower age estimation is predicted.

6.4.4 SED and physical properties of variable stars

The study of the circumstellar environment of candidate variables is important to understand the PMS evolution of stars. We constructed SEDs using the grid of models and fitting tools of Robitaille et al. (2006, 2007) for characterizing and understanding the nature of the sources in Cyg OB7. The grid consists of 20,000 YSO models at ten viewing angles for each model, resulting in a total of 200,000 SEDs. The SED fitting tool fits multi-wavelength data with those pre-computed models and provides the evolutionary stage and physical parameters such as disc mass, disc accretion rate and stellar temperature of YSOs. Fig. 6.9 displays sample SED for a variable source using the SED fitting tools. We obtained the physical parameters of YSOs using the relative probability distribution for the stages of all the good-fit models, defined by $\chi^2 - \chi_{min} \leq 3N_{data}$, where χ_{min} is the goodness of fit parameter for the best-fitting model, and N_{data} is the number of input observational data points. We estimated the χ^2 weighted parameters such as the average extinction (A_v), stellar mass (MASS), temperature (TEMP), stellar age (TIME), disc accretion rate (\dot{M}), the mass of the disc (M_{disc}), etc. The error in each parameter is obtained from the standard deviation of all well-fit parameters. The parameters and the corresponding errors of all the candidate variables are listed in Table 6.4. For some of the sources, the errors associated with few parameters are quite large because we are dealing with a large number of parameter space, with a limited number of observational data points. Additional observational data points in longer wavelengths would help constrain these parameters more precisely.

6.4.5 Variability and disc correlation

To investigate any correlation between NIR excess and rotation rates of our periodic/aproperiodic variables, we have used ($W1 - W2$) excess and an $\Delta(I-K)$ as defined by Hillendrand et al. (1998). I -band fluxes are thought to be dominated by pure photospheric emission, while K -band fluxes

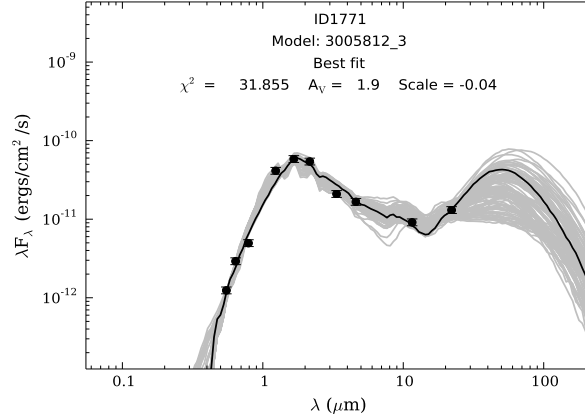


Figure 6.9: Sample SEDs for a variable source (ID1771) using the SED fitting tools of Robitaille et al. (2007). The solid black line shows the best fit and the gray lines show the subsequent well fits. The filled circles denote the input flux values.

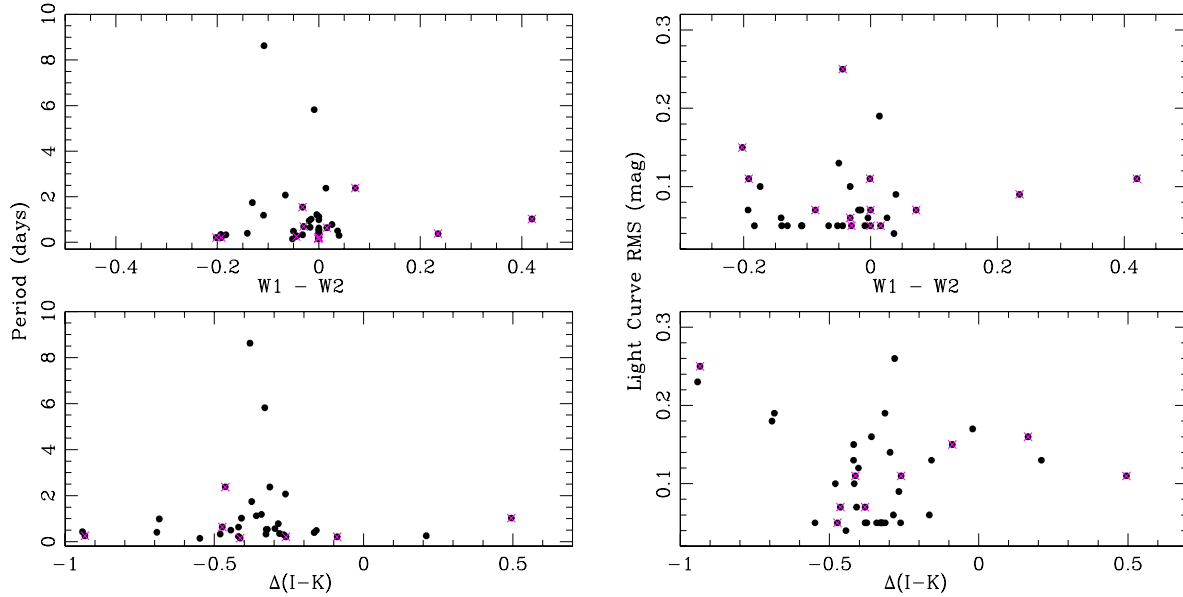


Figure 6.10: (*left*) Periods are plotted as a function of disc indicator $W1 - W2$ (upper panel) and NIR excess $\Delta(I - K)$ excess (lower panel) for periodic variables. (*right*) The light curves RMS (variability amplitude) are plotted as a function of $W1 - W2$ (upper panel) and $\Delta(I - K)$ (lower panel) for periodic and aperiodic variables.

can have additional fluxes from circumstellar disc (Hillenbrand et al. 1998; Rodriguez-Ledesma et al. 2010). The NIR excess from $(I - K)$ color could be written as,

$$\Delta(I - K) = (I - K)_{obs} - (A_I - A_K) - (I - K)_o \quad (6.6)$$

Where $(I - K)_{obs}$ is the observed magnitudes; A_I and A_K are interstellar extinctions in I and K -bands respectively. $(I - K)_0$ is the intrinsic color of a star. Without knowledge of spectral types, the intrinsic color is difficult to measure, and this is the case for our variables. However, it could be estimated from photometric measurements, extinction, and theoretical isochrones. We have measured the intrinsic colors $(I - J)_0$ as it is expected to be originating from photospheric emission from observed $(I - J)$ colors corrected by the average extinction of $E(B - V) = 0.30$ mag (see section 6.4.3). Using color information from Baraffe et al. (1998) and mean age of 4 Myrs, we estimated the intrinsic color $(I - K)_0$ from $(I - J)_0$. Although, all variable stars are of different age group, considering a single age will not cause a change drastically of the estimated parameter.

Fig. 6.10 (*left*) shows the distribution of all periodic variables as a function of $(W1 - W2)$ and $\Delta(I - K)$ excess emission. Fig. 6.10 (*right*) shows RMS scatter of all periodic/irregular variables in $(W1 - W2)$ and $(I - K)$ excess space. It is interesting to note that majority of stars cluster around $\Delta(I - K) = -0.5$ to -0.25 . Such anomalous distribution on diagram implies that majority variables are disc-less WTTSs. This study supports an important correlation that WTTS shows more periodic variation as compared CTTS. However, small CTTS sample on our study prevents to confirm the fact. No conclusive correlation was found between disc and variability characteristics.

6.5 Summary and conclusions

In this chapter, we have presented I band monitoring studies of young stars in the star-forming region LDN 1003 towards Cyg OB7 including deep optical VRI observations complemented with the NIR JHK and WISE 3.4, 4.6, 12 and 22 μm . The main results are summarized as follows:

1. The deep I -band (~ 20.5 mag) analysis enables us to probe the variability up to the low-mass end of pre-main sequence (PMS) stars. Using large RMS deviation of the light curve analysis from normal trend, visual inspection of the differential photometry light curves, periods, and phase light curves, we have identified 50 photometric variable stars. Among 5 are known from earlier studies, 45 are new variables from this studies. The periods of these variables are in the range of 0.14 to 8.62 days.
2. From SED analysis and location on $(J - H/H - K)$ CC Diagram space, we characterize 19 variable stars are CTTSs, 5 are WTTSs and rest could be either WTTS, MS or field stars.
3. The $(V/(V - I))$ CMD suggests that majority of variables, particularly CTTSs, have age < 10 Myrs.
4. To find out any correlation of disc and variability, we studied periods and RMS distribution in $(W1 - W2)$ and $\Delta(I - K)$ space. But, we don't find any conclusive evidence of the correlation between disc and variability amplitude.

Table 6.2: Catalog of the identified variable stars adopted.

ID	α_{2000} (deg)	δ_{2000} (deg)	$V - I$ (mag)	$R - I$ (mag)	I (mag)	J (mag)	H (mag)	K (mag)	W1 (mag)	W2 (mag)	W3 (mag)	W4 (mag)
8	314.499070	52.217150	...	1.091	19.887	16.543	15.830	15.480
				± 0.074	± 0.036	± 0.010	± 0.009	± 0.015				
25	314.501460	52.207570	3.445	1.308	16.909	12.895	11.799	11.374	11.025	11.025	10.718	9.090
			± 0.047	± 0.021	± 0.014	± 0.018	± 0.019	± 0.015	± 0.022	± 0.021	± 0.074	± 0.362
70	314.507090	52.335980	2.140	0.693	15.486	13.566	13.168	12.960	12.742	12.705	12.745	9.293
			± 0.167	± 0.030	± 0.022	± 0.001	± 0.001	± 0.002	± 0.036	± 0.037	$\pm \dots$	$\pm \dots$
97	314.510510	52.199980	2.289	0.846	18.464	16.235	15.637	15.419	14.156	14.348	12.811	9.229
			± 0.105	± 0.077	± 0.061	± 0.008	± 0.008	± 0.014	± 0.025	± 0.037	± 0.456	± 0.425
104	314.510660	52.355780	1.798	0.772	16.127	14.049	13.527	13.317	11.921	11.930	11.390	9.168
			± 0.045	± 0.031	± 0.025	± 0.002	± 0.001	± 0.003	± 0.022	± 0.022	± 0.132	± 0.426
135	314.514180	52.347800	2.285	0.959	18.127	15.328	14.550	14.261	14.121	14.262	12.907	9.374
			± 0.073	± 0.029	± 0.023	± 0.004	± 0.003	± 0.005	± 0.028	± 0.042	± 0.504	$\pm \dots$
250	314.530530	52.315900	1.777	0.767	17.525	15.408	14.885	14.669	14.582	14.765	12.520	8.705
			± 0.037	± 0.021	± 0.017	± 0.004	± 0.004	± 0.007	± 0.033	± 0.052	$\pm \dots$	$\pm \dots$
261	314.531720	52.341600	1.860	0.803	16.919	14.607	14.020	13.783	13.598	13.664	12.434	8.920
			± 0.039	± 0.024	± 0.020	± 0.002	± 0.002	± 0.004	± 0.025	± 0.031	± 0.302	$\pm \dots$
332	314.541330	52.330110	2.218	0.863	17.739	15.308	14.770	14.529
			± 0.147	± 0.023	± 0.015	± 0.004	± 0.004	± 0.007				
383	314.546470	52.181220	1.812	0.681	14.907	12.940	12.596	12.358	11.992	11.976	11.284	9.270
			± 0.017	± 0.039	± 0.009	± 0.001	± 0.001	± 0.001	± 0.023	± 0.023	± 0.118	± 0.448
491	314.559600	52.176170	3.803	1.609	14.419	9.567	8.181	7.669	7.259	7.452	7.276	7.081
			± 0.032	± 0.061	± 0.006	± 0.018	± 0.003	± 0.011	± 0.035	± 0.020	± 0.018	± 0.069
497	314.560940	52.287890	2.777	1.178	17.213	13.237	12.055	11.618	11.328	11.358	11.077	8.794
			± 0.118	± 0.084	± 0.020	± 0.027	± 0.027	± 0.022	± 0.036	± 0.037	± 0.109	$\pm \dots$
567	314.569610	52.186660	16.331	13.065	11.937	11.582	11.268	11.318	11.500	9.347
					± 0.040	± 0.027	± 0.027	± 0.020	± 0.023	± 0.021	± 0.141	
583	314.571050	52.340310	1.804	0.817	17.976	15.619	15.076	14.850
			± 0.058	± 0.028	± 0.019	± 0.005	± 0.005	± 0.009				
606	314.574430	52.276710	3.033	1.297	18.304	14.369	13.421	13.078	12.451	12.495	11.979	9.311
			± 0.116	± 0.031	± 0.024	± 0.002	± 0.001	± 0.002	± 0.023	± 0.024	± 0.235	
740	314.590740	52.276170	...	0.922	19.829	16.744	16.036	15.706
				± 0.117	± 0.051	± 0.012	± 0.011	± 0.018				
750	314.591910	52.203360	...	1.063	18.192	15.120	14.492	14.171	13.391	13.423	11.548	9.191
			$\pm \dots$	± 0.055	± 0.033	± 0.003	± 0.003	± 0.005	± 0.028	± 0.031	± 0.161	± 0.497
771	314.593660	52.273780	...	0.874	20.396	17.071	16.362	16.044
			$\pm \dots$	± 0.070	± 0.062	± 0.016	± 0.014	± 0.025	$\pm \dots$	$\pm \dots$	$\pm \dots$	$\pm \dots$
832	314.601430	52.197790	1.663	0.740	15.877	13.843	13.422	13.193	12.447	12.462	12.377	9.181
			± 0.034	± 0.034	± 0.020	± 0.001	± 0.001	± 0.002	± 0.026	± 0.027	± 0.423	$\pm \dots$
903	314.607610	52.178230	20.397	17.048	16.125	15.713
			$\pm \dots$	$\pm \dots$	± 0.072	± 0.015	± 0.012	± 0.018	$\pm \dots$	$\pm \dots$	$\pm \dots$	$\pm \dots$
954	314.613470	52.276230	...	1.237	21.399	17.992	17.358	17.091
			$\pm \dots$	± 0.117	± 0.080	± 0.035	± 0.035	± 0.064	$\pm \dots$	$\pm \dots$	$\pm \dots$	$\pm \dots$
1142	314.640970	52.261400	1.779	0.807	16.593	14.210	13.721	13.495	12.545	12.632	12.322	9.350
			± 0.043	± 0.010	± 0.006	± 0.002	± 0.002	± 0.003	± 0.024	± 0.025	$\pm \dots$	$\pm \dots$
1170	314.644980	52.205770	...	1.396	19.677	16.658	15.910	15.573
			$\pm \dots$	± 0.063	± 0.056	± 0.011	± 0.010	± 0.016	$\pm \dots$	$\pm \dots$	$\pm \dots$	$\pm \dots$
1259	314.659580	52.197280	1.805	0.925	18.050	15.207	14.499	14.217	13.780	13.740	12.748	9.371
			± 0.117	± 0.024	± 0.011	± 0.004	± 0.003	± 0.005	± 0.026	± 0.036	$\pm \dots$	$\pm \dots$
1269	314.661220	52.240640	2.379	1.071	18.394	15.483	14.842	14.497	13.104	13.090	12.661	9.407
			± 0.086	± 0.056	± 0.044	± 0.004	± 0.004	± 0.007	± 0.026	± 0.030	$\pm \dots$	$\pm \dots$
1350	314.671140	52.225650	1.841	0.906	17.428	14.762	14.227	13.965	13.200	13.331	12.525	9.446
			± 0.076	± 0.015	± 0.007	± 0.003	± 0.002	± 0.004	± 0.024	± 0.032	$\pm \dots$	$\pm \dots$
1422	314.682430	52.221340	...	1.122	20.288	17.143	16.324	16.062
			$\pm \dots$	± 0.116	± 0.068	± 0.017	± 0.014	± 0.026	$\pm \dots$	$\pm \dots$	$\pm \dots$	$\pm \dots$
1509	314.695810	52.328300	...	0.755	19.793	17.127	16.287	15.976
			$\pm \dots$	± 0.090	± 0.053	± 0.016	± 0.013	± 0.023	$\pm \dots$	$\pm \dots$	$\pm \dots$	$\pm \dots$
1516	314.698250	52.318010	20.504	17.361	16.468	16.144
			$\pm \dots$	$\pm \dots$	± 0.071	± 0.020	± 0.016	± 0.027	$\pm \dots$	$\pm \dots$	$\pm \dots$	$\pm \dots$
1549	314.704160	52.208170	20.178	15.795	14.590	14.071
			$\pm \dots$	$\pm \dots$	± 0.046	± 0.005	± 0.003	± 0.005	$\pm \dots$	$\pm \dots$	$\pm \dots$	$\pm \dots$
1558	314.704990	52.217530	...	1.256	20.650	17.581	16.265	15.945
			$\pm \dots$	± 0.157	± 0.078	± 0.025	± 0.015	± 0.025	$\pm \dots$	$\pm \dots$	$\pm \dots$	$\pm \dots$

ID	α_{2000} (deg)	δ_{2000} (deg)	$V - I$ (mag)	$R - I$ (mag)	I (mag)	J (mag)	H (mag)	K (mag)	W1 (mag)	W2 (mag)	W3 (mag)	W4 (mag)
1564	314.706910	52.329610	2.117	0.771	15.461	12.784	11.770	11.113	10.259	9.839	8.269	6.307
			± 0.118	± 0.026	± 0.011	± 0.026	± 0.023	± 0.024	± 0.022	± 0.020	± 0.023	± 0.049
1633	314.718430	52.300060	...	1.092	20.259	17.348	16.467	16.136	14.563	14.765	12.472	8.825
			$\pm \dots$	± 0.135	± 0.089	± 0.020	± 0.016	± 0.029	± 0.032	± 0.051	± 0.358	$\pm \dots$
1648	314.721390	52.312380	1.042	0.482	13.937	12.556	12.097	11.966	11.926	12.035	12.024	9.155
			± 0.017	± 0.010	± 0.006	± 0.017	± 0.017	± 0.027	± 0.022	± 0.021	± 0.286	$\pm \dots$
1748	314.744630	52.239510	...	1.690	18.229	12.868	11.346	10.790	10.444	10.448	10.332	9.198
			$\pm \dots$	± 0.022	± 0.011	± 0.019	± 0.017	± 0.022	± 0.022	± 0.020	± 0.055	± 0.448
1751	314.745840	52.304660	3.677	1.581	17.310	12.273	10.972	10.486	10.122	10.141	9.904	9.401
			± 0.062	± 0.012	± 0.006	± 0.020	± 0.017	± 0.022	± 0.023	± 0.021	± 0.043	$\pm \dots$
1771	314.749050	52.371800	2.283	1.009	15.722	12.425	11.248	10.577	10.193	9.615	7.288	4.832
			± 0.039	± 0.032	± 0.013	± 0.019	± 0.019	± 0.020	± 0.023	± 0.021	± 0.021	± 0.029
1786	314.751140	52.218480	3.096	1.362	16.564	12.357	11.294	10.892	10.637	10.669	10.629	8.856
			± 0.026	± 0.009	± 0.005	± 0.022	± 0.024	± 0.027	± 0.028	± 0.027	± 0.095	$\pm \dots$
3451	314.447400	52.343270	18.200	15.499	14.965	14.730	14.597	14.771	13.127	9.405
			$\pm \dots$	$\pm \dots$	± 0.080	± 0.004	± 0.004	± 0.008	± 0.032	± 0.054	$\pm \dots$	$\pm \dots$
3707	314.470000	52.342110	17.190	14.905	14.402	14.203	14.004	14.112	12.960	9.325
			$\pm \dots$	$\pm \dots$	± 0.018	± 0.003	± 0.003	± 0.005	± 0.026	± 0.037	$\pm \dots$	$\pm \dots$
3985	314.493250	52.137140	17.069	14.022	13.383	13.165	12.767	12.819	12.635	9.262
			$\pm \dots$	$\pm \dots$	± 0.089	± 0.002	± 0.001	± 0.002	± 0.024	± 0.025	$\pm \dots$	$\pm \dots$
6087	314.576760	52.171760	20.367	17.224	16.449	16.084
			$\pm \dots$	$\pm \dots$	± 0.076	± 0.018	± 0.016	± 0.025	$\pm \dots$	$\pm \dots$	$\pm \dots$	$\pm \dots$
6289	314.796590	52.197500	1.830	0.868	16.030	13.724	13.269	13.053	10.829	10.830	11.088	9.355
			± 0.022	± 0.020	± 0.019	± 0.001	± 0.001	± 0.002	± 0.023	± 0.021	± 0.116	$\pm \dots$
6506	314.729540	52.226320	...	1.304	19.935	16.363	15.563	15.163	13.429	13.473	11.947	9.001
			$\pm \dots$	± 0.098	± 0.051	± 0.009	± 0.007	± 0.012	± 0.024	± 0.029	± 0.193	$\pm \dots$
6509	314.780160	52.227280	2.203	1.027	17.412	14.400	13.614	13.308	13.064	13.038	11.879	8.670
			± 0.083	± 0.011	± 0.005	± 0.002	± 0.002	± 0.003	± 0.025	± 0.027	± 0.206	$\pm \dots$
6629	314.778760	52.248570	...	1.828	18.559	12.781	11.211	10.628	10.276	10.293	10.301	9.585
			$\pm \dots$	± 0.020	± 0.005	± 0.019	± 0.017	± 0.022	± 0.022	± 0.020	± 0.053	$\pm \dots$
6666	314.794140	52.255830	2.004	0.989	14.439	11.558	11.015	10.741	10.591	10.519	10.637	8.828
			± 0.021	± 0.006	± 0.006	± 0.015	± 0.015	± 0.022	± 0.022	± 0.021	± 0.077	$\pm \dots$
6747	314.761650	52.274440	3.242	1.442	16.077	11.715	10.871	10.446	10.371	10.136	10.347	9.434
			± 0.054	± 0.007	± 0.004	± 0.015	± 0.015	± 0.022	± 0.022	± 0.020	± 0.061	± 0.532
6828	314.753530	52.293470	1.668	0.767	17.056	14.850	14.308	14.089	13.779	13.919	12.409	9.322
			± 0.021	± 0.013	± 0.008	± 0.003	± 0.003	± 0.005	± 0.027	± 0.035	± 0.305	$\pm \dots$
6927	314.752250	52.311450	3.156	1.390	16.760	12.388	11.329	10.912	10.514	10.514	10.319	8.711
			± 0.031	± 0.012	± 0.008	± 0.023	± 0.026	± 0.032	± 0.022	± 0.020	± 0.066	$\pm \dots$

Table 6.3: Details of the variable stars.

ID	I_{mean} (mag)	RMS (mag)	Period (days)	Amp (mag)	Spectral Index (α)	Present Classification	Age* (Myr)	Mass** M_{\odot}
8	19.89	0.19	0.990	0.354	...	MS/Field
25	16.91	0.05	0.216	0.103	-1.347	CTTS	2.201±0.715	0.160±0.01
70	15.49	0.04	0.500	0.148	-3.236	MS/Field	5.145±0.894	0.584±0.037
97	18.46	0.11	0.210	0.241	-1.298	CTTS
104	16.13	0.05	5.820	0.117	-2.585	MS/Field
135	18.13	0.06	0.398	0.256	-3.966	MS/Field
250	17.53	0.05	0.330	0.157	-4.404	MS/Field
261	16.92	0.05	2.072	0.158	-3.573	MS/Field
332	17.74	0.05	0.533	0.182	...	MS/Field
383	14.91	0.05	0.639	0.144	-1.426	CTTS	6.107±0.946	0.900±0.029
491	14.42	0.07	0.345	0.184	-1.300	CTTS	0.346±0.243	0.237±0.022
497	17.21	0.05	0.692	0.112	-1.303	CTTS	7.088±0.513	0.250 ±0.02
567	16.33	0.13	0.492	0.335	-3.074	MS/Field
583	17.98	0.05	0.533	0.077	...	MS/Field
606	18.30	0.05	0.291	0.132	-2.250	WTTS
740	19.83	0.12	-2.085	WTTS
750	18.19	0.10	0.331	0.280	-1.927	WTTS
771	20.40	0.18	0.409	0.831	...	MS/Field
832	15.88	0.07	1.022	0.209	-1.973	WTTS
903	20.40	0.13	0.226	0.328	...	MS/Field
954	21.40	0.23	0.432	0.268	...	MS/Field
1142	16.59	0.07	-1.682	CTTS
1170	19.68	0.14	0.565	0.418	...	MS/Field
1259	18.05	0.09	0.305	0.293	-2.580	MS/Field
1269	18.39	0.19	2.377	0.204	-0.934	CTTS
1350	17.43	0.05	1.745	0.092	-2.067	WTTS
1422	20.29	0.15	0.632	0.272	...	MS/Field
1509	19.79	0.17	MS/Field
1516	20.50	0.26	0.352	0.487	...	MS/Field
1549	20.18	0.16	0.330	0.569	...	MS/Field
1558	20.65	0.13	0.255	0.444	...	MS/Field
1564	15.46	0.11	1.024	0.315	-1.692	CTTS	5.120±0.884	0.599±0.034
1633	20.26	0.15	0.211	0.375	-0.902	CTTS
1648	13.94	0.05	1.188	0.073	-4.471	MS/Field
1748	18.23	0.06	1.215	0.063	-1.323	CTTS
1751	17.31	0.07	0.946	0.053	-1.339	CTTS	1.817±0.511	0.130± 0.02
1771	15.72	0.16	-0.280	CTTS	4.457± 1.123	0.473±0.044
1786	16.56	0.06	1.546	0.062	-1.264	CTTS	3.965±0.761	0.243±0.017
3451	18.20	0.10	-4.092	MS/Field
3707	17.19	0.05	8.624	0.144	-3.607	MS/Field
3985	17.07	0.05	0.148	0.162	-2.823	MS/Field
6087	20.37	0.16	1.124	0.170	...	MS/Field
6289	16.03	0.11	0.154	0.303	-1.636	CTTS
6506	19.93	0.25	0.257	0.469	-1.220	CTTS
6509	17.41	0.06	0.782	0.074	-3.165	MS/Field
6629	18.56	0.07	0.662	0.090	-1.310	CTTS
6666	14.44	0.07	2.379	0.090	-1.236	CTTS	2.222±0.292	0.700±0.036
6747	16.08	0.09	0.380	0.142	-1.244	CTTS	2.248±0.751	0.233±0.024
6828	17.06	0.05	-3.245	MS/Field
6927	16.76	0.07	0.204	0.123	-1.360	CTTS	3.027± 0.338	0.200±0.03

 * Age and Mass are estimated from $V/V - I$ CMD (see text for details).

Table 6.4: Physical parameters of the candidate variable stars (see text for details)

ID	A_v (mag)	Age (Myr)	MASS (M_\odot)	RAD (R_\odot)	TEMP (K)	\dot{M}/yr ($10^{-6}M_\odot$)	M_{disc} ($10^{-3}M_\odot$)
8	2.75±1.09	3.95±3.75	0.41±0.43	2.67±2.83	3414±429	40.70±93.84	4.89±11.19
25	4.16±0.89	0.64±0.35	0.37±0.10	2.56±0.43	3510±195	0.88±2.46	0.83±2.24
70	1.31±0.40	5.53±2.31	0.81±0.29	1.40±0.73	4068±237	0.69±16.64	0.88±5.31
97	1.46±0.53	4.80±3.65	0.66±0.50	3.05±3.23	3772±426	73.67±132.12	6.43±13.74
104	1.80±0.53	5.22±2.42	0.98±0.31	1.54±0.39	4245±303	0.00±0.01	1.47±3.74
135	2.32±0.45	6.78±2.51	0.47±0.24	1.26±1.42	3669±211	9.42±58.14	1.13±4.52
250	2.03±1.31	2.83±3.82	1.13±0.95	4.59±3.19	4026±465	100.34±156.31	15.06±29.27
261	1.35±0.40	6.65±2.10	0.55±0.23	1.14±0.93	3785±204	3.43±41.06	0.69±4.55
332	1.47±0.66	6.13±2.73	0.44±0.43	1.52±2.35	3556±321	15.25±92.46	2.04±10.13
383	1.52±0.52	4.51±2.29	0.99±0.30	1.62±0.34	4271±385	0.00±0.00	0.22±1.33
491	5.00±0.00	0.27±0.00	1.07±0.00	5.59±0.00	4204± 0	0.48±0.00	0.78±0.00
497	4.55±0.84	1.24±0.59	0.53±0.13	2.17±0.55	3782±179	0.35±1.27	0.36±1.06
567	4.25±0.72	1.59±1.38	0.60±0.36	2.14±0.42	3760±450	0.21±1.15	0.32±1.41
583	1.55±0.83	4.96±3.87	0.74±0.80	3.36±4.44	3760±518	70.16±201.20	7.12±20.06
606	4.68±0.76	3.02±2.07	0.57±0.31	1.82±1.36	3766±294	1.59±12.64	1.92±7.38
740	2.58±0.93	2.83±3.77	0.62±0.53	4.18±3.36	3641±493	85.69±123.62	8.43±14.42
750	2.50±0.78	5.15±2.61	0.34±0.23	1.06±0.47	3427±360	0.79±17.63	0.50±2.07
771	2.57±1.12	1.06±2.77	0.62±0.61	5.09±3.02	3497±633	109.98±141.27	8.83±11.64
832	1.43±0.43	5.91±2.28	0.85±0.35	1.45±1.31	4092±289	5.09±62.95	1.45±6.75
903	3.71±1.19	3.59±3.60	0.16±0.11	1.72±1.21	3052±218	3.65±21.45	0.86±2.83
954	1.79±0.97	0.15±0.85	0.26±0.34	3.96±1.75	3043±429	54.41±81.50	4.28±5.68
1142	1.78±0.53	5.84±2.40	0.74±0.39	1.44±1.54	3960±337	6.90±67.19	1.73±6.89
1170	2.60±0.74	5.77±3.24	0.24±0.24	1.42±1.74	3254±266	13.00±51.73	1.47±5.78
1259	2.38±0.50	6.89±2.60	0.59±0.28	1.38±1.59	3792±286	12.98±67.68	2.05±7.32
1269	2.81±0.81	4.06±3.08	0.76±0.72	2.90±3.83	3785±511	52.27±168.96	6.10±17.36
1350	2.06±0.51	6.67±2.26	0.61±0.28	1.24±1.21	3828±283	5.85±53.04	1.32±5.85
1422	2.38±1.05	3.03±3.74	0.43±0.43	3.32±2.86	3434±452	58.71±102.22	5.79±11.56
1509	2.14±1.00	1.12±2.58	0.88±0.61	5.72±2.90	3952±735	121.78±123.22	11.94±16.62
1516	3.52±1.05	3.36±3.83	0.17±0.12	1.79±1.29	3077±197	7.47±29.50	1.30±3.60
1549	4.35±0.86	0.27±0.48	0.16±0.07	2.72±1.09	2964±179	3.42±8.51	1.51±3.20
1558	2.76±1.22	1.22±2.64	0.59±0.43	4.77±2.82	3647±438	71.90±104.61	7.84±13.35
1564	4.00±0.91	2.49±2.24	1.63±0.52	2.97±0.84	4719±441	0.13±0.47	7.91±12.13
1633	2.33±0.92	2.59±3.36	0.60±0.36	3.83±2.78	3729±360	82.50±107.98	8.44±14.77
1648	1.17±0.45	6.18±2.28	1.55±0.32	1.94±0.82	5009±759	0.02±0.32	2.08±10.04
1748	4.42±0.45	0.15±0.13	0.31±0.05	3.28±0.30	3378±134	2.05±1.37	2.34±2.48
1751	4.57±0.60	0.26±0.15	0.47±0.13	3.51±0.36	3686±169	3.56±3.53	1.45±1.73
1771	3.61±1.34	0.47±0.44	0.99±0.63	3.98±0.85	4094±444	2.11±4.89	8.24±11.68
1786	4.17±0.75	0.53±0.25	0.40±0.10	2.83±0.40	3576±174	0.84±2.10	0.73±2.21
3451	1.95±1.26	0.14±0.12	0.30±0.28	3.14±0.92	3218±391	9.06±50.47	4.76±6.78
3707	1.18±0.39	5.22±2.46	0.26±0.20	1.03±0.64	3321±266	0.95±18.38	0.40±3.72
3985	2.76±0.76	2.70±2.22	0.37±0.30	1.54±0.59	3416±437	0.46±9.49	0.51±2.91
6087	3.40±1.08	3.48±3.84	0.16±0.11	1.82±1.33	3050±212	8.70±28.93	1.11±3.26
6289	2.55±0.58	2.83±2.38	1.48±0.45	2.55±0.72	4615±347	0.03±0.12	4.97±11.80
6506	2.98±1.32	2.89±2.61	0.44±0.42	1.83±1.70	3467±536	14.64±68.89	2.51±6.47
6509	3.02±0.62	5.40±2.41	0.66±0.27	1.33±0.77	3899±294	1.43±23.47	0.87±4.29
6629	4.70±0.25	0.07±0.05	0.28±0.05	3.46±0.34	3290±149	2.45±1.76	2.90±2.55
6666	3.35±0.97	2.21±1.66	1.50±0.65	2.79±0.59	4625±619	0.10±0.60	0.02±0.20
6747	4.09±0.83	0.37±0.15	0.42±0.10	3.21±0.32	3619±160	1.53±2.96	0.49±1.12
6828	1.21±0.35	7.19±2.01	0.55±0.25	1.16±1.18	3785±191	6.54±50.73	1.11±6.38
6927	4.25±0.95	0.44±0.22	0.41±0.11	3.01±0.37	3585±161	1.33±2.78	0.48±1.30

Chapter 7

Summary and Future Work

In this dissertation work, one of the primary goals is to understand the star formation and young stellar objects (YSOs) of the Galactic young H II regions. Massive OB stars in H II environments have the influence that leads to new star-formation processes through several feedback mechanisms e.g. radiation driven implosion, collects and collapse processes. We have investigated the fundamental properties of YSOs in the Galactic young H II regions, e.g. their distance, reddening, stellar density, masses, ages including age dispersion, disc frequency, star formation mechanism, etc. With those parameter space, we understand the star-formation mechanism and scenario. Variable properties of these YSOs are also useful diagnostic techniques to characterize them. Low and intermediate mass stars build up their masses through accretion from their circumstellar disc. Circumstellar discs play an important role to moderate the accretion processes. Accretion and variable accretion properties could be detected from H_α emission and the light curve analysis, and those are undertaken here. An extensive study of the spectroscopic behavior of massive stars is studied as part of this work.

For observations on these young star-forming regions, we have carried out multi wavelength data from optical to radio bands to understand a comprehensive picture of those issues mentioned above. The deep optical *BVRI* and *I*-band CCD time series observations have been obtained from the 1.30-m Devasthal Fast Optical Telescope, ARIES, Nainital; 1-m Sampurnand

Telescope, ARIES, Nainital; and 2-m Himalayan Chandra Telescope (HCT), IAO, Hanle; slit spectroscopy and slitless spectroscopic observations have been taken at 2-m HCT. Near-Infrared (NIR) data in J , H , K bands were initially observed from 1.2m Mt. Abu Telescope. The NIR data in J , H , K bands have also been obtained from UKIDSS, WIRCAM, and 2MASS data archive. The Mid-Infrared (MIR) data have been obtained from the WISE and *Spitzer* space telescopes. Additional sets of data from IRAS (far-IR), FCRAO (radio), JCMT(radio) and NVSS(radio) are also used for this study. The main results obtained from our studies are given below.

NGC 2282: In chapter 3 of this thesis, we have presented multiwavelength studies of a young cluster NGC 2282 in Monoceros constellation, using deep optical BVI observations complemented with the archival data sets from IPHAS, UKIDSS, 2MASS and mid-IR data from *Spitzer* 3.6 and 4.5 μm . We have also used the spectroscopy observations of 8 bright sources in the cluster region. From the stellar surface density distribution of K -band data the radius of the cluster has been estimated to be $\sim 3.15'$ from the semi-major axis of the outer most elliptical contour. From spectrophotometry study of 8 bright sources, We have identified three early B-type members in the cluster. Among these B-type massive members, HD 289120, a B2V type star was classified earlier, and two stars (a Herbig Ae/Be star and a B5 V) are classified for the first time in this work. We have estimated the distance to the cluster as ~ 1.65 kpc from spectrophotometric analysis of those massive members. The K -band extinction map is estimated from $(H - K)$ colors using nearest neighborhood technique, and the mean extinction within the cluster area is found to be $A_V \sim 3.9$ mag. The extinction within the cluster region seems to be non-uniform. From slitless spectroscopy and IPHAS data, we identified 50 H_α emission line stars towards the region. We have classified 9 Class I and 75 Class II objects from mid-IR data. Other candidate YSOs are identified from near-IR $(J - H)/(H - K)$ CC diagram. We have identified 152 candidate YSOs from IR excess and H_α emission towards the region. We characterized these YSOs from various color-magnitude diagrams. From $V/(V - I)$ CMD, we have estimated the cluster age which is in the range of $\sim 2-5$ Myr. From mid-IR data, we

have estimated the disc fraction of $\sim 58\%$, which corresponds to an age of $\sim 2\text{-}5$ Myr. The masses of the candidate YSOs are found to be in the range ~ 0.1 to $2.0 M_{\odot}$ in the $J/(J-H)$ CMD. The morphology of the region has been studied from the spatial distribution of YSOs, stellar density distribution, the signature of dust in various optical-infrared images along with the extinction map.

In chapter 5, We have reported CCD I -band time series photometry of cluster NGC 2282 to identify and characterize the variability of PMS stars. The deep I -band photometry, down to ~ 20.5 mag, enables us to probe variability towards the low-mass end ($\sim 0.1 M_{\odot}$) of PMS stars. From the light curves of 1627 stars, we have identified 62 new photometric variable candidates. Their association with the region were established from H_{α} emission and infrared excess. Among 62 variables, 30 young variables show H_{α} emission, near-IR/mid-IR excess or both, and they are candidate members of the cluster. Out of 62 variables, 41 are periodic variables and show the rotation rate from 0.2 to 7 days. The period distribution shows a median period at ~ 1 day as seen in other young clusters (e.g. NGC 2264, ONC, etc.), but it shows uni-modal distribution unlike others having bi-modal distribution with slow rotators peaking at $\sim 6\text{--}8$ days. To investigate rotation-disc and variability-disc connection, we derived near-infrared (NIR) excess from $\Delta(I-K)$ and mid-IR excess from *Spitzer* $[3.6]\text{--}[4.5] \mu\text{m}$ data. No conclusive evidence of slow rotation with disc stars and fast rotation for discless stars is found from our periodic variables. A clear increasing trend of variability amplitude with IR excess is found for all variables. Period-mass correlation in the mass range $0.3\text{--}2.6 M_{\odot}$ show an evidence of fast rotation with decreasing masses at the lower end as seen in the literature.

Sh2-149: In chapter 4, we have presented deep WIRCAM HK , *Spitzer*-IRAC, radio continuum observations of the S149 complex. We explore its stellar and interstellar content, as well as the star-formation history of the region. The S149 cloud complex associated with sub-regions S149, S148, S147 and the region is extended towards S-E border. There are six IRAS sources, located at cold peak identified by mid-IR emission, and those are tracers of young massive stars in dust cocoon. S148 region spreads over relatively large H II area compared to other

sub-regions, where a high population of YSOs is seen. The half circular ring of S147 could be due to the collection of material at the H II interface, which might be a good example of the collect and collapse process. We studied spectroscopically two massive ionizing sources in the central region of S149, and S148. Furthermore, we find several pieces of evidence from 1.4GHz and IRAS observational data that suggest the presence of another at least two massive sources at the central cavity of S147. Using the IRAC and NIR CC diagrams, we identified 575 candidate YSOs, which includes 16 Class I, 39 Class II, 520 NIR excess sources. We find that high spatial distribution of YSOs along with the high column density location in CO map, with clustering around ionizing sources, indicating recent star-formation at multiple sites. In conclusion, it seems that multi-generation star formation is going on through out the molecular cloud complex. Several observational pieces of evidence suggest that the triggering star formation is possibly taking place at the immediate periphery of the S149 region. Whereas, those massive ionizing sources could have been formed spontaneously or by other processes at the massive cores.

Cygnus OB7: In chapter 6, we have studied *I* band monitoring studies of stars towards Cyg OB7 using deep optical *VRI* observations complemented with the NIR *JHK* and WISE 3.4, 4.6, 12 and 22 μm . The deep *I*-band (~ 20.5 mag) analysis enables us to probe the study of variability towards the low-mass end of PMS stars. Using root-mean-square (RMS) deviation technique from the differential photometry light curves, we have identified 50 photometric variable stars and subsequently verified by visual inspection of the light curve, period and phase light curve. Out of 50 candidate variables, 45 are new variables in this study and 5 are known from previous studies. Among these 45 new candidate variables, 40 show periodic or quasi-periodic variation. The periods of variable candidates exhibit in the range 0.14 to 8.62 days. From SED analysis and location on $J - H/H - K$ CCD space, we selected 19 variable stars are CTTSs, 5 are WTTS and rest could be WTTS, MS or other field stars. $V/(V - I)$ CMD suggested that majority of variables, particularly CTTSs have age < 10 Myrs. To find out any

correlation of disc and variability, we studied periods and RMS distribution in $(W1 - W2)$ and $\Delta(I - K)$ space. But, we don't find any conclusive evidence.

In **conclusion**, the three young H II regions in the present study are found to have diverse nature in their environments. Our multi-wavelength analysis helps to characterize the fundamental properties of these regions for the first time. Age analysis shows that the YSOs in two H II regions (NGC 2282 and Sh 2-149 complex) are having an age spread of 5 Myr, implying non-coeval star formation in these regions. The variable PMS stars in the studied region of Cygnus OB7, are slightly older (< 10 Myr). The presence of many periodic variable stars in this region suggest that they are probably transition disc CTTSs or WTTSs. The estimated mass range of YSOs in all three regions are $\sim 2.5 - 0.1 M_{\odot}$. We also identified the massive sources in the studied regions. The YSOs with circumstellar disc are found to be more in the number associated with young regions. All the three regions are found to have different star formation scenario. The cluster NGC 2282 is a well-isolated star forming region, which does not seem to have any influence on its surroundings. Whereas S149 complex is associated with a large molecular cloud, the local star formation seems to have influenced from its surrounding environments. But within the region, the massive star and its ionization front caused for the collect and collapse star formation scenario in it, and hence lead to new generation of star formation.

7.1 Future Plan

From my working experience on Galactic young and massive star-forming regions, I want to pursue my investigation further in this direction to address molecular gas properties using multi wavelength maps on H II regions, various properties of the YSOs like IR excess, H_α emission, variable phenomena. Those understandings could be linked to the understanding of their environment and formation. I have the plan to take up the following issues:

Feedback from massive stars: We have proposed high-mass/cluster formation scenario (Sh 2-149 complex) based on external feedback from high-mass stars. This constructive feedback mechanism could not only explain the formation of whole clusters with an observed decreasing age toward the inner regions, but could ensure the availability of material during cluster formation, and address various outstanding issues in high-mass star formation theory. Multi-wavelength observations in NIR, MIR along with high resolution ^{12}CO , ^{13}CO and ^{18}CO mapping will be conducted to explore the morphology, star formation activity and evolutionary status of YSOs associated with the dark embedded molecular clouds. Future study of these embedded molecular clouds in radio wavelength at GMRT and far-infrared for Herschel observations will be proposed to gain an idea about early star formation processes.

Circumstellar disc evolution and planet formation: In our multi-wavelength analysis of three star forming regions, we have mainly used the multi-wavelength photometry criteria to identify the candidate YSOs of the regions. Such molecular cloud is also courageous to probe the origin of our solar system because the presence of rare, short-lived radio nuclides in meteoritic samples has long suggested that the formation of the sun was excited by a massive star within a GMC (Goswami & Vanhala 2000; Lada & Lada 2003). With time circumstellar disc around CTTSs dissipates, and it becomes a discless or small disc in WTTSs. These WTTSs are considered to be the best place to search new planet.

Circumstellar disc evolution in low mass stars and brown dwarfs: The circumstellar disc accretion scenario is entirely different in massive stars and low mass PMS stars. This observed fact leads to some other basic ideas. Are the basic physical characteristics such as accretion time scale, size, mass, etc. of the circumstellar disc around brown dwarfs the same as for low mass stars? Establishing the properties of circumstellar disc around brown dwarfs and low mass stars will be one of the primary motivation for my future work.

Bibliography

- [1] Allen L. E., Calvet, N., & D'Alessio, P., et al. 2004, ApJS, 154, 363
- [2] Allen L. E., Storm K. M. 1995, AJ, 109, 3
- [3] Allen T. S. et al. 2008, ApJ, 675, 491
- [4] Alexander, M. J., Kobulnicky, H. A., Kerton, C. R., & Arvidsson, K., 2013, ApJ, 770, 1
- [5] Avedisova, V. S., & Kondratenko, G. I., 1984, Nauchnye Informasii, 56, 59
- [6] Anderson, L. D., Bania, T. M., Jackson, J. M., et al. 2009, ApJS, 181, 255
- [7] Anderson, L. D., Zavagno, A., Deharveng, L., et al. 2012, A&A, 542, A10
- [8] Azimlu, M., & Fich, M. 2011, AJ, 141, 123
- [9] Baraffe, I., Chabrier, G., Allard, F., & Hauschildt, P. H. 1998, A&A, 337, 403
- [10] Barentsen et al. 2011, MNRAS, 415, 103
- [11] Balona, L. A. 1984, MNRAS, 211, 973
- [12] Barentsen, G., Farnhill, H. J., Drew, J. E., et al. 2014, MNRAS, 444, 3230
- [13] Bergeat, J., Sibille, F., & Lunel, M. 1975, A&A, 40, 347
- [14] Basri, G., & Bertout, C. 1989, ApJ, 341, 340
- [15] Bessell, M. S., & Brett, J. M. 1988, PASP, 100, 1134

- [16] Bertoldi, F. 1989, *ApJ*, 346, 735
- [17] Bertin, E., & Arnouts, S. 1996, *A&AS*, 117, 393
- [18] Bertout, C., Basri, G., & Bouvier, J. 1988, *ApJ*, 330, 350
- [19] Bertoldi, F., & McKee, C. F. 1990, *ApJ*, 354, 529
- [20] Beuther, H., Zhang, Q., Sridharan, T. K., Lee, C.-F., & Zapata, L. A. 2006, *A&A*, 454, 221
- [21] Biazzo, K., Melo, C. H. F., Pasquini, L., et al. 2009, *ApJ*, 508, 1301
- [22] Bressan, A., Marigo, P., Girardi, L., et al. 2012, *MNRAS*, 427, 127
- [23] Blitz, L. 1979, *ApJ*, 231, L115
- [24] Blitz, L., Fich, M., & Stark, A. A. 1982, *ApJS*, 49, 183
- [25] Blitz, L. 1991, *NATO Advanced Science Institutes (ASI) Series C*, 342, 3
- [26] Blitz, L. 1993, *Protostars and Planets III*, 125
- [27] Bontemps, S., Andre, P., Terebey, S., & Cabrit, S. 1996, *A&A*, 311, 858
- [28] Bouvier, J. 2007, *Star-Disk Interaction in Young Stars*, 243, 231
- [29] Briceño, C., Calvet, N., Hernández, J., et al. 2005, *AJ*, 129, 907
- [30] Briceño, C., Luhman, K. L., Hartmann, L., Stauffer, J. R., & Kirkpatrick, J. D. 2002, *ApJ*, 580, 317
- [31] Briceño, C., Vivas, A. K., Calvet, N., et al. 2001, *Science*, 291, 93
- [32] Brinks, E., Braun, R., & Unger, S. W. 1990, *NASA Conference Publication*, 3084
- [33] Buckle, J. V., Hills, R. E., Smith, H., et al. 2009, *MNRAS*, 399, 1026
- [34] Calvet, N., Hartmann, L., Kenyon, S. J., & Whitney, B. A. 1994, *ApJ*, 434, 330

- [35] Camenzind, M. 1990, *Reviews in Modern Astronomy*, 3, 234
- [36] Caplan, J., Deharveng, L., Peña, M., Costero, R., & Blondel, C. 2000, *MNRAS*, 311, 317
- [37] Carpenter, J. M. 2001, *AJ*, 121, 2851
- [38] Carpenter, J. M., Hillenbrand, L. A., & Skrutskie, M. F. 2001, *AJ*, 121, 3160
- [39] Carpenter, J. M., Hillenbrand, L. A., Skrutskie, M. F., & Meyer, M. R. 2002, *AJ*, 124, 1001
- [40] Casertano, S. & Hut, P., 1985, *ApJ*, 298, 80
- [41] Casoli, F., Combes, F., Dupraz, C., Gerin, M., & Boulanger, F. 1986, *A&A*, 169, 281
- [42] Churchwell, E. 2002, *ARA&A*, 40, 27
- [43] Churchwell, E., Felli, M., Wood, D. O. S., & Massi, M. 1987, *ApJ*, 321, 516
- [44] Chini, R., Mezger, P. G., Kreyna, E., & Gemünd, H. P., 1984, *A&A*, 135, L14
- [45] Cieza, L., & Baliber, N. 2007, *ApJ*, 671, 605
- [46] Cody, A. M., & Hillenbrand, L. A. 2010, *ApJS*, 191, 389
- [47] Cody, A. M., Hillenbrand, L. A., David, T. J., et al. 2017, *ApJ*, 836, 41
- [48] Coker, C. T., Pinsonneault, M., & Terndrup, D. M. 2016, *ApJ*, 833, 122
- [49] Cody, A. M., & Hillenbrand, L. A. 2014, *ApJ*, 796, 129
- [50] Cohen J. G., Frogel J. A., Persson S. E., Ellias J. H., 1981, *ApJ*, 249, 481
- [51] Cohen, R. E., Herbst, W., & Williams, E. C. 2004, *AJ*, 127, 1602
- [52] Cohen, J. G., Persson, S. E., Elias, J. H., & Frogel, J. A. 1981, *ApJ*, 249, 481
- [53] Cohen, M., Tielens, A. G. G. M., Bregman, J., et al. 1989, *ApJ*, 341, 246

- [54] Comeron, F., & Torra, J. 1994, *ApJ*, 423, 652
- [55] Condon, J. J., Cotton, W. D., Greisen, E. W., et al. 1998, *AJ*, 115, 1693
- [56] Corradi et al. 2008, *A&A* 480, 409
- [57] Crampton, D., Georgelin, Y. M., & Georgelin, Y. P. 1978, *A&A*, 66, 1
- [58] Cutri, R. M., Skrutskie, M. F., van Dyk, S., et al. 2003, “The IRSA 2MASS All-Sky Point Source Catalog, NASA/IPAC Infrared Science Archive, <http://irsa.ipac.caltech.edu/applications/Gator/>
- [59] Cutri, R. M., Skrutskie, M. F., van Dyk, S., et al. 2012, *VizieR Online Data Catalog*, 2281
- [60] D’Antona, F., & Mazzitelli, I. 1994, *ApJS*, 90, 467
- [61] Dahm, S. E., & Simon, T. 2005, *AJ*, 129, 829
- [62] Dame, T. M., Ungerechts, H., Cohen, R. S., et al. 1987, *pJ*, 322, 706
- [63] Dame, T. M., Hartmann, D., & Thaddeus, P. 2001, *ApJ*, 547, 792
- [64] Deharveng, L., Lefloch, B., Kurtz, S., et al. 2008, *A&A*, 482, 585
- [65] Deharveng, L., Lefloch, B., Zavagno, A., et al. 2003, *A&A*, 408, L25
- [66] Deharveng, L., Schuller, F., Anderson, L. D., et al. 2010, *A&A*, 523, A6
- [67] Deharveng, L., Zavagno, A., Schuller, F., et al. 2009, *A&A*, 496, 177
- [68] Deharveng, L., Zavagno, A., & Caplan, J. 2005, *A&A*, 433, 565
- [69] Dobashi, K., Yonekura, Y., Matsumoto, T., et al. 2001, *PASJ*, 53, 85
- [70] Dobbs, C. 2013, *Astronomy and Geophysics*, 54, 5.24
- [71] Drew, J. E., Greimel, R., Irwin, M. J., et al. 2005, *MNRAS*, 362, 753
- [72] Dutta, S., Mondal, S., Jose, J., et al. 2015, *MNRAS*, 454, 3597

- [73] Elias, J. H., Frogel, J. A., Matthews, K., & Neugebauer, G. 1982, *AJ*, 87, 1029
- [74] Edwards, S., Strom, S. E., Hartigan, P., et al. 1993, *AJ*, 106, 372
- [75] Elmegreen, B. G., & Efremov, Y. N. 1997, *ApJ*, 480, 235
- [76] Elmegreen, B. G. 1994, *ApJ*, 425, L73
- [77] Elmegreen, B. G., & Lada, C. J. 1977, *ApJ*, 214, 725
- [78] Elmegreen, B. G. 1998, *Origins*, 148, 150
- [79] Evans, N. J., II 1999, *ARA&A*, 37, 311
- [80] Evans, N. J., II, Dunham, M. M., Jørgensen, J. K., et al. 2009, *ApJS*, 181, 321-350
- [81] Falgarone, E., Phillips, T. G., & Walker, C. K. 1991, *ApJ*, 378, 186
- [82] Fazio, G. G., Hora, J. L., Allen, L. E., et al. 2004, *ApJS*, 154, 10
- [83] Flaherty, K. M., Pipher, J. L., Megeath, S. T., et al. 2007, *ApJ*, 663, 1069
- [84] Fukuda, N., & Hanawa, T. 2000, *ApJ*, 533, 911
- [85] Garay, G., Moran, J. M., & Reid, M. J. 1987, *ApJ*, 314, 535
- [86] Girardi, L., Bertelli, G., Bressan, A., et al. 2002, *A&A*, 391, 195
- [87] Glushkov, Y. I., Denisyuk, E. K., & Karyagina, Z. V. 1975, *A&A*, 39, 481
- [88] González-Solares, E. A., Walton, N. A., Greimel, R., et al. 2008, *MNRAS*, 388, 89
- [89] Goswami, J. N., & Vanhala, H. A. T. 2000, *Protostars and Planets IV*, 963
- [90] Gutermuth R. A., Megeath S. T., Pipher J. L., Williams J. P., Allen L. E., Myers P. C., Raines S. N. 2005, *ApJ*, 632, 397
- [91] Gutermuth, R. A., Megeath, S. T., Myers, P. C., et al. 2009, *ApJS*, 184, 18

- [92] Gutermuth, R. A., Myers, P. C., Megeath, S. T., et al. 2008, *ApJ*, 674, 336-356
- [93] Haisch, K. E. Jr., Lada, E. A. & Lada, C. J., 2001, *ApJ*, 553, L153
- [94] Hartmann, L. 1998, *Accretion processes in star formation / Lee Hartmann*. Cambridge, UK ; New York : Cambridge University Press, 1998. (Cambridge astrophysics series ; 32) ISBN 0521435072.
- [95] Hartmann, L. 2002, *ApJ*, 566, L29
- [96] Hartmann, L., & Kenyon, S. J. 1996, *ARA&A*, 34, 207
- [97] Hayashi, C. 1961, *PASJ*, 13, 450
- [98] Helou, G., & Walker, D. W. 1988, *NASA RP-1190*, Vol. 7 (1988), 7
- [99] Herbig, G. H. 1960, *ApJS*, 4, 337
- [100] Herbig, G. H. 1962, *Advances in Astronomy and Astrophysics*, 1, 47
- [101] Herbig, G. H., & Bell, K. R. 1988, *Third catalog of emission-line stars of the Orion population.*, by G.H. gerbig and K.R. Bell. *Lick Observatory Bulletin #1111*, Santa Cruz: Lick Observatory, Jun 1988, 90 p., 1111
- [102] Herbst, W., Bailer-Jones, C. A. L., Mundt, R., Meisenheimer, K., & Wackermann, R. 2002, *A&A*, 396, 513
- [103] Herbst, W., Eislöffel, J., Mundt, R., & Scholz, A. 2007, *Protostars and Planets V*, 297
- [104] Herbst, W., Herbst, D. K., Grossman, E. J., & Weinstein, D. 1994, *AJ*, 108, 1906
- [105] Herbst, W., Rhode, K. L., Hillenbrand, L. A., & Curran, G. 2000, *AJ*, 119, 261
- [106] Hernández, J., Hartmann, L., Megeath, T., et al. 2007, *ApJ*, 662, 1067
- [107] Herczeg, G. J., Dong, S., Shappee, B. J., et al. 2016, *ApJ*, 831, 133
- [108] Herczeg, G. J., & Hillenbrand, L. A., 2014, *ApJ*, 786, 97

- [109] Henden, A. A., Templeton, M., Terrell, D., et al. 2016, VizieR Online Data Catalog, 2336,
- [110] Hester, J. J., Scowen, P. A., Sankrit, R., et al. 1996, AJ, 111, 2349
- [111] Heyer, M. H., Brunt, C., Snell, R. L., et al. 1998, ApJS, 115, 241
- [112] Holland, W. S., Bintley, D., Chapin, E. L., et al. 2013, MNRAS, 430, 2513
- [113] Hillenbrand, L. A. 1997, AJ, 113, 1733
- [114] Hillenbrand, L. A. 2002, arXiv: astro-ph/0210520
- [115] Hillenbrand, L. A., Strom, S. E., Calvet, N., et al. 1998, AJ, 116, 1816
- [116] Hiltner, W. A. 1956, ApJS, 2, 389
- [117] Hollenbach, D. J., & Tielens, A. G. G. M. 1997, ARA&A, 35, 179
- [118] Horner, D. J., Lada, E. A., & Lada, C. J. 1997, AJ, 113, 1788
- [119] Houck, J. R., Roellig, T. L., Van Cleve, J., et al. 2004, SPIE, 5487, 62
- [120] Irwin, J., Hodgkin, S., Aigrain, S., et al. 2008, MNRAS, 384, 675
- [121] Jacoby G. H., Hunter D. A., Christian C. A., 1984, ApJS, 56, 257
- [122] Jeans, J. H. 1928, Cambridge [Eng.] The University press, 1928
- [123] Joergens, V., Fernández, M., Carpenter, J. M., & Neuhäuser, R. 2003, ApJ, 594, 971
- [124] Jose J., Pandey A. K., Ogura K., Samal. M. R., Ojha D. K., Bhatt B. C., Chauhan N.,
Eswaraiah C., Mito H., Kobayashi N., Yadav R. K., 2012, MNRAS, 424, 2486
- [125] Jose J., Pandey A. K., Samal M. R., Ojha D. K., Ogura K., Kim J. S., Kobayashi N.,
Goyal A., Chauhan N., Eswaraiah C., 2013, MNRAS, 432, 3445
- [126] Joy, A. H. 1945, ApJ, 102, 168
- [127] Keenan, R. C., Barger, A. J., Cowie, L. L., & Wang, W.-H. 2010, ApJ, 723, 40

- [128] Kennicutt, R. C., & Evans, N. J. 2012, *ARA&A*, 50, 531
- [129] Kenyon, S. J., Yi, I., & Hartmann, L. 1996, *ApJ*, 462, 439
- [130] Kenyon S., & Hartman 1995, *ApJS*, 101, 117
- [131] Kerton, C. R., Arvidsson, K., Knee, L. B. G., & Brunt, C. 2008, *MNRAS*, 385, 995
- [132] Khanzadyan, t., et al. 2012, *A&A*, 542, 111
- [133] Kislyakov, A. G., & Turner B. E. 1995, *AZh*, 72, 168
- [134] Kirsanova, M. S., Sobolev, A. M., Thomasson, M., et al. 2008, *MNRAS*, 388, 729
- [135] Kley, W., & Lin, D. N. C. 1999, *ApJ*, 518, 833
- [136] Koenigl, A. 1991, *ApJ*, 370, L39
- [137] Koorneef J., 1983, *A&A*, 128, 84
- [138] Kurtz, S., Cesaroni, R., Churchwell, E., Hofner, P., & Walmsley, C. M. 2000, *Protostars and Planets IV*, 299
- [139] Kurtz, S., Churchwell, E., & Wood, D. O. S. 1994, *ApJS*, 91, 659
- [140] Kutner, M. L., Machnik, D. E., Tucker, K. D., & Dickman, R. L., 1980, *ApJ*, 237, 734
- [141] Lada, C. J. 1987, *Star Forming Regions*, 115, 1
- [142] Lada, C. J. 2005, *Progress of Theoretical Physics Supplement*, 158, 1
- [143] Lada, C. J., & Adams, F. C. 1992, *ApJ*, 393, 278
- [144] Lada, C. J., Elmegreen, B. G., Cong, H.-I., & Thaddeus, P. 1978, *ApJ*, 226, L39
- [145] Lada, C. J., & Lada, E. A. 1991, *The Formation and Evolution of Star Clusters*, 13, 3
- [146] Lada, E. A., & Lada, C. J., 1995, *AJ*, 109, 1682

- [147] Lada C. J., & Lada E. A., Climens D. P., Bally J., 1994, ApJ 429, 694
- [148] Lada, C. J., Muench, A. A., Haisch, K. E., Jr., et al. 2000, AJ, 120, 3162
- [149] Lada, C. J., Muench, A. A., Luhman, K. L., et al. 2006, AJ, 131, 1574
- [150] Lada, E. A., Depoy, D. L., Evans, N. J., II, & Gatley, I. 1991, ApJ, 371, 171
- [151] Lada C. J., Lombardi M., Alves J. F., 2010, ApJ, 724, 687
- [152] Lada, C. J., & Lada, E. A. 2003, ARA&A, 41, 57
- [153] Lada, C. J., & Wilking, B. A. 1984, ApJ, 287, 610
- [154] Lamm, M. H., Bailer-Jones, C. A. L., Mundt, R., Herbst, W., & Scholz, A. 2004, A&A, 417, 557
- [155] Lamm, M. H., Mundt, R., Bailer-Jones, C. A. L., & Herbst, W. 2005, A&A, 430, 1005
- [156] Landolt A. U., 1992. AJ, 104, 340
- [157] Langer, W. D., Castets, A., & Lefloch, B. 1996, ApJ, 471, L111
- [158] Lata, S., Pandey, A. K., Chen, W. P., Maheswar, G., & Chauhan, N. 2012, MNRAS, 427, 1449
- [159] Lawrence, A., Warren, S. J., Almaini, O., et al. 2007, MNRAS, 379, 1599
- [160] Leisawitz D., Bash F. N. & Thaddeus P., 1989, ApJS, 70, 731
- [161] Lefloch, B., & Lazareff, B. 1994, A&A, 289, 559
- [162] Lenz, P., & Breger, M. 2005, Communications in Asteroseismology, 146, 53
- [163] Littlefair, S. P., Dhillon, V. S., & Martín, E. L. 2005, A&A, 437, 637
- [164] Littlefair, S. P., Naylor, T., Mayne, N. J., Saunders, E., & Jeffries, R. D. 2011, MNRAS, 413, L56

- [165] Littlefair, S. P., Naylor, T., Burningham, B., & Jeffries, R. D. 2005, *MNRAS*, 358, 341
- [166] Lomb, N. R. 1976, *Ap&SS*, 39, 447
- [167] Lucas, P. W., Hoare, M. G., Longmore, A., et al. 2008, *MNRAS*, 391, 136
- [168] Luhman, K. L., Peterson, D. E., Megeath, S. T., 2004, *ApJ*, 617, 565
- [169] Lundquist M. J., Kobulnicky H. A., Alexander M. J., Kerton C. R., Arvidsson K., 2014, *ApJ*, 784, 111
- [170] Makidon, R. B., Rebull, L. M., Strom, S. E., Adams, M. T., & Patten, B. M. 2004, *AJ*, 127, 2228
- [171] Makovoz, D., & Khan, I. 2005, *Astronomical Data Analysis Software and Systems XIV*, 347, 81
- [172] Makovoz, D., & Marleau, F. R. 2005, *PASP*, 117, 1113
- [173] Matt, S., & Pudritz, R. E. 2005, *MNRAS*, 356, 167
- [174] Massey, P., Strobel, K., Barnes, J. V., & Anderson, E. 1988, *ApJ*, 328, 315
- [175] McKee, C. F. 1999, *NATO Advanced Science Institutes (ASI) Series C*, 540, 29
- [176] Ménard, F., & Bertout, C. 1999, *NATO Advanced Science Institutes (ASI) Series C*, 540, 341
- [177] Meyer, M. R., Calvet, N., & Hillenbrand, L. A. 1997, *AJ*, 114, 288
- [178] Megeath, S. T., Gutermuth, R. A., Allen, L. E., Pipher, J. L., Myers, P. C., & Fazio, G. G., 2004, *ApJS*, 154, 367
- [179] Mezger, P. G., & Henderson, A. P. 1967, *ApJ*, 147, 471
- [180] Mondal, S., Lin, C. C., Chen, W. P., et al. 2010, *AJ*, 139, 2026
- [181] Moran, J. M. 1983, *RMxAA*, 7, 95

- [182] Melikian, N. D., Karapetian, A. A., & Gomez, J. 2016, *Astrophysics*, 59, 484
- [183] Miyama, S. M., Narita, S., & Hayashi, C. 1987, *Progress of Theoretical Physics*, 78, 1051
- [184] Neugebauer, G., Habing, H. J., van Duinen, R., et al. 1984, *ApJ*, 278, L1
- [185] Nguyen, D. C., Jayawardhana, R., van Kerkwijk, M. H., et al. 2009, *ApJ*, 695, 1648
- [186] Nordhagen, S., Herbst, W., Rhode, K. L., & Williams, E. C. 2006, *AJ*, 132, 1555
- [187] Ojha, D. K., Tamura, M., Nakajima, Y., et al. 2004, *ApJ*, 608, 797
- [188] Oke J. B. 1990, *AJ*, 99, 5
- [189] Panagia, N. 1973, *AJ*, 78, 929
- [190] Panagia, N., & Felli, M. 1975, *A&A*, 39, 1
- [191] Pecaut M. J. & Mamajek, E. E., 2013, *ApJS*, 208, 9
- [192] Persi, P., Roth, M., Tapia, M., Ferrari-Toniolo M., & Marenzi, A. R., 1994, *A&A*, 282, 474
- [193] Petrossian, V. M., 1985, *ATR*, 22, 423
- [194] Phelps, R. L., & Lada, E. A. 1997, *ApJ*, 477, 176
- [195] Pomarès, M., Zavagno, A., Deharveng, L., et al. 2009, *A&A*, 494, 987
- [196] Prabhu, T. P. 2014, *Proceedings of the Indian National Science Academy Part A*, 80, 887
- [197] Puget, P., Stadler, E., Doyon, R., et al. 2004, *SPIE*, 5492, 978
- [198] Racine, R., 1968, *AJ*, 73, 233
- [199] Ramsay, S. K., Mountain, C. M., & Geballe, T. R. 1992, *MNRAS*, 259, 751
- [200] Rebull, L. M. 2001, *AJ*, 121, 1676

- [201] Rebull, L. M., Padgett, D. L., McCabe, C.-E., et al. 2010, *ApJS*, 186, 259
- [202] Rebull, L. M., Stauffer, J. R., Megeath, S. T., Hora, J. L., & Hartmann, L. 2006, *ApJ*, 646, 297
- [203] Reach, W. T., Megeath, S. T., Cohen, M., et al. 2005, *PASP*, 117, 978
- [204] Reipurth, B. 1983, *A&A*, 117, 183
- [205] Reipurth, B., & Schneider, N. 2008, *Handbook of Star Forming Regions, Volume I*, 4, 36
- [206] Rice, T., Wolk, S., Aspin, C., 2012, *ApJ*, 755, 65
- [207] Rieke, G. H., Young, E. T., Engelbracht, C. W., et al. 2004, *ApJS*, 154, 25
- [208] Rice, T. S., Reipurth, B., Wolk, S. J., Vaz, L. P., & Cross, N. J. G. 2015, *AJ*, 150, 132
- [209] Rice, T. S., Wolk, S. J., & Aspin, C. 2012, *ApJ*, 755, 65
- [210] Rodríguez-Ledesma, M. V., Mundt, R., & Eislöffel, J. 2010, *ApJ*, 515, A13
- [211] Robitaille, T. P., Whitney, B. A., Indebetouw, R., Wood, K., & Denzmore, P. 2006, *ApJS*, 167, 256
- [212] Robitaille, T. P., Whitney, B. A., Indebetouw, R., & Wood, K. 2007, *ApJs*, 169, 328
- [213] Russell, R. W. 1978, *A&A*, 67, 273
- [214] Sagar, R., Omar, A., Kumar, B., et al. 2011, *Current Science*, 101, 1020
- [215] Samal M. R., Ojha D. K., & Jose J., et al. 2015, *A&A*, 581, 5
- [216] Samal M. R., Zavagno A., Deharveng L., Molinari S., Ojha D. K., Paradis D., Tigé J., Pandey A. K., Russeil D., 2014, *A&A* 566, A122
- [217] Saraceno, P., Ceccarelli, C., Clegg, P., et al. 1996, *A&A*, 315, L293
- [218] Scargle, J. D. 1982, *ApJ*, 263, 835

- [219] Schmidt-Kaler Th., 1982, in Schaifers K., Voigt H. H., Landolt H., eds, Landolt-Bornstein, Vol. 2b, Springer, Berlin, p. 19
- [220] Scholz, A., & Eislöffel, J. 2004, *A&A*, 419, 249
- [221] Scoville, N. Z., Yun, M. S., Sanders, D. B., Clemens, D. P., & Waller, W. H. 1987, *ApJS*, 63, 821
- [222] Schmidt, K. H. 1958, *Astronomische Nachrichten*, 284, 76
- [223] Shu, F., Najita, J., Ostriker, E., et al. 1994, *ApJ*, 429, 781
- [224] Sicilia-Aguilar, A., Hartman, L. W., Hernández, J., Briceño, C., & Calvet, N. 2005, *AJ*, 130, 188
- [225] Sicilia-Aguilar, A., Hartmann, L., Calvet, N., et al. 2006, *ApJ*, 638, 897
- [226] Siess, L., Dufour, E., & Forestini, M. 2000, *A&A*, 358, 593
- [227] Skrutskie, M. F., Cutri, R. M., Stiening, R., et al. 2006, *AJ*, 131, 1163
- [228] Solomon, P. M., Rivolo, A. R., Barrett, J., & Yahil, A. 1987, *ApJ*, 319, 730
- [229] Spitzer, L. 1978, *Physical processes in the interstellar medium*, by Lyman Spitzer. New York Wiley-Interscience
- [230] Stassun, K. G., Mathieu, R. D., Mazeh, T., & Vrba, F. J. 1999, *AJ*, 117, 2941
- [231] Stetson, P. B. 1987, *PASP*, 99, 191
- [232] Stetson, P. B. 1992, *Astronomical Data Analysis Software and Systems I*, 25, 297
- [233] Strömgren, B. 1939, *ApJ*, 89, 526
- [234] Strom, K. M., Margulis, M., & Strom, S. E. 1989, *ApJ*, 345, L79
- [235] Strom, K. M., Strom, S. E., Edwards, S., Cabrit S., Skrutskie, M. F., 1989, *AJ*, 97, 1451

- [236] Stutzki, J., Stacey, G. J., Genzel, R., et al. 1988, *ApJ*, 332, 379
- [237] Surace, J. A., Sanders, D. B., & Mazzarella, J. M. 2004, *AJ*, 127, 3235
- [238] Sugitani, K., Fukui, Y., Mizuni, A., & Ohashi, N. 1989, *ApJ*, 342, L87
- [239] Sugitani, K., Fukui, Y., & Ogura, K. 1991, *ApJS*, 77, 59
- [240] Sugitani, K., & Ogura, K. 1994, *ApJS*, 92, 163
- [241] Sofue, Y., Takahara, F., & Hirabayashi, H. 1983, *PASJ*, 35, 447
- [242] Tapia, M., Persi, P., Bohigas, J., & Ferrari-Toniolo, M., 1997, *AJ*, 113, 1769
- [243] Tatematsu, K., Nakano, M., Yoshida, S., Wiramihardja, S. D., & Kogure, T. 1985, *PASJ*, 37, 345
- [244] Tauber, J. A., Lis, D. C., & Goldsmith, P. F. 1993, *ApJ*, 403, 202
- [245] Torres-Dodgen A. V., Weaver W. B., 1993, *PASP*, 105, 693
- [246] Van der Berg, S., 1966, *AJ*, 71, 990
- [247] van Dokkum, P. G. 2001, *PASP*, 113, 1420
- [248] Wachmann A. A., 1996, *Astr. Abh. Stern. Hamburg-Bergedorf*, 7, 341
- [249] Walborn N. R., Fitzpatrick E. L., 1990, *PASP*, 102, 379
- [250] Wang, W.-H., Cowie, L. L., Barger, A. J., Keenan, R. C., & Ting, H.-C. 2010, *ApJS*, 187, 251
- [251] Werner, M. W., Roellig, T. L., Low, F. J., et al. 2004, *ApJS*, 154, 1
- [252] Whitworth, A. P., Bhattal, A. S., Chapman, S. J., Disney, M. J., & Turner, J. A. 1994, *MNRAS*, 268, 291
- [253] Wright, E. L., Eisenhardt, P. R. M., Mainzer, A. K., et al. 2010, *AJ*, 140, 1868-1881

- [254] Williams, J. 2002, Hot Star Workshop III: The Earliest Phases of Massive Star Birth, 267, 237
- [255] Wilking, B. A. 1989, PASP, 101, 229
- [256] Wolk, S. J., Rice, T. S., & Aspin, C. 2013, ApJ, 773, 145
- [257] Yudin, R. V. 2000, A&AS, 144, 285
- [258] Zavagno, A., Deharveng, L., Comerón, F., et al. 2006, A&A, 446, 171
- [259] Zealey, W. J., Ninkov, Z., Rice, E., Hartley, M., & Tritton, S. B. 1983, ApL, 23, 119